PREDICTION AND ASSESSMENT OF CORROSION-FATIGUE IN OFFSHORE WIND TURBINES

OKENYI VICTOR ADEJO

B.Sc. (Hons), M.Sc. (Eng)

A thesis submitted in partial fulfilment of the requirements of Nottingham Trent University for the degree of Doctor of Philosophy

July 2024

Copyright statement

Declaration statement

I affirm that this work is my original creation. Any sections, ideas, or insights from external sources have been explicitly credited and referenced. The content presented in this thesis is based on research conducted following the official approval date and aligns with the postgraduate research guidelines provided by Nottingham Trent University.

Signature: ___Okenyi Victor Adejo_____

Date: _____31/07/2024_____

Dedication

I thank God for this opportunity. I dedicate this thesis to my parents, John and Rachel Okenyi, for their constant love and support. To my sisters, Faith and Grace, thank you for always believing in me. Thank you S.M. This success belongs to all of us.

Acknowledgement

I want to thank everyone who has supported me throughout my research journey at Nottingham Trent University.

I am deeply thankful to my director of studies, Dr. Shukri Afazov, for his invaluable guidance. His consistent availability and dedication have shaped my academic journey. To Dr. Petros Siegkas, I appreciate your believing in me and making this project possible. To Dr. Mahdi Bodaghi, I am grateful for your advice and readiness to support me through this research program. To Professor Neil Mansfield, I am grateful for deciding to invest in this research project through your approvals and provision of every resource to ensure the timely completion of this research project.

I've had the opportunity to collaborate with research laboratories and many dedicated researchers. I acknowledge Sheffield's Advanced Manufacturing Research Centre (AMRC) for material facilitation. I acknowledge Dr. Martin Alexander Eder and Søren Fæster from the Technical University of Denmark and Dr Tiziana Marrocco from the University of Strathclyde.

I'm grateful to Nottingham Trent University for funding this research and the Doctoral School's support. I appreciate NTU Global and Imaging, Materials and Engineering Centre (IMEC) for their funding consideration.

The technicians, research fellows, and staff at Nottingham Trent University have also been pivotal in my journey. I appreciate the technicians Iain Mitchell, Damien Goy, and Xzara Foster.

List of publications, conferences, and awards

Published

- Victor Okenyi, Mahdi Bodaghi, Neil Mansfield, Shukri Afazov & Petros Siegkas (2022). A review of challenges and framework development for corrosion fatigue life assessment of monopile-supported horizontal-axis offshore wind turbines, *Ships and Offshore Structures*, Taylor & Francis. DOI: 10.1080/17445302.2022.2140531
- Victor Okenyi, Shukri Afazov, Neil Mansfield, Martin Alexander Eder, Asger Bech Abrahamsen, Søren Fæster, Mahdi Bodaghi & Petros Siegkas (2023). Corrosive surface morphology-based methodology for fatigue assessment of offshore welded structures. *Fatigue & Fracture of Engineering Materials & Structures*, Wiley. DOI: 10.1111/ffe.14162
- Victor Okenyi, Mahdi Bodaghi, Neil Mansfield, Shukri Afazov & Petros Siegkas (2023). Stress analyses of high-rated capacity large diameter offshore wind turbines: Analytical and numerical analyses of uniform corrosion effects. *Proc IMechE Part C: J Mechanical Engineering Science*, Sage. DOI: 10.1177/09544062231208551
- Victor Okenyi, Shukri Afazov, Neil Mansfield, Petros Siegkas, Ahmad Serjouei, & Mahdi Bodaghi (2024). Fatigue testing approach utilising machining cutting forces and fixture design. *Experimental Mechanics*, Springer. DOI: 10.1007/s11340-024-01068-8

Publications Accepted

- Victor Okenyi, Mahdi Bodaghi, Neil Mansfield, Shukri Afazov & Petros Siegkas (2024). Soil Effects on Structural Integrity of Large Diameter Offshore Wind Turbine Substructure Using Finite Element Analysis: A Comparative Study. *Journal of Physics: Conference Series*. IOP Publishing.

Publications Under review

- Victor Okenyi, Shukri Afazov, Neil Mansfield, Petros Siegkas, Tiziana Marrocco, & Mahdi Bodaghi (2023). Material performance of submerged arc welded S355G10+M steel for offshore wind turbines. *Marine Structures*. Elsevier.

Conferences

- Modern Practice in Stress and Vibration Analysis (MPSVA 2022).
- Nottingham Trent University STAR Conference (2022).
- The Wind Energy Science Conference (WESC 2023).
- Seminar - NTU School of Science and Technology (2023)

Awards

- The Vice Chancellors Nottingham Trent University Studentship winner (2021)
- Turing Scheme Grant winner (2022)
- Imaging, Materials and Engineering Centre (IMEC) QR fund winner (2022)

Abstract

Offshore wind energy has seen substantial growth globally as part of a shift towards net zero. Offshore wind turbines with predominant fixed-bottom monopile support structures are near their end of service life, necessitating assessments of their remaining life. The sector confronts fatigue challenges, environmental concerns such as corrosion from harsh conditions as they expand into deep seas, damage assessment challenges, and design optimisation challenges.

This study aimed to develop a novel corrosion-fatigue damage theory for predicting corrosion-fatigue damage and remaining life in monopile-supported horizontal-axis offshore wind turbines.

The research methodology involved experimental investigations, analytical estimations, and computational modelling. The experimental work involved the fabrication of structural steel plates, mechanical tests, fatigue tests, and corrosion characterisation analyses. Analytical methods were applied using the beam theory, linear wave theory, and blade element momentum approach. Computational modelling involved applying finite element analysis in stress analysis for uniform corrosion and soil-structure interaction and assessing residual stress.

The results showed that the splash zone may accumulate the most damage over time owing to monopile thickness reduction and local pits. The fatigue life of materials appeared less influenced by thickness effects and more by a combination of stress concentration, residual stress, axial misalignment, and angular distortion. An S-N curve for corrosion-fatigue assessment applying a corrosion-based fatigue prediction model was developed. These results were integrated into a corrosion-fatigue damage theory applied to operational loads for predicting the remaining life of offshore wind turbines. In conclusion, the developed theory showed great promise for assisting engineers and stakeholders with vital information for corrosion-fatigue assessment of offshore wind turbines necessary for effective maintenance, decommissioning, and life extension.

Table of contents

List of figures

List of tables

List of abbreviations

AW	As-welded
FEA	Finite Element Analysis
HAOWT	Horizontal-axis Offshore Wind Turbine
HAZ	Heat-Affected Zone
HFMI	High Frequency Mechanical Impact
SAW	Submerged Arc Welding
SCF	Stress Concentration Factor
S-N	Stress- Number of Cycles
UTS	Ultimate Tensile Strength
WEDM	Wire Electro-Discharge Machining
3-D	Three-dimensional
IEC	International Electrotechnical Commission
IIW	International Institute of Welding
DNV	Det Norske Veritas
UK	United Kingdom
BS	British Standards
ASTM	American Society for Testing Materials

Nomenclature

σ_r^f	Stress Range (σ_r)	σ_a^f	Stress Amplitude (σ_a)
$\sigma_{max/min}$	Maximum/Minimum stress	σ_m	Mean Stress
R	Stress Ratio	N_f	Number of Cycles (N)
D_f	Damage	σ_{norm}	Nominal Stress
e	Axial Misalignment	α	Angular Distortion
T	Tension	C	Compression
s	Time (seconds)	HB	Brinell Hardness
σ_u	Ultimate Tensile Strength	N_d	Number of Cycles for the Specific Load Case
F	Applied Load	ki	Thickness Exponent
$\bar{a}$	Intercept of the Design S-N Curve with the Log N Axis	t	Thickness
L	Length	$K_{m-axial}$	Axial Magnification Factor
K_{m_T}	Total Stress Magnification Factor	K_{m-ang}	Angular Magnification Factor
σ_y	Yield Stress	H	Hardness
E	Elongation	T_w	Wave Period
C_sC_d	Structural Factor	α	Angle Between Wind Direction and Tower Axis
d	Depth	$c(t)$	Corrosion Loss
d_o	Original Thickness	τ_f	Shear Strength of Soil
γ'	Submerged Unit Weight of Soil	E	Young's Modulus
v	Poisson's Ratio	$\emptyset$	Internal Friction Angle
Ψ	Angle of Dilatancy	δ	Residual Friction Angle
c	Cohesion	σ^1	Effective Nominal Stress

σ_1'	First Principal Stress	σ_3'	Third Principal Stress
KeV	Energy	f_c	Corrosion Factor
f_n	Notch Factor	a	Pit Depth
q	Notch Sensitivity	f_s	Surface Factor
k_f	Fatigue Stress Concentration Factor	k_{scf}	Static Stress Concentration Factor
C_m	Material Constant	a	Material Constant
R_a	Surface Roughness	S_a	Arithmetical Mean Height
S_q	Root Mean Square Height	S_{40z}	Average Maximum Height
S_{sk}	Skewness	S_{ku}	Sharpness of the Surface Roughness
S_p	Highest Peak	S_v	Deepest Valley
r	Radius	σ'	Fatigue Strength Coefficient
b	Fatigue Strength Exponent	n	Number of Load Cases
Z	Height	At	Amplitude
A_s	Swept Area of the Blades	A	Cross-Sectional Area
M	Moment	$R(t)$	Structural Capacity After Corrosion Loss
F_y	Force in Y-direction	$\dot{U}$	Acceleration of Flow
KPa	Pressure (kilopascals)	F_{wave}	Wave Load on Monopile
F_T	Thrust Force	F_w	Wind Load on Tower
σ_b	Bending Stress	U	Velocity of Flow
σ_y^t	Tensile Stress in the Y-direction	M_T	Total Bending Moment
σ_b^t	Tensile Bending Stress	σ_b^c	Compressive Bending Stress
σ_y^c	Compressive Stress in the Y-direction	σ_c	Compression Stress
C_T	Coefficient of Thrust	ρ	Mass Density of Air
A_p	Projected Area	U_w	Wind Velocity

C_c	Shape Coefficient	R_e	Reynolds Number
V_m	Mean Wind Speed	V_b	Basic Wind Speed
$C_r(Z_e)$	Terrain Roughness Factor	$I_v(Z)$	Turbulence Intensity Factor
C_D	Coefficient of Drag	C_M	Coefficient of Inertia
k	Wavenumber	λ	Wavelength
D	Diameter	I	Moment of Inertia
y	Vertical Distance away from Neutral Axis	P	Perimeter Area Exposed to Seawater
K	Bending Factor	$d(t)$	Remaining Thickness

Chapter 1

Introduction

Offshore wind energy has witnessed remarkable growth, with installations in 2023 increasing by 16.1 Gigawatts from the value recorded in 2021, reaching a global capacity of 64.3 Gigawatts (Hutchinson, Zhao 2023). In 2022, the United Kingdom (UK) led the surge in Europe with a total offshore wind capacity of 14.1 Gigawatts, as reported in Figure 1.1. As a front-runner in this domain, the UK aims to amplify its capacity to 20-55 Gigawatts by 2050 (James, Ros 2015). This shift towards renewable energy sources, particularly offshore wind, is pivotal in diminishing reliance on carbon-based energy. A pivotal factor in making offshore wind energy cost-effective is enhancing the structural design and durability of offshore wind turbines. More offshore wind turbines require larger supporting substructures as installations venture into deeper waters, and their associated operational and maintenance costs escalate, as evidenced by European offshore wind farm data (Morthorst, Kitzing 2016).

In the UK, the predominant offshore wind turbine support structures are fixed-bottom types, with monopiles being the most popular due to their ease of installation and proven track records (Lombardi et al. 2013). With these structures designed to last approximately 20 years, it is noteworthy that some are already nearing their 15-year mark. In 2021 alone, 196 horizontal-axis offshore wind turbines (HAOWTs) commenced operations, 90 of which were founded on monopiles (World Forum Offshore Wind e.V. 2021). Innovations in this field are unceasing, with a record 15 Megawatt HAOWT prototype installed (Vestas 2022). This constant installation underscores the need to assess the longevity of existing and new large-diameter HAOWT monopiles. However, the wind sector faces challenges such as aerodynamic and hydrodynamic effects, soil-structure interaction, and design optimisation. Other concerns are related to environmental challenges owing to the rigorous operating conditions and high expenses associated with the complete lifecycle of these turbines. In addition to the physical asset management issues arising from their remote, deeper water locations and performance challenges, especially at the welds of structures such as monopiles, present hurdles such as the transient stress fields in welded monopile sections (Igwemezie et al. 2018).

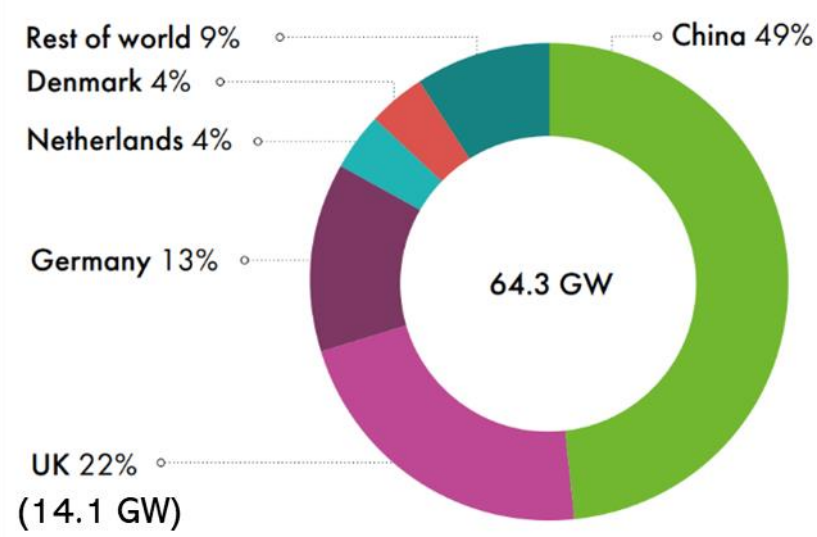

Figure 1.1: Total offshore wind power capacity as of 2022 (Hutchinson, Zhao 2023).

1.1 Monopiles in offshore wind turbines

Support structures for offshore wind turbines include jackets, gravity foundations, tripods, suction caissons, and monopiles, with some having floating substructures (O'Kelly, Arshad 2016). In the UK, monopiles are predominant and are used in approximately 96% of the offshore wind turbines (Higgins, Foley 2014). These monopiles are typically installed at sea depths of up to 35m but can also be used in deeper waters. During the first half of 2017, the UK witnessed the installation of 110 such foundations, indicating the growth of HAOWTs (Wind Europe 2017). Figure 1.2 shows a typical monopile design. HAOWT's monopiles are considered economical due to their reduced maintenance costs (Oh et al. 2013). With time, their size is increased for enhanced power generation, as tower height is directly related to wind speed (Lavanya, Kumar 2020). By 2025, a 15% increase in tower height, reaching approximately 150 m, is anticipated (Igwemezie et al. 2019). The incorporation of high-strength concrete to produce hybrid monopiles has been a research focus (Jammes et al. 2013; Chen et al. 2018; Ma, Yang 2020). All of these underscores the need for innovation and improvement of offshore structures.

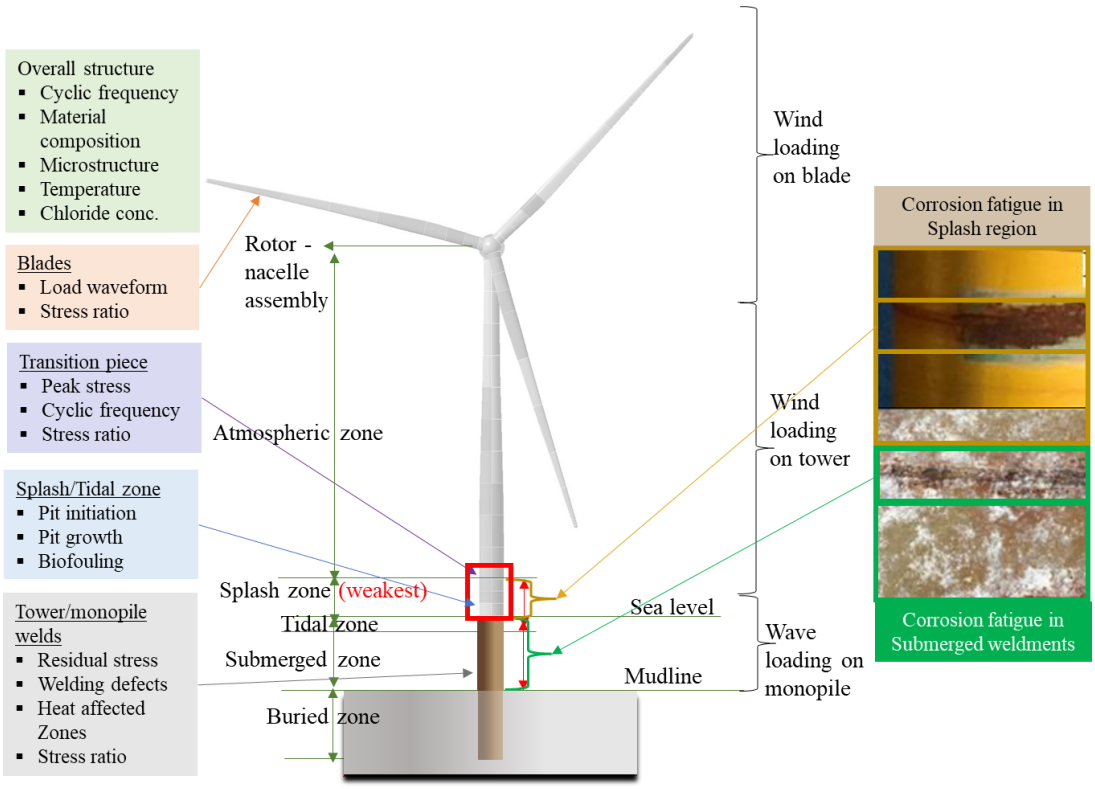

Figure 1.2: Different loading zones and in-service deterioration mechanisms in offshore wind turbines

Future offshore wind turbines will have larger rotor diameters and hub heights that match their increased power capacity. This also implies a greater overturning moment for the monopile. Recognising the stresses in these structures and understanding their environmental effects are critical. Figure 1.2 illustrates the different loading zones in a HAOWT in-service as well as the deterioration mechanism contributing to corrosion fatigue damage at the different parts of the support structure and entire wind turbine structure. Lateral loads introduce bending stresses in these monopiles, and the identification of critical stresses is crucial for assessing potential damage risks. The top thrust force on the HAOWTs during operation becomes significant due to its design for maximum power production. The loads and bending moments of large structures may pose concerns in deeper seas and under varying soil conditions. Past studies have mainly explored soil-pile interactions of wind turbine supports using numerical methods, accounting for soil profiles and dynamic effects below ground (Achmus et al. 2009; Ahmed, Hawlader 2016; Bisoi, Haldar 2014). Thus, the influence of soil profiles on stresses in submerged and base weld areas, especially for large-diameter HAOWT foundations under lateral forces, needs to be investigated.

Given their newer installation in deep seas, there is a growing need to study the mechanical behaviour of these support structures, especially large-diameter monopiles in HAOWT (Rejovitzky, Altus 2013; Adedipe et al. 2015). The potential challenges of larger loads and bending moments become more pronounced in deeper waters. Various experimental and modelling methods have been utilised to examine corrosion-fatigue using different damage theories (Bergara et al. 2017; Sun, Jahangiri 2019). More in-depth research is essential to better understand the fatigue mechanisms of these structures, particularly in harsh environments.

1.2 Corrosion-fatigue challenges in monopiles

Fatigue in HAOWT operation arises from cyclic stresses induced in marine conditions, where corrosion plays a significant role. Corrosion-fatigue describes the damage caused by repetitive loading in these corrosive surroundings (Suresh 1992). The presence of corrosion amplifies fatigue damage, leading to quicker crack growth in metals. This can result in fractures, swift deterioration, and system failures, with pitting corrosion being the primary concern. Corrosion-fatigue remains a vital issue in offshore wind turbine foundations (Dong et al. 2012). Maintenance against corrosion-fatigue is crucial since 98% of these foundations use structural steel (Ancona, Jim 2001). The significance of pitting to a structure's lifespan necessitates more research on its impact on wind turbine structural steel (Melchers 2010). This type of damage has been studied in various sectors, including power generation, aerospace, marine, oil and gas, and construction (Larrosa et al. 2018).

Uniform corrosion, pitting corrosion, and corrosion-fatigue are the major corrosion types in offshore wind turbine support structures(Price, Figueira 2017; Okenyi, Bodaghi, et al. 2023). A corroded transition piece as part of the HAOWT support structure is shown in Figure 1.3. Pitting is notably harmful and evolves over time owing to pit amalgamation, which leads to consistent volume loss (Melchers 2018). Pitting affects the structural integrity as the material undergoes thickness loss, resulting in escalated stresses and potential material failure if the strength limits are reached (Dong et al. 2012). Both uniform and pitting corrosion cause local stress, but the long-term implications are more pronounced with uniform corrosion.

Technological advancements in computation, the Internet of Things, and real-time monitoring have paved the way for improved HAOWT management. Digital twins create digital versions of real-world scenarios using embedded sensors to automate and optimise maintenance processes. Digital twin is particularly beneficial in deeper marine areas where manual checks are costly and risky (Wang 2020). Digital twins can help engineers make informed decisions that prolong the HAOWT lifespan. The purpose of the digital twin is to monitor corrosion fatigue and facilitate predictive maintenance in the support structure. Structural health in the splash zone which is the most susceptible zone of monopiles would be monitored for corrosion fatigue through the incorporation of sensors with damage models in data and simulation-driven models. However, more research is needed on the effects of corrosion on steel, especially the newer S355 thermomechanical rolled steel, as HAOWTs grow in size and the thickness effects become more pronounced.

Figure 1.3: Extent of corrosion in splash zone region (ABFAD 2020).

1.3 Importance of corrosion-fatigue assessment in monopiles

The challenges of corrosion-fatigue in offshore wind turbines and other offshore structures have been evident in the past two decades, based on reports of the collapse of many wind turbine support structures. These challenges are multifaceted, making research in this area intricate and paramount. Notably, aerodynamic forces during storms and typhoons are the primary culprits of these collapses, with the most damage occurring at the beginning and end of the life stages of the structures (Ma et al. 2019).

This underscores the necessity for a holistic methodology that can be applied to various welded offshore structures. The key to this is understanding the variations in local stresses across the support structure due to load fluctuations. In addition, there is insufficient insight into the role of the hub thrust force in influencing the total design and operational load which needs to be researched.

Due to their robust design and increasing diameter, monopile foundations dominate the foundation for offshore wind turbines (Igwemezie et al. 2019). Their increasing utilisation requires a comprehensive understanding of their mechanical behaviour, especially under dynamic loads. A key aspect to consider is the soil-structure interaction (SSI), which significantly influences the structure's dynamic properties and consequently contributes to fatigue damage in monopiles (Zaaijer 2006). However, existing studies have predominantly focused on soil-pile interactions in HAOWT support structures, leveraging numerical analyses to grasp the soil profile dynamics in the buried region (Achmus et al. 2009; Ahmed, Hawlader 2016; Bisoi, Haldar 2014). The stresses generated in monopiles and their response to lateral forces in large-capacity HAOWT, particularly concerning soil profile variations, need to be sufficiently addressed for recent large-diameter monopiles with high power capacity and deep-sea conditions.

As many offshore structures approach their end-of-life, a comprehensive fatigue life analysis incorporating corrosion impacts becomes essential to streamline in-service inspections, ensure reliability, and optimise operational efficiency. The welding quality, particularly in the heat-affected zone (HAZ), significantly affects the fatigue resistance of HAOWT monopiles, which are commonly constructed from welded hot-rolled structural steel plates. Indeed, such plates have demonstrated superior fatigue performance compared to normalised offshore steel (Igwemezie et al. 2018; Okenyi, Afazov, et al. 2023). However, factors such as manufacturing defects, stress concentration at welds, and corrosion pitting significantly affect structural steel material fatigue performance in offshore environments (Mehmanparast et al. 2017). Thus, there is a pressing need for a holistic fatigue assessment approach, especially for structural steel used in offshore applications. Structural steel, renowned for its weldability and durability according to British Standards (BS) 10025-2 (British Standards Institution 2019a), holds immense promise in the offshore, shipbuilding,

and construction sectors. Its application in HAOWT support structures is noteworthy (Igwemezie et al. 2018; Okenyi et al. 2022). Investigations into structural steel mechanical attributes, welding dynamics, and subsequent implications such as distortion and residual stress are crucial to maximise its potential. Fatigue, a pervasive concern across sectors such as aerospace and automotive, significantly undermines the structural integrity (Becker et al. 2021; Suryanarayana 2011). In several industries, metal components subjected to cyclic loading require meticulous design to avoid fatigue-induced failure. In applications such as bridges and wind turbines, components endure multidirectional cyclic loads, spawning unique stress scenarios under uniaxial loading (Dantas et al. 2021). Given these challenges, there is an evident demand for an innovative approach to ascertain and validate the fatigue resistance of offshore structural steel in HAOWTs promptly, thereby fostering industrial efficiency and cost-effectiveness.

1.4 Aim of research

This research aims to advance the understanding and development of methodologies for evaluating corrosion-fatigue as a material failure mechanism in large-diameter monopile-supported HAOWT to enable a novel fatigue damage and remaining life prediction pathway.

1.5 Objectives of research

To achieve the aim and ensure novelty in all aspects of this research, the research objectives and techniques designed for this purpose are:

1. To conduct an in-depth literature review to develop a digital twins framework. This framework assesses corrosion-fatigue in monopile-supported HAOWT by examining past and current evaluation methods.
2. To investigate the effects of uniform corrosion on the evolution of stress within different zones of a large-diameter monopile supporting the HAOWT using finite element analysis (FEA) and analytical model.
3. To conduct soil-structure interaction study and its subsequent impact on stresses within large-diameter HAOWT monopiles using FEA and the developed analytical model.

4. To establish an endurance life methodology centred on corrosion surface morphology-based theory to evaluate fatigue in the structural steel of HAOWT monopile weldments.
5. To examine the factors influencing the material fatigue performance of submerged arc butt-welded S355 structural steel using an established fatigue testing method.
6. To develop a novel corrosion-fatigue prediction damage theory by applying real wind and wave data from the Westermost Rough wind farm located in the North Sea within the stress predictive model, coupled with the corrosion surface morphology theory and standard fatigue accumulation technique to facilitate the prediction of the remaining lifespan of an HAOWT support structure.

1.6 Outline of thesis

Chapter 1 of this thesis introduces the monopile support structure of a HAOWT and provides an overview of the challenges of corrosion-fatigue. A research methodology for a corrosion-fatigue monitoring research plan detailing the testing and modelling is presented. Furthermore, the justification, aim, and objectives of the research are outlined. In Chapter 2, a theoretical background study is conducted to understand the underlying theories applicable to corrosion and fatigue in welded structures, as well as the factors influencing this material failure mechanism. Chapter 3 provides a further extensive review of literature focusing on materials used in HAOWT installation, previous work on modelling and soil effects consideration, endurance life approach for fatigue assessment, and assessment of digital tools for fatigue assessment in HAOWT to develop a novel framework. Chapters 4-8 address the objectives of the research in detail. Chapter 4 reports on stress analysis at welds for uniform corrosion and soil effects considering soil-structure interaction and develops the analytical model using a case study prototype 15 Megawatt offshore wind turbine which is verified using FEA. Chapter 5 conducts an experimental investigation of the material performance of submerge arc welded S355G10+M structural steel, including measurements of tensile properties, macrostructure, hardness, residual stresses, angular distortions and axial misalignments. In Chapter 6, a novel corrosion surface morphology-based methodology for fatigue assessment is presented.

In Chapter 7, fatigue testing is detailed using uniaxial testing, and the concept of machining for fatigue testing is introduced and verified. Chapter 8 combines the novelty of previous chapters to develop a novel fatigue theory incorporating corrosion considerations and applying real wind and wave load history to determine the fatigue damage and predict the remaining life of HAOWT support structures. Chapter 9 provides vital conclusions from this novel study and provides future recommendations based on the research. A schematic depicting the thesis outline is shown in Figure 1.4.

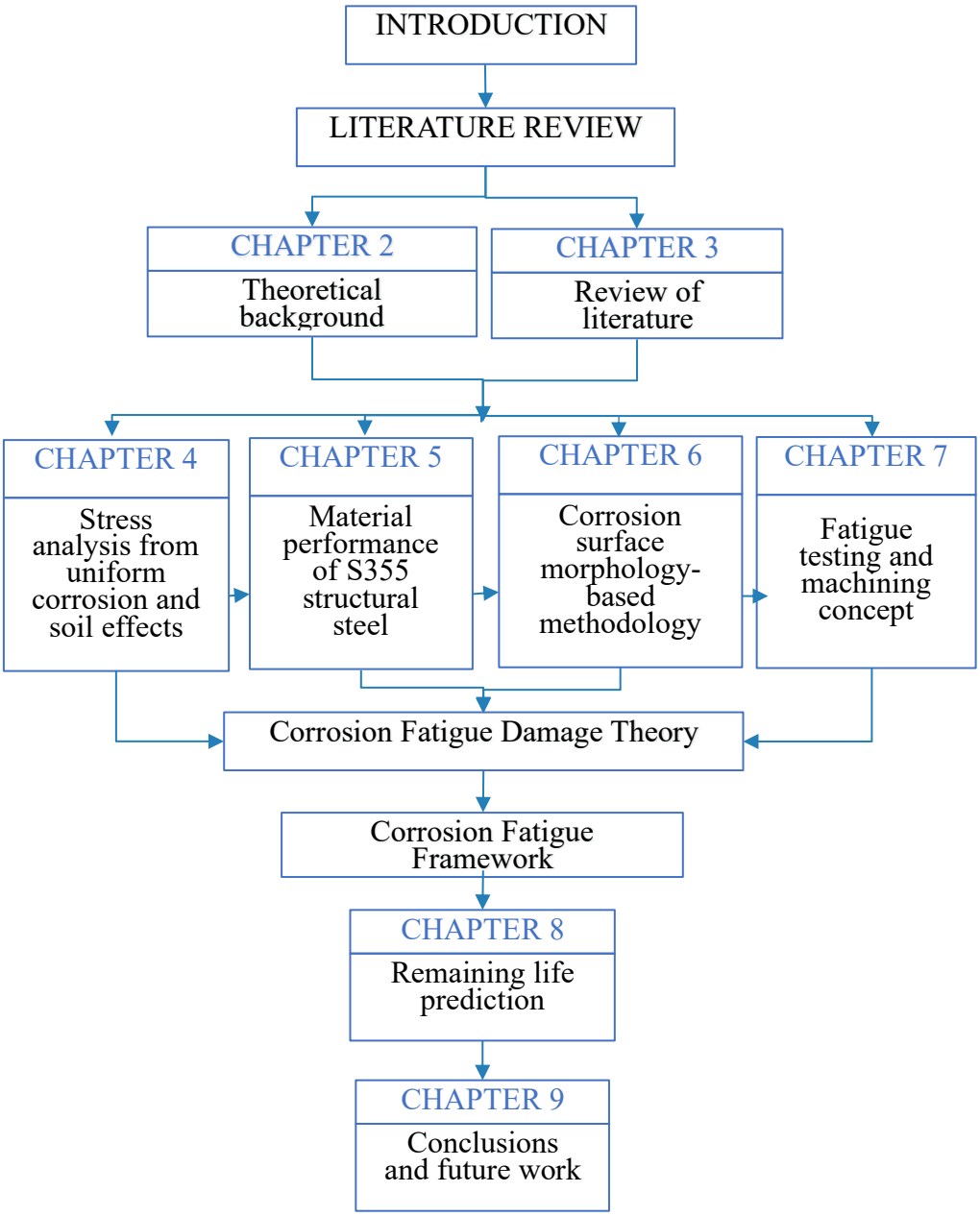

Figure 1.4: Outline of the thesis.

1.7 Outline of methods

The methodology applied in this research incorporates three primary assessment methods: experimental investigations, analytical estimations, and computer modelling as illustrated in Figure 1.5. The present study focuses on the experimental aspects related to the manufacture and production processes of structural steel plates utilised in the fabrication of monopiles for offshore wind turbines. Four primary sets of experiments were performed on the welded plates and cut specimens: mechanical tests, tests to characterise corroded materials, fatigue tests, and formulation of a concept for fatigue testing. Stress versus number of cycles (S-N) curves were created for specimens subjected to various conditions, including exposure to both air and corrosive environments.

This study applies analytical methods utilising the Euler-Bernoulli beam theory to analyse the HAOWT structure. Linear wave theory was utilised to describe sea waves in accordance with Morrison's equation, which accounts for hydrodynamic forces. The Blade Element Momentum approach was employed in conjunction with one-dimensional wave theory to ascertain the loads acting on the HAOWT. The integration of these theoretical frameworks, load scenarios, and empirical data collected from wind turbine installations was employed to construct an analytical framework for assessing cyclic stresses and estimating fatigue levels.

The study incorporated computational modelling by utilising FEA as a crucial aspect. This approach was employed to assess the stresses resulting from uniform corrosion, interactions between the soil and structure, and the impacts of residual stress. The contour method was applied to evaluate these residual stresses for the monopile and materials in its weld region. The findings derived from this study provide insights into the estimated corrosion level in the monopile, fatigue performance of the material, and impact of soil profiles at various sites where the monopiles were deployed. In summary, experimental investigations, analytical approximations, and computer modelling techniques were integrated to assess corrosion-fatigue degradation and predict the remaining fatigue life.

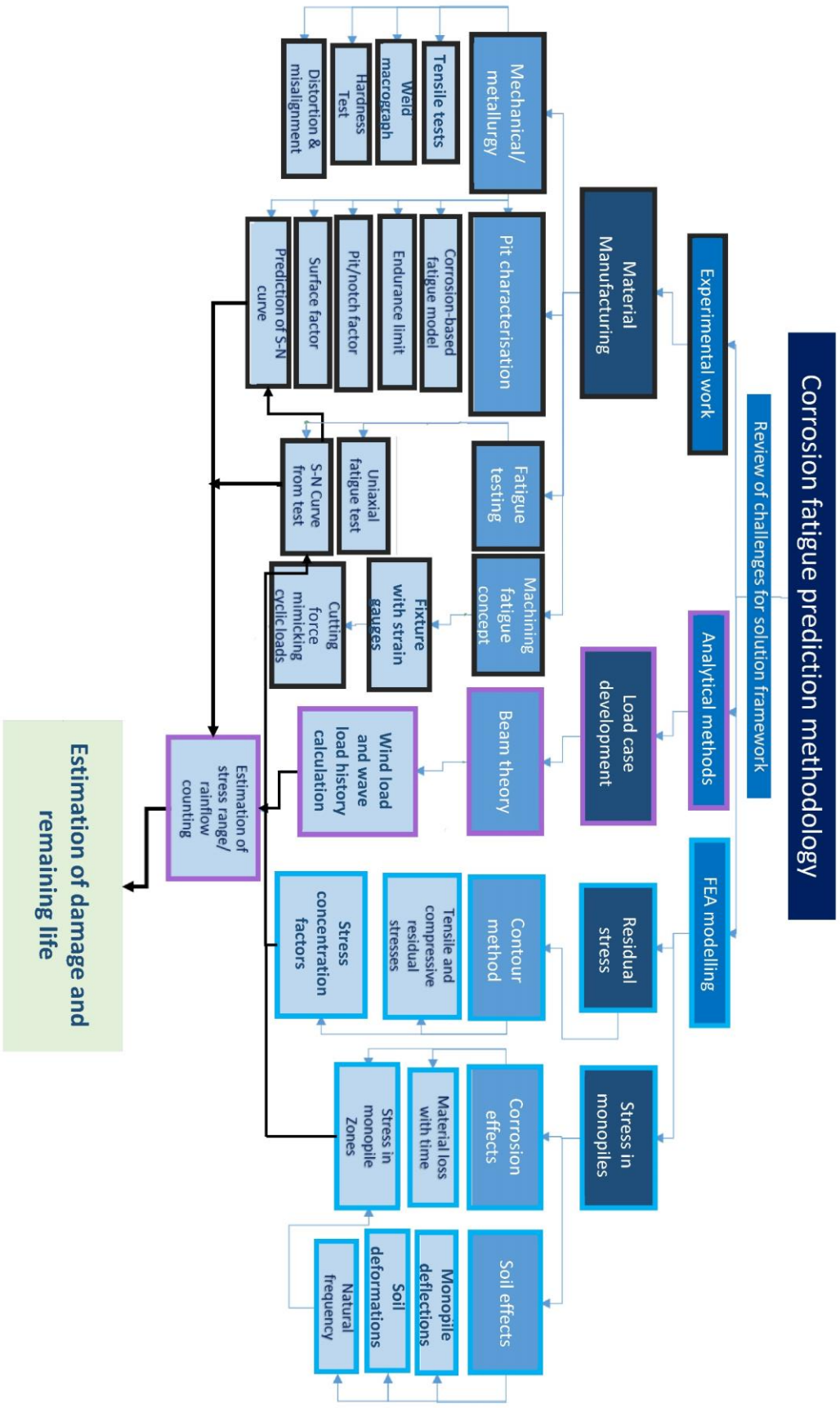

Figure 1.5: Overview of research methods.

Chapter 2

Theoretical background

This chapter explains the complexities of fatigue and corrosion in offshore structures. It explains the phenomena of fatigue and corrosion experienced in offshore structures, setting the stage for a more in-depth examination of the numerous loading and operational elements that contributed to or accelerated the corrosion-fatigue process. The chapter also offers an overview of various fatigue analysis methodologies and associated fracture mechanics models. Welded joints have received particular attention, as they are crucial sites that frequently display different fatigue behaviours compared to other sections of the structure. The chapter summarises the theoretical insights and connects them to the study's broader context. Overall, the chapter aims to provide a thorough comprehension of the theoretical concepts that are critical to fulfilling the study's research objectives.

2.1 Fatigue and corrosion in offshore structures

The interplay between corrosion and fatigue can have a damaging effect on metallic materials. Corrosion-fatigue is a time-dependent electrochemical process that usually occurs at specific locations, such as slip steps or the tip of a crack. Two primary mechanisms govern this process: anodic slip dissolution and hydrogen embrittlement. Anodic slip dissolution influences crack growth rates depending on loading conditions, such as frequency and stress waveform. Hydrogen embrittlement, on the other hand, is influenced by factors like the rate of protective film rupture, passivation rate, and the rate at which the solution is renewed (Suresh 1992).

However, there can also be instances in which corrosion mitigates fatigue. Some corrosion by-products may lead to "oxide-induced crack closure." This is a phenomenon in which the elasticity around a crack tip prevents further plastic deformation or reduces the stress intensity factor, thereby slowing the crack growth (Pippan, Hohenwarter 2017; Wu et al. 2020).

When evaluating the corrosion-fatigue strength, an increase in the resistance to pitting corrosion correlates with a decrease in the likelihood of failure at slip zones (Jaske et al. 1981). The rate of pitting corrosion varies based on the marine zone (Mathiesen et al., 2016), with monopiles exhibiting high rates. This makes them susceptible to becoming stress concentration areas, particularly around geometric discontinuities in the weld lines, which serve as initiation points for fatigue cracks.

Corrosion is generally influenced by chemical, physical, and even biological elements like biofouling and plant and animal life. However, when considering the interplay between corrosion and fatigue, other specific factors come into play, complicating their interactions. Corrosion-fatigue involving pitting follows a sequence of stages, including (i) initiation of the pit, (ii) growth of the pit, (iii) transition from pit to crack, and (iv) growth of both short and long cracks (Akid and Richardson 2010; Fatoba 2015). S355 does not form passive film like stainless steel or other high-alloy steels as this is associated with materials with higher chromium content which means that passive film breakdown is not a relevant stage for S355 steel.

Mechanical factors influencing corrosion-fatigue have been categorised into several groups: peak stress (Zhao et al. 2017), cyclic frequency, stress ratio (Okenyi et al. 2022), load waveform (Adedipe et al. 2016; Igwemezie, Mehmanparast 2020), and residual stress (Xin, Veljkovic 2020). Metallurgical factors include the alloy composition, microstructure (Nicolas et al. 2019), welding defects, heat treatment processes (Mehmanparast et al. 2017), and defect factors (micro-cracks, stress concentrations) based on manufacturing conditions (Serjouei, Afazov 2022; Okenyi, Afazov, et al. 2023). Environmental conditions like pH (Kolawole et al. 2019), temperature (Atkinson, Chen 1993), and electrochemical potential (Kovalov et al. 2018) also have an impact. Thus, both material and environmental factors, such as temperature and pH, can directly influence pitting, hence the corrosion-fatigue. As pitting creates localised stress concentrations, these sites become nucleation points for fatigue cracks.

2.2 Fatigue analysis methods and fracture mechanics models

In engineering, a comprehensive understanding of corrosion-fatigue necessitates a thorough investigation into the synergistic impact of mechanical factors and

aggressive environmental conditions. Evaluating such complex interactions is challenging. Within fatigue analysis, there are key methodologies, such as the stress-life method, strain-life method, and linear elastic fracture mechanics. These methods are integral to two main approaches: total life assessment and the damage tolerance approach. Both are crucial for determining the structural integrity and remaining life of engineering structures.

Combining S-N data as a total life approach to predict fatigue life and LEFM as a damage tolerant approach to analyse crack propagation in crucial locations enables full structural health monitoring. This combination improves damage diagnosis and prognosis by revealing fatigue behaviour and fracture risk. S-N data informs inspections, whereas LEFM assesses cracks to optimize maintenance decisions and actions.

The stress-life method as a total life fatigue assessment method is proficient at offering quantitative damage estimations; however, it has limitations. Factors such as surface finish, material thickness, and flaw size can introduce inconsistencies in the method (Fatoba 2015). Such limitations particularly affect the precise prediction of when and where cracks will be initiated. Despite these challenges, the total life method can still estimate material fatigue strength in both air and corrosive environments. In-depth reviews have been conducted on these approaches (Fatoba 2015; Larrosa et al. 2018), summarising both stress-life and linear elastic fracture mechanics methods and drawing important conclusions.

Fatigue failure primarily results from the cyclical or repetitive loading of materials, causing microscopic imperfections to develop into full-fledged cracks. These cyclic loads are often significantly lower than the yield strength of the material. The data representing these phenomena are typically plotted as an S-N curve, which charts stress ranges or amplitudes against the number of cycles to failure (Schijve 2009). The fatigue load cycles and their characteristics are presented in Figure 2.1 and are defined in Equations 2.1 to 2.4.

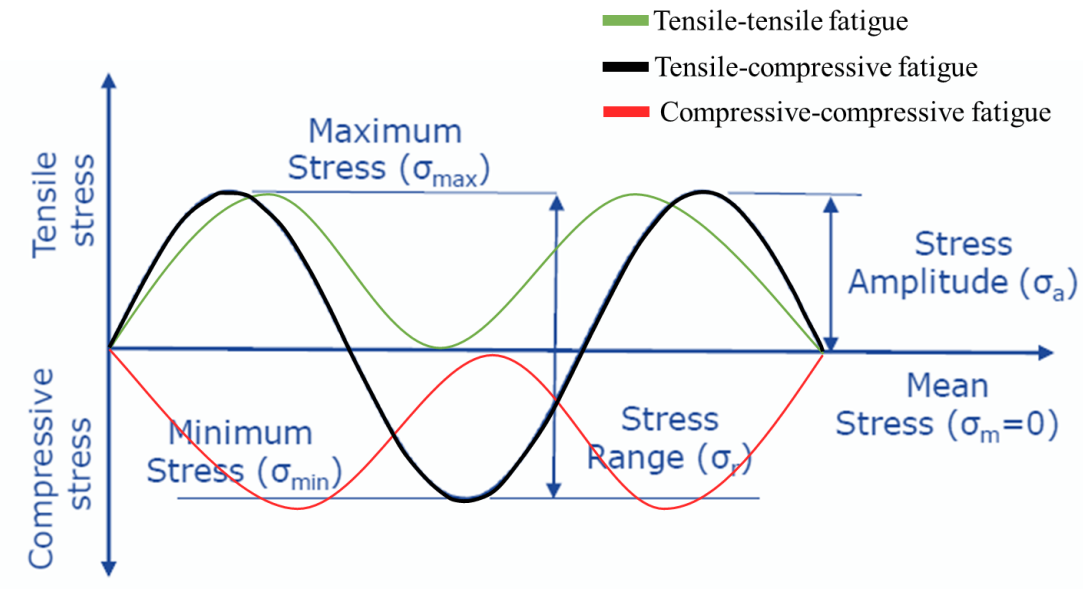

Figure 2.1: Definition of fatigue load cycles.

$$\text{Stress range, } \sigma_r = \sigma_{max} - \sigma_{min} = 2\sigma_a \tag{2.1}$$

$$\text{Stress amplitude, } \sigma_a = \frac{\sigma_{max} - \sigma_{min}}{2} \tag{2.2}$$

$$\text{Mean stress, } \sigma_m = \frac{\sigma_{max} + \sigma_{min}}{2} \tag{2.3}$$

$$\text{Stress ratio, } R = \frac{\sigma_{min}}{\sigma_{max}} \tag{2.4}$$

The Basquin relation in Equation 2.5 mathematically describes the S-N curve, allowing for the determination of a material's endurance limit. S-N curves can be divided into two regions: low-cycle fatigue and high-cycle fatigue. (Ólafsson et al. 2016; Ming et al. 2014).

$$\sigma_r = \sigma' \times {N_f}^b \tag{2.5}$$

where σ' is the fatigue strength coefficient, and b is the fatigue strength exponent.

The industry often employs the endurance-limit approach for practical applications. This approach distinguishes between a high-cycle fatigue region at (10^6) cycles and a low-cycle fatigue region at (10^3) cycles. In the high-cycle fatigue region, the stress amplitude remains constant, marking the endurance limit of the material. Meanwhile, in the low-cycle fatigue region, the stress amplitude diminished as the cycle number increased. Empirical data suggest that at 10^3 cycles, a material's fatigue strength is

approximately 90% of its Ultimate Tensile Strength (UTS), σ_u. These values, 0.9 and 0.5 are approximations based on extensive empirical research, especially for ferrous alloys (Bannantine et al. 1990; Serjouei, Afazov 2022).

$$\sigma_a^f = 0.9 \times \sigma_u \quad \text{at } 10^3 \text{ cycles} \tag{2.6}$$

$$\sigma_a^f = 0.5 \times (f_d f_s) \times \sigma_u \quad \text{at } 10^6 \text{ cycles} \tag{2.7}$$

The surface factor, f_s and the defect factor, f_d quantifies the level of imperfections present on a surface or in the subsurface of a material. For extremely smooth surfaces, this factor approaches a value of 1. Similarly, if there are no defects either on the surface or in the underlying layers, the defect factor is also set at 1.

The mechanical factors considered in Section 2.1 and the additional effect on fatigue life, are summarised in Figure 2.2. Understanding the complexities of corrosion-fatigue requires a multifaceted approach of blending mechanical factors with environmental considerations. Although the current methods provide valuable insights, they have limitations that necessitate ongoing research to refine these techniques for more accurate and comprehensive assessments. For more fatigue analysis of components that often experience complex loading conditions, the rainflow counting technique (Amzallag et al. 1994) allows these stress cycles to be deconstructed into simpler cycles. This streamlined approach aids in estimating fatigue damage using Miner's rule (Miner 1945), as follows:

$$D_f = \sum_{n=1}^{\infty} \frac{N_i}{N_{di}} < 1 \tag{2.8}$$

where D is the damage (<1), n is the number of load cases, N is the calculated number of cycles from the S-N curve, and N_d is the allowable number of cycles for the specific load case.

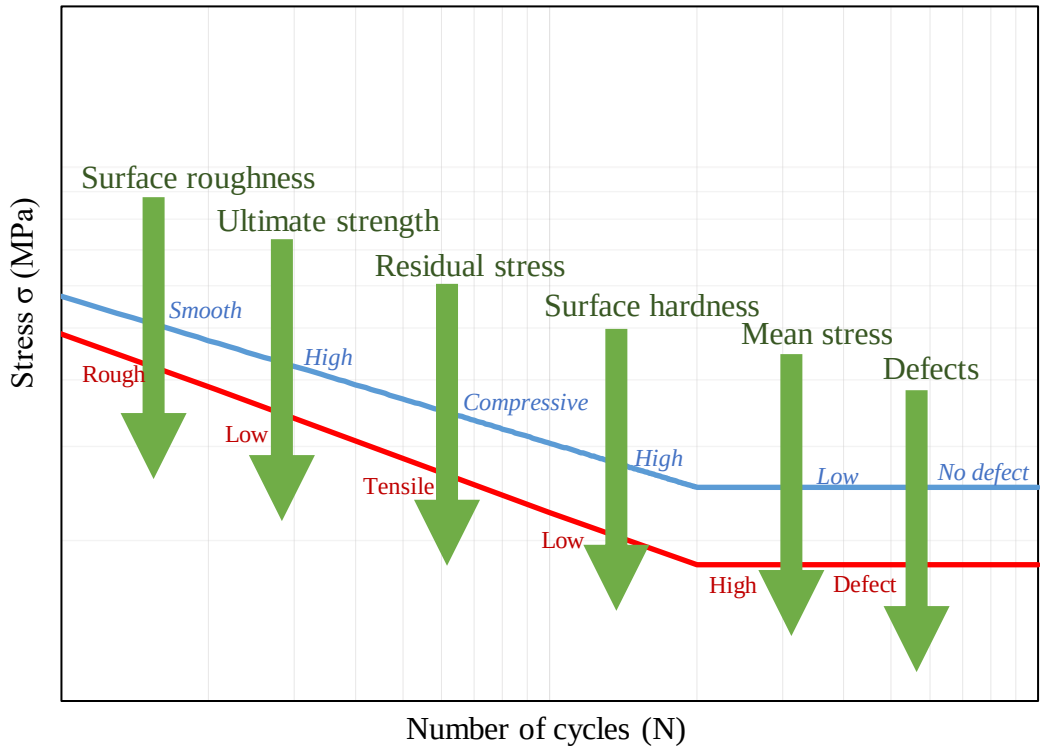

Figure 2.2: Influence of mechanical factors on S-N curves.

For the damage tolerance approach, linear elastic fracture mechanics is employed. Previously used models and theories for various fatigue life stages and damage predictions and several models that focus on crack growth in corrosion fatigue have been researched (Okenyi et al. 2022) (Appendix A9). These models become crucial once a crack has been initiated, as they can guide estimations of the crack's progression over time and help evaluate the potential risks leading to catastrophic failure of materials in service. What makes these models unique is their ability to forecast the period between crack initiation and the risk of ultimate structural failure based on certain assumed loads. Specifically, these models employ fracture mechanics methodologies to account for environmental influences on fatigue crack growth rates. Pitting corrosion-fatigue in the monopile of a HAOWT is a significant concern (Larrosa et al. 2018). This is because pitting corrosion-fatigue is integral to crack initiation and propagation, and it consequently affects the overall structural lifespan. However, current models using fracture mechanics still fully incorporate a comprehensive understanding of how mechanical, metallurgical, and environmental factors collectively contribute to pitting corrosion-fatigue.

The two predominant methods for assessing fatigue damage in metallic materials that are applicable to offshore wind turbine materials are the accumulative fatigue damage and fracture mechanics approaches. The former relies on S-N curves, whereas the latter utilises crack growth rate curves, plotting crack length against the number of cycles. Each approach has a distinct philosophical basis. The fracture mechanics approach is particularly adept at accurately modelling crack propagation until the point of fatigue failure.

By reviewing these fatigue life assessment methodologies, it is clear that the total life method can be enhanced. Specifically, S-N curves can be refined by incorporating variables such as material thickness loss, notch effects, stress concentrations, and surface conditions. These factors, including the quality of the remaining surfaces and manufacturing or installation-induced notches, are crucial as they can significantly impact the rate of corrosion-fatigue damage.

For damage-tolerant methods, employing a fracture mechanics model is particularly beneficial during the operational and wear-out stages. Such models can be used to monitor the progression of damage arising from crack growth and corrosion pits. This approach would have been invaluable for analysing a 2 Megawatt HAOWT, which reportedly experienced failure owing to welding defects (Ma et al. 2019). It is crucial to also consider the HAZ at material weldments when focusing on crack initiation

2.3 Fatigue of welded joints

Welded joints are both permanent and physically simple, requiring fewer components and lowering the complexity of the fabrication procedures. Welded connections, particularly butt welds, have higher stiffness, allowing for more effective load transfer. When properly done, the welded material can outperform the mechanical strength of other parts of the material, such as the HAZ and base metal. However, this welding method has significant drawbacks. For starters, the permanent nature of connections makes disassembly or changes difficult. Second, the heat introduced during welding might change the microstructure of the base metal, jeopardising its mechanical qualities and producing residual stresses. Finally, the process causes material shrinkage, which must be factored into the design estimates. Finally, achieving a high-

quality, dependable weld requires professional operation (Brockenbrough, Merritt 1999; Design 1999).

Arc welding is a fusion welding technique that facilitates the joining of metals through the application of intense heat and the introduction of filler metal. This process induces the melting and merging of the adjacent base metal. When metallic substances undergo solidification and subsequent cooling, they establish a metallurgical interconnection with one another. The arc welding system comprises three main components: a power source, an electrode, and the workpiece. The process of metal melting is facilitated by the generation of intense heat through an electric arc. This arc is created by an electric current passing between two electrodes, namely, the applied electrode and the workpiece. Within this process, the arc is sustained in a gas that has been heated and ionized to form plasma. The plasma serves to conduct the electric current and generate the intense heat necessary for melting the metals. The electrode used in this application can take the form of a non-consumable current-carrying stick or a stick/wire that not only melts but also provides a filler metal to join the workpieces (Singh et al. 2019; Singh, Singh 2019; Saidin et al. 2019; Schönmaier et al. 2021). The utilisation of submerged arc welding (SAW), which is a prevalent technique in the fabrication of monopiles for offshore wind turbines, was examined in the present study. Different types of arc welding are commonly employed in structural steels for offshore wind turbines (Jacob et al. 2019; Yusof, Jamaluddin 2014). Figure 2.3 depicts a representative example of a welded material and its components.

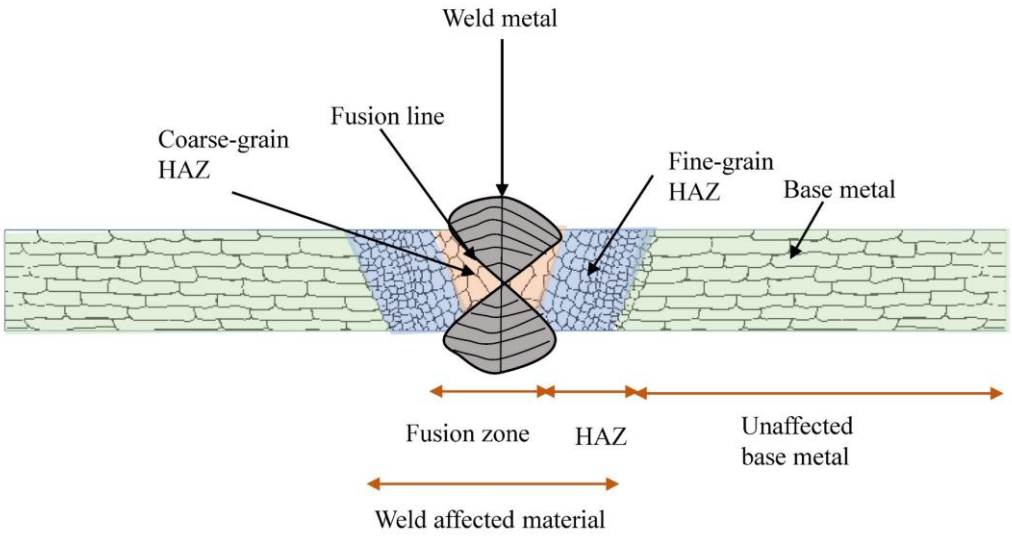

Figure 2.3: Weld zones and grain distributions for a butt-welded joint.

The discontinuities in a welded material are affected by various factors, such as the welding process utilised, the material employed, the type of weld formed, and the joint design. Furthermore, the proper alignment of the joint prior to welding, along with the prevailing working circumstances throughout the welding procedure, exerts substantial influence. It is important to acknowledge that the design criteria frequently vary depending on the specific application. Various fatigue design standards, including BS 7608 (British Standards Institution 2014a) and international organisations, such as the International Institute of Welding (IIW) (International Institute of Welding 2008) and Det Norske Veritas (DNV) (DNV 2016b), have provided recommendations and guidelines for assessing the fatigue life of welded structures. These guidelines include established S-N curves that consider multiple factors affecting fatigue loading.

Structures experience a diverse array of stresses throughout their life cycle, making fatigue assessment an intricate process that must consider these various stressors. In this study, nominal stresses, thickness correction, and stress magnification in welds were considered. The nominal stresses can be determined using beam theory. The stress is determined by evaluating the applied loads and cross-sectional area of the structure. When there is bending stress from misalignment due to the welding process, its effect is included, and the expression is given as (International Institute of Welding 2008):

$$\text{Nominal stress, } \sigma_{norm} = \frac{F}{A} + \frac{My}{I} \tag{2.9}$$

where F is the applied load, A is the cross-sectional area, M is the bending moment, I is the moment of inertia of the cross-section, and y is the distance to the neutral axis.

In welded constructions, the influence of plate thickness is considered if the location of the crack start is at a weld toe. According to the standards, welded connections with a maximum thickness of 25 mm exhibit fatigue resistance. However, owing to the detrimental effects of plate thickness on fatigue strength, the fatigue strength is decreased if the thickness is larger than 25 mm. The recommended S-N curves incorporate the thickness impact lowering of welded joints fatigue resistance (DNV 2016b):

$$log\ \mathrm{N} = log\,\overline{a} - \ m\ log\left[\sigma_r \left[\frac{t}{t_{ref}}\right]^{ki}\right] \tag{2.10}$$

where $\bar{a}$ is the intercept of N (number of cycles)-axis by the S-N curve, m is the negative inverse slope of the S-N curve, t is the material thickness and t_{ref} is the reference thickness (25 mm). Increase in material thickness can have a detrimental effect on fatigue as thicker sections can contain internal defects and residual stresses.

Arc welding processes can introduce axial misalignment and angular distortion in welded structures owing to the temperatures required during the welding process. This can lead to fatigue implications in the materials, leading to failure and reduced service life of the components where the welded material is used by stress magnification in the weld (Braun 2022; De Jesus et al. 2012; Gkatzogiannis et al. 2019; Kanishka, Acherjee 2023; Köder, Bohlmann 2014; Li et al. 2021; Ohta et al. 2003). Both axial and angular stress magnification factors have been assessed, and their expressions are given below (Ólafsson et al. 2016):

$$\text{Axial magnification factor, } K_{m-axial} = 1 + 3\,\frac{e}{t} \tag{2.11}$$

$$\text{Angular magnification factor, } K_{m-ang} = 1 + \frac{3}{4}\alpha\frac{L}{t} \tag{2.12}$$

where e is the axial misalignment, t is the plate thickness, α is the angular distortion, and L is the distance between the fixing points of the plates. Combining Equations 2.11 and 2.12, the overall total stress magnification factor is given in Equation 2.13 as (Ólafsson et al. 2016):

$$K_{m\_T} = 1 + (K_{m-axial} - 1) + (K_{m-ang} - 1) \tag{2.13}$$

The -1 in Equation 2.13 is used to remove the baseline or starting value. By subtracting 1, we're only looking at the extra stress caused by the angular distortion and axial misalignment. For joints subjected to axial loads, it is widely observed that the existence of axial and angular misalignments does not cause a substantial reduction in fatigue strength unless the total misalignment factor surpasses a threshold value of 1.3 (Maddox 1985). Furthermore, it can be argued that a majority of butt-welded joints, when subjected to axial loading, inevitably undergo secondary bending stresses. As a result, the S-N curves for fatigue assessment needs to account for this phenomenon, thereby recognising the significance of the secondary bending stresses. Strain gauges can strategically be placed at critical points to measure the strain and calculate the resulting bending stresses in a structure.

2.4 Conclusions on theoretical background

It was observed that corrosion may either accelerate fatigue, which is more likely, or mitigate fatigue based on a multitude of influencing factors, including environmental, mechanical, and metallurgical elements. While the total life method serves well in the design phases, the fracture mechanics approach offers more detailed insights for in-service monitoring. A hybrid method combining elements from both approaches could offer a comprehensive and accurate framework for assessing both crack initiation and propagation, thereby improving the fatigue life assessments of materials.

While welding offers advantages such as higher stiffness and load-bearing capacity, it introduces challenges such as changes in material microstructure, residual stresses, and risk of material shrinkage. This chapter highlighted various fatigue design standards for welded structures, as well as the impacts of welding defects and distortions on fatigue life.

Overall, this chapter provided an overview of theoretical foundation for further study of the multifaceted challenges associated with fatigue and corrosion in offshore structures. It not only establishes the key mechanisms and factors influencing these phenomena, but it also reviews the existing methodologies and limitations for their analysis. This chapter underscores the significance of understanding these intricacies for the effective design, assessment, and maintenance of offshore structures.

Chapter 3

Review of literature

This chapter presents a comprehensive analysis of corrosion-fatigue in HAOWT, spanning from material science to state-of-the-art computational methods. It begins by focusing on how corrosion-fatigue affects various zones in HAOWT, such as the base metal, HAZ, and weld zones. The chapter then dives into specialised applications such as the use of high-strength steels in HAOWT monopiles and examines the S-N curves specific to corrosion in S355 structural steels. The operational factors contributing to corrosion-fatigue were also scrutinised, highlighting the importance of real-world conditions in assessing material performance. This chapter introduces innovative approaches to monitoring and prediction, incorporating condition monitoring systems and artificial neural networks to assess fatigue in HAOWT structures. Finally, the emerging concept of digital twins is explored as a tool for real-time fatigue assessment in HAOWT structures, suggesting a future direction for both research and practical applications.

3.1 Corrosion-fatigue in structural steel for monopiles

In the fabrication of monopiles for HAOWTs, large plates of structural steel undergo both longitudinal and circumferential welding after rolling the plates (Jacob et al. 2018). A critical by-product of the welding process is the formation of the HAZ, which is known for its compromised fatigue resistance. These HAZ locations become important in HAOWTs serviceability under the impact of wind and wave loads. Empirical studies have underscored that weld zones serve as the typical location for the onset and progression of fatigue cracks (Mehmanparast et al. 2017). The intrinsic property of the HAZ is that it exhibits less fatigue resistance compared to the base metal, thereby amplifying the likelihood of failure in the HAZ (Kang et al. 2013). Additionally, research points out that crack initiation and its subsequent propagation from the HAZ into the base metal often follow the direction of the pipe thickness (Okenyi et al. 2022). One factor exacerbating this issue is the prevalent tensile residual stresses within the HAZ (Adedipe et al. 2015).

These tensile residual stresses contribute to an increase in the mean stress effects, particularly as fatigue cracks initiate and propagate through the welds (Tsay et al. 1999; Mehmanparast et al. 2016; Xin, Veljkovic 2020; Xu et al. 2021; Okenyi et al. 2022). Consequently, techniques like post-weld heat treatment have been suggested to alleviate tensile residual stresses, thereby potentially prolonging the operational lifespan of HAOWT monopile materials. During welding of S355 steels, slag particles become trapped within the weld metal and can greatly degrade the mechanical characteristics of the weld, including its toughness and resistance to fatigue. Slag inclusions provide significant challenges in the welding of thick sections, especially in the context of S355 structural applications(Wieczorska, Labuda 2023).

Further, it is noteworthy that fatigue crack growth in the HAZ is more pronounced when compared to the base metal in non-corrosive conditions (Adedipe et al. 2017). While existing literature touches upon fatigue crack initiation prompted by microstructural defects (Smaili et al. 2019a; Smaili et al. 2019b), the findings suggest that a meticulous examination of the weld and HAZ regions is indispensable for holistic fatigue assessment. There remains a research gap in understanding how environmental factors, such as pitting corrosion, influence fatigue performance in HAZ regions, especially as offshore environmental conditions become increasingly severe. It becomes abundantly clear that the HAZ is crucial in fatigue studies for HAOWTs. Not only because this zone possesses inherently lower fatigue resistance, but it also tends to accumulate detrimental residual stresses and shows accelerated crack growth under specific conditions. As such, future works could prioritise this region, particularly when aggressive corrosive conditions are also considered.

S355 structural steel is commonly employed in the construction of monopiles owing to its advantageous weldability features (Healy, Billingham 1998). Material selection guidelines are typically aligned with DNV-OS-B101 (DNV 2009). As the dimensions and sizes of HAOWTs enlarge, there is a growing focus on utilising high-yield-strength steels that demonstrate superior fatigue and corrosion resistance, particularly under the low-temperature conditions characteristic of offshore settings. The thermo-mechanically rolled variants, denoted by M grades, exhibit improved mechanical properties, as detailed in Table 3.1; these are produced through addition of de-oxidizing elements such as aluminium, silicon etc., to make the steel free of any

oxygen. The 'G' indicates a hot-rolled production process. S355 is especially prevalent in contemporary large offshore wind turbines, adhering to the BS EN10225 standards (British Standards Institution 2019a). These steels are acknowledged for their robust toughness and weldability (Igwemezie et al. 2018).

S355 as a type of structural steel, does not possess significant natural resistance to corrosion and is deficient in certain alloying elements such as greater levels of chromium or nickel, which are known to greatly enhance corrosion resistance (Gassama et al. 2015). The pitting resistance of S355 steel is typically lowered as a result of its reduced levels of chromium and nickel. This is particularly important in marine conditions, where chloride-induced pitting is a prevalent kind of corrosion (Heider et al. 2020). The pitting resistance equivalence number for S355G10+M steel is determined as 0.1233 from its chemical properties (Okenyi et al. 2024) indicating low pitting corrosion resistance but the additional protective coating measures in the weld region (Figure 1.2b) and the thermomechanical properties in Table 3.1 improves its corrosion resistance.

Thermomechanical treatments can enhance the microstructure of steel, resulting in increased density and uniformity. This improvement can partially reduce corrosion. Implementing mitigating measures is crucial for steels such as S355G10+M when utilised in severe maritime environments (Igwemezie et al. 2018). Nevertheless, there is a noticeable gap in the literature concerning the degradation of these materials due to corrosion-fatigue and the impact of the entire manufacturing sequence on the fatigue life of the material.

Table 3.1: Mechanical properties of steel grades in offshore applications to EN10225 (Oakley Steel 2021).

Mechanical properties	**EN10225 S355 TMCP Steels**	
Hot rolled plate	**S355G8+M**	**S355G10+M**
Yield, σ_y (MPa)		
< Ø16 mm	355	355
Ø16 mm - Ø25 mm	355	355
Ø25 mm - Ø40 mm	345	345
Ø40 mm - Ø63 mm	335	335
Ø63 mm - Ø100 mm	325	325
Tensile, σ_{UTS} (MPa)		

< Ø40 mm	470–630	470–630
Ø40 mm < Ø100 mm	470–630	470–630
Brinell Hardness	285	285
Elongation (%)	22	22
Modulus of elasticity (GPa)	205	205
Poisson's ratio	0.29	0.29
Machinability %	55	55
Charpy V-notch (J)	50@ −40 °C	50@ −40 °C

* Ø – Plate thickness; σ_{UTS} – Ultimate tensile strength

Various methods have been explored to mitigate corrosion in offshore wind turbine structures subjected to fluctuating loads and extreme environmental conditions. Techniques such as spray metallisation, galvanic anodes, and the application of an external current are prevalent in the literature (Masi et al. 2019; Momber 2011; Price, Figueira 2017). Additionally, zone-specific approaches, such as cathodic protection in submerged areas and specialised coatings in tidal, splash, and atmospheric zones, have been suggested. Strategies that focus on diminishing cyclic loading have also been studied. For example, integrating a three-dimensional (3-D) pendulum-tuned mass damper into a HAOWT support structure has been shown to lower vibration frequencies and substantially improve fatigue life (Mohammadi et al. 2018; Sun, Jahangiri 2019).

In a comprehensive examination of structural steels, multiple test setups and loading conditions were employed to evaluate their fatigue behaviour in air and under corrosive conditions. The primary steel variant under investigation was S355, although additional steels with comparable yields and UTS were also considered. The reported experiments were conducted under a variety of load-controlled fatigue loading conditions, such as rotational-bending, axial, and bending fatigue tests. These were conducted under varying stress ratios (R ratios), including R = -1, 0, 0.1, and 0.5, at different frequencies. The fatigue properties demonstrated sensitivity to several factors. The surface roughness, welding methodology, specimen thickness, and environmental context of the tests (either air or corrosive conditions) were observed to have a consequential impact. The mechanical properties were concurrently evaluated and are summarised in Table 3.2.

Table 3.2: Mechanical properties of fatigue-tested structural steel.

Structural Steel	σ_y **(MPa)**	**UTS (MPa)**	***t* (mm)**	***R***	***H* (Hv)**	***E* (%)**	**Ref.**
S355N, S355M	378, 442	560, 524	10	-1, 0	160-280	36, 33.5	(Sonsino 2009)
SPV490	579	628	20	-1, 0, 0.5	207	40	(Ohta et al. 2003)
SM50B	413	541	9	0	-	25	(Pedersen 2019)
SM50B	364	526	40	0	-	35	(Pedersen 2019)
S355J2	416.15	548.15	20, 25	0.5	270	28.5, 30.5, 33.5	(Ólafsson et al. 2016)
S355J2+N	469	566	15	0.1	-	-	(Gkatzogiannis et al. 2019)
S355J2+N	469	566	15	0.1	-	-	(Gkatzogiannis et al. 2021)
A106B	360.6	540.6	6.5	0.05	435	-	(Daavari, Sadough Vanini 2015)
316SS	248.3	495.6	7	0.1	100 - 110	42.7	(Fereidooni et al. 2018)
15KhSND	400	565	12	0	-	-	(Knysh et al. 2018)
S355J0, S355J2	382, 386	554, 556	3	-1	-	16.8	(Klusák, Seitl 2019)
S355J2	434	550	16	0.1	200 - 400	-	(Weich et al. 2009)
S355NL	378	555	10	-1, 0, 0.1	-	-	(Madia et al. 2018)
S355	355-550	470-630	5-10	0.1-0.2	-	-	(Nazzal et al. 2021)
16Mn	390	591	8	0.1	-	24.4	(Wang et al. 2009)
S460G2+M	460	598.09	10	0.1	150-203	17	(Saidin et al. 2019)
S355J2, S460	434, 460	550	30	0.1	-	31	(Ummenhofer, Weidner 2013)
S355J2	434	550	16	0.1	200-350	31	(Weich 2009)
S355	320-350	500-510	5	0.1	-	-	(Corigliano et al. 2017)
S355	425	557	10	-1	-	14	(Corigliano et al. 2020)

Q460-20	481	623	10	0.1	140-250	35.6	(Tong et al. 2021)
S355	400	510-680	5	0.1	340	22	(Leitner et al. 2014)
S355J2 + N	388	535	20	0.1	-	34	(Schiller et al. 2022)
S355J2	386	537	4	0.1	-	31	(Schaumann et al. 2010)
S355	-	580	6, 10	-1	165-240	-	(Čern, Sís 2016)
S355	360	534	6	0.1	200-400	-	(Sorger et al. 2018)
S355J2+N	355	490	5	0	-	-	(Köder, Bohlmann 2014)
S355J2+N	386	537	4	0.1	-	31	(Schaumann, Steppeler 2013)
S355J2+N	434	544	10	0		29	(Braun 2022)
S355GS+10	486	380	12	0.1	178-198	28.1	(Anandavijayan et al. 2021)

- *Information not reported,* * *H* – Hardness; σ_y -Tensile yield strength; *R* – Stress ratio; *E* – Elongation; *t*– Thickness.

The average UTS for the S355 steel was 546 MPa, and the mean yield strength was 412 MPa. Observations regarding hardness revealed variability across the material from the base to the weld zone, including the HAZ. Notably, the maximum hardness values were predominantly located in the weld region and often corresponded to the UTS of the material. For the S355 steel grades, the elongation was observed to fall within the range of 16.6% to 36%.

Welding techniques also warrant specific attention. According to Table 3.2, metal active gas (MAG) and SAW have emerged as the most prevalent welding methods. Arc welding techniques have found extensive applications in offshore structures, particularly in offshore wind turbines (Jacob et al. 2019; Yusof, Jamaluddin 2014). This multifaceted approach provided a nuanced understanding of structural steel behaviour under various conditions, providing the groundwork for optimising material selection for great fatigue performance in offshore applications.

S-N data reviewed from the literature have also been compared to the design standards (British Standards Institution 2014a; DNV 2016b; British Standards Institution 2005b; International Institute of Welding 2008) (Appendix A10). The design standards were found to be relatively conservative in terms of S-N curve values in both air and

corrosive conditions in artificial seawater and salt spray chamber. Welding influenced the structural steel fatigue life, as samples with one-sided welds, usually of smaller thickness, appeared to have better fatigue life than two-sided butt welds, whereas samples without a weld had significantly superior fatigue life. This is consistent with the well-known fact that the weld zone generates a discontinuity in the material and is frequently sensitive to the local pressures from which cracks typically initiate (Jacob, Mehmanparast 2021). However, it is important to note that cross weld test measures the combined strength of the weld, HAZ, and parent metal, often dominated by the stronger parent metal. This can hide the true strength and quality of the weld and HAZ, making it difficult to identify specific weaknesses or issues within the weld itself. The high frequency mechanical impact (HFMI) treatment and shot peening treated specimens demonstrated that both post-weld treatment procedures enhanced the fatigue life of the structural steels. The salt spray chamber and artificial seawater samples showed comparable fatigue responses in corrosive environments. However, when compared to the samples in air, it was observed that corrosion had a negative effect on the fatigue life of welded structural steel. In addition, from the collected literature on fatigue tests in air and corrosive environments, it was observed that corrosion contributed to an approximately 16% reduction in the fatigue performance of the S355 structural steel.

3.2 Finite element analysis application to monopile material

Engineering structures subjected to stresses can have their stress fields predicted using FEA, which can then be used in corrosion-fatigue assessments. Multiple scales of fatigue research have used FEA, which includes:

- The stress-assisted corrosion model used for pitting evolution research with the cellular automation finite element method (Saucedo-Mora, Marrow 2014; Fatoba et al. 2018; Cui et al. 2019). The model was able to provide helpful information on real-time diagnostics of corrosion-fatigue, such as the ability to associate changes in the depth, aspect ratio, and morphology of pits with time under the impact of stress.
- Information on the heterogeneous stresses, strains, and plastic states that lead to the initiation of cracks was obtained using a crystal plasticity finite element model

(Signor et al. 2016; Prithivirajan et al. 2021). This model was also able to provide useful information on shape change, rotation, and geometrical dislocations, all of which have been used in research on fatigue cracks. This model is helpful at both the mesoscopic and microscopic levels of analysis.

- Multiscale fatigue modelling, with the goal of predicting everything from the onset of pitting to the progression of long-term crack growth due to fatigue (Anagnostou et al. 2010; Ye et al. 2017). This model made use of a combination of macroscale and mesoscale approaches. The macroscale technique evaluates the global state of stress on the component, whereas the mesoscale approach determines the critical damage location and extracts boundary conditions from the larger model.

The construction sector has widely adopted high-strength steel owing to its notably high yield strength and cost-effectiveness (Xin and Veljkovic 2019). Studies on the application of FEA in many industries, such as aerospace, nuclear, and oil and gas, have been conducted by researchers (Deng 2009; Grbovic, Rasuo 2012; Guo et al. 2012; Topaç et al. 2012; Fatoba 2015). Finite element models for studying corrosion-fatigue in full-scale HAOWTs are often not utilised due to their significant computational requirements. However, recent progress in desktop computational capabilities, when combined with programming tools, has the potential to offer substantial benefits in terms of accurately capturing the deformation in all components at a faster pace. Figure 3.1 presents a comprehensive examination of several applications of FEA pertaining to the assessment of fatigue and corrosion-fatigue in steel materials utilised in offshore settings, specifically focusing on monopile support structures.

The examination presented in Figure 3.1 highlights the necessity of exploring the utilisation of FEA in the examination of fatigue initiation phenomena at a macroscale level, specifically for high-strength weldable steels employed in offshore applications. The inclusion of harsh environmental factors, particularly corrosion, would provide a valuable addition to the fatigue degradation phases in FEA models.

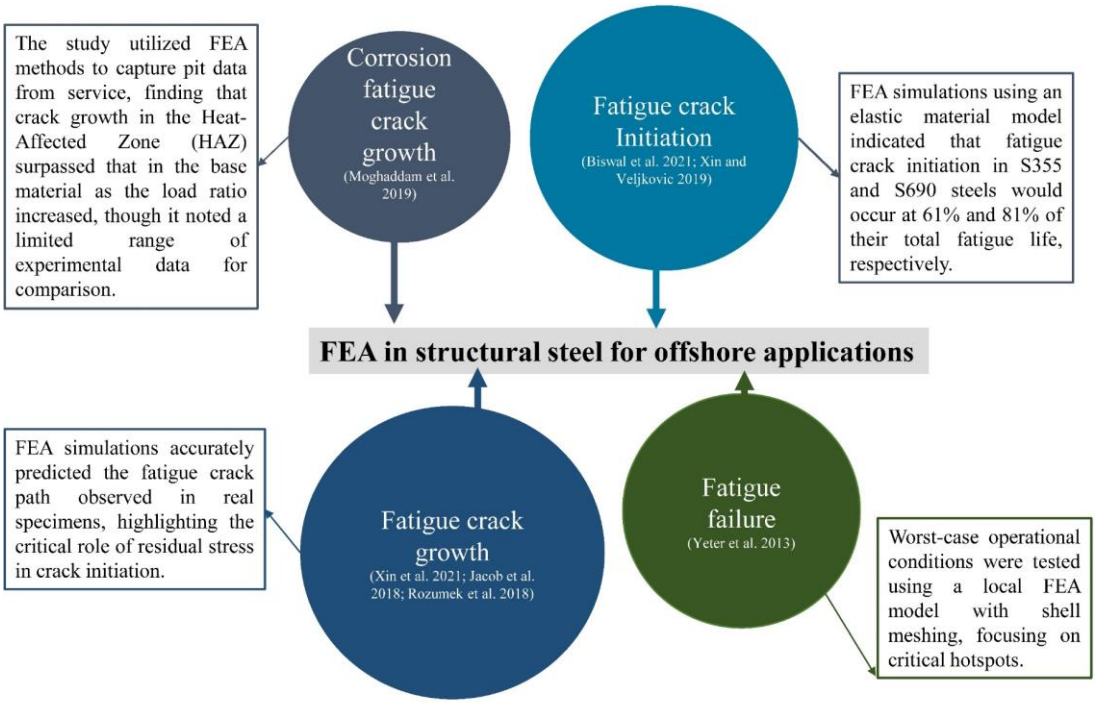

Figure 3.1: Review of FEA in structural steel for offshore applications.

Due to brittle martensite formed during rapid welding cooling, the HAZ is generally weaker than the parent or weld metal. Welding heat changes the steel microstructure, increasing hardness while decreasing toughness. Martensite production in the HAZ can weaken it, making it more vulnerable to stress corrosion cracking (Igwemezie et al. 2024).

The fatigue initiation data obtained from FEA studies on S355 (Biswal et al. 2021; Xin, Veljkovic 2019) is used to calibrate the material model, analyse local stress distributions at critical weld locations, and predict total fatigue damage over the operational life of monopile weldments. This data validates the accuracy of the FEA models, improves design approaches, and assesses the operational lifetime under service loading conditions.

For fatigue crack growth prediction, residual stress is incorporated by simulating the welding process in FEA, which calculates the thermal and mechanical effects to generate a residual stress profile. This profile is then superimposed with the applied stresses to determine the effective stress intensity factors at the crack tip. This

combined stress field is used to predict crack initiation and propagation, accurately reflecting the influence of residual stresses on fatigue behaviour (Xin, Veljkovic 2020).

There is a scarcity of existing research pertaining to the utilisation of cyclic loading in the context of pit-to-crack transition on localised models. Currently, there is a scarcity of scholarly research pertaining to the utilisation of cyclic loading in the context of the transition from a pit to a fracture in structural steel materials utilised in offshore scenarios. FEA has been observed to be vital for conducting fatigue damage investigations, revealing that the measured residual stress in welds can be equivalent to the yield stress of the material. The influence of additional mechanical parameters, such as the mean stress effect, which is characterised by the stress ratio R, can be observed in FEA studies. However, there is insufficient experimental data to effectively validate these findings in high-strength steels.

Several suggestions for future research in FEA could involve the incorporation of a welding interface that enables precise modelling of material characteristics and the capturing of microstructural evolution inside the HAZ. An additional factor to be considered is the utilisation of computational fluid dynamics in conjunction with a physics-based corrosion model to simulate the interaction between the monopile structure and seawater.

This modelling approach could forecast the distribution of pressure and its impact on corrosion and the formation of pits, particularly in the submerged region. The utilisation of computational fluid dynamics extends to the estimation of wind-induced loads and the comprehensive analysis of flow patterns within HAOWT farms. In addition, the integration of these models with a soil-pile model that accounts for varying soil conditions across different geographical regions may yield a more accurate depiction of the induced stresses in the vicinity of the soil-water boundary. The morphology of a pit, particularly its aspect ratio and location, can be effectively modelled and studied using FEA.

3.3 Operational factors affecting corrosion-fatigue

Corrosion-fatigue processes in HAOWTs are influenced by varying levels of harsh wave conditions, operational factors, and combinations of loads. The support structures of the HAOWT are engineered to withstand severe loading events that may be encountered over its operational lifespan, including, but not limited to, high wind gusts and challenging wave conditions. Design considerations often consider infrequent but significant wave loading events that occur approximately every 50 years (Arany et al. 2017). The occurrence of intense wave loads induces cyclic loading characterised by high velocity and acceleration, resulting in fatigue within the different monopile regions. The combination of these effects, along with the various corrosion zones outlined in DNVGL-RP-0416 (DNV 2016a), where the expected rates of material degradation per annum at different levels of exposure are identified, can cause severe corrosion-fatigue damages, especially in the splash zone. The corrosion zones and loads acting on the HAOWT are illustrated in Figure 3.2.

According to the BS EN International Electrotechnical Commission (IEC) 61400-1 (British Standards Institution 2019b), both regular operation and parked scenarios are characterised by significant cyclic loads, making them the primary fatigue load scenarios. As shown in Figure 3.2, the bending moments vary with cyclic loads as a result of the rotational movement of the blades during operation, the impact of wind forces acting upon the tower, and the influence of wave forces. Additional load scenarios that impact HAOWT structures include torsional, centrifugal, and gyroscopic forces (Igwemezie et al. 2019). The primary influence on HAOWT monopile-supported structures is often attributed to the thrust force exerted on the rotor (O'Kelly, Arshad 2016; Gentils et al. 2017). The recommendation by DNV-OS-J101 (DNV 2014) suggests the provision of design guidelines for loading combinations in both typical and high wind and wave scenarios. This allows the evaluation of the structural performance of offshore wind turbines under the most severe conditions. In reality, loading situations are characterised by their complex and stochastic nature, as they exhibit variations across time (DNV, Risø 2002). These characteristics collectively indicate that the service life of monopile-supported HAOWTs is influenced by corrosion zones, loading sequence, and operating states, highlighting the importance of their accurate assessment for corrosion-fatigue and fatigue life.

Furthermore, it is imperative to consider the soil-structure interaction, which encompasses the natural frequency of the structure, during the design process. In the conceptual design phase for a HAOWT, careful consideration must be given to the installation site, as it significantly impacts the wind and wave forces required to achieve the desired power production capacity of the wind turbine and its structural performance. During the preliminary phases of the design process, it is imperative to allocate attention to the determination of appropriate dimensions for various components, including but not limited to monopile diameter, blade dimensions, wall thickness, and embedded length. This is crucial for establishing and maintaining structural stability. Subsequently, an estimation of the loading conditions is conducted, encompassing the ultimate limit states, serviceability states, and fatigue limit states. In the concluding phases, it is imperative to incorporate design evaluations pertaining to safety, natural frequency, deflection, corrosion, and fatigue life estimation to comprehensively evaluate the long-term performance of the structure.

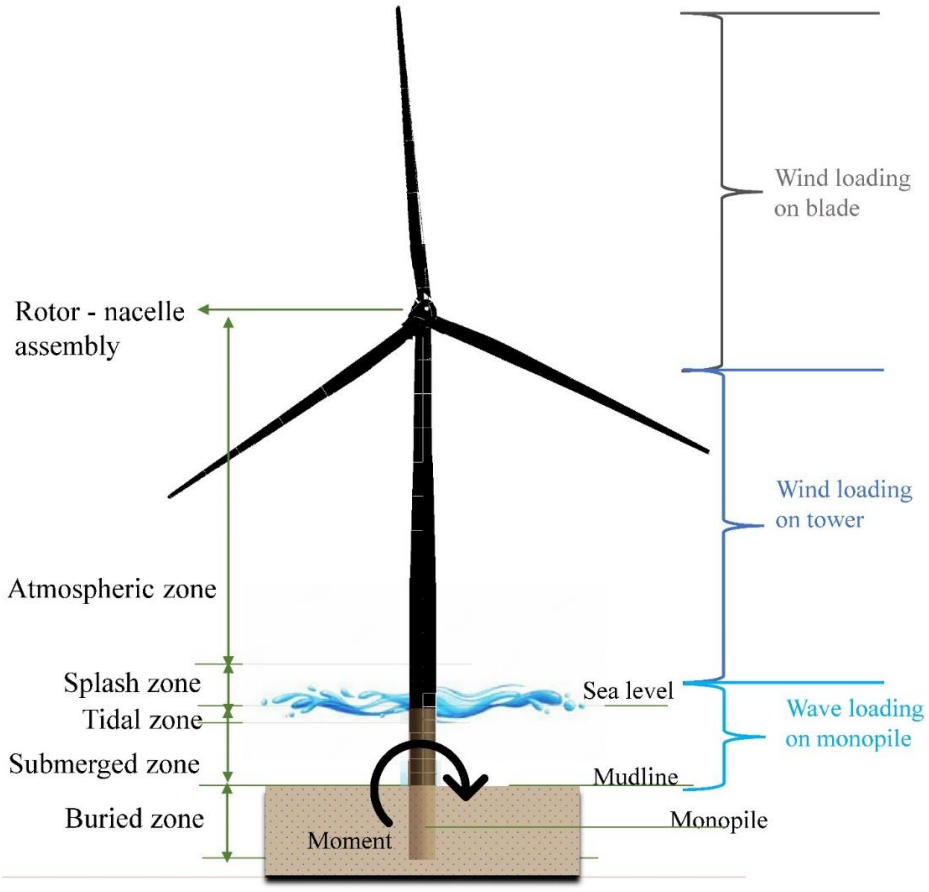

Figure 3.2: Simplified loads on wind turbine and monopile zones.

3.4 Condition monitoring and machine learning application to fatigue assessment in HAOWT

The implementation of condition monitoring techniques holds promise for enhancing structural reliability and mitigating maintenance expenses. The implementation of a preventative maintenance method is of utmost importance in the context of condition monitoring. This technique mitigates the risks associated with physical inspections and guarantees the long-term functionality of offshore wind structures. In addition to time-based preventive maintenance, there are two more types of maintenance approaches, namely corrective maintenance and predictive maintenance, both of which are condition-based in nature. Various condition-monitoring techniques are commonly employed in offshore wind turbines, including vibration analysis, strain monitoring, acoustic emission, thermography, electric signals, and the shock pulse method (Dhillon, 2002).

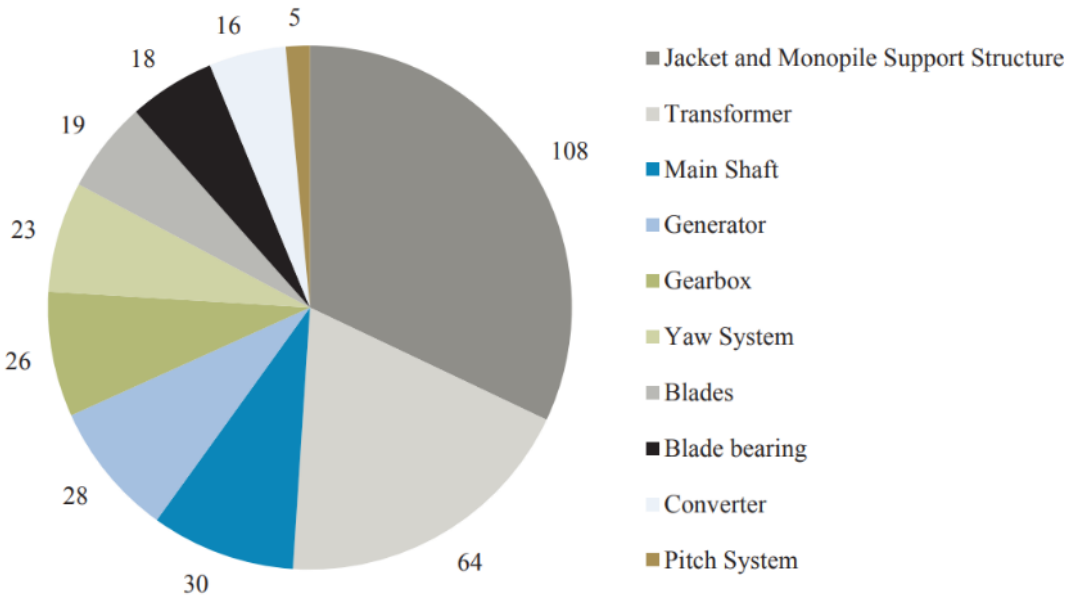

Figure 3.3: Reported component failure modes in offshore wind turbines (Scheu et al. 2019).

The findings derived from the failure mode analysis are shown in Figure 3.3. The monopiles of the offshore wind turbines exhibited the highest number of failure scenarios. Research on same components showed that major failures result in significantly longer downtimes across all components. The support structure (28.01 days), drive train (15.47 days), and gearbox (18.38 days) have particularly high

downtimes for major failures. Although annual failure rate for support structure is relatively low, its high downtime indicated that any major issues in this component are particularly disruptive (Faulstich et al. 2011).

3.4.1 Condition monitoring techniques and applications

The utilisation of condition monitoring techniques presents potential benefits in the evaluation of reliability for offshore wind turbines. This involves the application of data acquisition and signal processing tools to monitor various components of the turbine. An assessment of the effectiveness of condition-based maintenance of offshore wind turbines was conducted (Scheu et al. 2019). The study revealed that the signals derived from diverse measurements necessitated intricate analysis to accurately determine the remaining lifespan of the components. Additionally, it has been reported that the implementation of a real-time damage-calculating system would offer more practical and viable options.

3.4.2 Supervisory control and data acquisition systems

Supervisory control and data acquisition systems, along with wind turbine condition monitoring systems, are utilised as tools for condition monitoring of offshore wind turbines. These tools provide a cost-effective means of data sensing and collection. Supervisory control and data acquisition systems possess the functionality to collect real-time operational metrics, encompassing variables such as thermal readings, electrical currents, pressures, and meteorological indicators such as wind speed and direction. Data points are logged at consistent 10-minute time segments and employ a sampling frequency of 1 Hz, a rate generally considered to be on the lower end of the spectrum. These systems hold significance for researchers engaged in the field of damage diagnostics and prognostics and for companies involved in operations and maintenance. Wind turbine condition monitoring systems are useful for performing both diagnosis and prognosis operations. The integration of these systems has the potential to be advantageous in higher-capacity offshore wind turbines. The implementation of smart monitoring has been proposed and promoted in automated monitoring systems to assist engineers in identifying anomalies in collected data and overall structural performance (Tchakoua et al. 2014).

3.4.3 Structural health monitoring in HAOWT

Several studies have focused on examining the structural health monitoring instruments employed in monopiles (Bang et al. 2012; Devriendt et al. 2014; Zhou et al. 2019; Jeong et al. 2020) to conduct static and dynamic analyses. These investigations involved the utilisation of accelerometers and wireless sensors to measure the strain and deflection resulting from bending. In their study, Ziegler et al. (2017) utilised a stochastic extrapolation technique in conjunction with a singular strain monitoring measurement to provide predictions regarding strains in various regions of the structure. Most of these studies have been conducted on HAOWTs that have the same dimensions as those seen in real-world applications. Nevertheless, it is possible to conduct laboratory testing on smaller versions of HAOWTs in a faster and more comprehensive manner when considering size effects. This can also be done to create and verify health monitoring technologies and fatigue evaluation methodologies. The utilisation of real-time condition monitoring is prevalent in various wind turbine components, including the blade, gearbox, nacelle, and drivetrain. However, its application in assessing fatigue damage is rather limited despite its potential for identifying significant critical failure positions. The integration of FEA and fatigue analyses, along with the incorporation of experimental data obtained by real-time condition monitoring, has the potential to provide real-time estimates of fatigue damage from these monitoring systems. These calculations can then be utilised to estimate the remaining life of these offshore structures.

3.4.4 Artificial neural networks application and benefits

Artificial neural network is a common machine learning method that is commonly employed as a predictive tool utilising data (Arcos Jiménez et al. 2017). This technique has the potential to be utilised for both pattern tracing and data output approximation. The utilisation of multi-layer networks for nonlinear generalisation is a crucial aspect in the implementation of tools for enhancing dependability, optimising performance, and facilitating maintenance in wind power generation (Hertz 2018). A feedforward network was employed to evaluate fatigue life using aerodynamic and hydrodynamic forces as input variables (Tian et al. 2011). The use of back-propagation and radial basis function neural networks has also been observed alongside the growing availability of more substantial data. Consequently, this has led to an increased

adoption of neuro-fuzzy networks (Ata, Kocyigit 2010). The utilisation of artificial neural networks has been documented in various research studies. For instance, the application of artificial neural network in wind power forecasting has been explored (Lin, Liu 2020). Additionally, researchers have investigated the optimisation of support structure design for HAOWTs using artificial neural network (Stieng, Muskulus 2020; Ziane et al. 2021).

Furthermore, there has been a focus on the application of artificial neural network for fault detection in the tower structure of HAOWT (Qiu et al. 2020). The diverse range of applications where artificial neural networks have proven valuable has been highlighted. According to the authors, 38%, 29%, 23%, and 10% of these applications involved forecasting tasks, fault detection, control, and design, respectively (Marugán et al. 2018). A multi-layer perception and back-propagation artificial neural networks were utilised to forecast low-cycle fatigue in 316 L (N) stainless steel. The primary inputs for the artificial neural network model were temperature, strain rate, and amplitude. The predicted fatigue life results had a strong correlation with the experimental results, particularly when comparing the root mean square values (Srinivasan et al. 2003). Most time-based forecasts using artificial neural networks have demonstrated superior performance compared to frequency-based predictions. While frequency-based prediction methods are known for their speed, empirical evidence suggests that they tend to yield conservative fatigue life projections (Durodola et al. 2017). One restriction of artificial neural networks is their predictive capabilities, particularly when attempting to extrapolate beyond the boundaries of the current dataset. Artificial neural networks that is employed to forecast the fatigue life in the context of low cycle fatigue may not possess the capability to effectively extrapolate data to anticipate high cycle fatigue, particularly when data pertaining to high cycles is absent. Several studies have utilised artificial neural network for predicting fatigue crack growth and corrosion-fatigue (Haque, Sudhakar 2001; Gope et al. 2015; Wang et al. 2017; Mortazavi, Ince 2020). Among these studies, the back-propagation network has been the most commonly employed approach. A comparable neural network architecture was also utilised in a single-layer feed-forward artificial neural network for the purpose of predicting fracture growth (Huang et al. 2006).

One of the several benefits associated with the utilisation of artificial neural network in HAOWT is their capacity to efficiently carry out rapid computations for real-time

monitoring (Marugán et al. 2018). Artificial neural networks techniques have predominantly been utilised in various studies to analyse and model the behaviour of critical components in wind turbines, including rotors, blades, generators, gearboxes, and bearings. However, only a limited number of investigations have focused on tower structures and the characterisation of structural steel materials. The potential utilisation of this technology could encompass fault diagnostics and prognostics of monopile components, as well as the monitoring of loads through the utilisation of strain gauge measurements (Ziegler et al. 2017).

3.5 Digital twin application to fatigue in HAOWT

The concept of digital twin is discussed as an operational representation of a physical asset. It comprises three essential elements: (i) a digital model that represents the physical asset, (ii) retrieval of a continuously changing dataset, and (iii) dynamic updating of the model (Wright & Davidson, 2020). Theories that underlie physical systems and the data gathered from them are utilised to construct a model that effectively duplicates these physical systems, resulting in precise representations. The integration of sensor data into simulations enables the prediction of real-time performance, forecasting, and fault detection. The rapid progress and implementation of Internet of Things have facilitated the swift transfer of collected data from various scales using sensor technology. This capability holds potential advantages for the utilisation of digital twins in various applications. The utilisation of historical data collected from physical components has the potential to facilitate the anticipation of future component failures within engineering systems. Numerous digital twins software tools are presently accessible or being developed by technology vendors in the industry. This implies a growing expectation for the widespread application of digital twin technology across different economic sectors, including engineering. For instance, this innovation has been leveraged in the manufacturing sector for the refinement of product optimisation in the automotive domain to augment vehicle efficacy for asset maintenance in both the oil and gas, renewable energy fields, and more areas (Errandonea et al. 2020). Simulation-based and data-driven digital twins have the potential to offer advantages in condition monitoring for physical assets and their maintenance. The application of digital twins, specifically in industrial applications, has been researched (Liu et al. 2021), as illustrated in Figure 3.4, and it

was observed that life extension in the end-of-life phase requires deeper research. In HAOWT, digital twins can enhance manufacturing by inputting real-time monitoring and production control data to ensure quality. Regular inspection intervals, informed by predictive maintenance data, minimize downtime. Manufacturer data, including material properties and performance metrics, is collected, and integrated into the digital twin for virtual evaluation and ongoing performance predictions. This enables precise assembly, continuous monitoring, and proactive maintenance throughout the turbine's lifecycle.

According to a review of digital twin applications in HAOWTs, the prominent domains are damage prediction and condition monitoring (Sivalingam et al. 2018; Johansen, Nejad 2019; Knezevic et al. 2019). It was deduced that the development of a digital twin for a simple drivetrain test rig demonstrates the fact that real-time condition modelling is case-specific and not easily generalised; however, digital twin shows potential for application to HAOWTs, particularly in accounting for unique environmental boundary conditions. A significant number of digital twin implementations have been observed in the energy industry. The utilisation of digital twin technology for the evaluation of fatigue has been extended to various sectors, including the aerospace industry (Leser et al. 2020), oil and gas semisubmersible drilling rigs with the aid of reduced-basis FEA, and corrosion management techniques (Adey et al. 2020; Okenyi et al. 2022), industrial machines (Zhidchenko et al. 2019), and general engineering systems (Ekoyuncu et al. 2019). Frameworks for predictive maintenance have been put forth in the field of physics, which rely on the use of physical phenomena models, such as fatigue models derived from sensor data (Georgoulias et al. 2019). These frameworks aim to forecast the remaining lifespan of offshore structures. Cloud-based distributed computing systems have the potential to provide remote access to high-speed computational capabilities and effective data storage, leading to possible cost reductions. The utilisation of cloud-based machine learning skills can be applied to digital twin material degradation frameworks, which are employed for estimating damage and predicting the remaining life of structural steel in offshore wind turbines (Ekoyuncu et al. 2019). The utilisation of digital twin frameworks for the purpose of real-time diagnostics and long-term prognostics have the potential to enhance the efficiency of inspection scheduling.

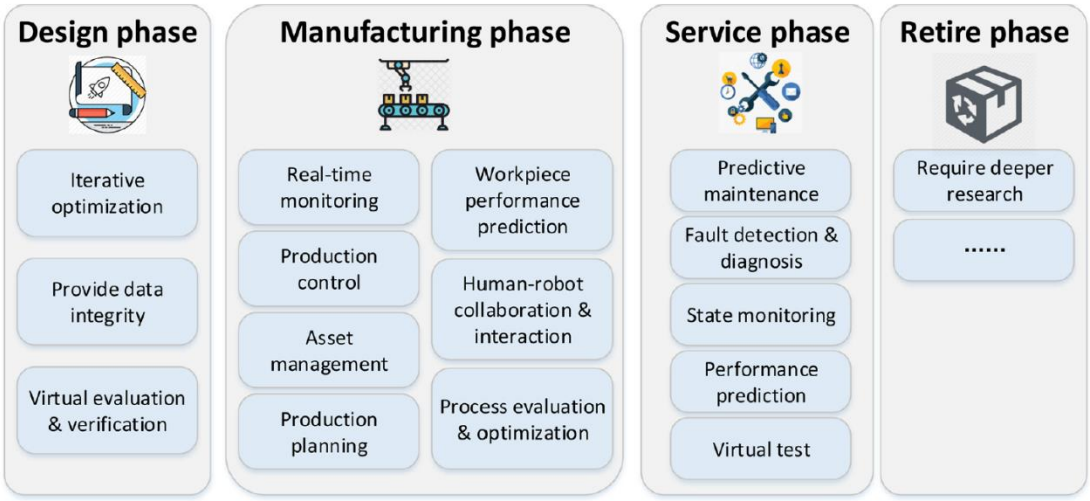

Figure 3.4: Digital twin applications in the engineering industry (Liu et al. 2021).

3.6 Corrosion-fatigue challenges and framework development

From the comprehensive review of corrosion-fatigue in offshore wind turbines and their support structures, the intricacies of the complex loading conditions, including high wind gusts, wave events, and torsional forces, that contribute to cyclic loading and fatigue are highlighted. Different zones within monopile structures face varying degrees of corrosion, adding an additional layer of complexity to fatigue assessment. Soil-structure interactions also influence the structural fatigue performance by affecting the natural frequency. The commonly used S355 structural steel has its own set of variables, with properties such as yield strength and welding methodology playing a critical role in fatigue life. There are research gaps when it comes to empirical data validating the behaviour of these high-strength steels, particularly concerning how pits transition to fractures in corrosive environments. Simulation techniques, such as FEA and computational fluid dynamics models, are valuable but still in the developmental phases for practical, full-scale applications. The existing design standards are conservative and require updating. Finally, the text observes that harsh environmental conditions lead to worsened fatigue performance and a reduction in the fatigue life of S355 steel. Various corrosion mitigation techniques have been mentioned, but their efficacy under fluctuating loads and harsh conditions remains a subject for further investigation. The application of condition monitoring and machine learning techniques can also be extended to fatigue applications in monopile materials.

These corrosion-fatigue challenges are thus summarised as design challenges and design/physical challenges, as presented in Figure 3.5.

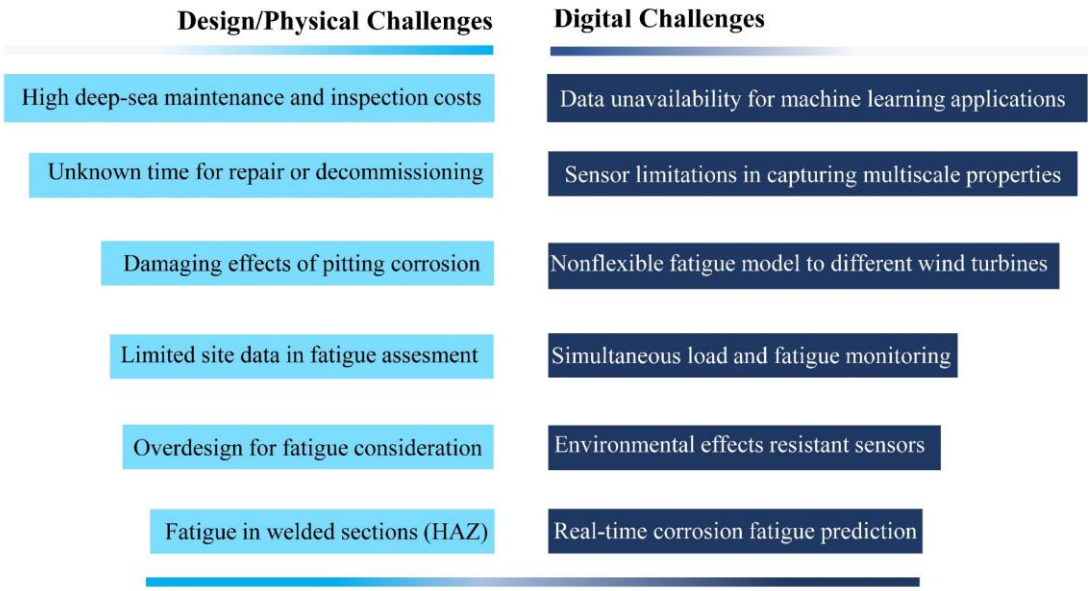

Figure 3.5: Corrosion-fatigue challenges in offshore wind turbines.

Several frameworks have been proposed in the literature for general condition monitoring. However, there is a notable gap in the availability of frameworks that integrate condition monitoring specifically for wind power generation with fatigue assessments. Digital twins utilised in wind power applications exhibit a greater emphasis on predictive capabilities than prescriptive ones. The ability to decrease maintenance and repair costs can be realised through the development of data-driven and simulation-based digital twins for both current and new HAOWTs. Cloud computing is a potential avenue for augmenting the implementation of additional digital technologies in highly available and optimised web-based applications. Fatigue monitoring in HAOWT can be enhanced by the integration of physics-based FEA, fifth-generation (5G)-Internet of Things technologies, and the use of sensors for data gathering, data analytics, and machine learning technologies, such as artificial neural networks.

A digital twin framework is provided in Figure 3.6, taking into account the highlighted issues of corrosion-fatigue and the literature research to offer a comprehensive

overview. The fatigue assessment framework using digital twins for offshore wind turbines can be effectively utilised by conducting material characterization testing to provide S-N curves, which encompass notch effects, stress concentrations, and surface and pitting effects. The considered mechanism of corrosion fatigue of the monopile from Figure 3.2 also makes it possible to apply FEA to the splash region which represents the most susceptible monopile region to corrosion fatigue damage, serving as an exemplary approach to corrosion-fatigue assessment. The datasets will be utilised for the algorithm training of artificial neural network models. These models can effectively acquire real-world data from operational HAOWT. By incorporating rainflow algorithms in conjunction with damage calculations, such as Miner's rule, it is feasible to forecast the remaining lifespans of these turbines. Consequently, these predictions can be employed to inform maintenance and decommissioning operations.

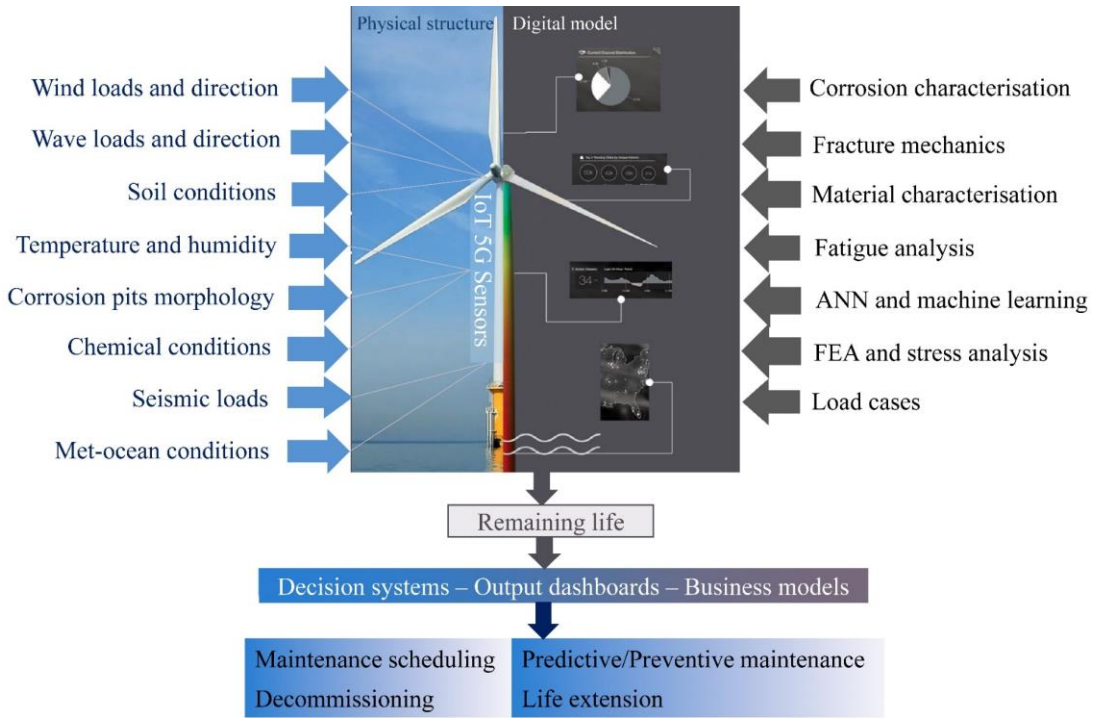

Figure 3.6: Fatigue assessment framework using digital twins for offshore wind turbines.

Chapter 4

Stress analysis from uniform corrosion and soil effects

There is still room for improvement in understanding the fluctuations of local stresses throughout the entire support structure caused by variations in the load, particularly the thrust force at the hub, which is the primary contributor to the overall operational load. Furthermore, there is a shortage of research on the utilisation of FEA for quantifying the extent of uniform corrosion in wind turbine support structures across various corrosion zones to better understand the stress variations in towers and monopiles. As the size of future HAOWTs is expected to increase, there will be a need to mitigate the impact of stresses from wind and environmental effects. The primary objective of this chapter is to analyse the stress in various corrosion zones of the monopile to identify the support structure component that is most vulnerable to damage. This analysis is particularly important for design purposes. Additionally, the chapter investigated the impact of different soil profiles on the natural frequency of the structure. It also assessed how soil variability affects the lateral deflection response of the recently installed 15 Megawatt HAOWT, which is currently the largest prototype installed. Therefore, understanding the risks associated with potential mechanical and environmental damage is crucial for the life assessment of support structures for large-diameter HAOWT.

4.1 The 15 Megawatt HAOWT design case study

The International Energy Agency, while working with National Renewable Energy Laboratory, the Technical University of Denmark, and University of Maine, has undertaken a collaborative initiative aimed at advancing the offshore wind technology. As part of this effort, they developed a conceptual reference model for a high-capacity 15 Megawatt HAOWT. This model functions as a standard against which research projects can be evaluated. It is based on the design of a first installed prototype HAOWT machine. It is equipped with a tapered tubular tower that provides support

for the rotor-nacelle assembly, which has a total weight of 1017 tons. The rotor-nacelle assembly is situated at an elevation of 150 m above ground level, whereas the rotor diameter extends over 240 m.

The monopile structure, which has a uniform cross-section, has a vertical extension 30 m below the mean sea level at the mudline. The transition piece, which is 15 m in length, functions as the connecting component between the monopile and the tower. The geometrical specifications of the monopile indicate that the structure has a base thickness of 55.34 mm and a base diameter of 10 m. Similarly, the top of the tower is characterised by a thickness of 24.00 mm and a diameter of 6.5 m. An illustration of the HAOWT is presented in Figure 4.1, with further properties provided in Appendix A1. This research provides a comprehensive analysis of large-diameter, high-capacity HAOWT in deep sea conditions to enhance our understanding of these structures.

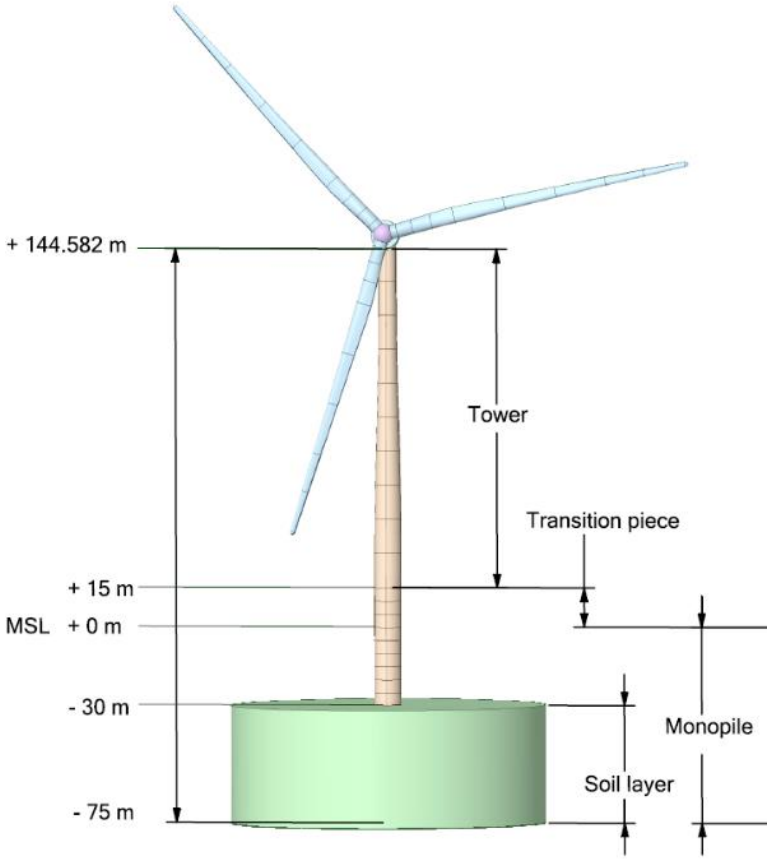

Figure 4.1: Adapted 15 Megawatt wind turbine geometry with modelled soil layer.

4.2 Development of load cases

In the structural analysis of this support structure, the ultimate limit states -based approach is employed, considering specific characteristics such as wind, wave, soil, and frequency. Data for this analysis were sourced from an extensive study that evaluated the meteorological and ocean characteristics of 23 offshore sites in the United States (Stewart et al. 2016). As indicated in Table 4.1, the mean wind speed was modelled using a Weibull distribution based on time-series data. This model also helped to compute the mean velocity and the corresponding significant wave height via a spectral peak period. For the project site, at a height of 10 m, the met-ocean characteristics include a 50-year maximum wave height and a 50-year 10-minute extreme wind speed. These specific met-ocean conditions were foundational in defining the design load cases for both standard operational and extreme conditions (Table 4.1).

In terms of load classification, offshore wind turbines are subject to various forms of loads, as categorised by BS EN 61400-3 (British Standards Institution 2019c). These include gravitational, aerodynamic, and hydrodynamic (both static and dynamic), actuation, ice, and wake loads. The formulas for calculating these environmental conditions and loads are detailed in DNV-RP-C205 (DNV 2010). In this chapter, focus was placed on analysing inertia and gravitational loads, aerodynamic and hydrodynamic loads, and the impact of soil. The analysis revealed that the effects of the current and hydrostatic loads are negligible. Moreover, the tilting moment was examined and found to be inconsequential (Shittu et al. 2020). The most critical loading scenario was identified to be yaw-misaligned parking conditions, coupled with excessive wind speeds and extreme coherent gusts that change direction. In this context, the maximum bending moments and vertical stresses were examined, with shear stress deemed negligible.

Table 4.1: Load cases based on wind and wave conditions (Gaertner et al. 2020).

Load case number	Mean Wind Speed (m/s)	Significant Wave height (m)	Spectral Peak Period (s)	Wind load on rotor (kN)	Max wind load on tower (kN)	Wave load on monopile (kN)	Turbine state
1	4	1.102	8.515	750	14.514	9.043	Operating
2	6	1.179	8.31	1229	34.192	9.971	Operating
3	8	1.316	8.006	1771	62.546	11.605	Operating
4	10	1.537	7.651	2563	99.722	14.229	Operating
5	12	1.836	7.441	2021	145.827	18.336	Operating
6	14	2.188	7.461	1708	200.944	24.546	Operating
7	16	2.598	7.643	1542	265.141	33.121	Operating
8	18	3.061	8.047	1417	338.474	44.116	Operating
9	20	3.617	8.521	1333	420.995	54.650	Operating
10	22	4.027	8.987	1229	512.744	59.762	Operating
11	24	4.516	9.452	1188	613.761	60.144	Operating
12	40	9.686	16.654	625	1759.068	143.341	Parked (extreme 1 yr return)
13	50	11.307	18.505	485	2782.64	124.77	Parked (extreme 50 yr return)

4.2.1 Wind load on rotor

The wind load on the rotor of an HAOWT is determined by the wind speed and the turbine's aerodynamic design. One key variable is the thrust force F_T, which is generated by the lateral forces acting on the rotor. This force is of particular importance, as it induces the most substantial bending moment near the monopile's base, making its accurate calculation essential for comprehensive structural analysis. To evaluate *the* F_T at the hub, a reference to the turbine's power curve is needed, which provides essential information such as the angle of attack. This angle, in turn, provides the thrust coefficient. In the technical report for the 15 Megawatt HAOWT (Gaertner et al. 2020), aerodynamic coefficients are provided as illustrated in Figure 4.1. These coefficients define the relationship between both the power and thrust coefficients and the wind speed. Notably, at 10.59 m/s, when the rated wind speed and thrust force are predicted to be at their highest, the generator produces the most power.

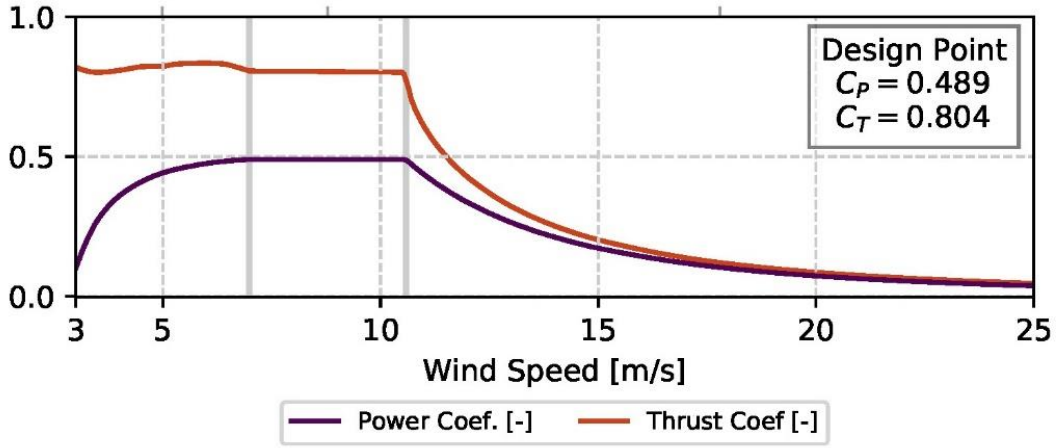

Figure 4.2: Aerodynamic coefficients for 15 Megawatt wind turbine (Gaertner et al. 2020).

Thus, the mean thrust force operating at the hub can be found in Equation 4.1 (Ishihara, Qian 2018):

$$F_T = 0.5\, C_T \rho A_s {U_w}^2 \tag{4.1}$$

where C_T is the coefficient of thrust obtained from the aerodynamic coefficient graph, ρ is the mass density of air (1.225 kg/m³), A_s is the swept area of the blades, and U_w is the wind velocity.

4.2.2 Wind load on tower

The mean wind velocity determines the wind load acting on the wind turbine tower F_w. These wind loads are created by minor lift forces and mainly drag forces from the wind. Equation 4.2 is the formula commonly used for the estimation of this load in accordance with the recommendations provided by DNV-RP-C205 (DNV 2010).

$$F_w = 0.5\, C_c \rho A_p {U_w}^2 Sin\ \alpha \tag{4.2}$$

where *Cc* is the shape coefficient based on the Reynolds number R_e, A_p is the area projected by the member normal to the direction of the force, U_w indicates the wind velocity averaged over a time interval at a height Z above the mean water level or onshore ground, ρ is the density of air, and α is the angle between the axis of the exposed tower and the wind direction.

The limitation of Equation 4.2 is that it does not account for the structure's dynamic behaviour. The BS EN 1991-1-4:2005 standard (British Standards Institution, 2005a) was employed to address this limitation. The detailed calculation for the wind load on tower calculations according to BS EN 1991-1-4:2005 are provided in Appendix A2. In this approach, the basic wind speed V_b was derived from the mean wind speed V_m, taking into account the specific conditions and terrain category. This was calculated using the terrain roughness factor $C_r(Z_e)$. Additionally, the turbulence intensity factor $I_v(Z)$ was calculated based on the maximum height Z along the monopile and tower from the seabed for the section under consideration. A uniform structural factor C_sC_d of 1.15 was applied to all calculations. It was observed that an increase in the wind velocity led to a proportional increase in the force experienced by the wind turbine tower.

4.2.3 Wave load on monopile

The wave load impacting the monopile was determined using Morrison's equation, as outlined in Equation 4.3. This calculation adheres to the linear wave theory and fulfils the criteria specified in DNV-OS-J101 (DNV 2014), which requires the monopile's diameter to be less than one-fifth of the wavelength. For the studied HAOWT, the conditions align with the intermediate wave states. Equations 4.4 and 4.5 provide the values for the horizontal flow velocity and horizontal flow acceleration, respectively, as recommended by BS EN 61400-3-1:2019+A11 (British Standards Institution 2019c).

$$F_{wave} = 0.5C_D\rho D|U|U + C_M\rho A\dot{U} \tag{4.3}$$

$$Velocity\ of\ flow, U = \frac{\pi H cosh(k+(z+d))}{T_w sinh\ (kd)} \cos At \tag{4.4}$$

$$Acceleration\ of\ flow, \dot{U} = \frac{2\pi^2 H cosh(k(z+d))}{{T_w}^2 sinh\ (kd)} \sin At \tag{4.5}$$

where ʎ is the wavelength, k is the wavenumber (= 2π/ ʎ), D is the monopile diameter, ρ is the density of water (1029 kg/m³), A is the cross-section area of the monopile in the vertical plane, z is the positive height above mean sea level, d is the depth from mean sea level to the mudline, T_w is wave period, and At denotes the wave amplitude.

The coefficient of drag C_D and inertia C_M are selected as 1.2 and 2.0, respectively (DNV, Risø 2002). It is assumed that the largest wind load corresponds to the time for the largest wave load for this analysis, according to the design code (British Standards Institution 2019b).

Table 4.1 summarises all loads applied to the HAOWT, including the wind force on the tower and the wave on the monopile. The maximum values of wind force on tower are also summarised in Table 4.1, while calculations as a function of height were considered in the analysis (detailed calculations are found in Appendix A2).. A Weibull distribution was used to analyse both wind speed over time and wave height against frequency. From the distribution analysis of the wave height and frequency, a correlating spectral peak period was obtained, forming the basis for the load case presented in Table 4.1.

4.3 Analytical model for stress calculations in the monopile

The analytical model for the HAOWT is first presented, followed by the uniform corrosion loss and soil models. To calculate stresses in tubular structures such as joints and members, beam theory is employed to estimate the nominal tensile and compressive stresses (DNV 2014). Specifically, the Euler–Bernoulli cantilever beam model, supplemented with masses that represent the rotor-nacelle assembly and blade, has been adapted for use with monopiles (Gupta, Basu 2018). In this model, the soil is depicted as a fixed base but subsequently modelled, and both aerodynamic and hydrodynamic forces act on the cantilever beam, as demonstrated in Figure 4.3. This is done to quantify the bending stresses under tensile and compressive conditions within both the tower and the monopile, given specific loading scenarios.

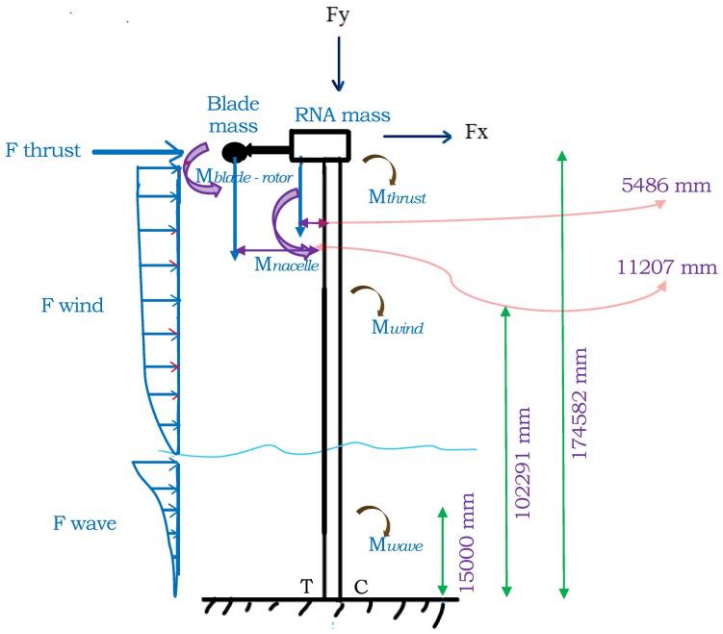

Figure 4.3: Beam theory for analytical formulations of 15 Megawatt wind turbine.

Key parameters, such as the cross-sectional area *A* of the tower and monopile, along with the moment of inertia *I*, are determined using Equations 4.6 and 4.7 (Appendix A3). Subsequently, the total bending moment M_T is computed by considering each force, direction, and weight that influences the structure around the base (compression–tension (C-T)), as outlined in Equation 4.8. The bending stress σ_b is derived from Equation 4.9, while the compressive stress σ_c is found using Equation 4.10. Both the bending and compressive stresses act in the vertical y-direction. The bending moments create shear stress in the vertical direction, which has a zero value at the locations with the maximum stresses owing to bending; hence, it is neglected. There is a shear stress due to the lateral forces which do not act in the vertical direction, and it is quite small in magnitude; hence, it is neglected. Accounting for all the stresses in the vertical y direction, the total stress in the y-direction, σy, is represented by Equation 4.11. Maximum tensile and compressive stress values due to bending moments are described by Equations 4.12 and 4.13, where positive values indicate tension and negative values signify compression.

$$A = \frac{\pi}{4}(D^2 - d^2) \tag{4.6}$$

$$I = \frac{\pi}{32}(D^4 - d^4) \tag{4.7}$$

$$M_T = (M_{thrust} + M_{wind} + M_{wave}) - (M_{Blade-rotor} + M_{nacelle}) \tag{4.8}$$

$$Bendng\ stress, \sigma_b = \frac{My}{I} \tag{4.9}$$

$$\text{Compression stress, } \sigma_c = \frac{F_y}{A} \tag{4.10}$$

$$\text{Total stress (y-direction), } \sigma_y = \sigma_c + \sigma_b \tag{4.11}$$

$$Maximum\ tensile\ stress, \sigma_y^t = \sigma_c + \sigma_b^t \tag{4.12}$$

$$Maximum\ compressive\ stress, \sigma_y^c = \sigma_c + \sigma_b^c \tag{4.13}$$

4.3.1 Material loss due to uniform corrosion model

A uniform corrosion model was applied to examine its impact on the stress distribution in HAOWT support structures. Accurate long-term integrity predictions necessitate detailed corrosion modelling over the structure's lifespan (Melchers 2005). Assessing the damage due to stress levels is crucial for estimating the remaining operational life of wind turbines, especially under harsh and deteriorating conditions. This involves accounting for material thickness reduction (Melchers, Beck 2018).

Table 4.2 illustrates the corrosion zones in offshore wind turbine supports as per the DNVGL-RP-0416 guidelines (DNV 2016a). Understanding the effect of material loss on stress evolution over time is particularly beneficial for designing high-capacity large HAOWTs under marine conditions and providing a vital component for subsequent fatigue studies.

Table 4.2: Corrosion rate over time for long-term monopile stress assessment per DNVGL-RP-0416 (DNV 2016a).

Distance from mean sea level (m)	Corrosion Zones	Corrosion rate (mm/yr)	Average loss (mm/yr)
(-75) - (30)	Buried Zone	0.06–0.10	0.08
(-30) - (-5)	Submerged Zone	0.10–0.20	0.15
(-5) - 0	Tidal Zone	0.05–0.25	0.15
0 - (+15)	Splash Zone	0.20–0.40	0.3
(+15) - (+28)	Atmospheric Zone	0.05–0.075	0.0625

This model calculates the HAOWTs bending stresses as a function of thickness loss by altering the inner and outer monopile diameters. For example, a similar model was employed to predict the remaining lifespan of steel offshore structures reasonably and accurately, where structural capacity is largely determined by cross-sectional dimensions (Melchers 2005). This approach is indispensable because corrosion interacts synergistically with applied stresses and other mechanical damage factors, as indicated in Equations 4.14 and 4.15.

$$\text{Structural capacity after corrosion loss, } R(t) = \sigma[A - P \cdot c(t)] \tag{4.14}$$

$$R(t) = k \cdot \sigma_b \cdot [d(t)]^2 = k \cdot \sigma_b \cdot [d_o - 2 \cdot c(t)]^2 \tag{4.15}$$

where $R(t)$ is the structural capacity after corrosion loss, σ_b is the maximum stress in bending, $d(t)$ is the remaining thickness, d_o is the original thickness, A is the cross-sectional area under stress, P is the perimeter area exposed to seawater, $c(t)$ is the corrosion loss, and k is the bending factor taken as 0.25 for the elastic-plastic material response. Equation 4.6 (cross-sectional area) and Equation 4.7 (moment of inertia) were adapted in the analytical model to incorporate varying corrosion rates from Table 4.2 over time.

4.4 Finite element modelling for uniform corrosion and soil effects

The 15 Megawatt HAOWT support structure, as detailed in Section 4.1, was modelled and simulated using ANSYS (ANSYS Inc. 2004) static and modal analyses. The research focused on evaluating the structural responses under the load cases for wind and waves from 0 to 50 m/s (Section 4.2). For illustrative purposes, we applied loads for a specific scenario with a wind speed of 8 m/s, as shown in Figure 4.4. The wind and wave forces are modelled in the same direction, and all sea states are regarded to be in just one direction according to IEC 61400-1:2019 for ultimate limit state conditions (British Standards Institution 2019b). The consideration of different load directions can provide a further understanding of how different stresses are distributed across the tower structure. However, considering the worst condition enables the analysis of the ultimate limit state conditions and allows for comparative analyses of the thickness loss due to corrosion.

The rotor-nacelle assembly and turbine blades are represented as point masses in the model. Gravitational acceleration was applied to these point masses, as well as to the entire tower structure. The thrust force is applied as a remote force acting at the centre of the rotor because when wind moves over the blades, it creates forces of lift and drag. These forces result in a net thrust force acting on the blades, pushing them in the direction opposite to the wind flow and transferring them to the rotor. The force on the tower was uniformly applied from the splash to the top of the tower, as different wind speeds were experienced at different heights on the tower, and these zones were exposed to the effect of wind. The wave force was applied to the tidal and submerged zones as a uniformly distributed force, as different wave forces are experienced at different heights on the monopile. The monopile was constructed from S355 structural steel, which is frequently used for such support structures (Igwemezie et al. 2018). In modelling the monopile and tower, isotropic elastic material properties were assumed. The material properties employed included a Young's modulus of 200 GPa, Poisson's ratio of 0.3, and material density of 7850 kg/m^3 (Gaertner et al. 2020). Thicknesses across the different corrosion zones were adjusted using shell elements to reflect the actual material degradation due to corrosion. Stresses in the four zones: atmospheric, splash, tidal, and submerged zones of the support structure were determined. It is crucial to note that corrosion-induced thickness loss not only changes the stress distribution but also affects other dynamic properties of the wind turbine, such as its natural frequency.

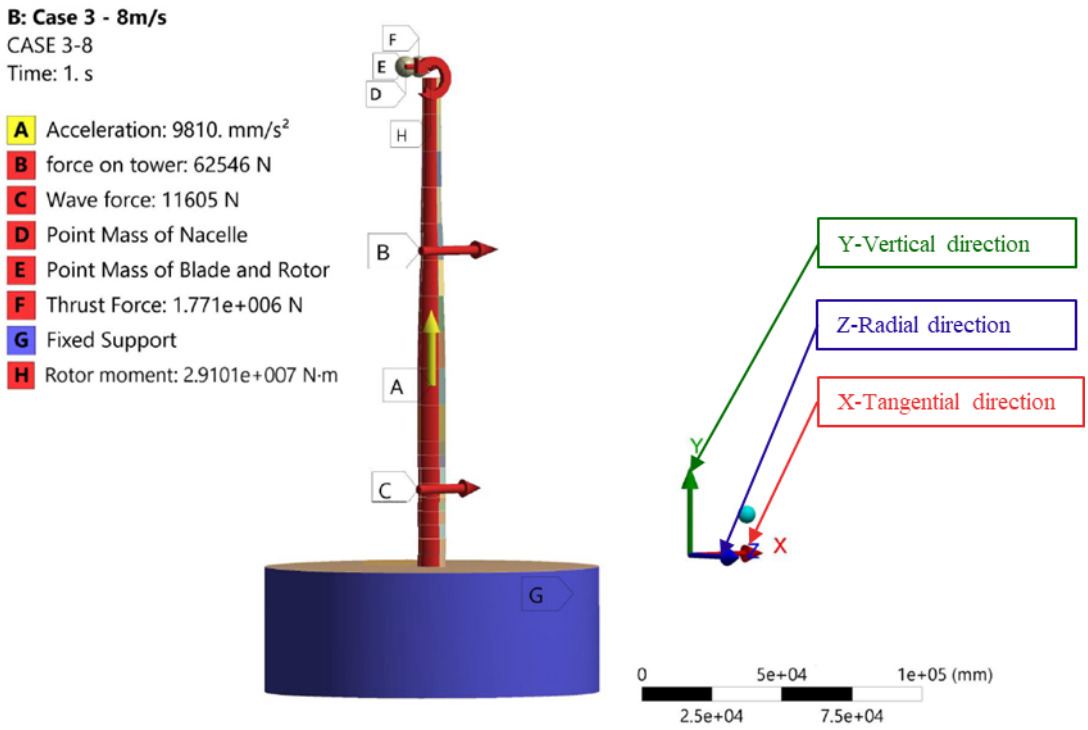

Figure 4.4: Finite element model for stress analysis.

The Mohr-Coulomb soil model for nonlinear analysis was applied to the soil geometry to effectively capture the elastoplastic behaviour of the soil. Specifically, two types of non-linearities were considered and applied between the soil geometry and the monopile wall in the buried region in soil modelling: material non-linearity through the Mohr-Coulomb model and contact non-linearity by incorporating frictional contacts in the soil-structure interaction (Oh et al. 2018). Structural loads from the HAOWT lead to soil deformation, a phenomenon modelled by considering the soil's shear strength and its dependency on effective normal stresses, as indicated in Equation 4.14. Equation 4.15 defines the Mohr-Coulomb yield surface in 3-D space (Oh et al. 2018).

$$Shear\ strength\ of\ soil\ \tau_f = c + \tan \emptyset \tag{4.14}$$

$$\left(\overline{\sigma_1'} + \overline{\sigma_3'}\right) \sin \emptyset + 2c \cos \emptyset - \left(\overline{\sigma_1'} - \overline{\sigma_3'}\right) = 0 \tag{4.15}$$

where c is cohesion, σ^1 is the effective nominal stress, σ_1' is the first principal stress, σ_3' is the third principal stress, and $\emptyset$ is the internal friction angle.

Soil conditions under both drained and undrained scenarios were explored, revealing varying degrees of effective stress change (Stromblad 2014). This implies that changes

in stress between the soil particles, which are dependent on the soil profile, are directly correlated with stress variations in the HAOWT tower and monopile under loading.

The Mohr-Coulomb soil model was used to model the soil-structure interactions to offer an accurate depiction of dense sand characteristics, as documented in previous studies (Achmus et al. 2009; Depina et al. 2015; Yu et al. 2022). This type of soil is predominantly found throughout the North Sea region, which hosts the majority of Europe's offshore wind turbines (Wind Europe, Wood Mackenzie 2020). The Mohr-Coulomb soil model utilises 3-D continuum elements (Oh et al. 2018). A soil model with a diameter of 120 m and depth of 65 m was modelled for monopile embedment, which met the minimum dimensions specified by the American Petroleum Institute (American Petroleum Institute 2007) to generate minimum boundary effects. For uniformity and comparison, soil layers were not extended beyond the specified 65m depth. This method for representing soil is more accurate, although it requires high computational power (Martinez-Luengo et al. 2017). The natural frequencies of the HAOWT were analysed, focusing on the first bending mode shape, as it is the dominant one owing to lateral loads in the x-direction.

A comparison between different soil properties was also conducted to understand their effect. Three geographically distinct soil parameters were used to represent offshore conditions, each transitioning from loose to stiff materials, such as clay and sand. These parameters were based on site test data for the North Sea, East China Sea, and Irish Sea, as presented in Table 4.3 (Augustesen et al. 2009; Martinez-Luengo et al. 2017; Oh et al. 2018) where Model 0 is the FEA model where the fixed boundary conditions were used and no soil was modelled. In the FEA model, for cohesive layers in clay, an initial cohesion value of 10 KPa and 20 KPa was used for medium and hard cohesive clay respectively, while 22 KPa was applied for sand. The dilatancy angle for sands was taken as 5˚ as a non-cohesive soil. Also, γ’ represents the submerged unit weight of soil, Es is the Young’s modulus, v is the Poisson's ratio (minimum value of 0.28 and 0.4 was used for sands and clay respectively. Where not specified), Ø is the internal friction angle, and Ψ is the angle of dilatancy. Additionally, the residual cohesion is given as 0.8 times the initial cohesion, and the residual friction angle δ was obtained from previous research recommendations (Singh, Goel 2011; Raj 1981) based on the plasticity level of soil from experimental works.

Table 4.3: Soil parameters applied in the finite element model.

FEA Model	Location	Soil type	Soil parameters						
			Depth (m)	γ' (kN/m^3)	E_s (Mpa)	ν	$\emptyset$ (°)	Ψ (°)	δ (°)
Model 1	North Sea	Sand	0.0 – 4.5	10	130	0.28	45.4	15.4	45.4
		Sand	4.5 – 6.5	10	114.3	0.28	40.7	10.7	40.7
		Silty sand	6.5 – 11.9	10	100	0.28	38	8	38
		Silty sand	11.9 – 14.0	10	104.5	0.28	36.6	6.6	36.6
		Silty sand	14.0 – 18.2	7	4.5	0.28	27	0	27
		Sand	18.2 – 65.0	10	168.8	0.28	38.7	8.7	38.7
Model 2	East China Sea	Lean clay	0.0 - 12.0	8.19	30.8	0.4	26	0	21
		Silty sand	12.0 - 26.3	9.19	73.4	0.36	33	3	33
		Poorly-graded sand	26.3 - 27.5	10.19	104*	0.35	35	5	35
		Lean clay	27.5 - 30.3	9.19	135	0.35	20*	0	15
		Poorly-graded sand	30.3 - 39.0	10.19	104*	0.35	35	5	35
		Lean clay	39.0 - 42.0	9.19	135	0.35	20*	0	0
		Weathered soil	42.0 - 46.0	9.19	79.8	0.33	30	0	20
		Weathered rock	46.0 - 65.0	11.19	94.32	0.31	32	2	21
Model 3	Irish Sea	Sand	0.0 - 2.4	11	22.7	0.28*	42	12	42
		Sand	2.4 - 5.4	11	33.3	0.28*	42	12	42
		Sand	5.4 - 8.0	11	44.3	0.28*	42	12	42
		Clay	8.0 – 11.0	10	300	0.4*	20*	0	15
		Clay	11.0 - 13.0	10	230	0.4*	20*	0	15
		Clay	13.0 - 65.0	10	320	0.4*	20*	0	15

* *Where not given, standard values across literature have been adapted.*

The tower and monopile were modelled using 4-node SHELL181 elements to account for their thickness. Convergence analyses were performed to identify the optimal element size given the large scale of the model. A coarse mesh could overestimate the stress by making the model overly stiff, whereas a finer mesh could prolong the computational time and potentially cause convergence problems (Yeter et al. 2019). Element ranging in size from 10 to 4,000 mm were tested, and stress outcomes were specifically examined in the tension and compression zones of the splash region. As illustrated in Figure 4.5, an element size of 150 mm was found to be optimal for achieving accurate stress predictions without compromising computational efficiency. The model, when meshed with this optimal 150 mm element size, resulted in 275,246 nodes and 381,193 elements. All FEA computations were carried out using a 4-core parallel distributed memory system on an Intel Core i7-10510U CPU with 16 GB RAM. The use of shell elements also allows the incorporation of material loss due to corrosion by changing the element thickness value of the shell element. Solid elements were used to successfully capture soil effects. Displacements and rotations are considered using 3-D SOLID186 quadratic elements in both the soil and pile domains. Fixed support was applied to the sides and bottom of the soil layer on the symmetrical model. The soil-structure interaction interface was modelled using a friction contact between the soil and the monopile. Contact friction coefficient values of tan (tan (2/3) δ) were used between sand and pile layers, while undrained shear strength of clay was used as friction coefficient between pile and clay (Jung et al. 2015).

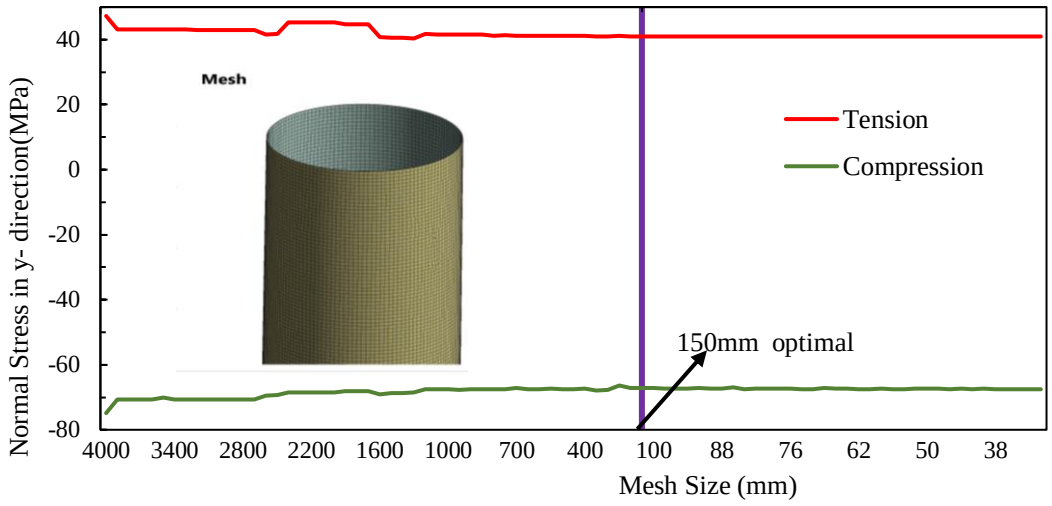

Figure 4.5: Results from mesh sensitivity analysis with stresses at the splash zone.

4.5 Results and discussion of stress analyses of large offshore wind turbine monopile

4.5.1 Effect of wind and wave forces on wind turbine

Figure 4.6 displays the calculated forces exerted on the 15 Megawatt HAOWT, as outlined in Section 4.2. During its operation, the HAOWT will experience the highest thrust force (2.563 MN) at a wind speed of 10.59 m/s. Previous research studies on 5 – 6 Megawatt capacity HAOWTs have reported a thrust force of 2 MN (Gentils et al. 2017), 1.42 MN (Arshad, O'Kelly 2016) and 1.63 MN (Arany et al. 2017). These values show that the thrust force experienced by HAOWTs increases as their power capacity increases. The wind force of the rotor decreased as the wind turbine approached its cut-out speed or when it was out of operation. In addition, the wind force acting on the tower increased with rising wind speeds. A similar relationship was observed between the wave force and mean wind velocity, corroborating a theory that directly relates wind speed to wave height (Michel 1999).

The wind force on tower, thrust force at hub and wave force on monopile were taken to act unidirectionally in the tangential x direction for ULS conditions according to IEC 61400-3 standard (British Standards Institution 2019c). The HAOWT will experience a tower force of 1.76 MN based on an extreme wind speed of 40 m/s recorded in a year (Section 4.2). Over a 50-year return period, a peak wind force of 2.78 MN was measured at an average wind speed of 50 m/s. Therefore, it was concluded that the thrust force typically exhibited the highest magnitude during the HAOWT's operation. Special attention was recommended for wind forces acting on the tower when the turbine was parked, particularly in the case of wind gusts, as they could lead to higher cyclic loads and potential fatigue damage (Karimirad, Moan 2012). These observations are particularly relevant for damage monitoring in the context of anticipated climatic changes, which could result in more frequent high wind and wave forces.

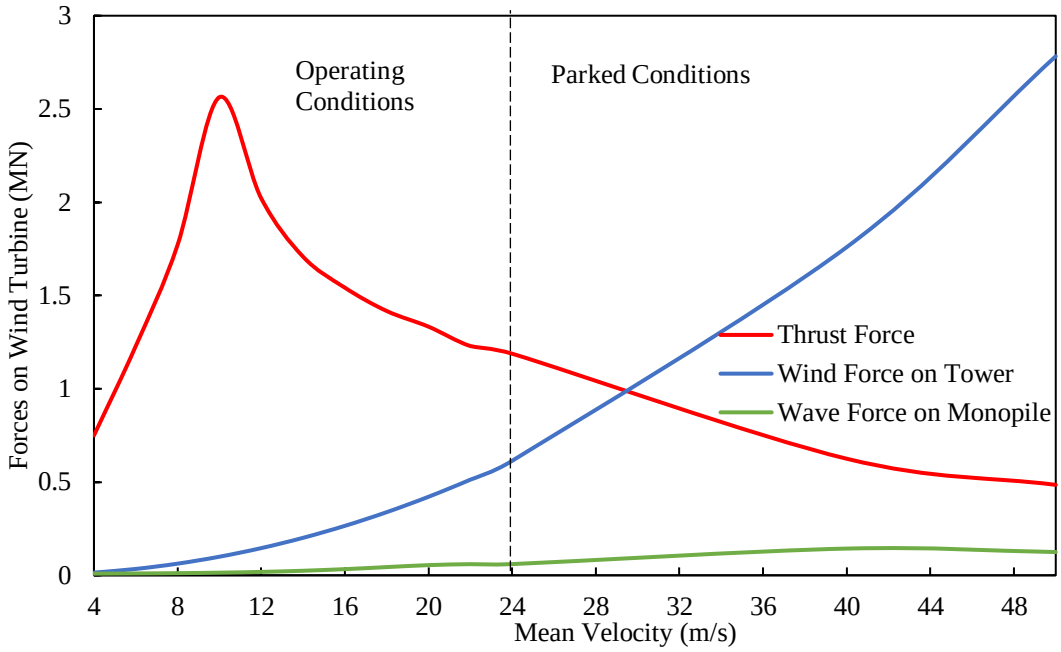

Figure 4.6: Effect of wind velocity on forces acting on wind turbine for normal and parked conditions.

4.5.2 Effect of wind velocity on stresses in the vertical direction at different monopile zones

The relationship between the mean wind velocity and normal vertical direction stresses in the support structure was examined. In the absence of wind and wave loads, the support structure material experienced compression due to the HAOWTs self-weight, which was significantly contributed to by the mass of the rotor-nacelle assembly. The thrust force was identified as having the most significant impact on bending stresses owing to both its high magnitude and its elevation above the mud line, which generated a larger bending moment. Figures 4.7 and 4.8 display the predicted stress values for both tension and compression across different zones in the support structure, as calculated through analytical and FEA models (data in Appendix A4).

A strong correlation between the results from both models was observed, lending credence to the methodologies employed for stress prediction. The highest bending stress was observed in the submerged zone near the mudline, as this area was subjected to the greatest bending moment. Accordingly, this suggests that the HAZ of the weld above the mud line is the most susceptible to potential fatigue crack initiation (Jacob

et al. 2019). Figure 4.7 revealed that the maximum tensile stresses were observed in all zones for both operating conditions and all mean wind speeds. Specifically, at the rated speed of the wind turbine (10.59 m/s), the tensile stresses in the vertical direction reached values of 76.74 MPa and 67.5 MPa in the submerged and atmospheric zones, respectively. In the parked condition, the submerged zone similarly exhibited the highest tensile stress in the vertical direction.

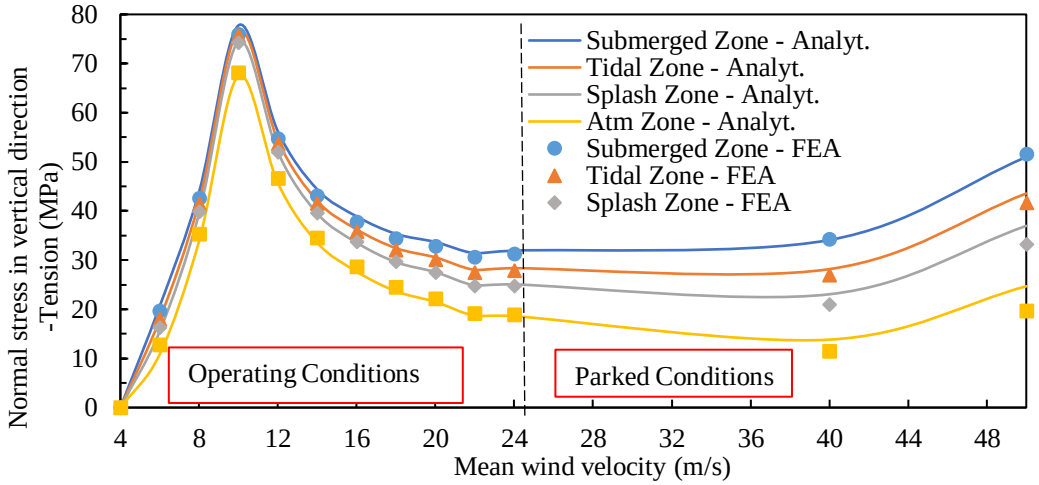

Figure 4.7: Wind velocity effects on tensile stress in the vertical direction.

In Figure 4.8, the compressive stresses in the vertical direction generally exhibited a higher absolute magnitude than the tensile stresses. This increase in compressive stress was attributed to the additional weight that contributed to the compressive bending stresses. The strategic placement of the tower-top masses on the wind turbine significantly reduced the overall bending effects during wind force exposure. This feature enhanced the high-capacity performance of the large wind turbine by reducing the tensile stresses. Regarding the operating conditions, the splash zone registered marginally greater stress levels than the submerged zone under maximum power production. Also, when the HAOWT was in parked conditions, higher stresses were observed in the submerged zone. These stress distributions were specific to the transition piece region of the HAOWT and could differ if the geometry of this transition piece was accounted for.

Comparative analysis between Figure 4.7 (predicted stresses) and Figure 4.6 (generated forces) revealed analogous patterns. Specifically, thrust forces dominated during operational states, whereas parked conditions led to elevated stresses, indicating the predominant influence of wind and wave effects in this state. The FEA

results closely aligned with the analytical findings across all considered wind speeds. The maximum observed compressive stress was approximately 107 MPa, which is less than one-third of the yield stress of the S355 steel. During the transition from parked to operational states, the zone experiencing the highest stresses shifted from the submerged to the splash zone, specifically in the transition piece region. This suggests that the lowest weld in this region is the most susceptible to fatigue damage when the HAOWT is not in operation. The main failure mechanism could be fatigue at the weld HAZ owing to the lower fatigue strength. In addition, there will be a higher stress concentration at the weld toe if not machined, or if pits are developed in the HAZ.

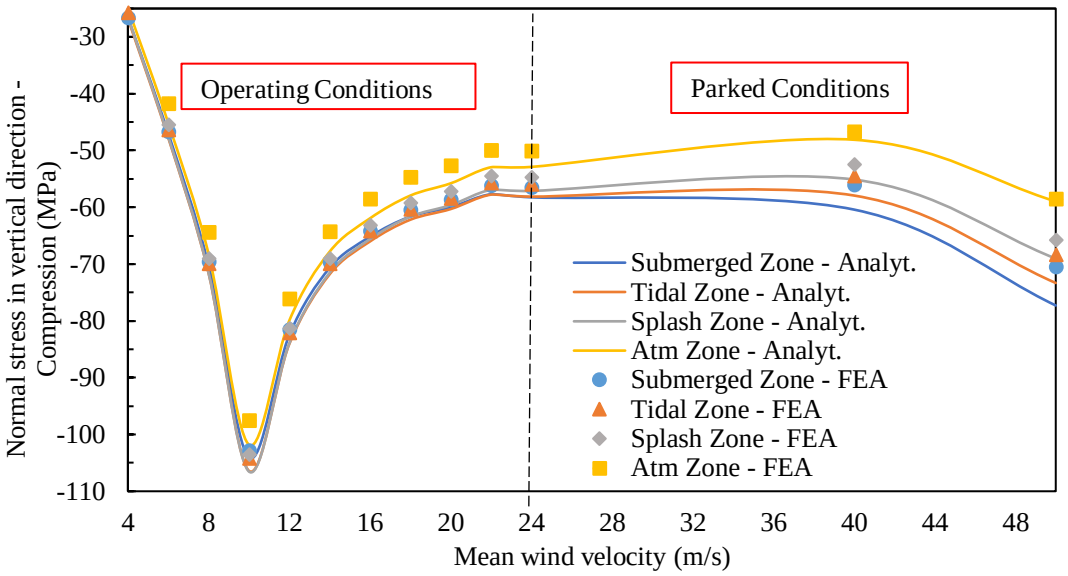

Figure 4.8: Wind velocity effects on compressive stress in the vertical direction.

4.5.3 Effects of long-term corrosion loss rate on the evolution of stresses

The impact of uniform corrosion on the stress fields in HAOWTs with large diameters was evaluated across four different zones: atmospheric, splash, tidal, and submerged. Stress predictions were made in terms of tensile and compressive stresses in the vertical direction at varying mean wind velocities. The corrosion rates in these zones were also assessed based on the exposure time and thickness loss. From 2184 simulation runs using FEA and analytical calculations, a consistent correlation was observed, with an average difference of 3.64% between the two methods. The FEA

computational time was approximately 4 hours for all cases, whereas the analytical model executed in Excel took merely one second (Appendix A5).

The results of the long-term corrosion loss rate on the evolution of stresses for the splash zone are presented in Figures 4.9 and 4.10. The results for all zones are presented in Appendix A6. The location of the maximum tensile stress shifted from the submerged to the splash zone over time, attributable to a higher corrosion rate in this region (DNV 2016a). The maximum bending stress was observed in the splash zone, particularly for compressive bending stresses. Notably, extreme stress values were identified at wind speeds of 10.59 m/s and 24 m/s; the latter being the cut-out speed at which a wind turbine ceases operation (British Standards Institution 2019b). A similar pattern in corrosion loss over increasing exposure days was observed elsewhere (Melchers 2005). Despite the similar trend, there is a tiny discrepancy in the corrosion loss values between the analytical and FEA predicted results at 50 m/s mean wind velocity in the atmospheric zone tensile zone (Appendix A6; Figure A6-7). This could be due to the FEA findings being obtained at boundary conditions where the wave load was applied or the fact that the distribution of the applied loads in the FEA (based on nodal distribution) differs slightly from the load distribution of the analytical solutions.

Overall, all results demonstrated an increase in both tensile and compressive stresses over time, correlating directly with the corrosion rates. For instance, stresses increased from 76 MPa to 81 MPa in the submerged zone and from 74 MPa to 87 MPa in the splash zone over 20 years at a wind speed of 10 m/s. This suggests a heightened stress level in the splash zone beyond the seventh year of operation, underscoring the need for corrosion monitoring (Figure 4.10). The highest compressive stress observed was 124 MPa in the splash zone after 20 years, as predicted by the analytical model. Given that the typical yield stress for structural steel used in towers and monopiles is above 355 MPa, the risk of permanent deformation is minimal. However, the risk could become significant at wind speeds exceeding 50 m/s, where the maximum compressive stresses were noted to be 82 MPa, or in cases where the corrosion rates are higher than the specified by the standard (See Table 4.2).

This suggests that it is important to consider corrosion throughout the design process and that the loss of material caused by corrosion should be monitored during service

to prevent any potential hazards of failures, such as the initiation and propagation of fatigue cracks. An additional remark may be made regarding the presence of compressive stresses with the highest magnitudes. Notably, these compressive stresses can cause permanent deformations if they surpass the yield stress of the material. The exposure of support structures, such as towers and monopiles, to corrosive conditions leads to the formation of pits. The coalescence of these pits is the primary reason for employing the uniform thickness loss model. When analysing a tapered tubular section, it is important to note that the thickness of the steel tower might vary. This variation in thickness resulted in different degrees of thickness loss across different zones, with the most severe loss occurring in the splash zone.

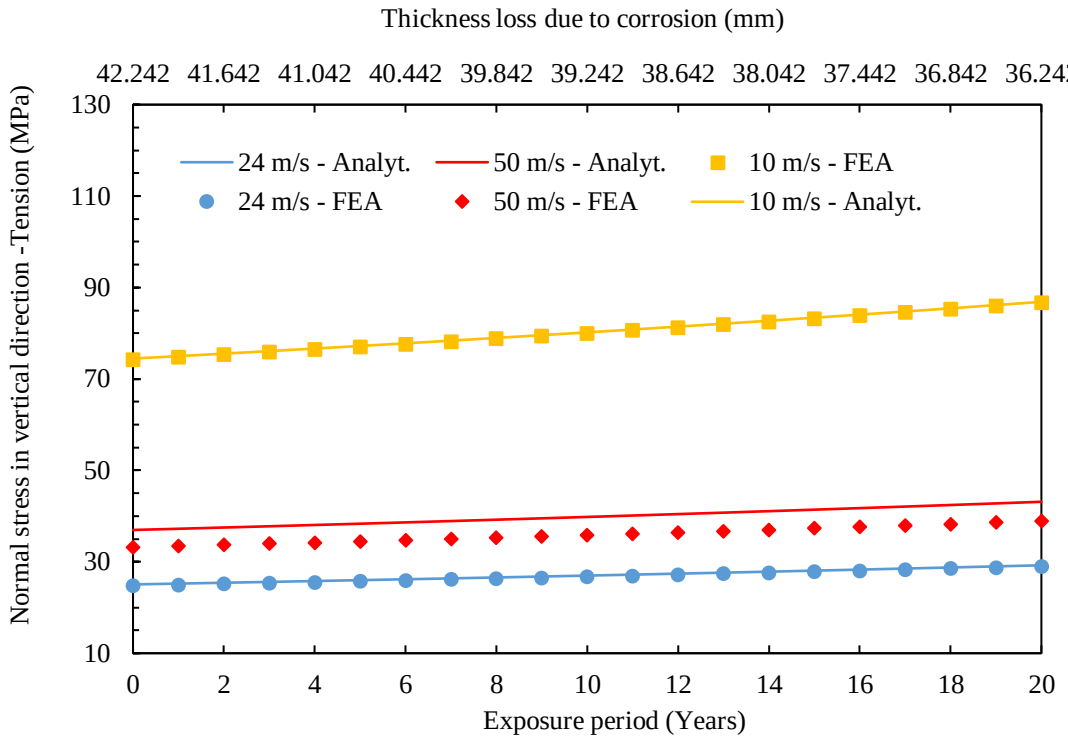

Figure 4.9: Effect of uniform corrosion on tensile stress at the splash zone.

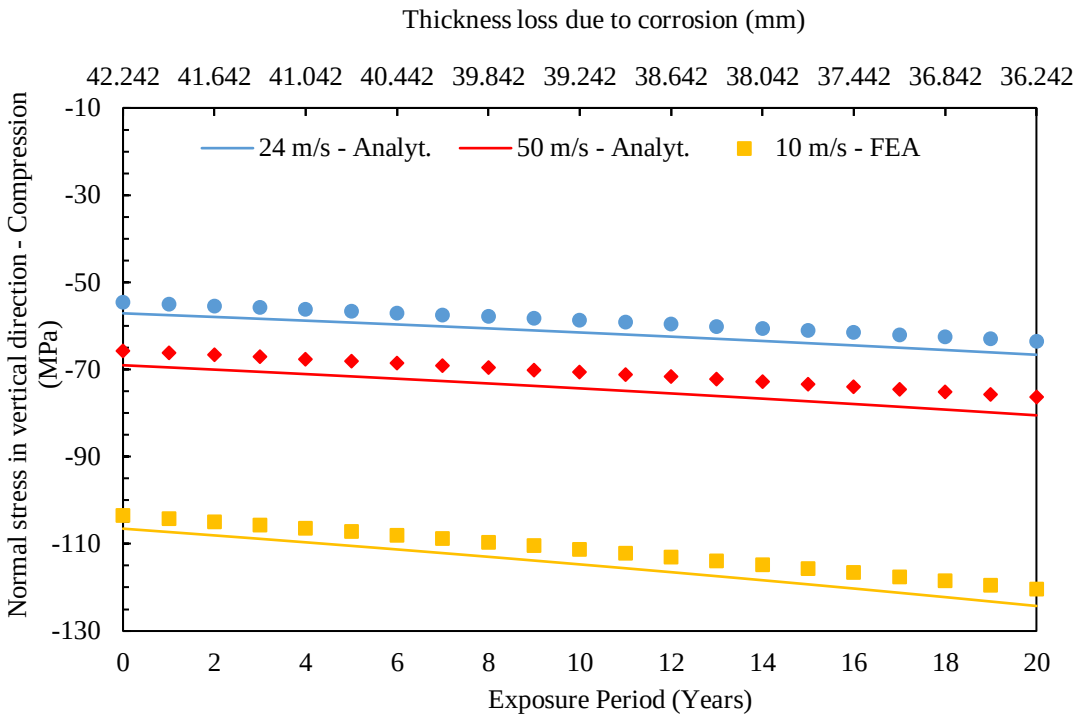

Figure 4.10: Effect of uniform corrosion on compressive stress at the splash zone.

4.6 Results and discussion of soil-structure interaction of large diameter offshore wind turbine monopile

4.6.1 Effect of soil profiles on lateral response of monopile

The 15 Megawatt HAOWTs monopile with a buried depth of 45 m was considered across three distinct soil profiles: medium to dense sand, silty sand transitioning to lean clay and rock, and sand transitioning to clay. Figure 4.11 illustrates the deformations observed throughout the support structure of the 15 Megawatt HAOWT (details found in Appendix A7). Based on the wind load of 1771 kN, wave load of 62.5 kN on tower and a 11.6 kN thrust force values for a wind speed of 10.59 m/s which is the maximum power production speed for the 15 Megawatt HAOWT (Table 4.1), the estimated deformations at the tower-top section were 1.99 m under fixed support conditions, 2.64 m in the North Sea, 2.8 m in the East China Sea, and 2.65 m in the Irish Sea. This observation showed that soil profile variations could significantly affect the deformation of large-diameter HAOWT structures. Moreover, the study found that omitting soil modelling could lead to an underestimation of deformation, a factor crucial to the design process.

Findings from Model 1 (North Sea) and Model 3 (Irish Sea) (from Table 4.3) indicated comparable levels of tower deformation, suggesting that the initial three layers of sand likely had a similar range of stiffness. Model 2, representing conditions in the East China Sea, exhibited the most deformation due to low soil shear strength in the majority of its soil layers. This deformation was primarily observed in soil layers composed of silty sand and lean clay. These deformations could be used to assess the associated risks as well as the suitability of soils for large-diameter HAOWTs. When examining this tapering tubular structure, it was found that the buried and submerged sections had a larger diameter of 10m. As the thickness decreased towards the upper portion, an increase in the lateral response was observed. This finding showed a correlation between the diameter of the support structure and its deformation.

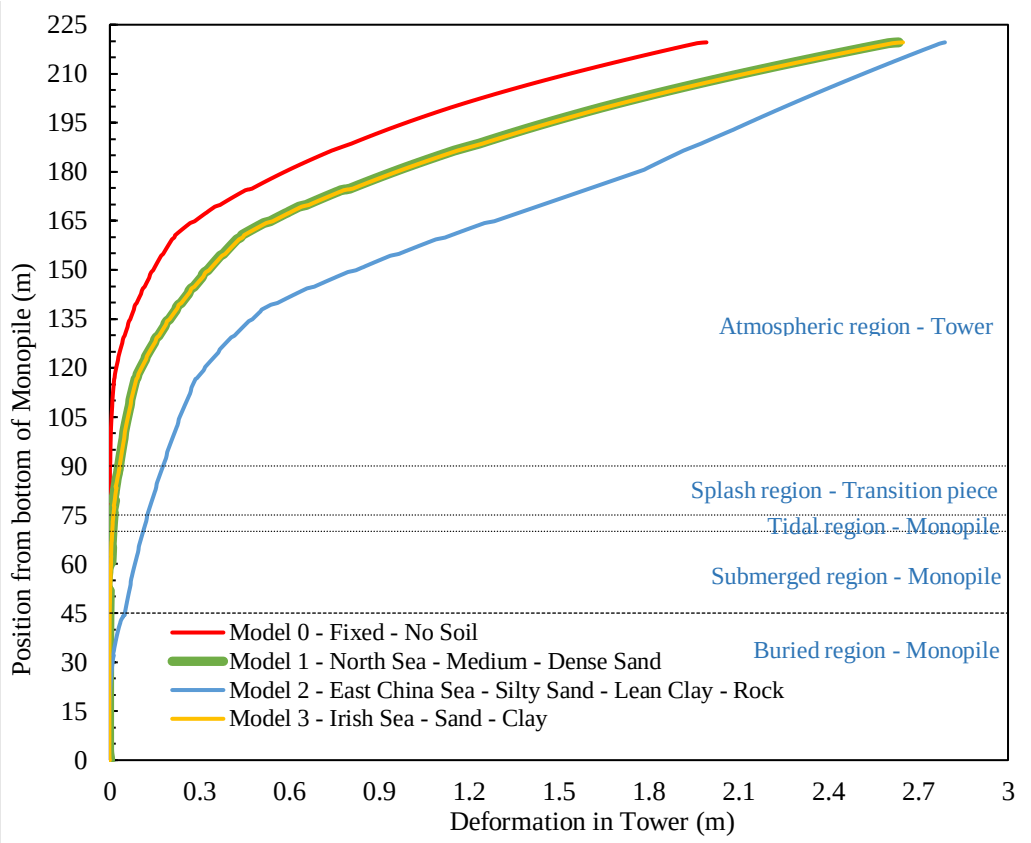

Figure 4.11: Deformations based on different soil profiles in monopiles.

Additionally, Figure 4.12 illustrates the maximum deformations in the foundation for all soil models under the load-dominant X-axis. Based on this data, Model 2 (East China Sea) exhibited the highest degree of foundation deflection, measuring 0.05 m. This observed value was 50% below the prescribed threshold of 0.1 m as stipulated in

the design standard (DNV 2018), and was within the range of values reported in a comparable study on a 5 Megawatt offshore wind turbine (Gentils et al. 2017). The lateral reactions of the soil model in the North Sea and East China Sea showed notable similarities.

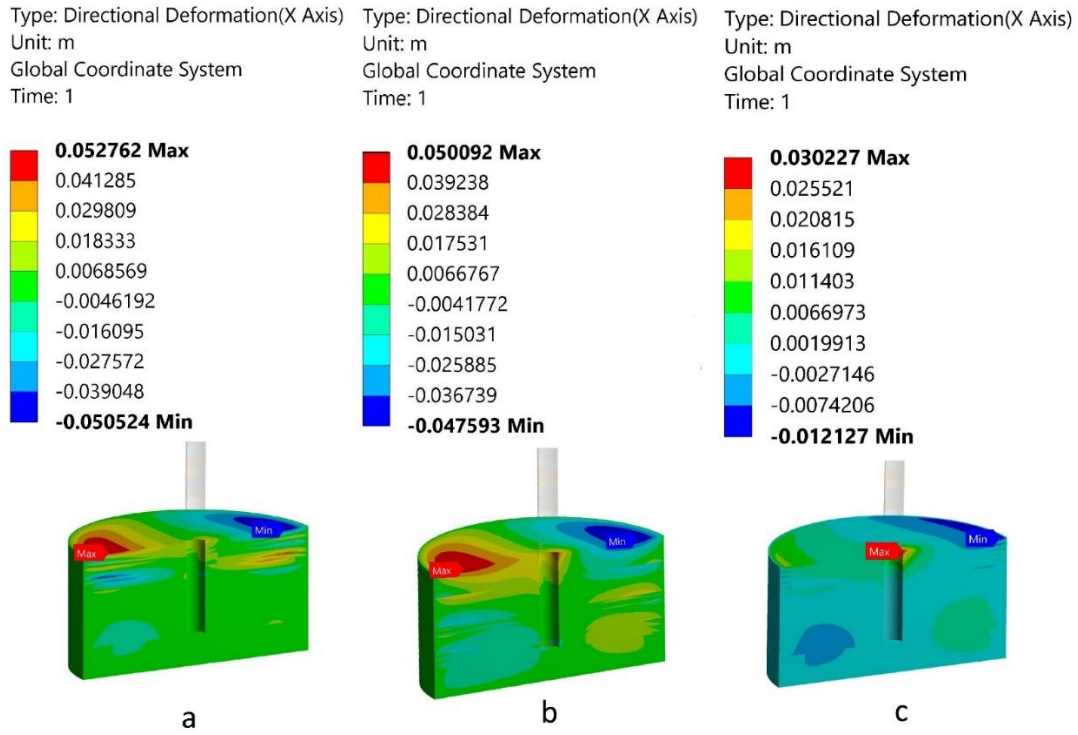

Figure 4.12: Deformation in soil profiles: a) model 1- North Sea, b) model 2-East China Sea, c) model 3- Irish Sea.

4.6.2 Effect of soil on natural frequency in monopile

The natural frequency for the HAOWT was found to be between the 1P and the 3P regions, which correspond to a frequency band of 0.10 Hz to 0.38 Hz (Gaertner et al. 2020) ("1P" is the frequency of one complete rotor rotation, while "3P" is the blade passing frequency per rotation). This range encompasses all possible wind speeds. The dominant mode shape was found to be the first bending mode shape, which acted in the lateral (x) direction of the loads. Model 0, which assumed rigid soil or fixed boundary conditions, yielded a natural frequency of 0.16887 Hz (see Table 4.4). This was consistent with the reported natural frequency of 0.17 Hz (Gaertner et al. 2020). Models incorporating various soil conditions produced natural frequencies close to this value. The maximum percentage difference was only 11.7% when compared with the rigid soil model. Consequently, it was demonstrated that all soil profiles stayed within

the recommended frequency band of 0.1 - 0.38 Hz. These findings indicate that soil conditions should be considered in the modal (frequency) analysis during the design stage.

Table 4.4: Soil variation with natural frequency in the support structure.

Model	Soil Profile Location	Natural Frequency At The Bending Mode (Hz)
Model 0	-	0.16887
Model 1	North Sea	0.1552
Model 2	East China Sea	0.15117
Model 3	Irish Sea	0.15412

4.6.3 Effect of soil profiles on stresses evolution

Figures 4.13 illustrates the changes in stresses in the vertical direction of both the tower and monopile zones (detailed in Appendix A8). These predicted stresses were analysed and compared across the support structures in the vertical y -direction (Figure 4.4). Applying a peak power production velocity of 10 m/s in the models offered insights into the maximum stresses the structures could experience, thereby proving useful for industrial-proof analyses. In both the tension and compression scenarios, a gradual rise in stress was observed, peaking in the splash region before subsequently declining along the length of the support structures. A maximum variation of 9.5% in the stress levels in the support structure was noted for all soil models.

The highest bending stress in compression was recorded in the splash zone, registering at 148.64 MPa. This zone corresponded to the section where the shell wall thickness and bending stiffness began to decrease. This area, located in the transition piece, was found to be more vulnerable to damage under peak operational conditions than other regions of the sub-structure. Tensile and compressive stress results in the vertical direction correlated with the maximum and minimum principal stresses, respectively, indicating that stresses in the vertical direction were the dominant factors. Soil

modelling showed that tensile stresses were lower and compressive stresses were higher compared to the fixed support condition (Model 0).

Thus, in fatigue or structural analyses of HAOWT, the use of a fixed support condition will be a conservative approach. For proof analyses, soil modelling resulted in higher compressive stresses, making it more useful for assessing permanent deformations. Among the three soil models examined, Model 1 (North Sea) yielded the lowest stress levels, a positive observation considering the high concentration of offshore wind farms in this region (Sánchez et al. 2019). Moreover, these stress levels were significantly lower than the yield stress of offshore S355 steel.

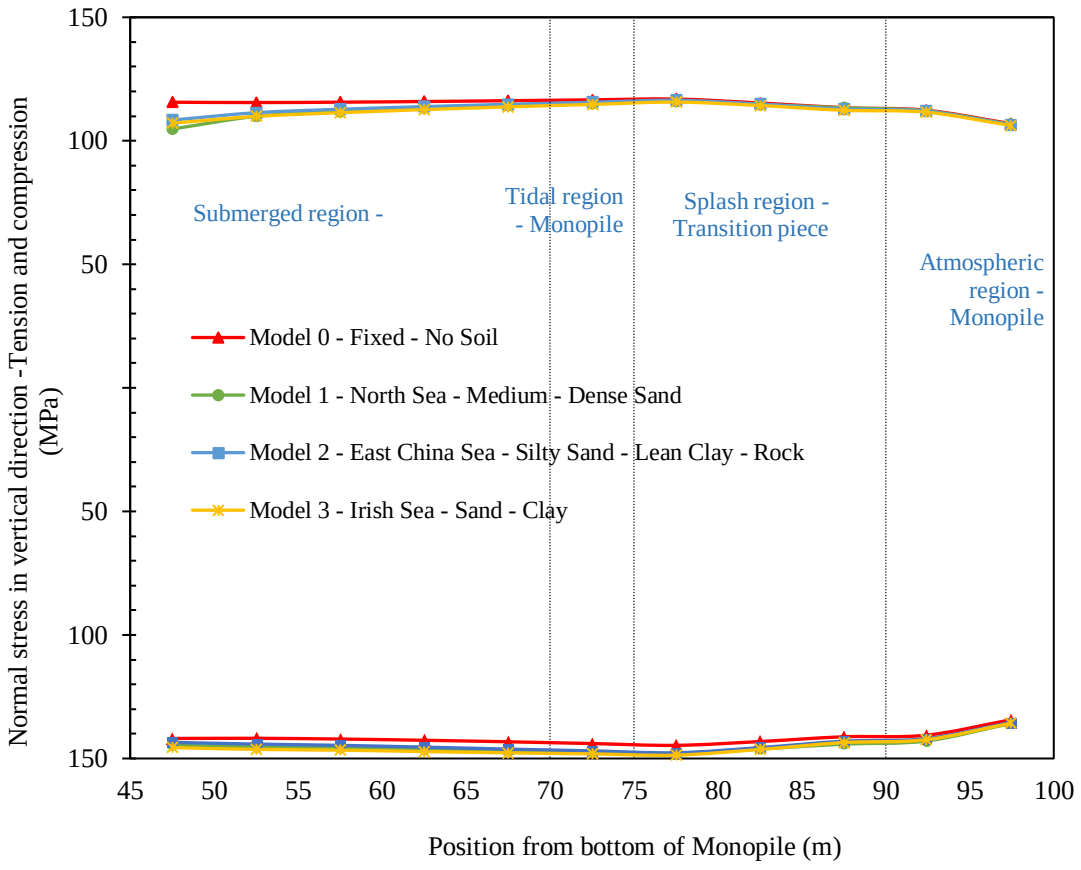

Figure 4.13: Soil effects on tensile and compressive stresses in the vertical direction.

4.6.4 Conclusions

In the analysis of high-capacity HAOWTs, it was observed that increasing rotor diameters and hub heights influence the overturning moment in the monopile, reducing induced tensile stresses. The combined effects of the HAOWT's weight and wind and wave loads result in compressive stresses, beneficially neutralizing some tensile stresses. These stresses, at their peak, were observed to remain below the risk levels of permanent deformation for material S355. The analytical calculations closely correlated with FEA results, validating their accuracy for predicting stresses in varying conditions, including corrosion effects. Moreover, the research showcased a capability to predict nominal stresses, which could be integrated with S-N curves for comprehensive fatigue characterisation. For soil-structure interaction, reduced support structure thickness heightened deformation, yet all monitored deformations stayed within design guidance limits. Soil profiles from various regions met frequency requirements of design codes. Additionally, the importance of considering soil effects in HAOWT assessments was underscored, with the North Sea's medium to dense sand profile being deemed ideal for 15 Megawatt large-diameter HAOWT installations.

Chapter 5

Experimental investigation of material performance of submerged arc welded S355G10+M structural steel

This chapter explores the performance characteristics of S355G10 +M structural steel, specifically designed for offshore wind turbines. Emphasis was placed on tensile tests, hardness assessments, distortion measurements, and residual stress analysis. To achieve this, a combination of experimental procedures, finite element modelling tools, and macrographs was employed. The unique contribution of this chapter lies in its focus on understanding the performance and manufacturing processes of the specialised S355G10+M steel grade. This is particularly relevant for large-size and high-capacity offshore wind turbines, especially as they are increasingly being deployed in offshore construction projects located in deep seas, where G10 refers to depths up to 100 m below sea level. The insights garnered from this chapter are vital for comprehending the factors that influence the fatigue performance of offshore structures.

5.1 Manufacturing of specimens

5.1.1 Submerged arc welding for producing butt-welded plates

S355G10+M rolled plates (1000 mm × 200 mm) with four distinct thicknesses of 6, 10, 15, and 20 mm were butt-welded using a single-wire submerge arc welding (SAW) process as applied to fabrication of plates in HAOWT monopiles (Igwemezie et al. 2018; DNV 2009). Table 5.1 presents the chemical compositions of both the base metal and weld material, with the latter employing an EN ISO 14171-A: S3Si (IABCO 2.4/3.2 mm) solid wire electrode and EN ISO 14174: SA FB 155 AC H5 flux (detailed in Appendix B1). The mechanical properties of weld material and base metal are outlined in Table 5.2 (details of manufacturer's specification in Appendix B2). The UTS for the weld material is slightly greater than the base metal as per specification.

Table 5.1: Chemical composition of S355G10+M and weld material.

Base metal – Element (wt%)									
C	Si	Mn	P	S	N	Al	Cu	Cr	Ni
0.07	0.25	1.37	0.014	0.003	0.005	0.048	0.03	0.04	0.04
V	Ti	Nb	Mo	B	EV1*	EV2*	EV3*	EV4*	Nb+V
0.004	0.014	0.03	0.001	0.0003	0.15	0.33	0.11	0.05	0.03
Weld material - Element (wt%)									
C	Si	Mn	P	S	Cr	Ni	Mo	Cu	N
0.11	0.3	1.75	0.007	0.005	0.03	0.02	<0.01	0.01	0.004

* EV1=C+Mn/20+Mo/15+Ni/60+Cr/20+V/10+Cu/20+Si/30+5xB

*EV2=C+Mn/6+Mo/5+Ni/15+Cr/5+V/5+Cu/15

* EV3=V+Nb+Ti

* EV4=Cr+Cu+Mo+Ni

Table 5.2: Mechanical properties of S355G10+M and welding material.

Material	**Yield stress (MPa)**	**UTS (MPa)**	**Elongation (%)**
Base Metal	422 - 510.5	483 - 559	27 - 30.5
Weld material (As-welded)	501	590	29

The SAW was conducted on the hot-rolled plates at the Advanced Manufacturing Research Centre at Sheffield to industry standards and specifications. Prior to welding, the edges of the steel plates were cleaned to eliminate contaminants such as dirt and rust. Double V-grooves were machined into the edges, as depicted in Figure 5.1. The plates were then clamped and aligned using fixtures to minimise gaps. The SAW setup included a power source, wire feeder, welding torch, and flux delivery system. Welding settings, including wire feed speed and voltage, were adapted based on the material thickness and are detailed in Table 5.3. The flux shielded the molten weld pool as an arc melted the electrode, flux, and base metal, thereby creating a molten weld pool that moved steadily along the joint. The multipass welding sequence varied with the material thickness, as shown in Figure 5.2. The dwell time which is the period the heat source or weld pool is maintained at a specific location for successive layers, using the length of weld and travel speed, was approximately 2 min. After each pass, the slag layer formed by the solidified flux was brushed off. Welding was carefully done following the BS EN 1011 standard for steel arc welding (British Standards

Institution 2001). Before starting the main weld, test runs were done to get the best welding quality. These tests made sure the welding settings were right to avoid defects and ensure good weld strength. Post-welding inspections were performed through visual analysis and dye penetration inspection, adhering to the BS EN ISO 3452 standards (British Standards Institution 2015). These nondestructive testing methods verified the absence of leaks, joint flaws, and cracks. Key SAW process steps are illustrated in Figure 5.3. There was no application of post-weld heat treatment to the welded plates. This is also the case for the production of monopiles and towers.

Table 5.3: Welding parameters for butt-welded S355G10+M structural steel.

Parameters	**Values based on thickness**			
	6 mm	**10 mm**	**15 mm**	**20 mm**
Weld passes	2	3	6	12
Current (A)	390	393.3	396.6	400
Arc voltage (V)	26.5	27.6	27.75	28
Wire feed rate (m/min)	1.7	1.7	1.7	1.7
Wire stick-out (mm)	25	25	25	25
Travel speed (mm/min)	390	383.3	363.3	383.1
Preheat/inter-pass (°C)	21 - 36	21 – 70	21 - 90	21-133
Heat input (kJ/mm)	1.590	1.666	1.824	1.749
Current polarity	DC+	DC+	DC+	DC+

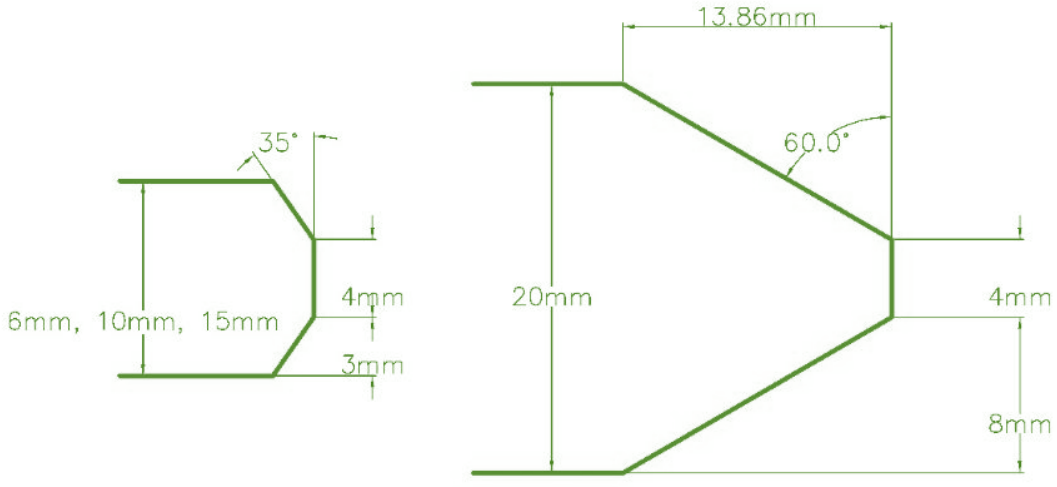

Figure 5.1: Weld details for butt weld specimens of various thicknesses.

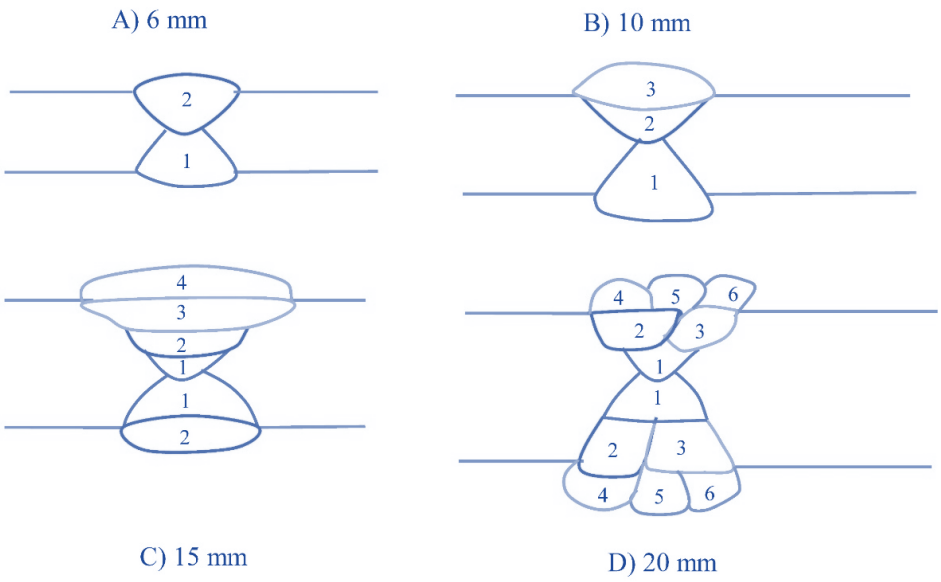

Figure 5.2: Deposition sequence used in the SAW process.

Figure 5.3: SAW steps: a) After Dye penetration inspection, b) Plate clamping, c) Welding setup, d) SAW process.

5.1.2 Water jet cutting and wire electro-discharge machining of butt-welded plates

For the preparation of samples for material testing, four welded plates with thicknesses 6mm, 10 mm, 15 mm, and 20 mm were waterjet cut. Plates with dimensions 330 mm × 200 mm were originally cut from larger SAW plates measuring 1000 mm × 200 mm. The waterjet cutting was conducted on the 87000 Psi Dynamic Waterjet XD machine employing a high-precision technique. This method combined a high-pressure water jet with a garnet abrasive, facilitating a cold-cutting process that preserved the integrity of the material. Unlike traditional cutting methods, such as cropping, laser cutting, or plasma cutting, this approach mitigated issues related to the HAZ, stress generation, and structural alterations. Figure 5.4a shows an example of a dog-bone sample, while Figure 5.4b illustrates the sequence of the process, from which additional specimens were derived for tensile and fatigue testing. The end of the plate was cut with wire electro-discharge machining (WEDM) needed to obtain the residual stresses using the contour method. Figure 5.5 visually describes the faces of the specimens prepared using WEDM, specifically referring to specimens located along and across the weld. The Sodick AQ750L WEDM system was employed with a wire diameter of 0.25 mm. To prevent breakage of the wire, the feed rate was controlled using a variable circuit for the different sections of the plates. The average speed of the wire was recorded to be 1.4 mm/min for all plates.

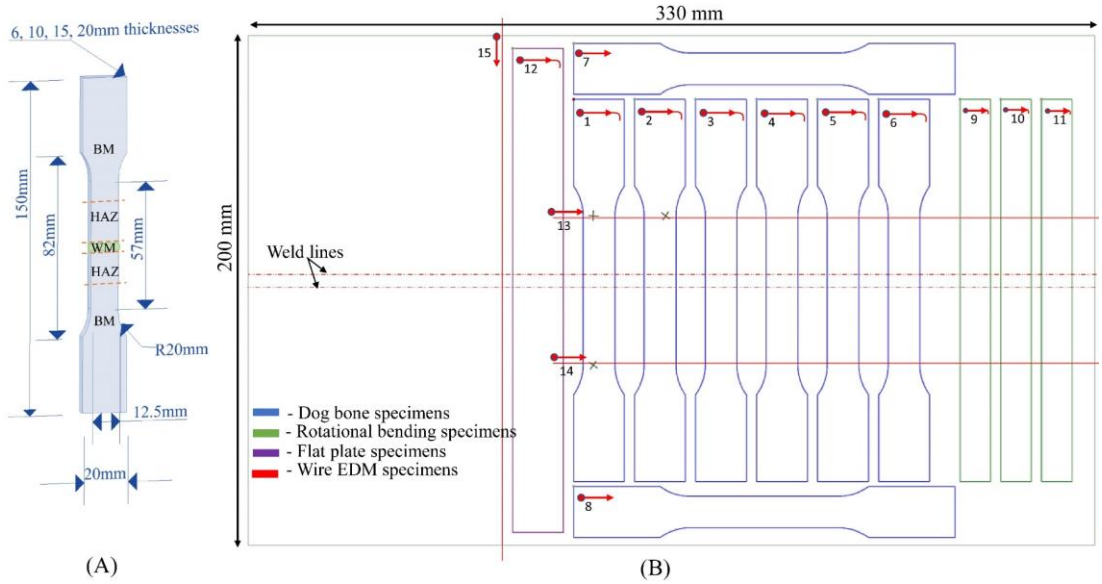

Figure 5.4: a) Tensile and fatigue test specimen dimensions, b) Waterjet cutting sequence.

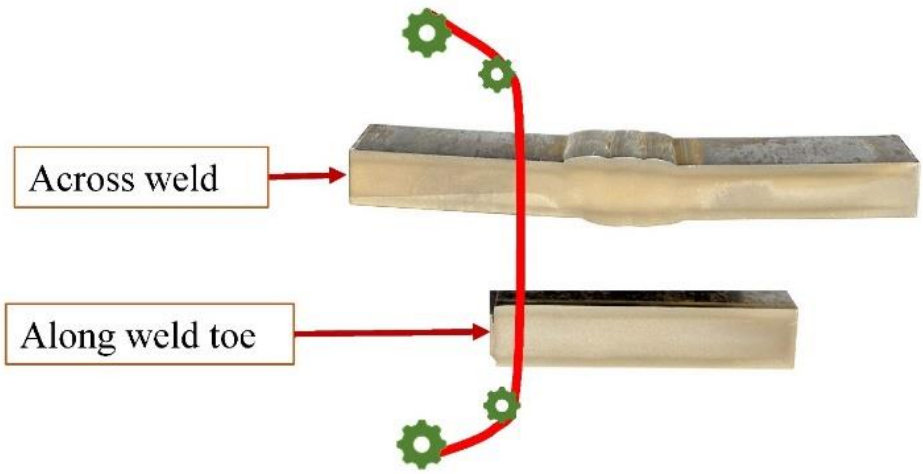

Figure 5.5: Direction of cut from wire electrodischarge machining.

5.2 Tensile testing

Tensile properties of the butt-welded S355G10+M using SAW were assessed using across-weld specimens. Static tensile testing was conducted to extract mechanical attributes, verify the manufacturer's reported yield and UTS, and set a targeted load level for subsequent fatigue testing. The tests complied with the American Society for Testing Materials E8 standard (American Society for Testing Materials 2022). The dimensions of the specimens are depicted in Figure 5.4a and a 400kN uniaxial servo-hydraulic system served as the testing equipment (Figure 5.6). Prior to initiating the test sequences, the accuracy of the equipment was verified and calibrated. The stress-strain curve was plotted up to the point of material failure. Both the welded and plain specimens of each material thickness were tested to confirm the manufacturer's data. The static tensile tests were conducted at a displacement rate of 2 mm/min.

Figure 5.6: Tensile testing equipment.

5.3 Hardness and weld macrograph testing

The Brinell hardness was assessed through cross-sectional measurements taken from various regions of the material, specifically focusing on the base metal, HAZ, and welded material. These measurements were conducted using a 100kN universal testing machine (Figure 5.7), conforming to EN ISO 6506-1 standards (British Standards Institution 2014b). It was ensured that surfaces of selected specimens were free of imperfections and smooth from polishing to ensure proper indentation. A 20 kN force was applied to the steel cross-section and maintained for 15 s using a 10 mm diameter spherical indenter. For each material thickness, two samples were examined to gather comprehensive data for different regions of the specimen. The diameter of the spherical indentation was measured on a macroscopic scale, from which hardness

values were derived. These values were then used to generate contour plots using MATLAB (The MathWorks Inc. 2022).

Multiple factors were found to influence the structural properties of S355 steels, such as its chemical composition, thermal treatments, and cooling rates. It was observed that the use of controlled rolling and cooling techniques could refine the microstructure of thermo-mechanically controlled steel, optimising its strength, ductility, and toughness for various engineering applications. For the welded samples, the surface was prepared by sanding with silicon carbide sheets of multiple grades of 60, 120, 240, 320, 400, 600, and 800 grit sizes. Subsequently, the samples were etched in a 12M hydrochloric acid solution. The study primarily focused on macrographs of the HAZ, as previous fatigue tests have suggested that it is a likely point of failure (Adedipe et al. 2016; Mehmanparast et al. 2017; Okenyi et al. 2022).

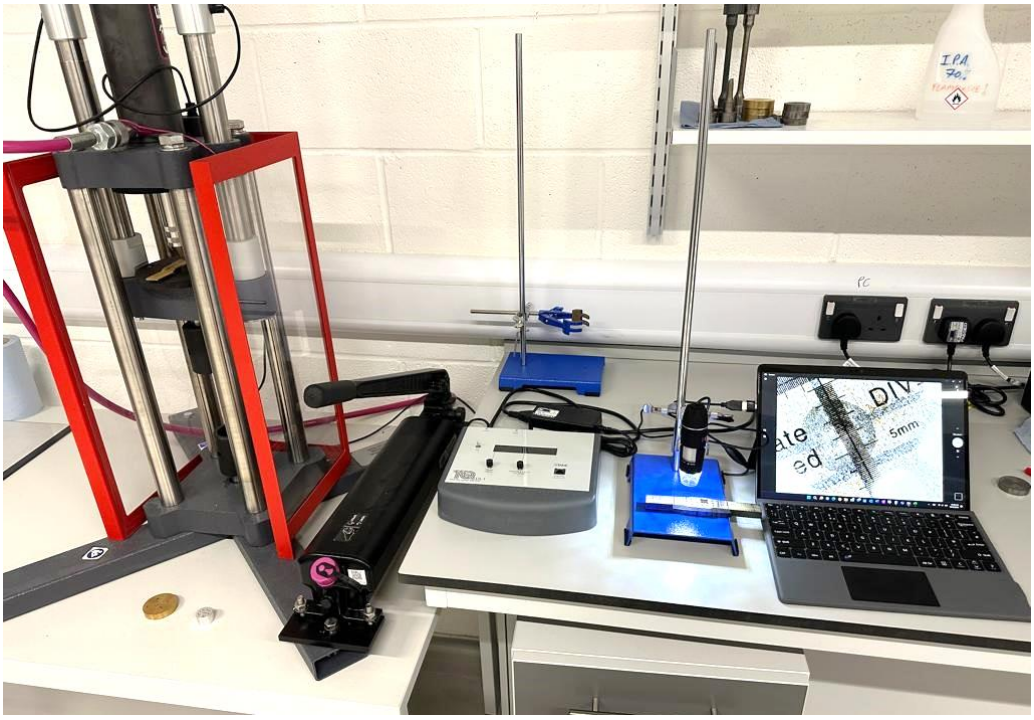

Figure 5.7: Hardness testing of S355G10+M structural steel specimens.

5.4 Weld-induced angular distortion and axial misalignment measurements

Distortion in both the longitudinal and transverse directions is a common issue during the welding of plates, significantly affecting material performance. To measure this distortion, a 3-D scan of the welded plates was initially performed using the GoScann50 optical scanner (Figure 5.8). The optical scanner, with a 0.5 mm resolution and 0.1 mm accuracy, was calibrated using a calibration plate. Its performance was validated by comparing scanned dimensions with actual plate dimensions and referenced the ISO 10360-8:2013 (International Organisation for Standardisation 2013) standards for tolerances using optical sensors. The results showed consistent accuracy in capturing surfaces, edges, and geometry against the real steel plates and CAD designs. Subsequently, the generated mesh was prepared using VXElements software (Creaform Inc. 2021) and imported into GOM Inspect software (ZEISS Group 2021). Using this software, the distortion angles in the transverse direction were extracted. To better visualise the extent of the distortion, the scanned meshes were aligned with the nominal computer-aided design models for plates of 6, 10, 15, and 20 mm in thickness. Contour plots depicting the distortions were generated from this alignment. Additionally, the boundaries of the plates were delineated to obtain accurate values for angular and longitudinal distortions, as well as axial misalignments. These values were sourced from cross-sectional analyses conducted across plates.

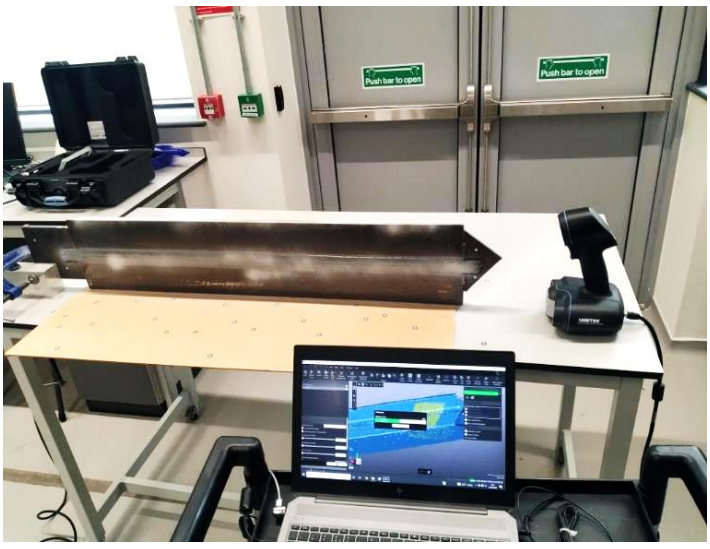

Figure 5.8: 3-D scanning of welded plates.

5.5 The contour method

The contour method was applied to evaluate residual stresses in materials (Prime 2001). Plates of S355G10+M were cut transversely and longitudinally across the weld using WEDM. Measurements were taken using a high-precision Coordinate Measuring Machine equipped with Nikon non-contact laser scanners. These scanners demonstrated a single point spacing of 22 μm and an accuracy of 1.8 μm. The acquired mesh data from the Coordinate Measuring Machine were imported into the GOM software for alignment. Data smoothing was applied but showed negligible differences, confirming the precision of the Coordinate Measuring Machine measurements. Thus, the opposite of the measured profile was applied as nodal displacement boundary conditions in a FEA model of the cut parts. A static analysis was executed on the S355G10+M structural steel. The material was assumed to possess isotropic elastic properties. For the analysis, the following material parameters were utilized: a Young's modulus (E) of 200 GPa, a Poisson's ratio (ν) of 0.3, and a material density (ρ) of 7850 kg/m³. To ensure the accuracy and convergence of the results, an element size of 1 mm was employed. Furthermore, the chosen element for modelling was the 3-D structural solid element, specifically SOLID185.

The nodal displacements were mapped in ANSYS Mechanical, as shown in Figure 5.9, both longitudinally and transversely across the weld. Subsequently, an elastic stress analysis was conducted. The back-calculated stresses derived from the FEA provided an estimate of the residual stress components acting perpendicular to the plane of the cut. The CMM laser scanner was calibrated using ISO 10360-2:2009 [(International Organisation for Standardisation 2010) in a controlled environment. A CAD model of the specimens was created for accurate representation. After scanning the structural steel, point cloud data was compared with the CAD model. Deviations were analysed using GOM software to identify discrepancies. The scanner's performance was assessed in accordance with ISO 10360-8:2013 (International Organisation for Standardisation 2013). This evaluation encompassed various metrics: the maximum probing form error, using 25 representative points in translatory scanning mode; the maximum probing size error, using all measured points in the same mode; and the maximum probing dispersion value, considering 95% of the measured points in translatory scanning mode. All these checks ensured the accuracy of the measurements.

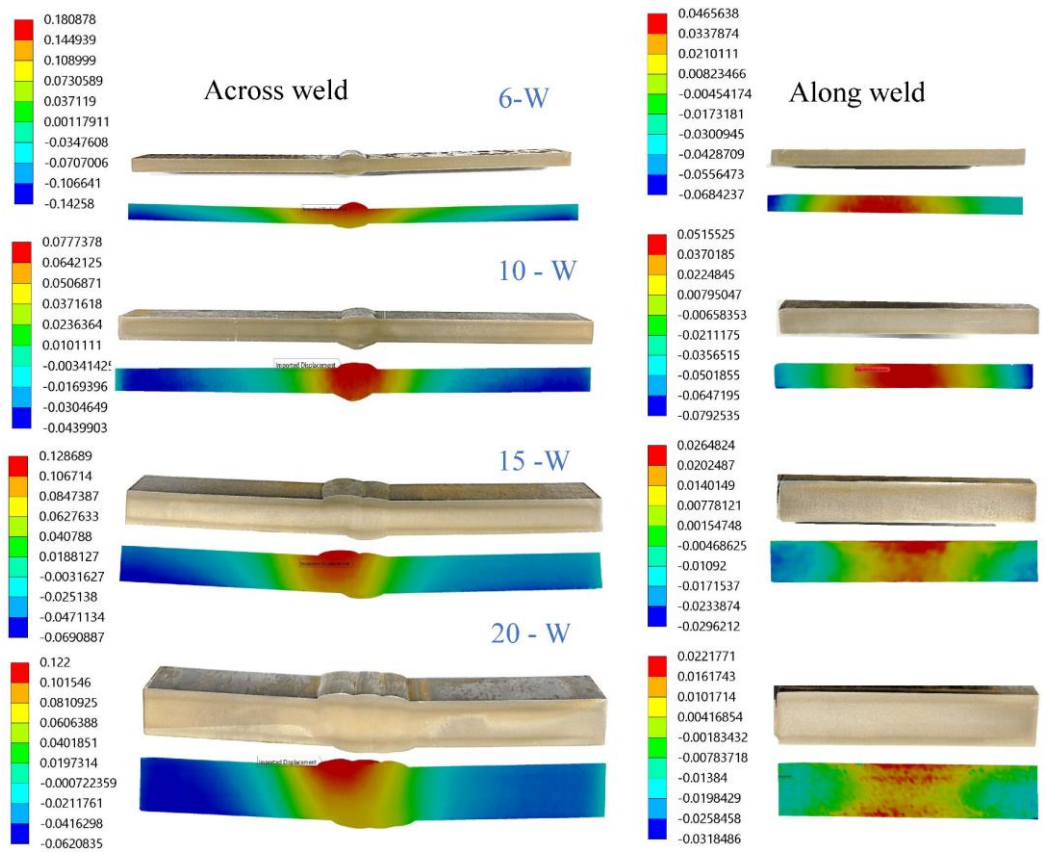

Figure 5.9: Displacement across and along the weld for welded specimens (values in mm).

5.6 Results and discussion of material performance of submerged arc welded S355G10+M structural steel

5.6.1 Tensile tests results

Fractured specimens were primarily observed in the base metal near the HAZ, as illustrated in Figure 5.10. This suggests that the welded section comprised a stronger welded material, corroborated by the data in Table 5.2. Similar observations regarding fractures in the base metal were made in previous studies on S355 material (Jacob et al. 2018; Ólafsson et al. 2016). The 0.2% offset method was used to calculate the yield stress which ranged from 361.4 – 438.9 MPa. It should be noted that weld mechanical strength alone cannot be tested unless with digital image correlation or making specimens from the weld section only. Figure 5.11 presents the stress-strain relationships for the 6 mm thick plain and welded specimens, while Table 5.4 compiles all the tensile test results for the plain and welded specimens. The experimentally

determined tensile strengths were either close to or slightly below the manufacturer's specifications. However, these exceeded the minimum required strength levels. In line with other reported results (British Standards Institution 2019a; Igwemezie et al. 2018), the yield strength of the plain specimens was found to decrease as the plate thickness increased. This trend was also observed for the welded specimens. Despite their lower yield strengths, the welded specimens exhibited higher ultimate strengths, leading to failure in the base metal. The ductility, measured as the amount of plastic deformation that occurs before fracture, was greater in the plain specimens than in the welded specimens (Figure 5.11). The elongation before fracture in the welded specimens (Table 5.4) was lower than that in the plain specimen, indicating that the welded specimens were more brittle.

There are differences observed in conducting static tensile tests on plain base material and welded specimens as observed in Figure 5.10. Failure occurred in the region of the plain specimen that had the lowest tensile strength, whereas for the welded specimen, tensile failure occurred in the base material owing to the strong weld quality and the fact that the localised increase in stress exceeded the strength of the adjacent base material, leading to failure in the base material region. There is a more uniform stress distribution in plain specimens over their cross-section, while the opposite is true for welded specimens. The plain specimens provided the S355G10+M inherent properties, while the welded specimens provided an understanding of the joint properties.

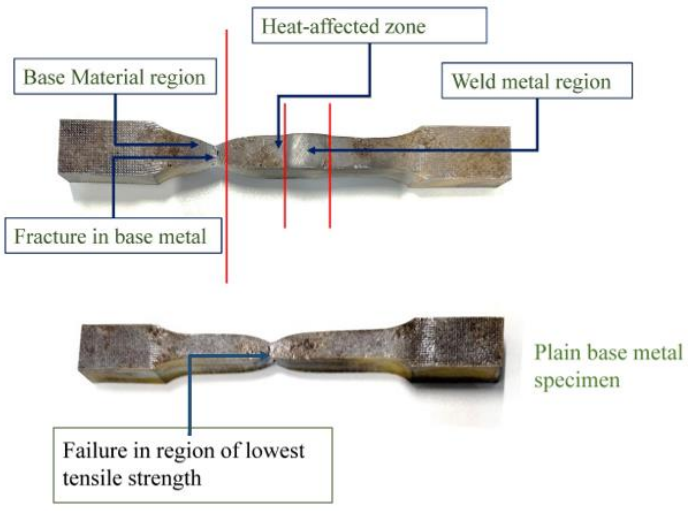

Figure 5.10: An exemplar of tensile failure in the S355G10+M specimens observed for all thicknesses.

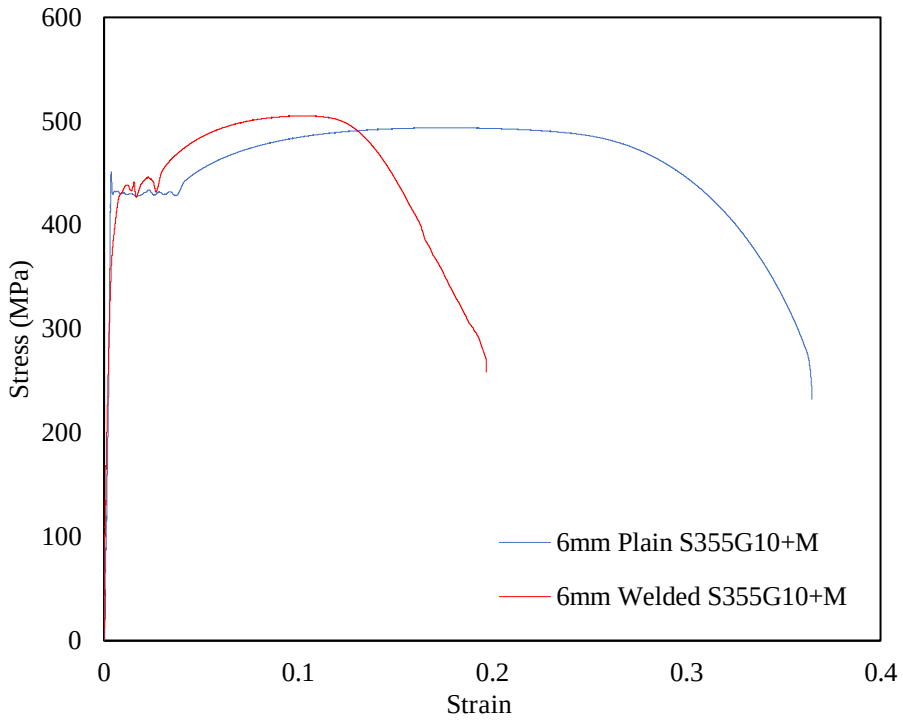

Figure 5.11: An exemplar of a stress-strain relationship for plain and welded specimens of 6 mm thickness also observed for all thicknesses.

Table 5.4: Summary of the tensile test results for butt-welded S355G10+M.

Material condition	**Yield stress (MPa)**	**UTS (MPa)**	**Elongation (%)**
6 mm plain samples (Manufacturer specification)	455	515	30.2
6 mm plain samples (6 – P)	447.3	493.7	22.7
6 mm welded samples (6- W)	436	505.1	19.7
10 mm plain samples (Manufacturer specification)	510.5	559	28.5
10 mm plain samples (6 – P)	438.9	515.4	25.4
10 mm welded samples (6- W)	432.6	552.6	16.6
15 mm samples (Manufacturer specification)	422	483	30.5
15 mm plain samples (6 – P)	363	469.6	27.3
15 mm welded samples (6- W)	338.6	519.4	20.1
20 mm samples (Manufacturer specification)	467.8	535	27
20 mm plain samples (6 – P)	362.8	520.9	26.5
20 mm welded samples (6- W)	361.4	524.8	20.3

5.6.2 Hardness and macrograph tests results

The hardness test results are depicted in Figures 5.12 - 5.15, illustrating the variations in hardness values for welded specimens ranging from 6 mm to 20 mm in thickness. A noticeable trend was the increase in hardness with increasing specimen thickness, peaking at 207 HB in the welded material for the 20 mm specimens. Subsequently, the hardness values decreased minimally from the HAZ to the base metal. These results aligned well with the existing literature on S355 steels (Sonsino 2009; Tong et al. 2021; Ummenhofer, Weidner 2013; Weich et al. 2009). The lower value of hardness at 6 mm could be due to the fact that a high force is applied to a mall thickness with an indenter, resulting in a larger indenter diameter. This is also visible for the base metal from the obtained results. By increasing the thickness, the results start to be more consistent Thus, this data implied that offshore wind turbine monopiles with thicknesses ranging from 65 to 90 mm are likely to exhibit consistent hardness values. Furthermore, it was noted that the HAZ width expanded as the specimen thickness increased. This was attributed to the need for additional weld passes and, consequently, more heat energy input, leading to an enlarged HAZ.

In reviewing the hardness contour plots (measurements detailed in Appendix B3) presented in Figures 5.12- 5.15. It was observed that hardness could be directly linked to yield and UTS and could serve as an indicative parameter for potential failure points in static tensile tests. The hardness value observed in the HAZ has a negligeable reduction showing that hardness value obtained is satisfactory, it indicates effective SAW process and a proper control of welding parameters. This indicates that the HAZ retains its mechanical integrity with controlled martensite formation, balancing toughness, and hardness to prevent cracking. Other contributing factors affecting material properties are elongation (Table 5.4) and microstructural changes. Also, the good hardness value suggests a well-formed interconnected dendritic structure, resulting from controlled cooling during welding, indicating uniform solidification. This contributes to consistent mechanical properties across the weld.

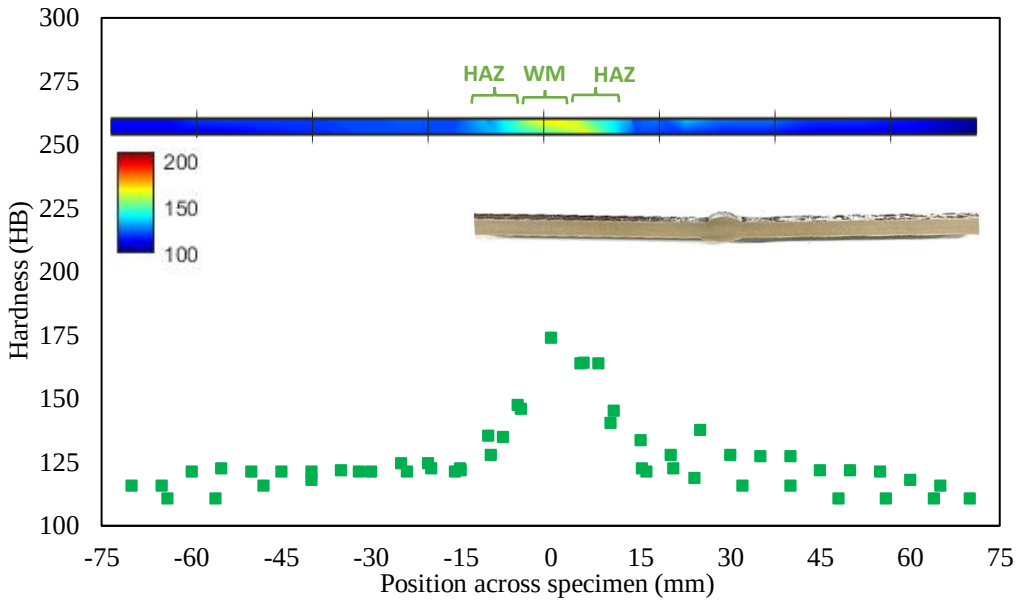

Figure 5.12: Hardness results for 6 mm welded specimens.

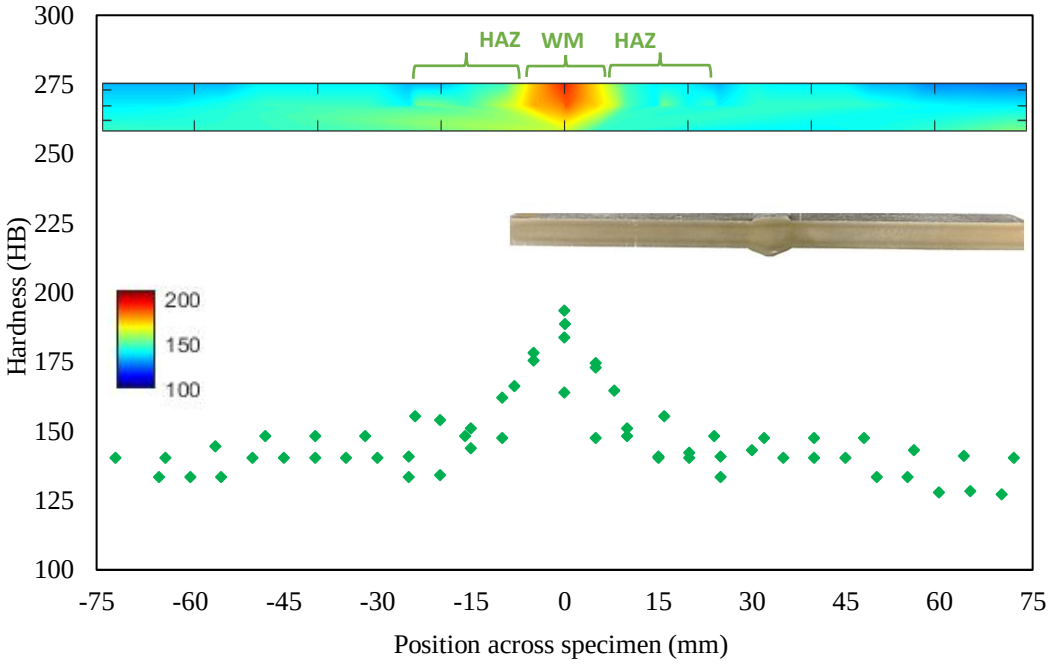

Figure 5.13: Hardness results for 10 mm welded specimens.

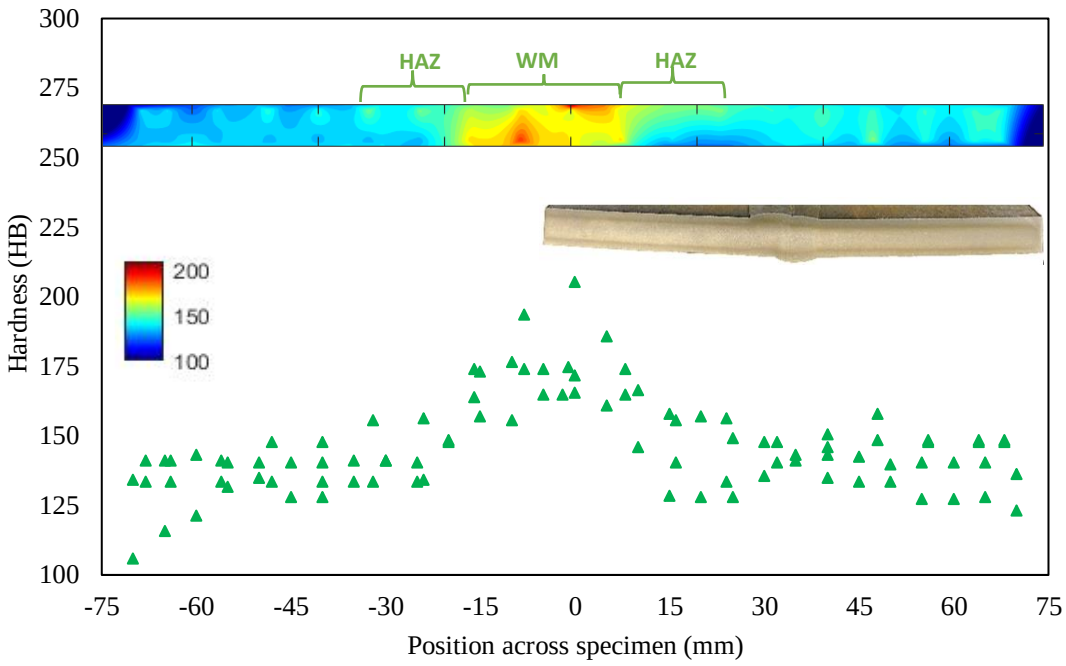

Figure 5.14: Hardness results for 15 mm welded specimens.

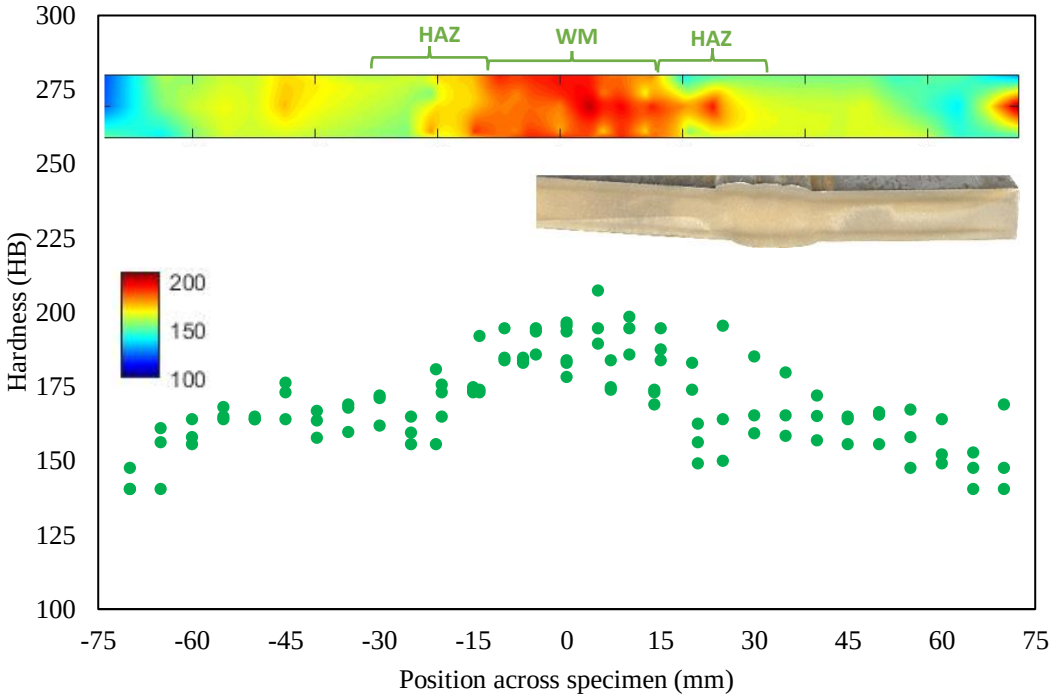

Figure 5.15: Hardness results for 20 mm welded specimens.

The structure of S355G10+M steel at a microscopic and macroscopic level significantly affects its mechanical performance, especially in challenging sea conditions. Figure 5.16 shows the grain morphology in both the welded material and HAZ. The SAW process performed on the S355G10+M plates resulted in distinct grain

structures that served as indicators of weld quality and integrity. Columnar grains were observed in the welded material, which is a characteristic typically associated with the transition from the liquidus to the solidification phase of the material. Also, the linear elongated streaks in the weld material indicated slag inclusions. In addition, the HAZ exhibited smaller equiaxed grains. Apart from some etching pores, the weld quality was notably high, as evidenced by the absence of common flaws, such as porosity, hot cracking, or keyholes. The grain size and composition of the steel, shown in Figure 5.16, are vital for its strength. Fine grains, especially in the weld metal, increase yield and tensile strength, offering better resistance to impact and static loads in offshore settings. Elements like manganese, nickel, and chromium, as seen in Table 5.1, provide corrosion resistance, strength, and toughness which are essential attributes for marine environments. Thus, managing and optimizing the microstructure of S355G10+M steel is crucial for its performance in offshore applications.

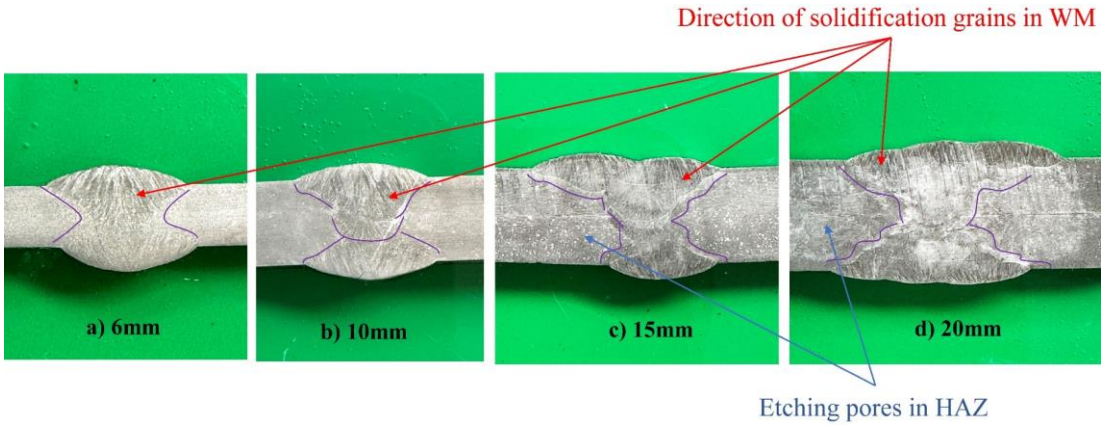

Figure 5.16: Macrostructure highlighting weld passes and grain morphology.

5.6.3 Distortion results - angular distortion and axial misalignment

Figure 5.17 illustrates the distortion seen from the top view (in the vertical direction) of the S355G10+M steel plates. The distortion resulted from several factors, including the plate's length, which caused longitudinal shrinkage and thermal expansion during welding. Other factors, such as clamping, high heat input, and a large volume of welded material, also contributed for the distortion generation. Despite efforts to minimise these factors, distortion primarily stems from residual stress, causing both longitudinal and transverse distortions. This issue is especially relevant in large-scale manufacturing, where many plates are typically rolled and welded. Plates with

thicknesses of 6 and 10 mm exhibited slight uniform bending, while those with thicknesses of 15 and 20 mm displayed a butterfly shape. Thinner plates demonstrated higher levels of distortion, which was attributed to their lower stiffness. In the context of offshore wind turbines, axial misalignment in welds is particularly critical owing to the monopile shape and is covered by comprehensive guidelines. The shipbuilding standard (International Association of Classification Societies 2013) suggests that the maximum distortion in flat welded plates should not exceed 5 mm, allowing for an upper limit of 10 mm. All distortions measured in this study were within these guidelines.

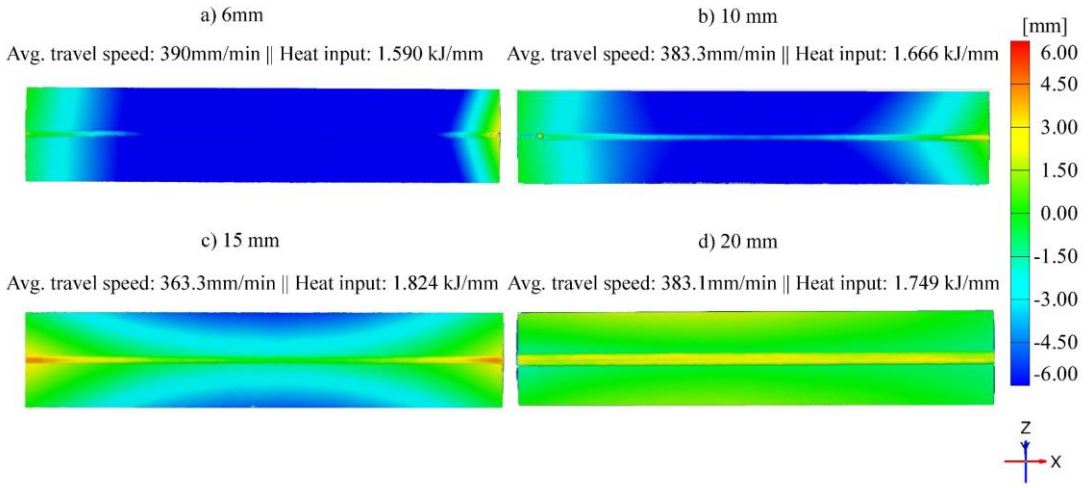

Figure 5.17: Distortion shapes of welded plates and weld parameters.

Figure 5.18 presents the angular distortion values, defined as the angles from the weld's centre to its ends in the lateral direction. The highest average angular distortion was observed in the 15 mm plates, linked to their butterfly shape. While factors such as travel speed and heat input affect distortion (Adamczuk et al. 2017), the thickness of the material also plays a role. Higher angular distortion values were noted towards the end of each plate. This was likely due to a redistribution of residual stresses after unclamping and because each weld pass had the capacity to introduce additional distortion. These values exceeded the maximum recommended 1˚ limit in the B90 quality set by BS EN ISO 5817:2023 (British Standards Institution 2023). Figure 5.19 revealed the axial misalignment measurements for each plate thickness (measured data are detailed in Appendix B4). On average, the misalignment worsened with increased thickness, particularly in the second half of the plates. The highest misalignment value of 0.65 mm was recorded for the 20 mm plates, which remained below the 3 mm limit

suggested by design standards (British Standards Institution 2023; DNV 2016b; DNV 2015; International Association of Classification Societies 2013). Both angular distortion and axial misalignment can alter the structural geometry, resulting in uneven load distribution and potentially decreasing the fatigue life of the structure.

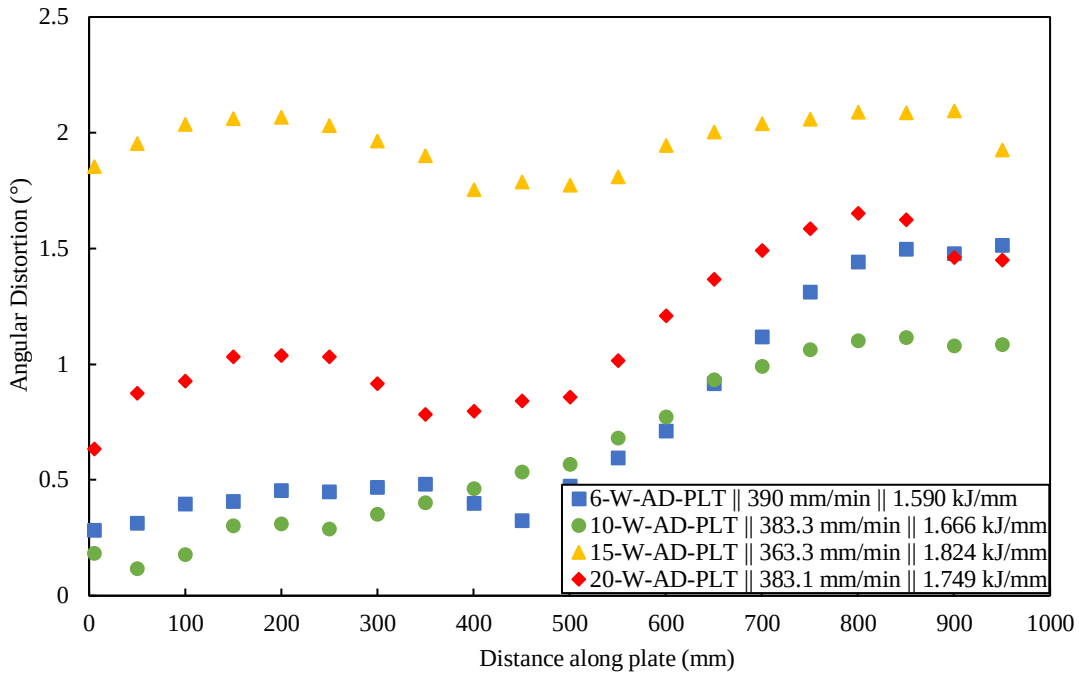

Figure 5.18: Angular distortion along the plate.

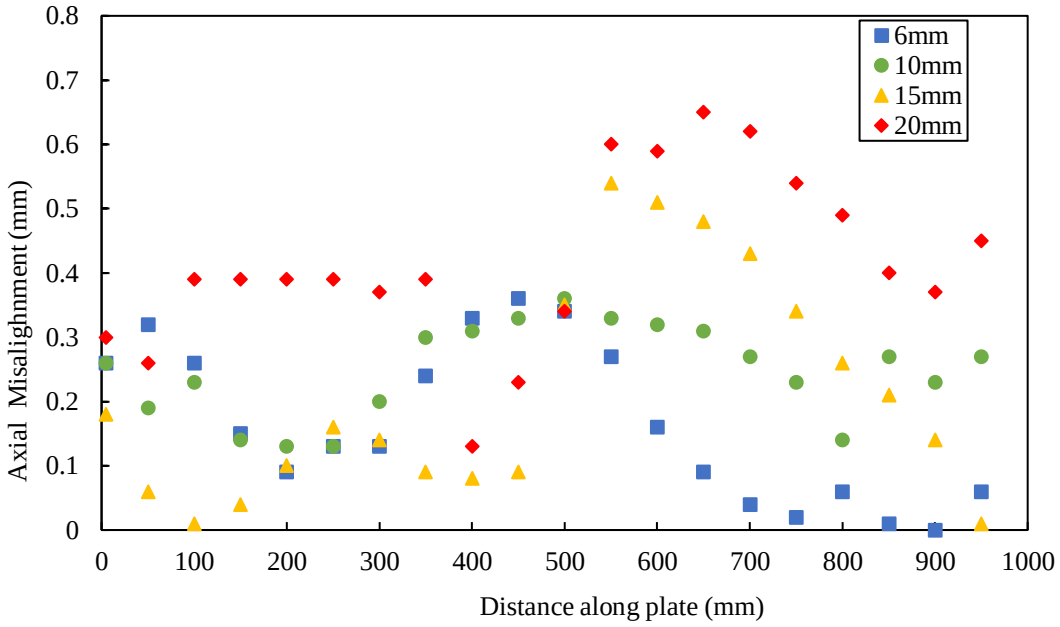

Figure 5.19: Axial weld misalignment along the plate.

5.6.4 Residual stress results

In Figures 5.20 and 5.21, the residual stresses across and along the welded specimens are presented for each material thickness. Figure 5.20 shows that the welded region had high tensile residual stresses, whereas the base metal region exhibited the most significant compressive residual stresses across the weld. In Figure 5.21, the highest tensile residual stresses were predominantly found near the weld. A comparative analysis of measurements across and along the weld indicated that the average peak average tensile residual stresses across the weld at 580 MPa were notably higher than those along the weld at 350 MPa averagely. These figures are aligned with the residual stress data for comparable steel materials (Jacob et al. 2018). For all residual stress results, as the thickness of the specimens increased, the maximum value of the residual stress also increased. This trend was attributed to the higher heat input required for welding thicker materials, leading to more significant temperature gradients and uneven cooling rates. Such differential cooling rates created a non-uniform stress distribution, resulting in increased residual stresses in thicker specimens. Multiple welding passes, often necessary for thicker materials, add more heat and subsequent cooling cycles, further accumulating residual stresses.

In HAOWT monopile applications, the tensile residual stress values along the weld are especially pertinent for fatigue assessment. This is because the stress direction in the vertical direction is in line with the lateral loading stresses exerted by wind and wave on the HAOWTs (Section 4.5). Residual stresses across the weld are relevant when hoop stresses have critical implications for material performance, as found in pressure vessels. The measurements indicated that these residual stresses could both contribute to the material yield strength and affect fatigue performance by increasing the mean stress levels. Elevated tensile residual stresses were found to speed up crack initiation and growth under both atmospheric and underwater conditions, as well as under corrosion-fatigue loads (Jacob et al. 2018). These results underscored the necessity for a comprehensive understanding and effective management of residual stresses in welded structures like offshore monopiles. Implementing appropriate welding procedures, stress-relief treatments, and regular inspection and maintenance could mitigate the negative impact of high residual stresses on structural integrity and lifespan.

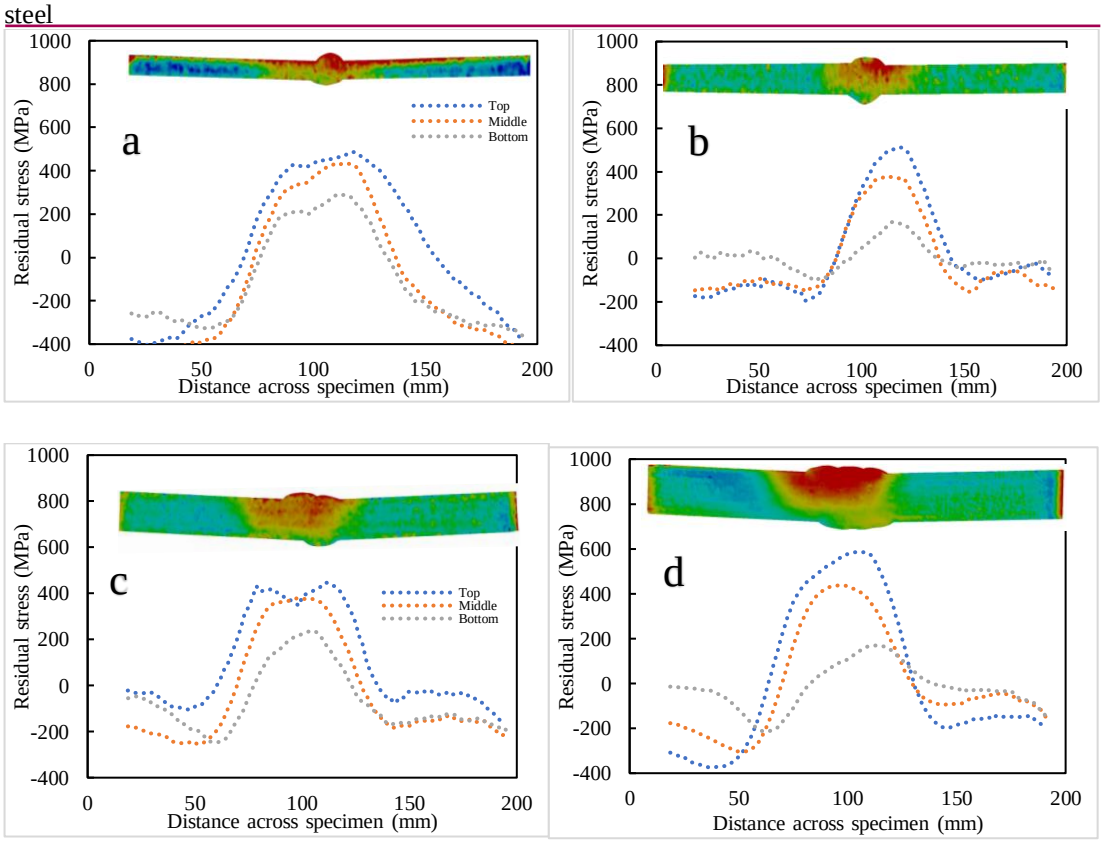

Figure 5.20: Residual stress results across the weld for: a) 6 mm, b)10 mm, c)15 mm, and d) 20 mm.

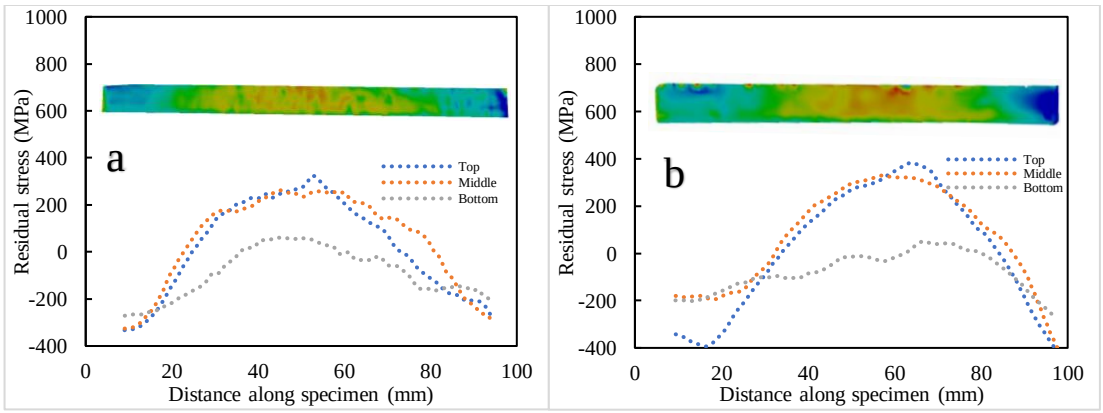

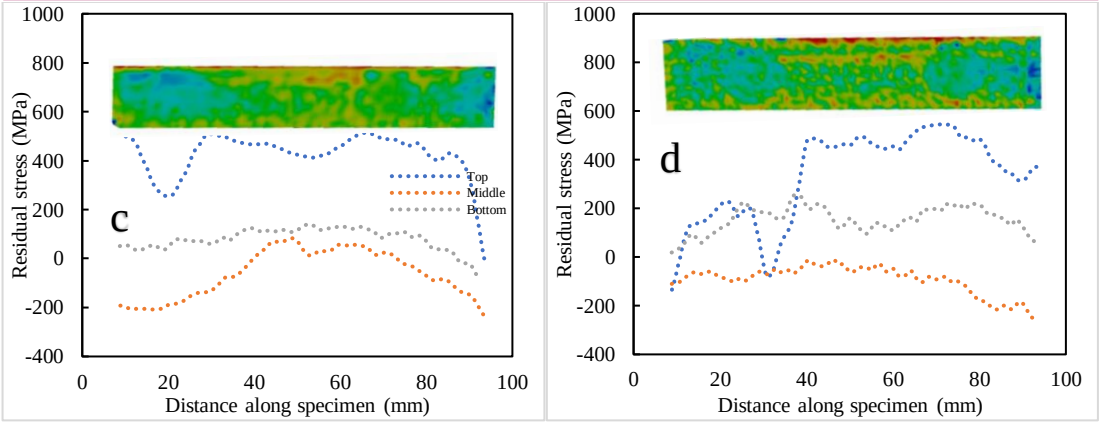

Figure 5.21: Residual stress results along the weld for a) 6 mm, b)10 mm, c)15 mm, and d) 20 mm.

5.6.5 Conclusions

The submerged arc welding of S355G10+M sheets displayed high-quality welds for offshore wind turbine monopiles. Fractures in the static tensile test specimens occurred in the base material, showcasing the superior strength of the welded section. Hardness experiments established consistency as material thickness increased, with the transition region between the HAZ and base material highlighted as a potential vulnerability under cyclic loading. Distortion measurements identified increased axial misalignment and angular distortion along the plate, while an evaluation of residual stresses indicated prominent tensile stresses in the weld area, negatively affecting fatigue strength. Moreover, stress concentrations at weld toes and other welding-induced vulnerabilities, such as distortions and microcracks, significantly impacted the steel's fatigue life and posed potential corrosion risks in marine settings. Nonetheless, the fatigue strength of the welded S355G10+M specimens exceeded established code recommendations, affirming their appropriateness for marine structures like offshore wind turbine supports.

Chapter 6

Fatigue testing

This chapter gives an analysis of a series of uniaxial fatigue tests conducted on welded S355G10+M structural steel specimens that are widely employed in the manufacturing of monopile support structures utilised in HAOWT installations. The fatigue life and strength were evaluated using an Instron servo-hydraulic testing system. The fatigue results obtained were subjected to a comparative analysis with established design codes and relevant studies. The impact of the specimen thickness on the fatigue life was also assessed. Stress concentrations related to fatigue were also considered. The detailed observation of the fracture contributed to the comprehension of the failure mechanism induced by cyclic stress.

6.1 Fatigue testing of S355G10+M structural steel

Uniaxial fatigue tests were conducted on welded dog-bone specimens using a 250 kN Instron servo-hydraulic testing system (Figure 6.1). The stress range values utilised in uniaxial fatigue testing ranged from 150 to 300 MPa. The uniaxial fatigue tests were conducted at 10 Hz frequency, with a stress ratio of R = 0.5, using dog-bone specimens that were obtained with minimal levels of misalignment and distortion in accordance with the standards outlined in BS EN ISO 5817:2023 (British Standards Institution 2023). The plain specimens were also subjected to testing for calibration purposes, and each thickness was evaluated separately. The relationship between the number of cycles to failure obtained from uniaxial fatigue testing and the applied stress range was analysed using a logarithmic scale on both axes and is presented subsequently in the discussions (calibration data in Appendix D1).

Figure 6.1: Uniaxial fatigue testing machine applied to specimens at Advanced Materials Research Laboratory, Strathclyde.

6.2 Machining for fatigue testing concept

Machining for fatigue testing complements the research aim and objectives by introducing a novel and efficient fatigue testing technique which aligns with the goal of developing innovative methodologies, supports the comprehensive evaluation of S355G10+M fatigue performance in monopile weldments under simulated in-service loads as experienced in installed conditions (parked or operating).Traditional methods for fatigue assessment, such as uniaxial or rotating-bending loading tests, are often expensive and time-consuming, especially at low frequencies (Parareda et al. 2023). These tests aimed to establish S-N curves, which could be influenced by various factors like surface morphology and manufacturing defects (Sanaei, Fatemi 2020).

Although ultrasonic fatigue testing systems present an alternative, they also have limitations concerning specimen size, monitoring, and costs (Ebara 2006; Peng et al. 2012).

In contrast to these established methods, this study introduced a novel approach to fatigue testing that employed machining processes to induce cyclic stresses. The method was demonstrated using welded samples, specifically imitating the in-service loading conditions found in wind turbine monopile structures. This innovative technique holds the promise of providing a more efficient and cost-effective way of assessing fatigue life, potentially reducing product and process development lead times. Fatigue testing on unique specimen shapes necessitated the extensive development of specialised jigs to replicate in-service loads, a process that consumed significant time and resources. To address this, a novel concept that employs machining processes for fatigue testing was introduced. The underlying principle was that cutting forces generated during machining processes, such as milling, are cyclic in nature and serve as loading conditions to induce stress fields in the test component which in this case is a welded specimen of structural steel S355G10+M.

Figure 6.2 depicts a clamped sample of S355G10+M attached to a specially fabricated fixture. A block of raw, unmachined sacrificial material was affixed to the top of the fixture. This block underwent machining, transferring the cutting forces to the welded specimen through a bending moment. The type of cutting tool (e.g. end mill, ball end mill, drill, and grinding wheel), cutting parameters (depth of cut, feed rate, and spindle speed), and type of cutting operation (up milling, down milling, drilling, and grinding) allow for the induction of cutting forces along the three axes of the Cartesian coordinate system. The variety of cutting tools and machining operations grants flexibility to emulate in-service loads. However, this adaptability needs to be harmonised with the dimensions of the raw material block and the design of the fixture, which is capable of directing the distribution of induced forces through purposefully designed fixture supports. By inducing cutting forces, the test components can be subjected to various types of loads, including combinations of bending, tension, compression, and torsion.

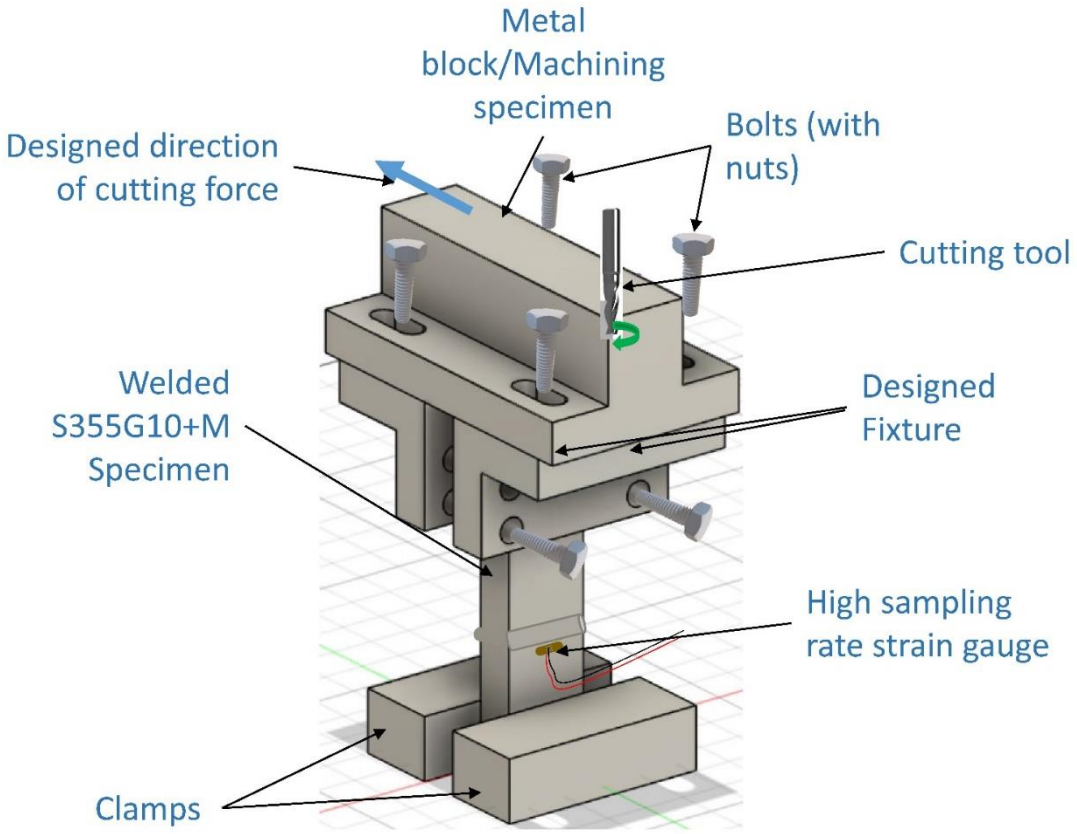

Figure 6.2: Setup for fatigue testing concept using machining.

6.3 Results and discussion of fatigue test and cyclic of fatigue loading using machining

6.3.1 Fatigue strength assessment

In Figure 6.3, the fatigue behaviour of the S355G10+M specimens was analysed across four different thicknesses. The range of cycles to failure was observed to be between 10^4 and 10^6, with fatigue stress values ranging from 120 to 234 MPa. These results were aligned with the design codes specified by FAT Class 90 in air, as per the International Institute of Welding (International Institute of Welding 2008), and Class D in air (DNV 2016b).

Fatigue strengths for specimens of different thicknesses (6 mm, 10 mm, 15 mm, and 20 mm) were recorded as 128.2 Mpa, 125.7 Mpa, 104.5 MPa, and 95.8 MPa at 2×10^6

cycles. Notably, the 20 mm specimen closely aligned with the requirements of the IIW-FAT 90 code (International Institute of Welding 2008). The impact of the thickness on the fatigue life of butt-welded S355G10+M specimens under uniaxial fatigue was found to be minimal. Factors such as stress concentrations, residual stresses, and distortions such as axial misalignment and angular deviation could have also influenced the fatigue life (Pedersen 2019).

Three key stages resulting from cyclic loading were identified in the fractured specimens: crack initiation, crack propagation, and final fracture (Figure 6.3). Fatigue cracks tended to propagate along planes where the shear stress was the highest. The existence of stable fatigue crack growth region was observed from the subtle transition between crack propagation and aggressive final fracture, suggesting that the nominal stresses were high. Moreover, the macroscopic shape of the fractured surface, as shown in Figure 6.4, reinforced the understanding that failures occurred due to tensile stresses from cyclic loading.

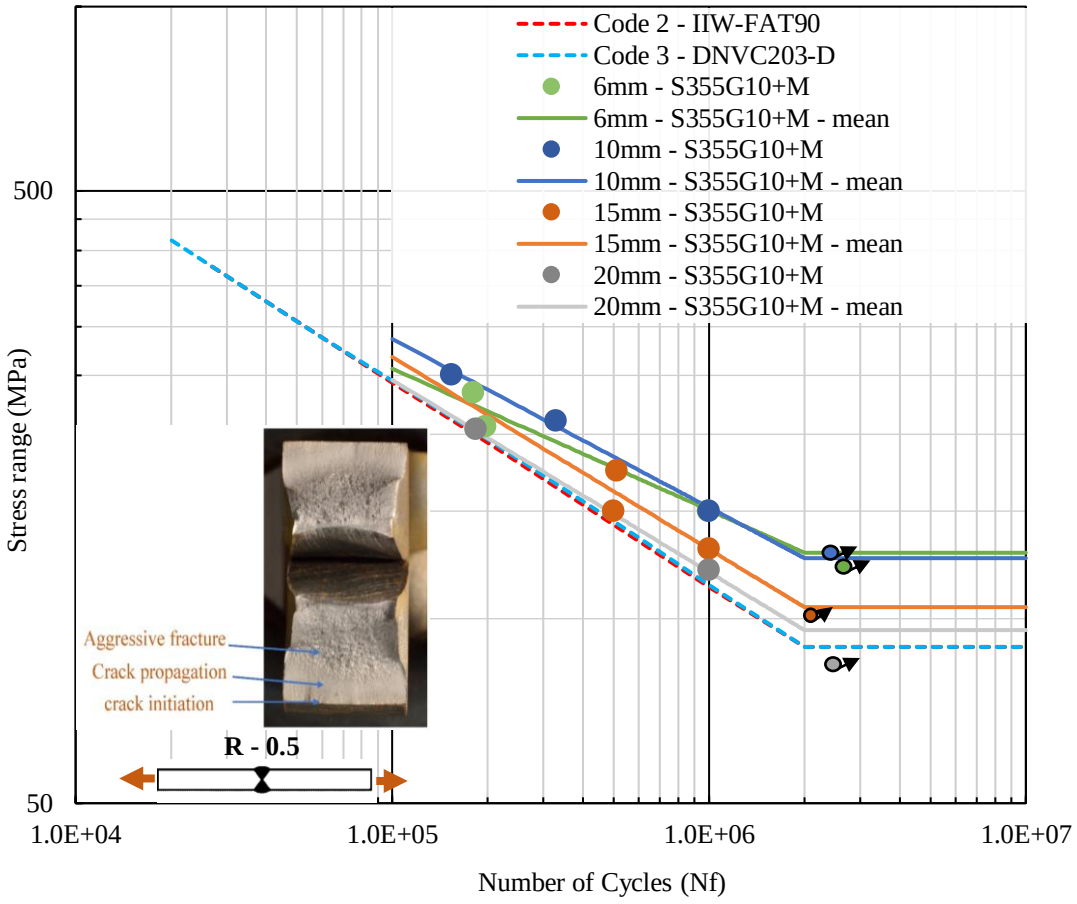

Figure 6.3: S-N curve for S355G10+M structural steel.

The presence of stress concentration significantly impacts fatigue because it involves the occurrence of localised stresses resulting from welding in areas such as notches, pits, weld joints, and sharp geometric transitions. FEA was employed to investigate this phenomenon. A two-dimensional plane stress finite element analysis was conducted. Quadratic 8-node elements were used to build the mesh. Modelled notches were divided into 1 µm sections for finer meshing, and corners were rounded to prevent stress singularities at sharp notches. The material characteristics used were a Young's modulus of 200 GPa, a Poisson's ratio of 0.3, and a material density of 7850 kg/m^3. A nominal stress of 1 MPa was applied to the welded geometry, and the results are depicted in Figure 6.4, which illustrates the stress concentration factor due to the weld. The location of the maximum stress concentration factor values corresponded with the location of the fracture from the fatigue tests, indicating that these locations were sites where cracks initiated and propagated under cyclic loading. This highlights the influence of local stresses, particularly in cases where welds are not machined, as found during the installation of monopiles of wind turbines.

While both pits (Table 7.2) and welds (Figure 6.4) introduced stress concentrations, they did so through distinct mechanisms. Nevertheless, it could be argued that their combined effects were more pronounced. When a pit is formed near or within a weld zone, the collective impact of the weld's geometrical discontinuity and the pit could have amplified the overall stress concentration factor, potentially increasing the risk of fatigue crack initiation and propagation. Imperfect welds often lead to microstructural changes and vulnerability to corrosion. Thus, in environments conducive to corrosion, a welded area might have been more susceptible to pitting, further influencing the stress concentration factor.

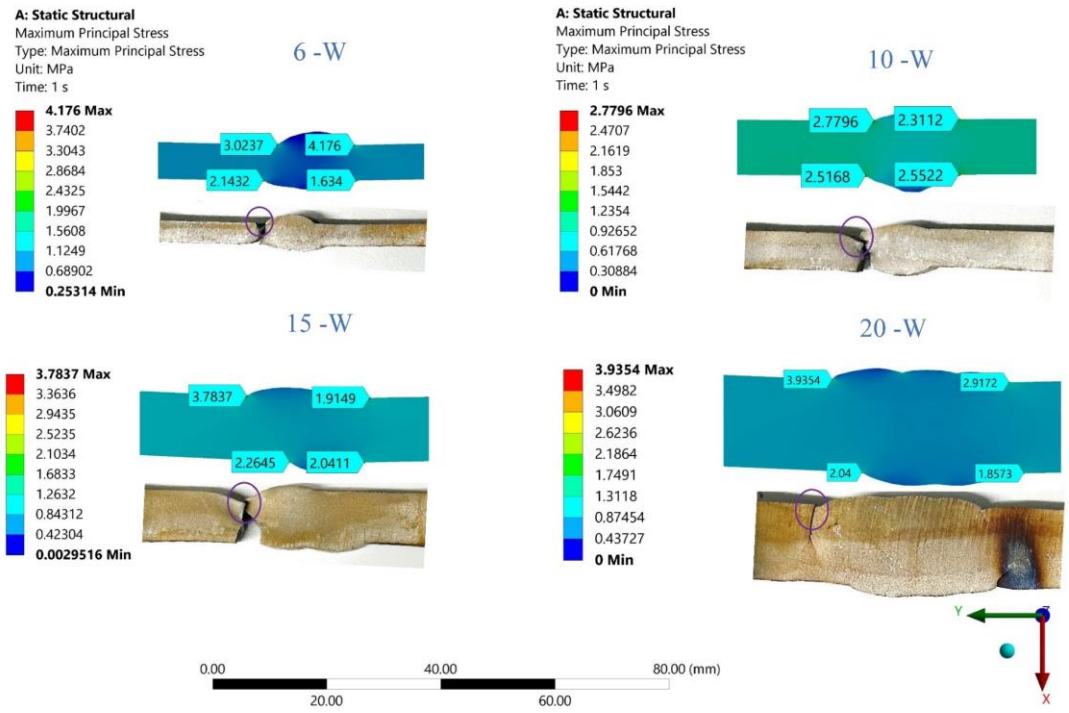

Figure 6.4: Influence of stress concentration on fractured welded S355G10+M specimens.

In addition to the impact of residual stresses and stress concentration factor on the fatigue strength of S355G10+M, misalignment in the butt-welded joint under axial loading can introduce extra bending stresses. These bending stresses, when factored into the SN curve, can contribute to the obtained fatigue strength values. This would also have resulted in elevated stress levels on one of the surfaces located within the welded material, thereby resulting in increased stress in the specimen. The presence of slight geometric imperfections increased the stresses measured during fatigue testing. The stress magnification factors for misalignment and angular distortion have been previously determined based on both global and local stress effects (DNV 2016b; International Institute of Welding 2008) (axial misalignment =1.15 for butt weld). The values of the axial misalignment factors for 6, 10, 15, and 20 mm were 1.18, 1.11, 1.11, and 1.10, respectively, and were in the same range as the recommended value. Considering the total secondary bending effects, overall total stress magnification factor from the combination of angular distortion and axial misalignments given in Equation 2.13 gave combined values of 1.09, 1.08, 1.06, and 1.06 for 6, 10, 15, and 20 mm, respectively. This clearly indicated that although there was no substantial reduction in fatigue strength since values were less than 1.3 (Maddox 1985), an increase in thickness led to a decrease in the effect on secondary

bending stresses. In conclusion, apart from the influence of the stress concentration factor effect on fatigue life, the material performance of S355G10+M structural steel in offshore wind turbine support structures can be affected by axial misalignment, distortion, and residual stress.

6.3.2 Verification of fatigue testing using milling

Figure 6.5 illustrates the fatigue testing setup using a milling machine tool. A high-sample-rate strain gauge was interfaced with the InstruNET data acquisition system (GW instruments Inc 2016). For each test, the system recorded at a sample rate of 1666.7 samples per second. A two-flute cutting tool with a 10 mm diameter was utilised. The milling parameters were chosen as follows: radial depth of cut of 5 mm, axial depth of cut of 4 mm, feed rate of 0.075 mm per tooth, and spindle speed of 500 rpm. These conditions were selected to produce cyclic stresses in the axial direction at the weld toe, which is a critical area for fatigue crack initiation in offshore monopile structures. Preliminary trials revealed that stresses of approximately 50 MPa were measured at the weld toe, where the strain gauge was installed.

However, the milling process introduces self-excited vibrations, commonly known as chatter. This phenomenon restricts the ability to increase cutting forces. To overcome this limitation and induce higher stresses at the weld toe, a 5 mm hole was drilled into the 10 mm thick welded sample. This modification enhanced the stress levels at the weld toe without altering the cutting forces, effectively increasing bending stresses while achieving stable milling conditions.

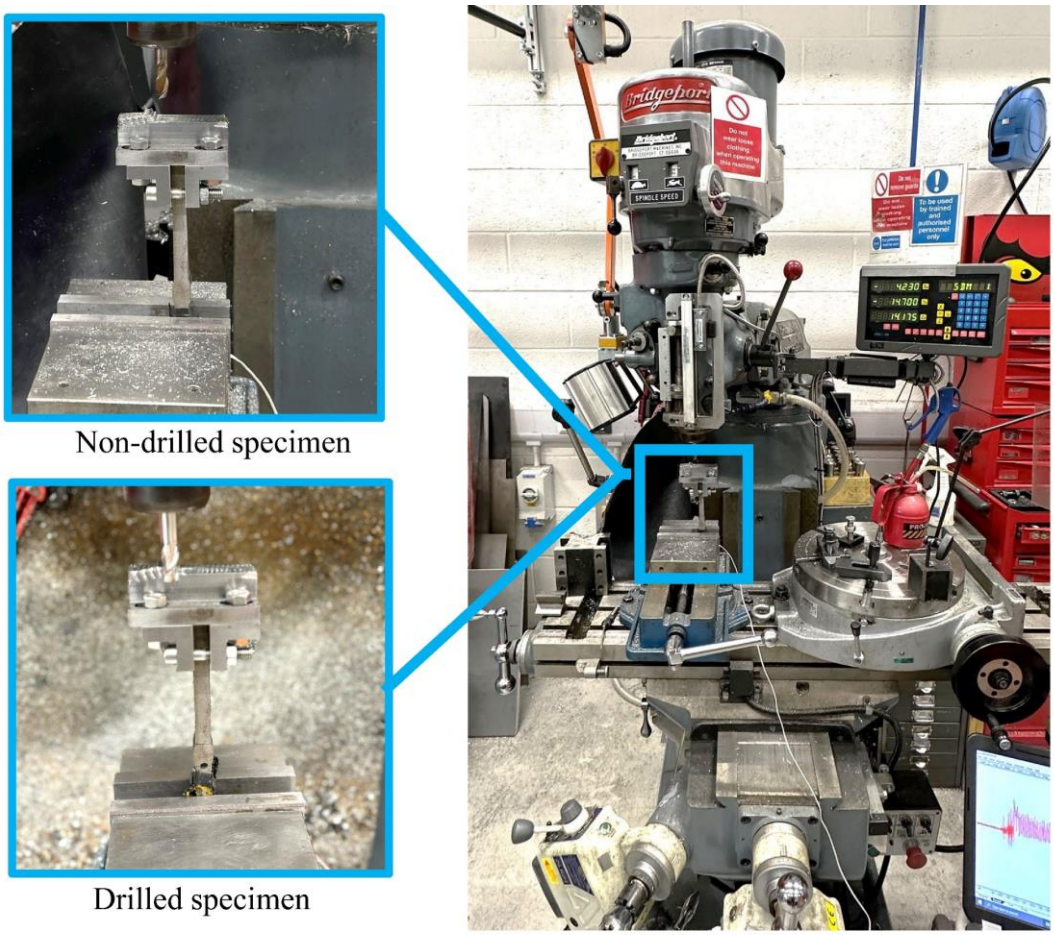

Figure 6.5: Fatigue testing using a milling machine tool

The results from the machining process are presented in Figures 6.6 and 6.7, showing stress-time data for both drilled and non-drilled specimens (brief data detailed in Appendix D2). The peak stress values recorded were 211 MPa for the drilled specimens and 59 MPa for the non-drilled ones under conditions of cyclic tension. In monopile applications for wind turbines, bending stresses are primarily induced by wind loads, and the stress ratio is approximately zero. The conducted test indicated that the minimum stress approached zero during certain cycles, while the maximum average stress was around 200 MPa. This was particularly true for the drilled specimens, which had a reduced cross-sectional area and consequently experienced elevated stress levels. Unlike conventional fatigue testing setups, where the cyclic loading is monotonic and the mean stress remains constant, this methodology allows for variations in the mean stress.

This fatigue testing concept enabled the simulation of cyclic loading conditions, replicating the varying wind speeds and weather changes experienced by offshore

wind turbine monopiles. By altering the depth of cut and feed rate, the induced stresses can be tailored to mimic varying wind load conditions. To expedite the testing process, the spindle speed could be increased, thus achieving a greater number of cycles in a reduced timeframe. For subsequent fatigue analysis, the rainflow counting method (Amzallag et al. 1994) can be applied to the measured stress cycles, and fatigue damage can be calculated.

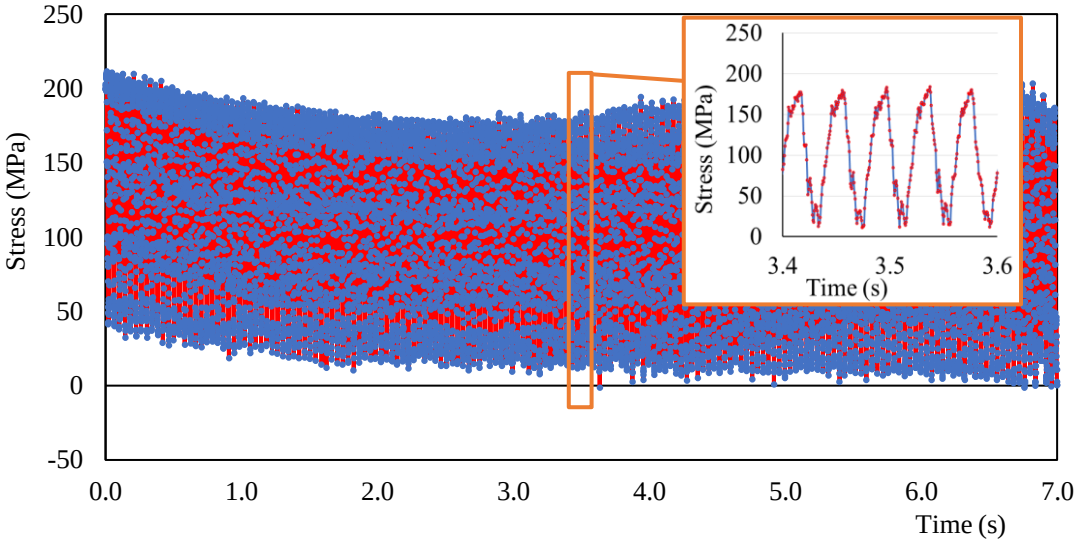

Figure 6.6: Stress-time data for a drilled specimen

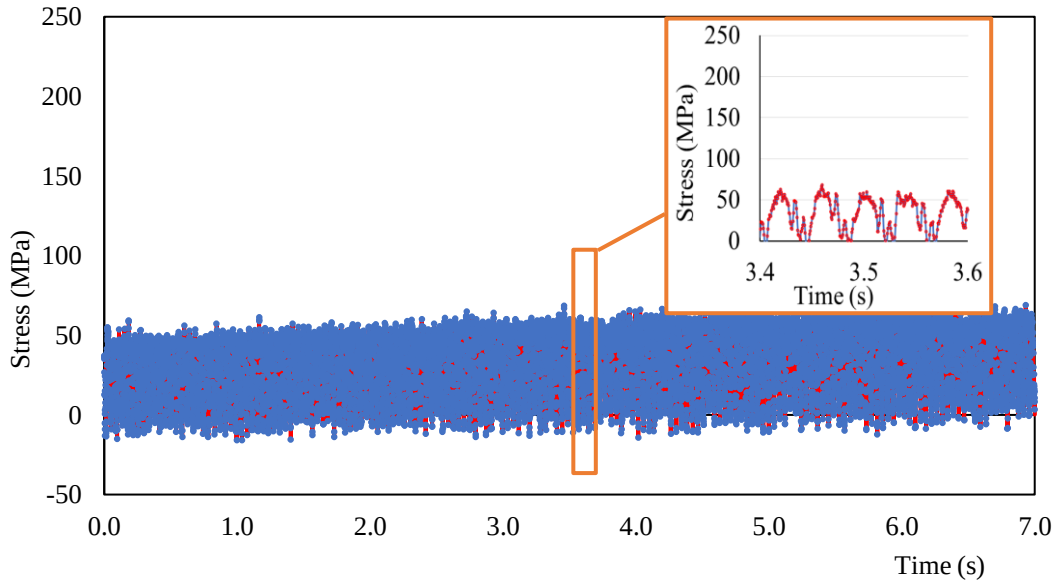

Figure 6.7: Stress-time data for a non-drilled specimen

6.3.3 Conclusions

The study analysed the fatigue behaviour of S355G10+M specimens across different thicknesses, with findings consistent with established design codes. Stress concentrations resulting from welding in areas like notches and pits greatly influenced fatigue, with the stress concentration factor directly correlating to fracture locations in fatigue tests. The effects of pits and welds were found to be compounded when present simultaneously. Fatigue strength was further influenced by factors like residual stresses, misalignment in the butt-welded joint, and slight geometric imperfections. Axial misalignment, distortion, and residual stress also played crucial roles in affecting the material performance of S355G10+M structural steel in offshore wind turbine support structures. Using a milling machine tool for fatigue testing enabled the simulation of varied cyclic loading conditions particular to offshore wind turbine monopiles, offering a more dynamic testing approach that accounts for varying wind conditions.

Chapter 7

Corrosion surface morphology-based methodology for fatigue assessment

This chapter assesses fatigue at the weld under corrosive conditions using a unique corrosion-based fatigue model for fatigue life evaluation of offshore welded structures. The original contribution of this study is a corrosion factor concept that accounts for the effects of corrosion pits on welded S355 steel fatigue performance. Image analysis techniques were employed to characterise the corrosion pit surface roughness, size, and aspect ratio. The corrosion factor was calculated utilising the pit size, aspect ratio, and surface roughness using notch and surface fatigue theories. Critical pit fatigue S-N curves were predicted and compared to fatigue standards. The novel corrosion characterisation approach and corrosion-based fatigue model for fatigue S-N curve prediction showed promise in estimating offshore structural life. Hence, it could subsequently be applied in the prediction of corrosion-fatigue in HAOWT when coupled with fatigue damage assessments.

7.1 X-ray computed tomography

The corrosion characteristics of welded S355J2+N steel samples that were pre-corroded were performed. This grade of steel has the same mechanical and chemical properties as S355G10+M (details reported in Appendix C1), with the minor difference being that S355J2+N has wider applications in offshore structures, whereas S355G10+M is specific to offshore wind turbines (Igwemezie et al. 2019). Thus, the use of S355J2+N structural steel helps the corrosion-fatigue model to have broader applications in offshore welded structures. To mimic the corrosive conditions of a realistic offshore setting, salt spray chamber conditions were applied to lab-scale dog-bone-shaped welded specimens. Although corrosion typically evolves over time, the focus of this study was on the impact of specific corrosive environments. The specimens were assessed under salt spray chamber conditions and compared with the same structural steel tested under both salt spray chamber and artificial seawater corrosive conditions for validation in accordance with the standard (DNV 2016a).

Excess weld metal can provide reinforcement to a weld joint and can induce stress concentrations if not well machined. However, Figure 7.1 depicts a sample in which excess welded material was well machined off prior to the corrosion. It was the intention that only stress concentration factors from pits to be analysed.

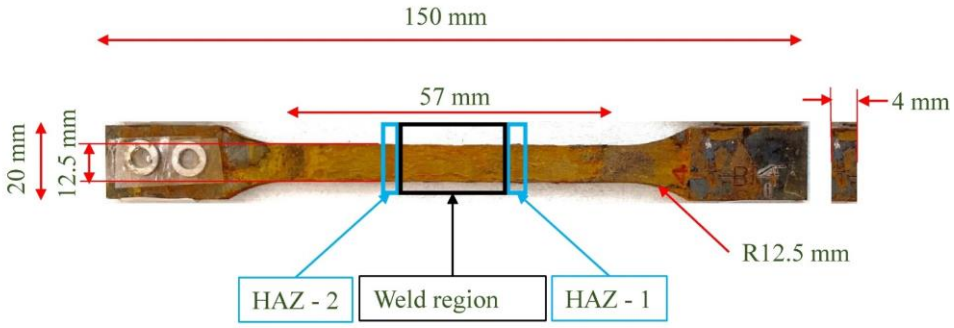

Figure 7.1: Pre-corroded S355J2+N structural steel specimen.

The S355J2+N sample was subjected to X-ray computed tomography scanning to characterise its pre-corroded surface. A Zeiss Xradia 520 Versa was employed for the scans, utilising an X-ray energy level of 160 keV and an exposure duration of 13 s. A total of 3601 projections were collected, encompassing a 360-degree rotation of each sample. These projections were captured on a 2k × 2k pixel charge-coupled device detector. Reconstruction of the scans was performed using the Feldkamp, Davis, and Kress filtered back projection algorithm (Feldkamp et al. 1984). The reconstructed volumes had dimensions of 2k × 2k × 2k with a voxel size of 12.63 µm. Following the completion of the scanning process, 3-D renderings were produced by applying a constant threshold to the reconstructed volumes, as shown in Figure 7.2a - 7.2c. This approach facilitated a detailed examination of both the structure of the specimen and corrosion-induced defects. This study focused on the HAZ to identify areas most susceptible to fatigue-prone crack initiation regions in welds, as found in previous studies (International Institute of Welding 2008; Köder, Bohlmann 2014; Kolios et al. 2019; Sorger et al. 2018). For corrosion characterisation, Avizo 3-D software (Thermo Fisher Scientific 1995) was used. This allowed for the visualisation of corroded surfaces based on a segmentation process. A consistent threshold masking value of 47,000 was applied across all scans. The generated 3-D surfaces were left unsmoothed to offer a realistic view of the actual surface, as depicted in Figure 7.2d.

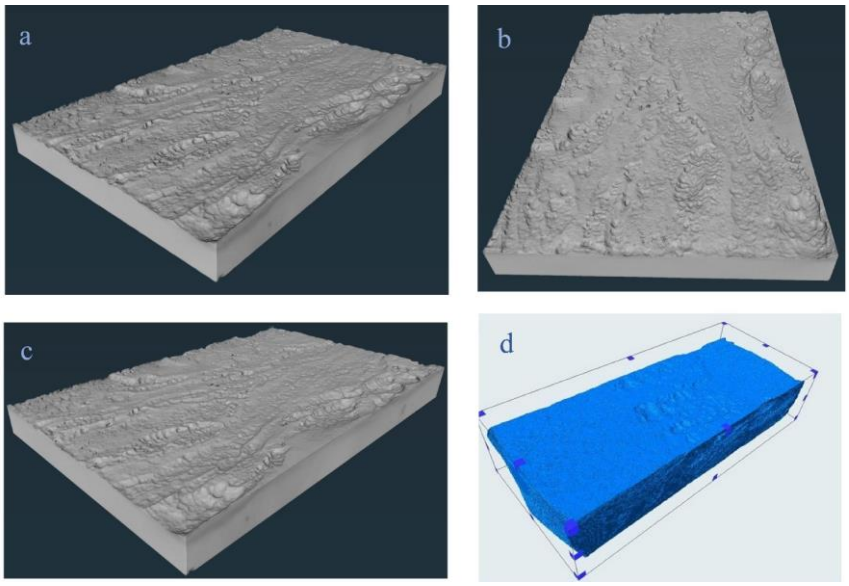

Figure 7.2: a-c) Corroded specimens obtained from 3-D CT scanning of a corroded sample, d) Segmented surface in Avizo.

The GOM Inspect software (ZEISS Group 2021) was utilised to analyse the pre-corroded 3-D surface. The software aligned this corroded model to its uncorroded counterpart using the uncorroded edges as reference points. Following the alignment, a surface deviation contour map was generated. The pit depth (a) was determined based on the calculated surface deviation values. Additionally, the pit diameter (D) was identified and characterised by a circular shape at the surface. This methodology was applied to analyse several pits that were critical in terms of their large diameter and great aspect ratio (a/D).

7.2 Surface roughness estimation using a python code

An evaluation of the surface roughness of the corroded samples was carried out using Python code (Python Software Foundation 2022) developed by Klingaa et al. (2019). This tool employs a fitted-ellipse method grounded in a geometry-fitting technique, enabling both qualitative and quantitative assessments of the corroded surface of the specimen (Klingaa et al. 2019). The effectiveness of this method depends on the quality of the computed tomography scans. For this study, high-quality scans were used to improve the efficiency of the method. An image stack was manually added to the ImageJ software (Ferreira, Rasband 2018). Python code was then executed after

setting a threshold value in ImageJ, thereby automating the subsequent image analysis and computations. The Python script produced 3-D scatter plots that utilised the vertices of meshed surfaces to visualise both the computed tomography scanned surface and fitted elliptical surface. The first step involved importing 1178 image stacks into ImageJ to establish a segmentation threshold. These image stacks were categorised into two groups: steel elements (pixels with grayscale values above the threshold, representing the denser material) and air (pixels with grayscale values below the threshold, representing the less dense material). The Renyi Entropy function within ImageJ was used to refine the segmentation of the grayscale images into the features of interest and the background. Subsequently, these segmented image stacks were imported into the Python code, and analyses were conducted based on the established segmentation thresholds. Finally, standard ISO 25178-2:2021 guidelines (International Organization for Standardisation 2021) were followed to generate parameters describing the surface texture.

7.3 Corrosion-based fatigue methodology and model

In Figure 7.3, a methodology based on corrosion surface morphology is presented for evaluating the fatigue life of welded steel in offshore applications exposed to corrosive environments. This methodology involves three main components: corrosion characterisation, fatigue modelling, and the prediction of S-N curves. Corrosion characterisation entailed the identification of the pit size, pit shape (aspect ratio), and surface roughness at the corroded pit locations. The identified parameters (size, aspect ratio, and surface roughness) were subsequently utilised as inputs in a fatigue model. This model followed the endurance limit approach applied in a previous study (Serjouei, Afazov 2022).

The model incorporated a notch theory to consider the effects of pit size and aspect ratio, focusing on the notch sensitivity of the material. Additionally, the surface roughness resulting from corrosion was integrated into the fatigue model using a surface theory. Details on how the corrosion factors were incorporated into the Basquin equation are provided below. The fatigue model was developed to predict S-N curves based on the inputs derived from corrosion characterisation.

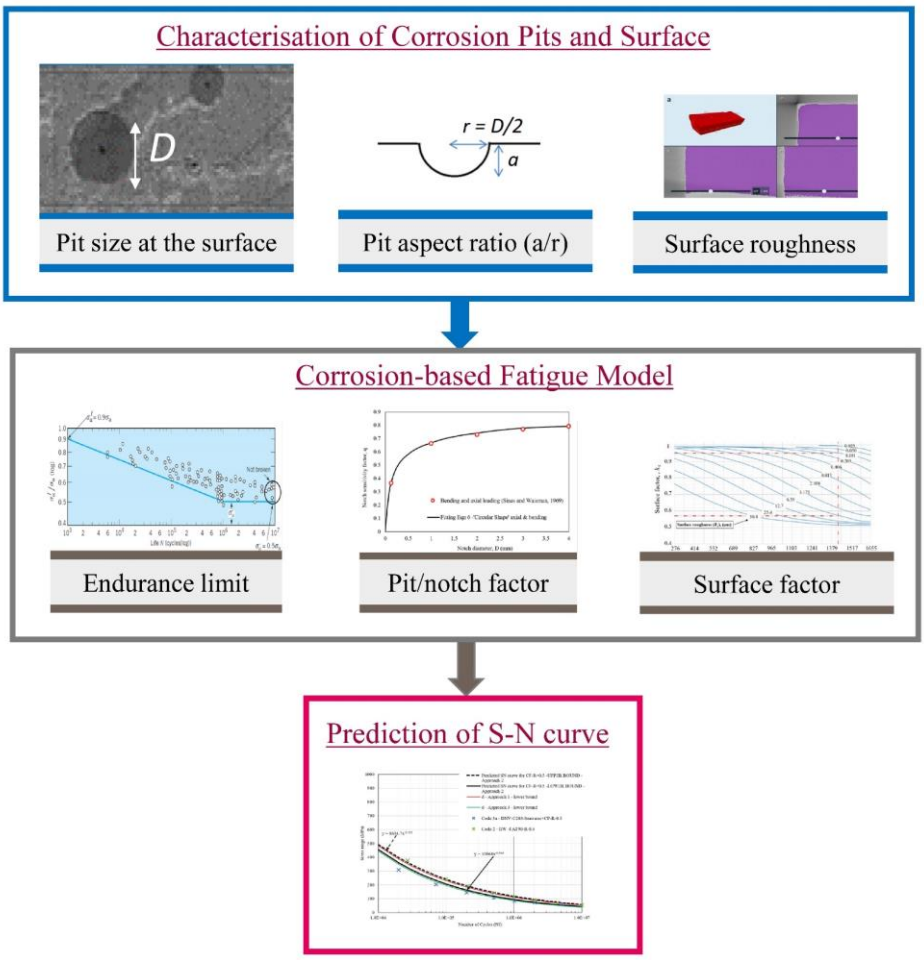

Figure 7.3: Corrosion-based fatigue methodology.

This model highlights the significance of surface corrosion and welding-induced defects on the fatigue strength of the material. In industrial settings, the endurance limit approach is commonly employed. This approach differentiates between a high-cycle fatigue region at 10^6 cycles, where the stress amplitude generally remains stable at the endurance limit of the material, and a low-cycle fatigue region at 10^3 cycles, where the stress amplitude decreases as the cycle count increases. Equation 6.1 indicates that, at 10^3 cycles, the material's fatigue strength is approximately 90% of its UTS. The endurance limit approach states that the material can withstand stress levels close to its full strength before fatigue is set in at these lower cycles. Equation 6.2 shows that, at 10^6 cycles, the material's fatigue strength was approximately equal to half its UTS. These approximations for the endurance limit of 0.9 and 0.5 are based on empirical observations and experimental data, particularly for ferrous alloys (Bannantine et al. 1990), and are given by:

$$\sigma_a^f(N = 10^3) = 0.9 \times \sigma_u \quad \text{at } 10^3 \text{ cycles} \tag{6.1}$$

$$\sigma_a^f(N = 10^6) = 0.5 \times \sigma_u \quad \text{at } 10^6 \text{ cycles} \tag{6.2}$$

where σ_a^f is the fatigue stress amplitude, N is the number of cycles, and σ_u is the UTS.

The mean stress effect, σ_m, using the Goodman approach is introduced together with a newly defined corrosion factor, f_c , into Equation 6.2 to obtain Equation 6.3.

$$\sigma_a^f = 0.5 f_c \sigma_u \left(1 - \frac{\sigma_m}{\sigma_u}\right) \quad \text{at } 10^6 \text{ cycles} \tag{6.3}$$

The impact of the pit morphology and surface roughness determines the corrosion factor. Considering both the corrosion factor and the effect of mean stress, as represented by the stress ratio *R* which is not applied in low cycle region because there is no failure but applied at the high cycle region where there is failure, the fatigue model based on the endurance limit is presented in terms of a stress range, σ_r^f (Serjouei, Afazov 2022; Okenyi, Afazov, et al. 2023) as:

$$\sigma_r^f = 1.8\sigma_u \quad \text{at } 10^3 \text{ cycles} \tag{6.4}$$

$$\sigma_r^f = \frac{\sigma_u f_c}{1 + 0.5 f_c \left(\frac{1+R}{1-R}\right)} \quad \text{at } 10^6 \text{ cycles} \tag{6.5}$$

The corrosion factor reduced both the endurance limit at 10^6 cycles and the mean stress owing to the pitting and tensile mean stresses, respectively. Equations 6.4 and 6.5 are then used to generate two data points that correspond to the S-N curves at 10^3 and 10^6 cycles, respectively. Subsequently, these two data points were incorporated into the Basquin equation (Equation 6.6). This integration allowed for the derivation of the material fitting constants denoted as A and n.

$$\sigma_r^f = A N_f^{\,n} \tag{6.6}$$

The corrosion factor f_c, is defined to represent both the shape of the pit, including its size and aspect ratio, as well as the surface roughness at the pit location. To capture these characteristics, f_c, is formulated as the product of a notch factor, f_n and a surface factor, f_s, as given by:

$$f_c = f_n f_s \tag{6.7}$$

The notch factor, f_n, is determined by considering the pit as a notch on the corroded surface, as per the notch theory (Peterson 1945), and it is given by:

$$f_n = \frac{1}{k_f} \tag{6.8}$$

Equation 6.8 shows the relationship between the notch f_n and the fatigue stress concentration factor k_f. Since the fatigue stress concentration factor, k_f, represents how much stress is amplified by a pit or notch under cyclic loading. Its inverse would be the fraction of the real stress to the amplified stress. Thus, the range of f_n 's validity was between 0 and 1. The notch sensitivity of the material, q, and the static stress concentration factor, k_{scf}, can be used to calculate the fatigue stress concentration, as shown in Equation 6.9 (Sines et al. 1959).

$$k_f = 1 + (k_{scf} - 1)q \tag{6.9}$$

The notch sensitivity, *q*, is dependent on the diameter of the notch, *D*, (Peterson 1945) and is given by:

$$q = \frac{1}{1+\frac{C_m}{D}} \tag{6.10}$$

The static stress concentration, k_{scf}, for a notch with an aspect ratio (*a/r* or *a/0.5D*) is given by (Peterson 1945):

$$k_{scf} = 1 + 2\sqrt{\frac{a}{0.5D}} \tag{6.11}$$

After substituting Equations 6.9 – 6.11 into Equation 6.8 and rearranging, the notch factor can be given by:

$$f_n = 1 - \frac{2\sqrt{2aD}}{D+C_m+2\sqrt{2aD}} \tag{6.12}$$

Peterson (1945) established that the notch sensitivity of steel is dependent on its UTS. An average UTS value of 546 Mpa was reported for S355 steel in Table 3.2. The material constant C_m, was determined to be 1.05 and was obtained through curve fitting to the notch sensitivity data, as depicted in Figure 7.4.

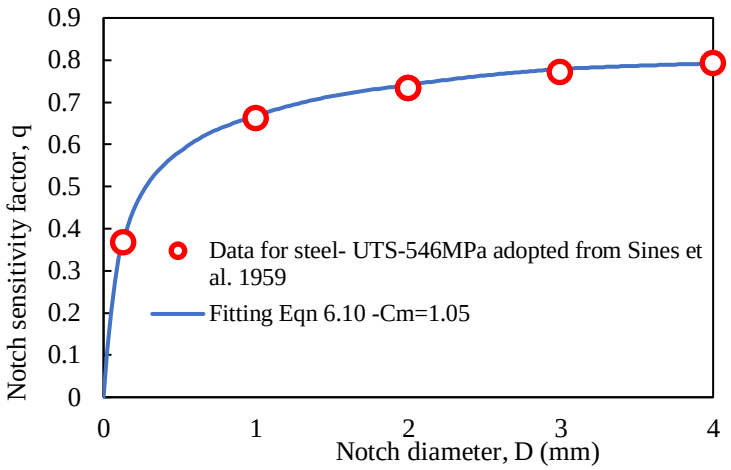

Figure 7.4: Notch sensitivity factor for fitting material constant.

Surface factor f_s is determined to be dependent on the UTS and the average surface roughness R_a (Serjouei, Afazov 2022). The validity range for f_s differs based on the material type, surface finish, and specific R_a measurements. Typically, f_s values ranged between 0.5 and 1. A value of 1 signifies that surface roughness does not detrimentally impact fatigue strength, whereas values less than 1 indicate a decrease in fatigue strength due to the surface finish. This relationship is illustrated in Figure 7.5. After obtaining f_s values from Figure 7.5 and f_n values from Equation 6.12, these were incorporated into Equation 6.7 to calculate f_c. Subsequently, f_c was inserted into Equation 6.5 to determine the stress range, given that the UTS and R values of the steel material were known. Utilising Equation 6.6, an S-N curve was generated for each analysed pit.

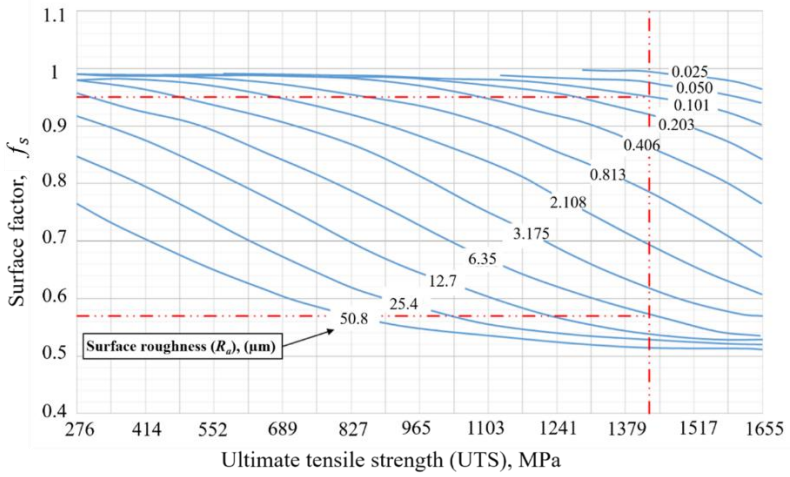

Figure 7.5: Fatigue surface factor plotted against UTS and surface roughness (Serjouei, Afazov 2022).

7.4 Results and discussion of corrosion surface morphology-based methodology for fatigue assessment

7.4.1 Pit characterisation in heat-affected zones

Surface deviations were calculated for both the corroded and uncorroded specimens in two HAZs (HAZ 1 and HAZ 2), as depicted in Figure 7.6. For the uncorroded specimens, the surface deviations at both HAZ 1 and HAZ 2 were found to be within a range of ±40 µm. However, the corroded specimens exhibited significantly higher surface deviations, reaching ±400 µm in the HAZs. A demarcation line between the weld and HAZ regions revealed different rates of material loss owing to corrosion in these zones.

More pits were observed in the HAZ regions than in the weld areas, as shown in Figures 7.6b and 7.6d. This observation suggests that the weld regions possessed higher resistance to corrosion than the HAZ regions. Although it was not definitively determined, there is a possibility that the heat from welding caused microstructural changes and contributed to the HAZ being more susceptible to pitting corrosion. This is an area for future research. Ten critical pits in each HAZ were measured and analysed. The diameters of these pits were characterised by fitting a circular shape to the pit surfaces. Additionally, the depths were recorded by measuring the surface deviation from the top of each pit to its centre, as exemplified in Figure 7.7.

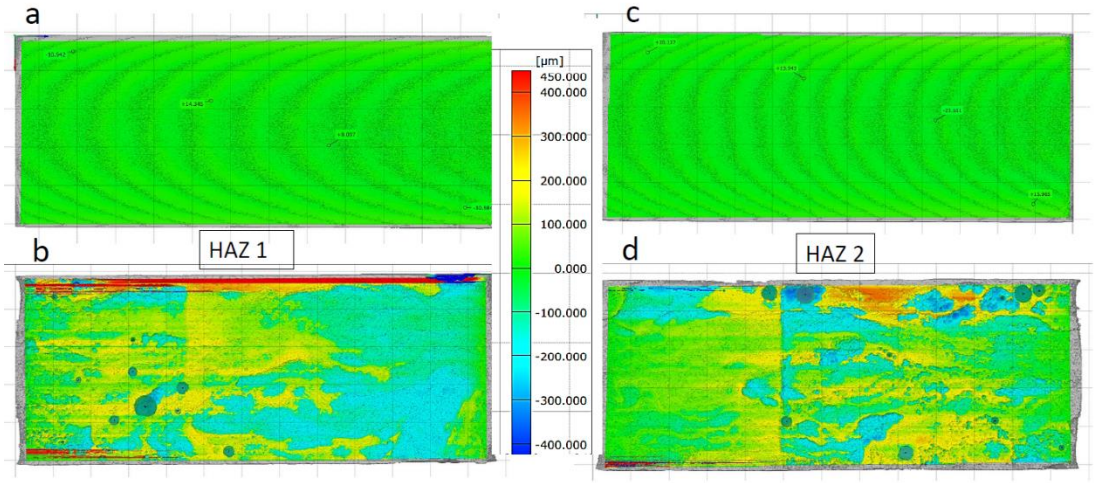

Figure 7.6: Surface deviation plot for a) uncorroded HAZ 1, b) corroded HAZ 1, c) uncorroded HAZ 2, and d) corroded HAZ 2.

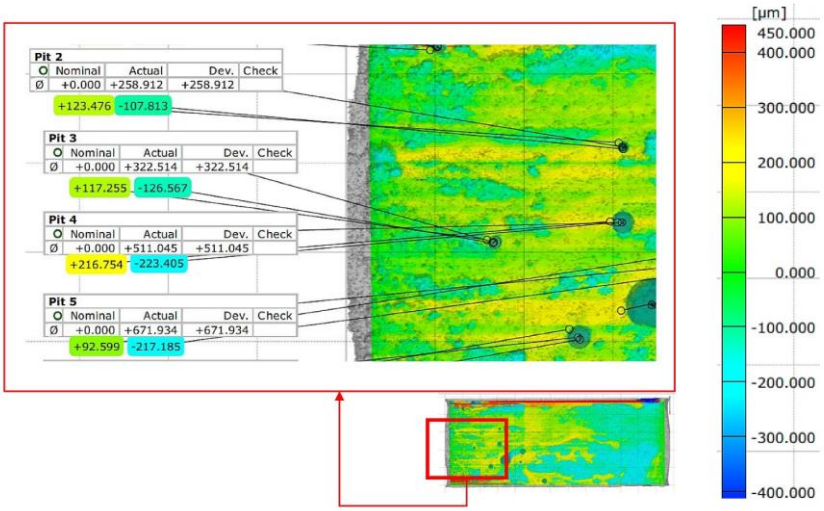

Figure 7.7: Pit diameter and depth obtained on the actual pit surface.

7.4.2 Surface roughness and pit depth probability analysis of corroded S355 steel

Surface roughness measurements were conducted on the steel surface to evaluate the textures of the corroded samples. These measurements are depicted in Figure 7.8, while Figure 7.9 shows the statistical analysis of the probability distribution related to random variable depth to further understand the nature of pits i.e., the probability density of the depth measurements. The characteristics of the surface texture were identified, and the surface properties are listed in Table 7.1, according to ISO 25178-2:2021 (International Organization for Standardisation 2021).

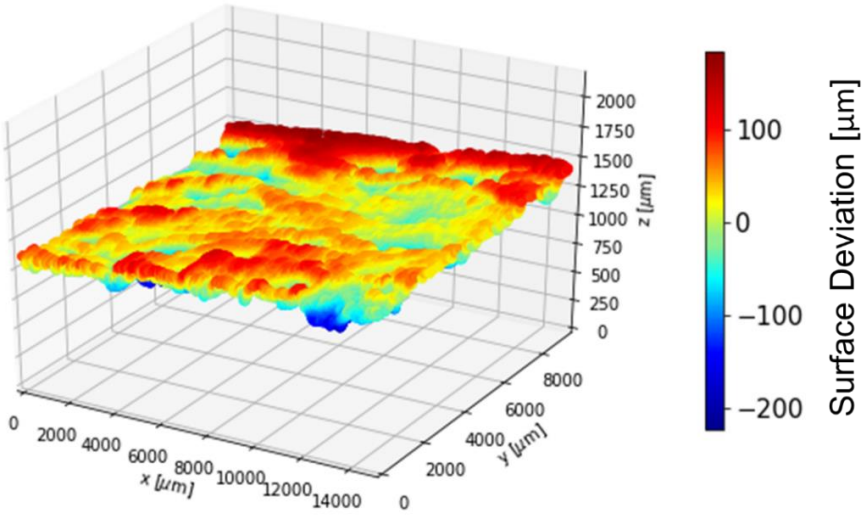

Figure 7.8: Surface deviation from the corroded sample.

Table 7.1: Calculated surface properties for corroded surfaces.

Property	Values
Voxel size	12.6338 µm
S_a - arithmetical mean height of the surface compared to the mean plane of the surface ≈ Ra	43.68 µm
S_q -root mean square height of the corroded surface	57.43 µm
S_{40z} - Average maximum height	402.81 µm
S_{sk} - skewness of the observed surface	-0.203
S_{ku} - measure of the sharpness of the surface roughness	3.648
S_p - highest peak observed within the sampling area	183.83 µm
S_v - deepest valley observed within the same sampling area	-223.84 µm

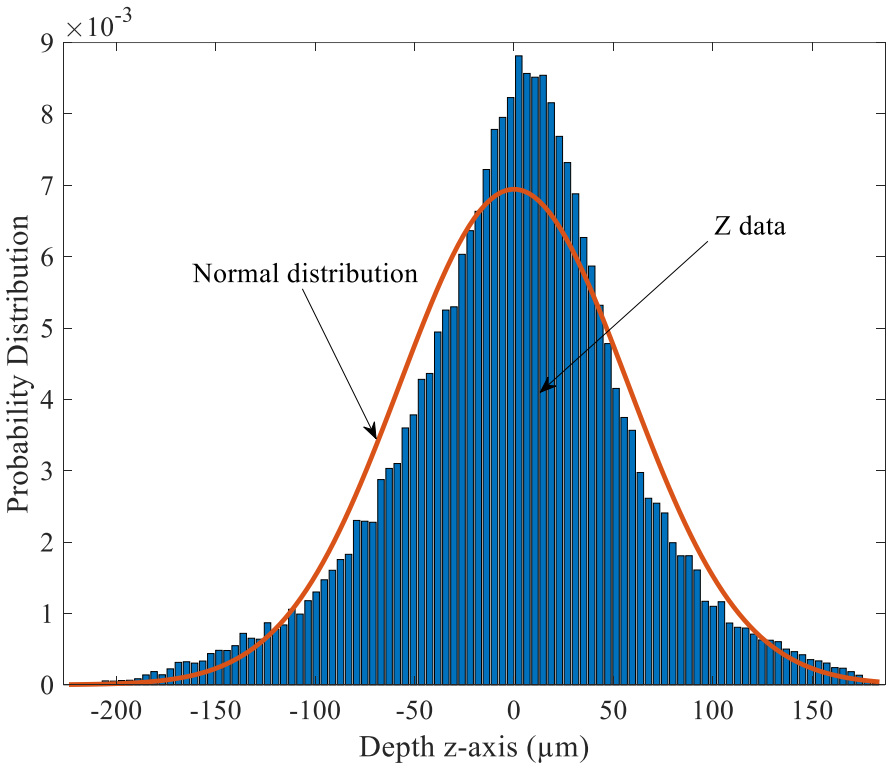

Figure 7.9: Probability density distribution of variable Z (x, y) for the pre-corroded specimen (normal distribution).

Given that S_a is an area-based parameter and R_a is line-based, the corrosion surface in this study was assumed to lack directional bias, making R_a similar to S_a. A R_a value of 43.68 µm was recorded and incorporated into the corrosion-based fatigue model. The skewness S_{sk} was measured to be -0.203, which is less than zero, indicating that most

measurement points lay above the mean plane and that the valleys were deeper than the peaks. This was consistent with the expectations for a corroded surface that forms pits.

Kurtosis S_{ku} was measured to be 3.648, a value greater than 3, suggesting a sharply textured surface. Both skewness and kurtosis values are essential for determining the nature of localised corrosion or pit formation. The negative skewness in the probability density function indicates the presence of deeper, less frequent pits on the surface. The kurtosis value indicated a long tail distribution in statistical terms, which is expected when there are less frequent but deep pits. These findings agree with prior studies that characterised corrosion (Nugroho et al. 2021; To et al. 2018). Therefore, Figure 7.9 presents the probability density distribution of variable Z (x, y) for the pre-corroded specimen for the salt spray chamber corrosive condition. For comparison, a previous study reported a R_a value of 16.5 µm after 80 days in salt spray chamber (Gkatzogiannis et al. 2019). A 43.68 µm Ra value obtained in this study for 365 days means we have comparable R_a values. While acknowledging that corrosion modifies both the surface topology and texture over time, corrosion can be affected by additional factors such as salinity, temperature, and oxygen concentration.

7.4.3 Predicted S-N curves for corrosion-fatigue assessment

The measured pit properties were applied to the corrosion-based fatigue model (Section 6.3) to predict SN curves. Table 7.2 shows the characterisation of pit properties along with associated fatigue-related factors. Pits were randomly chosen based on their diameter and depth, as measured in Figure 7.7, and were selected from both HAZ locations to represent both shallow and deep pits. The corrosion-based fatigue model used in this study predicted that cracks would originate from a pit with a circular shape at the surface, establishing that the static stress concentration factor at the surface is 3. Pits with an aspect ratio less than one were categorised as shallow, whereas those with an aspect ratio greater than one were identified as deep pits. For the deep pits, the static stress concentration exceeded 3, and the location of the maximum stress was at the bottom of the pit when viewed from the surface. In contrast, for shallow pits, the maximum stress was located at the circular surface shape of the pit, maintaining a static stress concentration factor of 3.

Values for the notch sensitivity factor were derived from Figure 7.4 and adapted for S355 structural steel, taking into account the pit diameter. The fatigue stress concentration factor, k_f values were calculated by inserting the known notch sensitivity factor, q, and static stress concentration factor k_{scf} into Equation 6.9. A surface factor of 0.67 was determined by correlating the measured average surface roughness, R_a of 43.68 µm from Table 7.1, with the UTS of 546 MPa, as shown in Figure 7.5. The notch defect factor f_n values were acquired by integrating the fatigue stress concentration factor, k_f into Equation 6.8. Consequently, the corrosion factor f_c values were computed using Equation 6.7 as a product of the 0.67 surface factor and the notch defect factor.

Table 7.2: Pit measurements and estimated corrosion factors.

Zone	Pit diameter, D (mm)	Aspect ratio, a/r	Pit Type	Static SCF, K_{scf}	Notch sensitivity factor, q	Fatigue SCF, K_f	Notch defect factor (f_n)	Corrosion factor, f_c (0.67x f_n)
	0.838	1.0853	Deep	3.084	0.66	2.375	0.421	0.282
	1.001	0.2970	Shallow	3	0.67	1.730	0.578	0.387
	0.307	0.7505	Shallow	3	0.515	1.892	0.528	0.354
	0.938	0.8656	Shallow	3	0.66	2.228	0.449	0.301
HAZ	0.659	1.0801	Deep	3.079	0.63	2.309	0.433	0.290
1	0.291	2.1094	Deep	3.905	0.61	2.772	0.361	0.242
	0.612	1.1267	Deep	3.123	0.65	2.380	0.420	0.281
	0.792	0.7550	Shallow	3	0.64	2.112	0.473	0.317
	0.428	1.4067	Deep	3.372	0.609	2.445	0.409	0.274
	0.315	1.2042	Deep	3.195	0.54	2.185	0.458	0.307
	0.351	1.4131	Deep	3.378	0.58	2.379	0.420	0.281
	0.259	1.7866	Deep	3.673	0.57	2.524	0.396	0.265
	0.323	1.5120	Deep	3.459	0.575	2.414	0.414	0.277
	0.511	1.7226	Deep	3.625	0.65	2.706	0.370	0.248
HAZ	0.672	0.9221	Shallow	3	0.62	2.191	0.456	0.306
2	0.533	0.9765	Shallow	3	0.585	2.156	0.464	0.311
	1.207	0.8089	Shallow	3	0.69	2.241	0.446	0.299
	0.309	2.1242	Deep	3.915	0.62	2.807	0.356	0.239
	0.175	2.9473	Deep	4.434	0.585	3.009	0.332	0.222
	0.605	1.1816	Deep	3.174	0.63	2.370	0.422	0.283

The range of the corrosion factors for the deep pits was identified to be between 0.222 and 0.307. The minimum corrosion factor was considered to be the most critical defect, theoretically indicating where crack initiation should occur. However, in practice, other analysed critical pits could also serve as initiation points. Two S-N curves were generated using corrosion-based fatigue models, as described in Section 6.3.

This curve utilised the minimum and maximum corrosion factors (0.222 and 0.307) and were then compared with experimental S-N data points collected at stress ratios of R=0.5 and R=0.1. The fatigue tests conducted in this chapter were mainly referenced from the existing literature and were selected to fit the specific corrosion conditions under consideration. The experiments focused on the evaluation of the surface roughness and computed tomography scanning of the specimens. The innovation lies in the development of a fatigue model to clarify the relationship between pitting corrosion and fatigue, aiming to predict the fatigue strength in structural steel.

Fatigue testing was conducted on specimens of S355J2+N that were subjected to butt welding at the Technical University of Denmark (Ólafsson et al. 2016). The experiments were conducted in the laboratory at room temperature. The specimens were subjected to axial tension-tension fatigue testing. The experiments were conducted using stress ratio of R=0.5. For these specimens, the welded material was machined to replicate ideal conditions and ensure that the specimens could be accommodated within the testing apparatus. The specimens were tested in an artificial seawater corrosive environment while using a cooling unit throughout the duration of the test. The experiment was carried out at a frequency of 8 Hz (Ólafsson et al. 2016).

For specimens tested at R=0.1, they remained in the as-welded condition. They were subjected to a pre-corrosion process in a salt spray chamber corrosive environment for a duration of 10 days, after which they were subsequently evaluated in dry conditions. The experiments were carried out at a high frequency of 110 Hz (Gkatzogiannis et al. 2019), and failure in all fatigue tests occurred by complete rupture. The frequency of 8 Hz for axial tension-tension fatigue tests balanced realistic operational conditions with reasonable testing duration, allowing the artificial seawater environment to interact with the material. However, 110 Hz high-frequency testing was developed to quickly assess fatigue life after a salt spray chamber pre-corrosion process. Both

frequencies collected useful data under different environmental and operational conditions, improving fatigue performance understanding.

Figure 7.10 contains the predicted S-N curves and the outcomes of all fatigue test series related to the mean stress range values. To maintain consistency, the fatigue strength at 5×10^6 cycles was utilised for both the predicted and experimental data. Nonetheless, the projected S-N curve adhered to the guidelines outlined in the fatigue design standard (DNV 2016b), wherein the fatigue strength was determined based on the measurement obtained at 2×10^6 cycles.

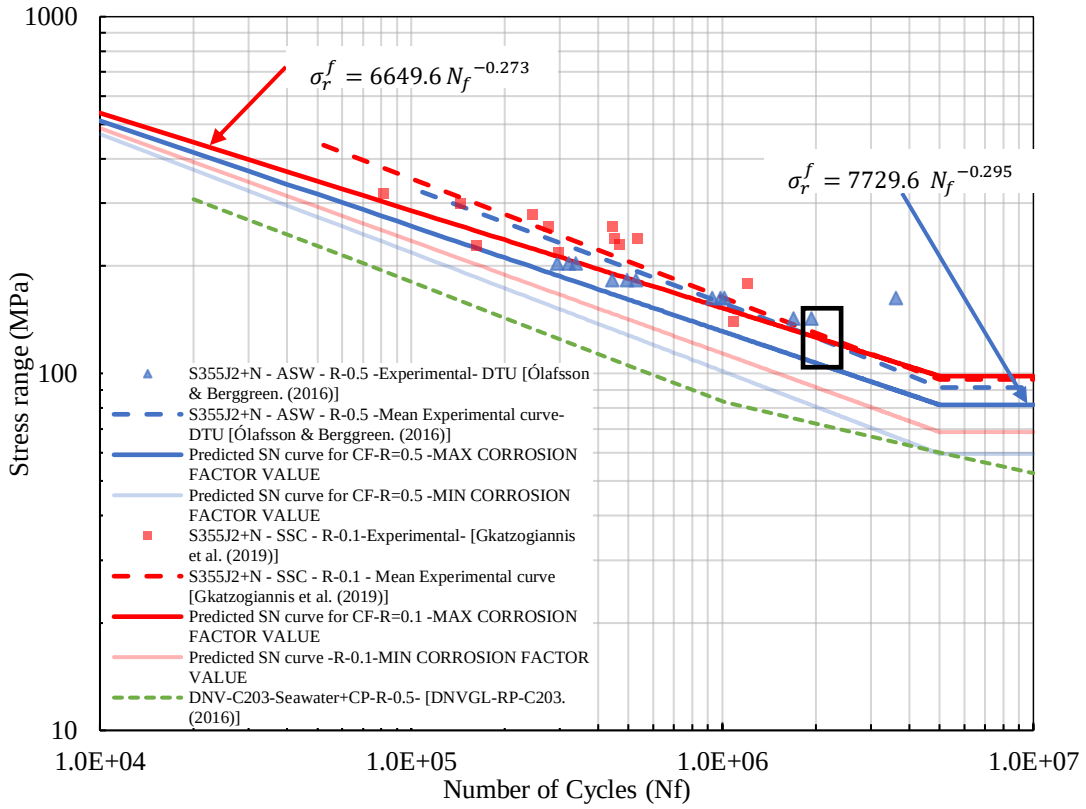

Figure 7.10: Predicted and experimental S-N curves compared with fatigue code.

The predicted mean S-N curves for R values of 0.5 and 0.1, representing the minimum corrosion factor (MIN CORROSION FACTOR) value, were natural with the data points of curve D in the DNVGL-RP-C203 (DNV 2016b) fatigue design standard which was already at mean minus two standard deviations. The rationale for selecting the curve from the code (detail category D4) in this study was based on the similarity between the background and conditions of the curve for this study. The results were generated from fatigue tests on butt-welded specimens under corrosive conditions which is the same as the conditions of the material utilised for prediction in this research. The outcomes derived from the forecasts with R values of 0.5 and 0.1, representing the maximum corrosion factor value (MAX CORROSION FACTOR), are depicted in Figure 10 (data detailed in Appendix C2). These results were verified through fatigue tests conducted on S355J2+N specimens exposed to corrosive conditions.

The findings obtained in the high-cycle and low-stress range zones provide evidence of the impact of the corrosive environment. At a fatigue life of 2×10^6 cycles and a stress ratio (R) of 0.5, the predicted fatigue strength was 107 MPa, whereas the tested fatigue strength was 126 MPa. At a fatigue life of 2×10^6 cycles and a stress ratio (R) of 0.1, the estimated and experimentally determined fatigue strengths are 126.3 MPa and 130 MPa, respectively, as depicted in Figure 7.11. A comparison between the predicted and experimental test results show the considerable potential of the proposed technique for accurately predicting the fatigue strength of corroded structural steel. Furthermore, this methodology can be effectively utilised in the assessment of fatigue in welded marine structures. The prediction achieved at R of 0.1 exhibited higher accuracy compared to the prediction obtained at R of 0.5. This subtle variation can perhaps be attributed to differences in the corrosive environment and test frequency to which the specimens were exposed. In this chapter, the strength of the proposed model to account for the influence of mean stress, a crucial factor in evaluating the fatigue life of maritime structures under cyclic loading conditions, has been demonstrated.

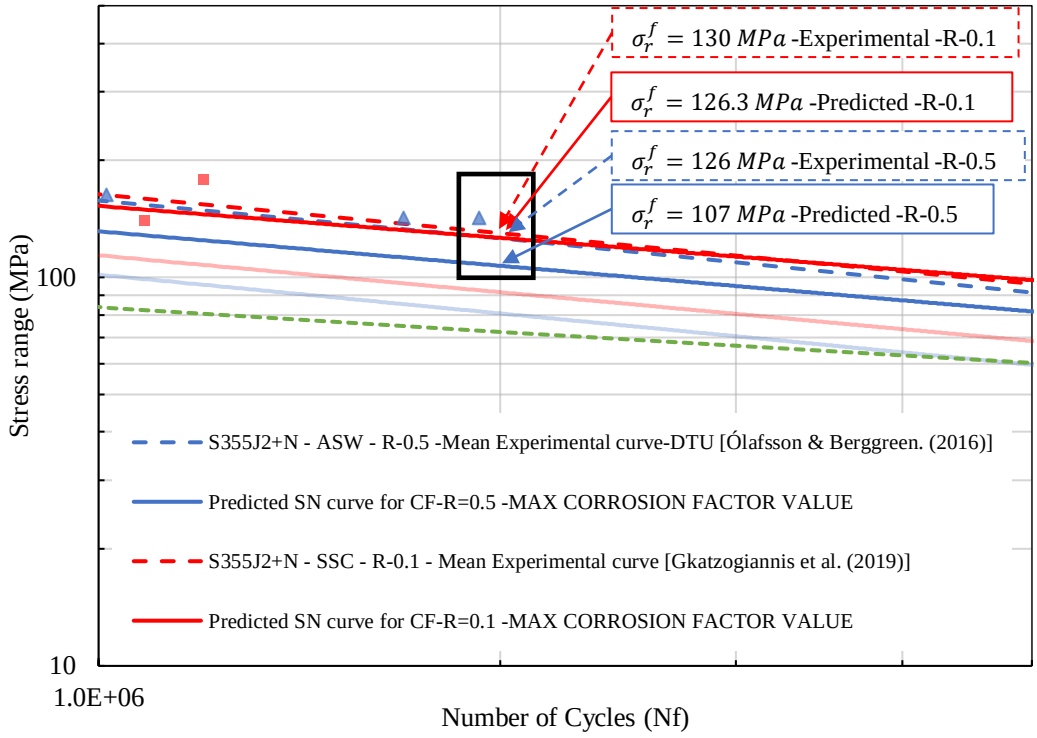

Figure 7.11: Comparison of predicted and experimental fatigue strengths.

7.4.4 Conclusions

The proposed corrosion-based fatigue methodology provided a commendable prediction for the S-N curve of corroded S355J2+N welded steel, aligning closely with laboratory fatigue tests. Specifically, the model exhibited a minor deviation of 2.8% at stress ratio R = 0.1 and a more pronounced 15.1% deviation at R = 0.5 under corrosive conditions. Moreover, the corroded surface characterization revealed critical defects, especially deep pits in the HAZ, with corrosion factors ranging from 0.222 to 0.307. This straightforward characterisation approach, which encompassed measurements of pit diameter, depth, and surface roughness, offers practical utility for inspecting large HAOWTs. Importantly, the model's ability to account for mean stress effects enhances its utility for realistic fatigue assessments under variable wind and wave-induced stress fields.

Chapter 8

Remaining life prediction of corrosion-fatigue in offshore wind turbines support structure

This chapter provides an in-depth focus on the demonstration of the prediction of the remaining life of corrosion-fatigue in the support structures of offshore wind turbines considering mechanical and environmental conditions. The 15 Megawatt HAOWT, with its detailed description of the already provided in Chapter 4 is utilised for corrosion fatigue damage assessment and remaining life demonstrations. An open-source data from the Westermost Rough offshore wind farm has been incorporated into the novel corrosion-fatigue damage theory obtained in this research. Thus, the details of its installation site, load parameters including wind and wave data, are provided. The theoretical foundations of corrosion-fatigue damage, employing key models and theories relevant to the study, were subsequently discussed. This was followed by the application of rainflow counting techniques and fatigue damage assessment methods to the wind and wave data, laying the groundwork for subsequent corrosion-fatigue life predictions. The chapter concludes with discussions on the remaining life of HAOWT support structures, specifically analysing their fatigue damage based on wind and wave data. Overall, the chapter synthesised theory, empirical data, and analytical methods to offer informed predictions about the impact of corrosion-fatigue on the remaining life of offshore wind turbine support structures, informed by works from Chapters 4 to 7.

8.1 Meteorological data and load parameters

8.1.1 Installation site

Open-source data from the Marine Data Exchange provides wind speed and direction data in 2014 from the station at the Westermost Rough offshore wind site located at the coordinates 53.804480°N, 0.132848°E as illustrated in Figure 8.1. The North Sea which has the highest concentration of offshore wind turbines in Europe (Wind Europe, Wood Mackenzie 2020). This chapter demonstrates a validation scenario

where the considered 15 Megawatt HAOWT in this study is installed in the North Sea to determine its corrosion fatigue damage and estimate its remaining life incorporating the developed corrosion-fatigue damage theory to conclude this research.

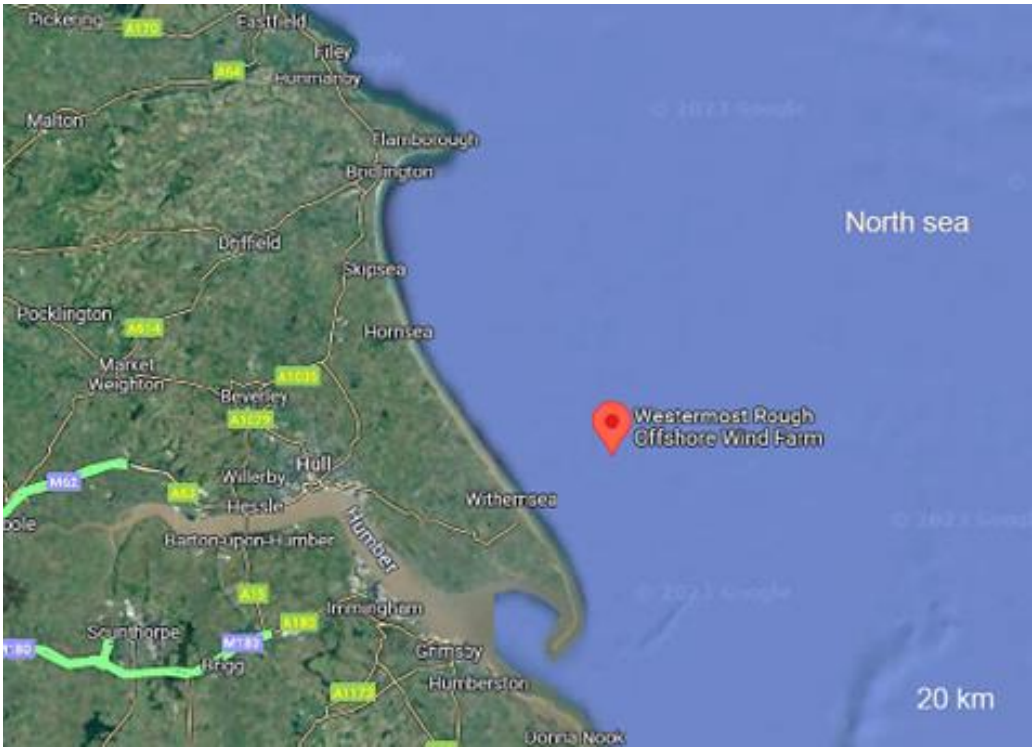

Figure 8.1: Location of installation site and measurements (Courtesy Google maps)

8.1.2 Wind data

Open-source data from the Marine Data Exchange provides wind speed and direction data for every 10 min from the Westermost rough offshore wind site is presented in Figure 8.2 (Appendix E1). A total of 48,379 data points were obtained after processing of data to represent 1-year data. The wind data were obtained at different heights. Based on the HAOWT under consideration, wind is experienced on the tower and the rotor-nacelle-assembly. Additionally, the wind experienced by the rotor-nacelle-assembly includes the consideration of the blade swept area. Averagely, based on the area exposed to wind, the rotor-nacelle-assembly including the blade swept area, experiences higher values of wind speed in Figure 8.2. the maximum wind speed observed was 30.5 m/s. Subsequently, the wind load on rotor and wind load on tower is estimated using Equation 4.1 and 4.2 respectively.

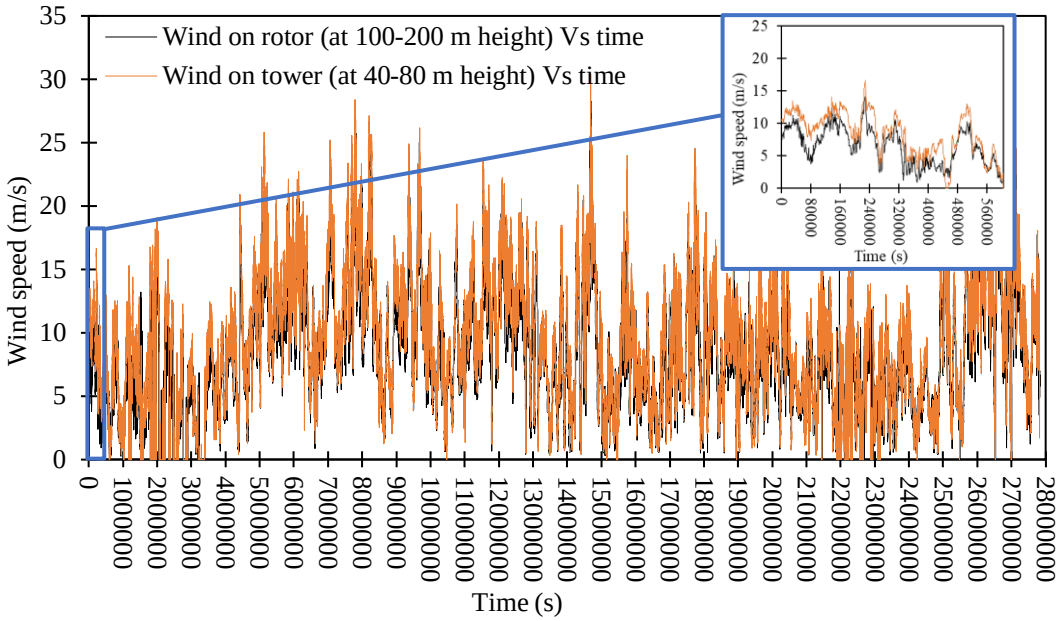

Figure 8.2: Wind speed versus time data for 1-year.

The statistics of wind data across eight different directions (north, northeast, east, southeast, south, southwest, west, and northwest directions) were determined to provide insight using Weibull distribution (Detailed in Appendix E2). In offshore environments, wind direction consistency is crucial for optimizing turbine performance and ensuring durability against repeated wind loads. From Table 8.1, based on the probability of mean wind speed occurrence, the highest probabilities are for the Southwest and West directions, both at 0.23. This suggests that these are the dominant wind directions at the site. In contrast, Northeast has the lowest probability of occurrence, which might indicate that wind rarely comes from this direction as also observed from Figure 8.3. This will serve to optimally orient the HAOWT to harness the most energy from these prevailing winds if installed at the location under consideration.

The Southwest direction has the highest scale parameter (11.92), which, combined with its high probability, suggests this direction not only occurs frequently but also often brings higher wind speeds. Northeast direction has the lowest scale parameter, indicating that winds from this direction are both infrequent and generally slower. With the values of shape parameter usually in the range of less than 2 or greater than 2, most values are greater than 2, indicating a general consistency in wind speed for all directions. However, Southwest direction has the highest shape parameter (2.465), suggesting that it has the most consistent wind speeds compared to other directions.

The Southwest direction has the highest mean wind speed of 10.59 m/s which corresponds to the rated wind speed of the HAOWT which is its design speed at which there is maximum power production, reinforcing its importance as a key direction for energy production at this site. Northeast has the lowest mean wind speed (Figure 8.3), which combined with its low probability of occurrence, indicates it contributes least to the potential energy production at the site.

Table 8.1: Weibull distribution for wind data

Direction	Probability of occurrence	Scale parameter	Shape parameter	Mean wind speed (m/s)
North	0.11	9.73	1.888	8.61
Northeast	0.06	6.66	2.319	5.9
East	0.08	6.66	2.232	5.9
Southeast	0.08	7.35	1.853	6.51
South	0.1	9.83	1.836	8.73
Southwest	0.23	11.92	2.465	10.59
West	0.23	11.54	2.441	10.25
Northwest	0.11	8.9	2.219	7.89

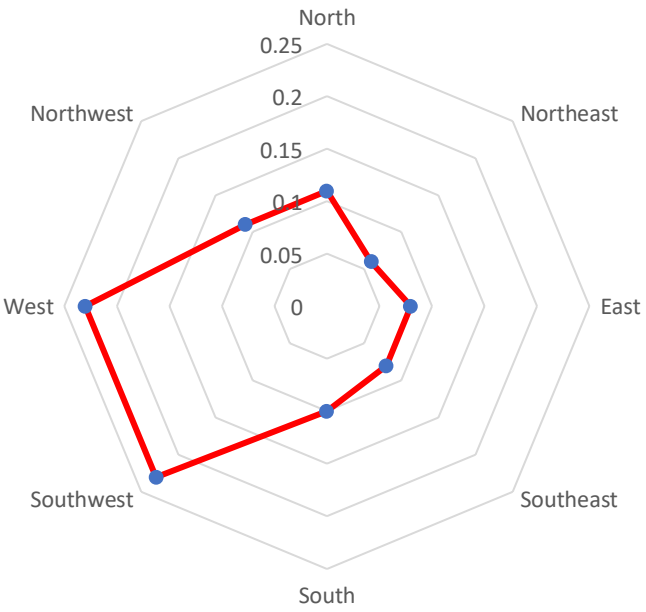

Figure 8.3: Wind data directional probability based on 1-year wind data.

8.1.3 Wave data

Figure 8.4 illustrates the wave height as a function of time, showcasing data derived from genuine average measurements obtained from the North Sea (Bonaduce et al. 2019; Jörges et al. 2021). The graphical representation underscores the variability and randomness of oceanic waves, a crucial parameter for offshore wind turbine considerations. The accompanying data shows wave height fluctuating between 0.09 and 8.4 m (Jörges et al. 2021), mirroring average recorded values from the north sea. According to IEC 61400-3 standard (British Standards Institution 2019c) recommendations, it is evident that the significant wave height, in conjunction with the wave peak spectral period, stands as the paramount wave parameters necessary for approximating wave-induced loads on offshore wind turbine support structures. It's imperative to understand that the depicted wave data was synthesized employing principles from the Pierson-Moskowitz spectrum (Appendix E3) for wave parameters modelling. This computational approach, married with actual measurement range, serves as an effective method to simulate real-world wave conditions.

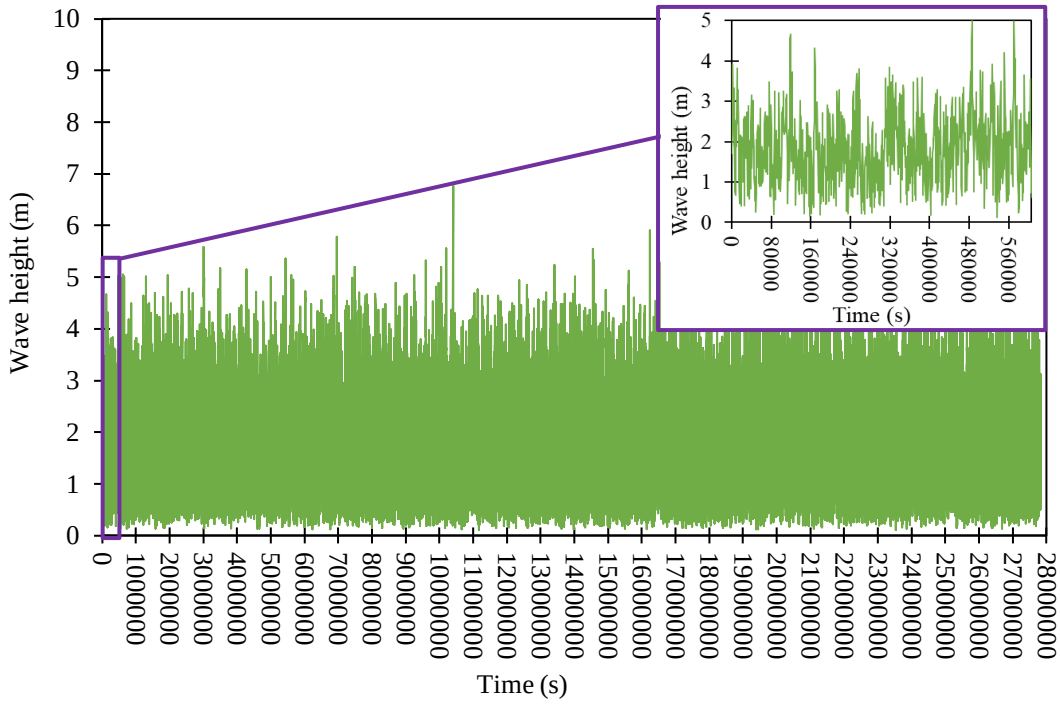

Figure 8.4: 1-year generated wave data based on recorded wave height in North Sea.

8.2 Corrosion-fatigue damage theory

To facilitate the prediction of the remaining life of the HAOWT support structure with respect to the corrosion-fatigue, a novel corrosion-fatigue damage theory was developed (Figure 8.5). Wind force (from wind speed versus time) and wave force (from wave period-wave height versus time data) are analysed and input into the analytical model (Section 4.3). The analytical model already exists for the HAOWT based on the beam theory, where cyclic bending stresses in tension and compression are obtained in the support structure (tower and monopile) zones as a function of time from which stress versus time history data is obtained. Also, from finite element modelling, stresses in the HAOWT support structure were predicted to determine the most critical zones under the influence of uniform corrosion.

For material characterisation, the endurance life approach was applied through the integration of a corrosion factor into the endurance limit equations in the corrosion characterisation study. Experimental tests were conducted on pre-corroded welded specimens of S355 structural steel, which is commonly employed in HAOWT support structures. Subsequently, we generated a novel S-N curve that encapsulated the effects of corrosion, stress concentration. Residual stresses are incorporated into S-N curves by adjusting for its influence on mean stress and stress range. This curve was further validated through fatigue testing methods under corrosive conditions.

In the subsequent analytical damage quantification, we employed rainflow cycle counting algorithms to dissect the stress-time history, thereby ascertaining both the range and frequency of stress cycles. This procedural step was instrumental in projecting the operational life cyclic stresses of the HAOWT. The application of Miner's rule for fatigue damage facilitated the computation of cumulative damage by summing the ratios of actual cycles to the cycles leading to failure, based on the newly established S-N curve.

Finally, the quantified corrosion-fatigue damage values were transferred to the analytical worksheets. These values served as key metrics for estimating the remaining operational life of the HAOWT support structures, factoring in their expected operational years. This comprehensive approach effectively bridges the gap between theoretical models and real-world conditions, providing a robust methodology for predicting corrosion-fatigue in offshore wind turbines.

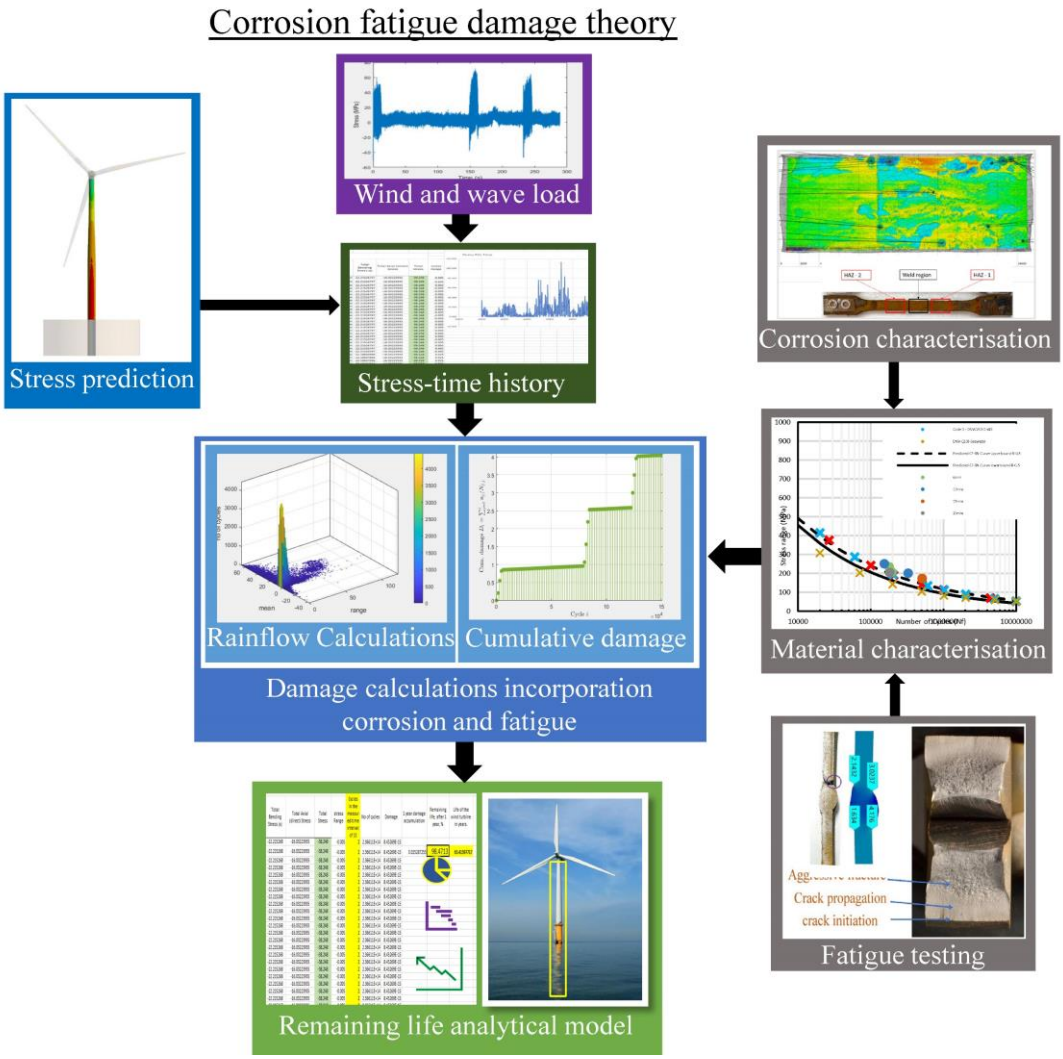

Figure 8.5: Corrosion-fatigue assessment damage theory.

8.3 Results and discussion of corrosion-fatigue remaining life prediction demonstration

8.3.1 Stress versus time history results

The stress versus time history obtained from the application of the wind and wave data (Section 8.1.2 and 8.1.3) is presented in Figure 8.6. This figure particularly illustrates the stress time history in the splash zone of the 15 Megawatt HAOWT subjected to the dynamic forces of wind and waves. The splash zone is the region of a marine structure that is intermittently submerged and exposed due to wave action, making it particularly vulnerable as observed from uniform corrosion effects (Chapter 4). The stress values fluctuate between approximately -35.5 MPa and 68 MPa. This considerable range

demonstrates the highly variable nature of the loads experienced in the splash zone, with both tension (positive stress) and compression (negative stress) observed. It is evident that the majority of the stress values lie in the positive range, indicating that tensile cyclic stresses dominate the splash zone's response under the combined effects of wind and wave loading.

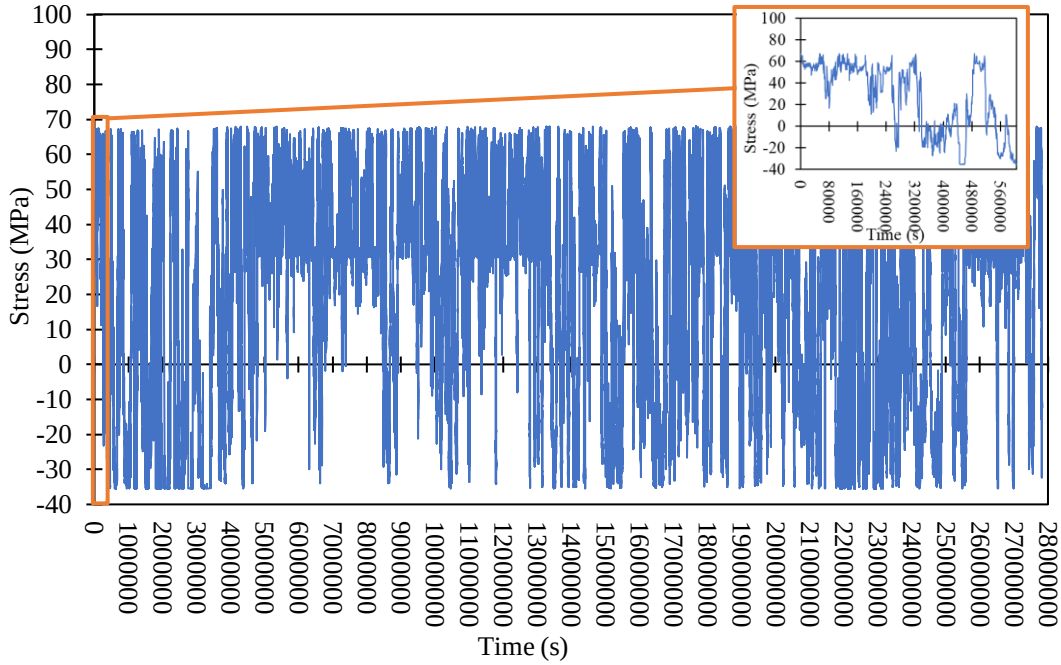

Figure 8.6: Stress versus time data from wind and wave load application to 15 megawatt HAOWT.

8.3.2 Rainflow counting

The Rainflow cycle counting approach (Amzallag et al. 1994) was utilised to determine the overall quantity of stress cycles associated with stress range bins, as well as to generate a stress range distribution using rainflow matrices. The Rainflow cycle counting algorithm is described in detail in Appendix E4. The outcomes obtained from the rainflow cycle counting method are depicted in Appendix E5, while the rainflow matrix histogram representing the stress cycle is displayed in Figure 8.7.

Most of the cycles are densely concentrated around the lower cycle ranges and closer to the zero cycle mean which indicates that most of the stress variations in the HAOWT are of low amplitude. Significant peak was observed for stress cycle range of around 35 Mpa and a cycle mean close to zero. This suggests that this specific stress cycle of approximately 35 Mpa occurred a significant number of times (405 times). Thus, this

cycle will play a vital role in fatigue damage and remaining life estimation. The data points become sparser as we move towards higher cycle mean. This suggests that high average stress levels (positive or negative) with varying ranges were less frequent in the observed period.

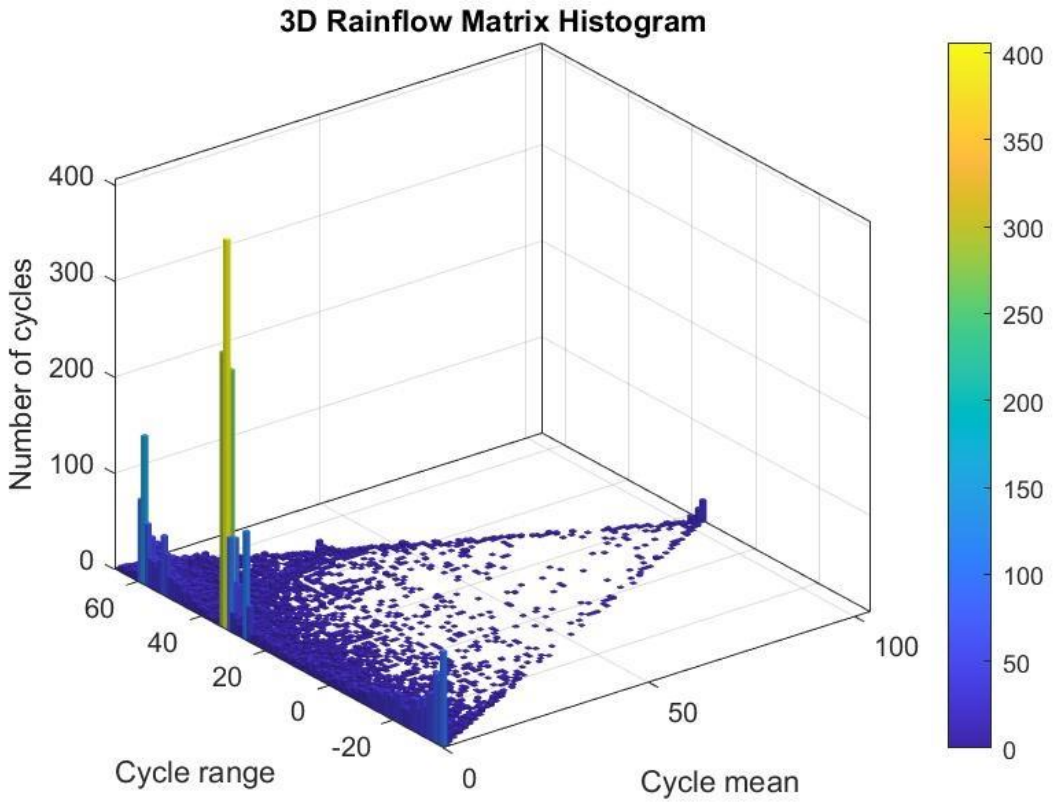

Figure 8.7: 3-D rainflow matrix diagram.

8.3.3 Corrosion-fatigue damage and remaining life prediction demonstration

The loads operating on HAOWT support structures are significantly influenced by the directionality of the wind and associated waves, as stated in the IEC 61400-3 standard (British Standards Institution 2019c). Hence, unidirectional assumptions regarding the movement of winds and waves were applied to calculated fatigue damage of the 15 megawatt HAOWT if placed in the North Sea. In the context of designing HAOWTs, the IEC standard suggests the use of a unidirectional assumption for ultimate limit state design. This recommendation, outlined in Appendix A of the IEC standard, is intended to address the most severe conditions that may arise. Multidirectional have not been

included as the directionality of wave data and yaw angles are not available. Regardless, the conditions for ultimate limit state were satisfied. As such, corrosion-fatigue damage and remaining life have been determined and the results presented considering unidirectional wind in Figure 8.8 for the HAOWT.

The steepness of the curve seems to change around 2,500 cycles. This suggests that the rate of cumulative damage accumulation accelerated from this point onwards. This could be due to an increase in the amplitude or frequency of cycles or a combination of both. In the rainflow matrix diagram, we observed that the most significant cycle counts were around lower amplitude cycles. This likely contributed to the earlier, gentler slope of the cumulative damage curve and that for steeper section, the S355 material may have encountered more damaging stress cycles, possibly the ones with higher amplitude or mean stresses.

The accumulated damage from Figure 8.8 is 3.459E-5 which provides a remaining life of 99.9965% after one year. This shows that even though there has been some accumulation of damage, a substantial portion of the structures fatigue life remains. The splash zone is particularly susceptible to corrosion-fatigue due to the simultaneous effects of mechanical loading (from waves, currents, etc.) and corrosive elements (saltwater). The consistent accumulation of damage even at lower cycle counts will have been influenced also by the corrosive environment, which reduces the structures fatigue resistance. This demonstration is based on a 1-year wind and wave data with the corrosion fatigue model based on the corrosion fatigue of one year corroded HAOWT support material. Thus, considering that corrosion will worsen with time with its non-linear nature, corrosion-fatigue damage and remaining life will increase with time. Consideration of assessment of specimen corroded for up to 20 years (design life of HAOWT) will be considered as future work.

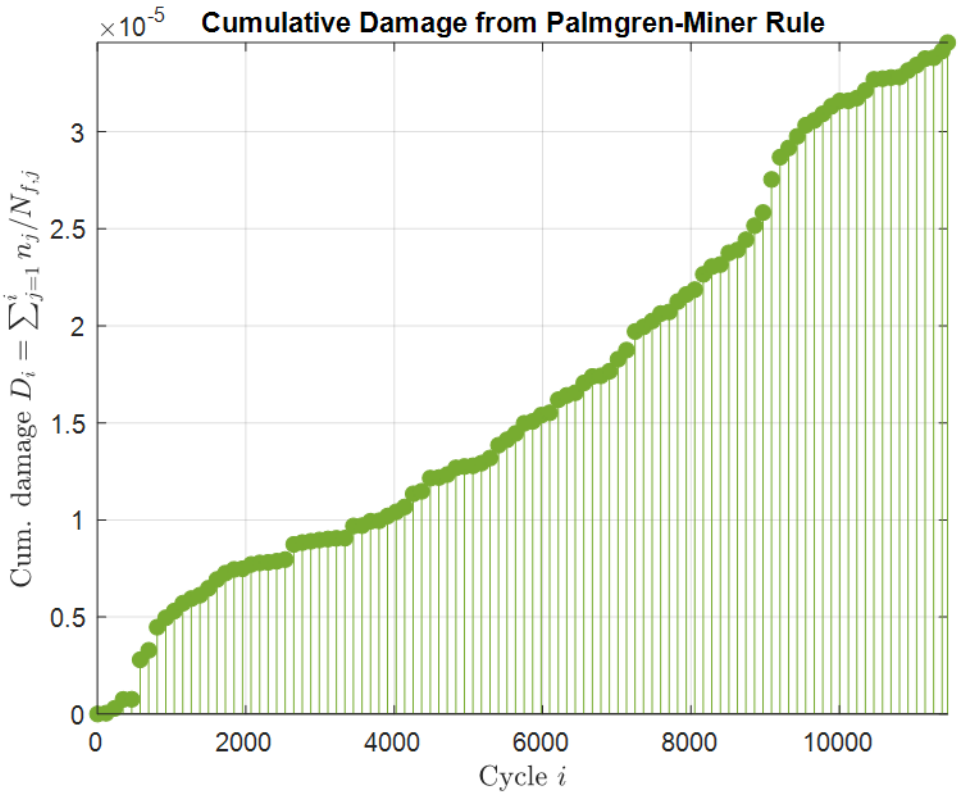

Figure 8.8: Estimated corrosion-fatigue damage and remaining life based on 1-year wind and wave data in 15 MW HAOWT.

8.3.4 Conclusions

The Marine Data Exchange has provided wind speed and direction data for the Westermost Rough offshore wind site located in the North Sea, a region known for its dense concentration of offshore wind turbines. This data is used in a testbed scenario for a 15 Megawatt HAOWT, aiming to determine its corrosion fatigue damage and estimate its remaining life. The wind patterns highlight the Southwest and West directions as dominant, both in terms of frequency and intensity, while the Northeast winds are rare and generally slower. The Southwest direction's wind speed matches the HAOWT's rated wind speed, indicating its significance for energy production. Furthermore, the oceanic waves exhibit a wide range of heights, with the significant wave height and wave peak spectral period being critical parameters for assessing wave-induced loads on offshore wind turbine support structures.

In evaluating the corrosion-fatigue of the HAOWT support structure, the splash zone, intermittently submerged due to wave action, is identified as especially vulnerable. Stress values in this zone are varied, with tensile cyclic stresses being predominant. The stress cycle data showcases the bulk of the stress variations being of low amplitude, yet a notable peak at a stress cycle range of around 35 MPa is observed, underscoring its importance in fatigue damage assessment. The cumulative damage, reveals a minor damage accumulation, translating to a vast remaining life of 99.9965% after a year, based on the data which has been recorded every 10 minutes. However, the corrosion-fatigue, influenced by both mechanical loads and corrosive factors, will exacerbate over time, given the non-linear nature of corrosion as well as the frequency of the wind and wave data. Industrial assessments should consider examining corrosion effects over the typical 20-year design life of HAOWTs using wind and wave data obtained at higher frequency.

Chapter 9

Summary of findings

9.1 Summary of chapter findings

This study focused on the prediction and assessment of corrosion-fatigue in HAOWT support structures. All the set objectives of the study have been achieved with novelty in all parts, and the conclusions based on each set-out object are presented subsequently.

Review of challenges and development of a digital twins framework for fatigue assessment in HAOWTs

- The wind energy sector faces a myriad of challenges as it scales up. These challenges include aerodynamic and hydrodynamic effects, complex soil-structure interactions, and harsh environmental conditions in deeper waters. These new operational conditions amplify corrosion-fatigue issues in HAOWTs, making the early implementation of mitigating techniques such as cathodic protection and vibration reduction crucial.
- Another significant concern is the role of pitting, which gives rise to crack initiation, thereby reducing the overall fatigue life. Current fatigue S-N curves need to incorporate the influence of pit size and morphology, especially in the weldments of offshore wind turbine support structures. On the machine learning front, artificial neural networks, particularly those employing back-propagation algorithms, have shown efficacy in quickly predicting the environmental conditions affecting HAOWTs. However, their performance is highly dependent on the data quality used for training. This makes the role of fatigue simulations based on FEA crucial, as they can supply high-quality data for training these networks, thereby reducing computational costs.
- The developed framework for corrosion-fatigue assessment highlighted the emerging role of digital twin technologies in condition-based and predictive maintenance. The concept is promising and requires more practical applications, potentially in collaboration with industry stakeholders. A comprehensive digital twin would ideally integrate elements such as FEA,

material characterisation, artificial neural networks, data analytics, and Internet of Things technologies with smart sensors to comprehensively tackle the multifaceted challenge of corrosion-fatigue in offshore wind turbines.

Stress analysis from uniform corrosion effects

- As more high-capacity HAOWTs are expected to be built, the rotor diameter and hub height will increase, resulting in an overturning moment in the monopile. It was found that the overturning moment counterbalances the moments generated due to wind, leading to a reduction in the induced tensile stresses. In addition, at the peak production of the analysed HAOWT design, a thrust force of 2.563 MN can be experienced. However, when the HOWTs are in a parked condition, the dominant forces are due to the wind and wave forces acting on the tower and monopile.
- The overall weight of the entire HAOWT induced compressive stresses, which were beneficial to neutralise some of the tensile stresses generated from the wind and wave loads. However, the compressive stresses increased, but their magnitude remained less than one-third of the yield stress of the material (i.e. S355); hence, there was no risk of permanent deformation. The predicted stresses for the as-designed HAOWT structure showed that the highest tensile stresses were approximately 78 MPa at the submerged zone, which is an indication that there might be risks of fatigue crack initiations in the welds.
- The presented analytical calculations showed a close correlation with the FEA results for a range of wind velocities and material losses due to corrosion. This shows that the two methods are in agreement with their predictions of the stress field, and they can be used for further fatigue analyses considering the transient nature of the stress due to the constantly changing wind velocity over time, as well as the corrosion impact on the material. The analytical model could be used for real-time fatigue damage calculations to estimate the remaining life of HAOWT structures due to its capability to conduct fast calculations.
- This research demonstrates a capability for the prediction of nominal stresses, which may be paired with S-N curves that take into consideration the size and morphology of the corrosion pits for complete and precise characterisation of

fatigue. In addition to the conducted stress analyses under uniform corrosion conditions, modal FEA was performed to predict the natural frequency of the HAOWT. It was demonstrated that the natural frequency in the bending mode was within the standard requirements.

Soil structure interaction

- From the soil-structure interaction study, it was observed that as support structure thickness reduced, deformation increased with the maximum tower top deflection value of 2.8 m observed in a silty sand-lean clay soil located in East China Sea. In addition, the deformations in all models in the foundation were within the allowable displacement of 0.1 m specified in the design guidance. All three modelled soil profiles representing soil conditions from the North, Irish, and East China Sees, as well as a model representing rigid soil, resulted in natural frequencies in the range of 0.15 - 0.17 Hz, which is within the requirements of the design codes to be in the range of 0.1 - 0.38 Hz. The material loss due to corrosion also contributed to a reduction in the stiffness of the tower, but the predicted frequency values were within the band of the recommended frequencies.
- The highest stresses in the vertical direction were compressive and occurred at the splash region of the transition piece in all models, where the shell wall thickness and bending stiffness reduction began. A maximum percentage difference of 9% was observed in both tension and compression in the support structure by comparing the three soil models as well as the rigid soil model. It was found that the soil profile of medium to dense sand located in the North Sea is suitable for the installation of this 15 Megawatt large-diameter HAOWT, meeting the design code requirements for proof analyses, deformations at the soil, and natural frequency.

S-N curve prediction from corrosion-based fatigue methodology and testing

- The proposed methodology was applied to a welded S355J2+N steel where a predicted S-N curve at stress ratio R = 0.5 for a corroded surface was found to

be in close correlation with the fatigue-tested S355J2+N butt welded steel tested in the laboratory. At R = 0.1, the performance of the predictive model is commendable, as it closely aligns with the experimental findings, with a minor deviation of only 2.8% under similar salt spray chamber corrosive conditions. At R = 0.5, a deviation of 15.1% was observed.

- The corroded surface has been characterised where critical defects have been observed in the HAZ to show the presence of deep pits, which have corrosion factors between 0.222 – 0.307. The characterisation of a corroded surface consisted of measuring the pit diameter, pit depth, and surface roughness. The simplicity of the adopted characterisation method enables its pragmatic implementation for the inspection of large HAOWT in practice. The capability of the model to consider the mean stress effect provides the advantage of conducting more realistic fatigue assessments for a transient stress field induced by cyclic wind and wave loads.

Material performance and fatigue testing

- The SAW process was meticulously carried out on S355G10+M sheets of different thicknesses, and the use of a double V-groove and multipass approach allowed for maximum weld quality that met the standards required for offshore wind turbine monopiles. The weld material and HAZ were distinguished by boundaries of heat dissipation caused by the material's melting and subsequent solidification. The hardness experiments on S355G10+M steel specimens revealed that with increased thicknesses, hardness values will be consistent. In the hardness plots, the transition region between the HAZ and base metal displayed a slightly reduced hardness that was still greater than the hardness of the base metal. This region was identified as a potential weak point owing to probable microstructural changes and was the region where the material failed under cyclic loading.
- The static tensile test specimens were fractured in the base metal, indicating that the welded section was constructed from a stronger weld material. It was found that the welded specimens had lower yield strengths and higher ultimate strengths than the plain specimens. Thus, because the plain specimens began

to deform plastically at higher stress levels and withstood greater stress levels before ultimately breaking, they were more ductile.

- Distortion measurements revealed an increasing trend of axial misalignment and angular distortion along the plate. The direction along the plate had a greater influence on these characteristics than the plate thickness. Secondary bending stresses due to misalignment and angular distortion undoubtedly influenced the load distribution and fatigue strength of the S355G10+M specimens. The evaluation of residual stresses in S355G10+M steel showed large tensile stresses along and across the weld, resulting in a negative contribution to the fatigue strength. The analysis showed that there was a direct link between the thickness of the material and the amount of residual stress owing to the different heat inputs and cooling rates.
- Stress concentrations at the weld toe initiated cracks, indicating their significant impact on fatigue life. Even though the stress concentrations can be mitigated after welding, the development of corrosion pits in the HAZ could be a source of local stress and crack initiation. The findings suggest that the fatigue life of the butt-welded S355G10+M specimens is less affected by the thickness and more influenced by the stress concentration and tensile residual stresses. Despite the axial misalignment and angular distortion of the specimens, the SAW of S355G10+M showed a fatigue strength greater than the fatigue strength in codes used for the design of HAOWT. This indicates that the investigated material and SAW process are suitable for the manufacture of welded marine structures, including HAOWT support structures (e.g. monopiles).
- The machining for fatigue testing method showed that cyclic stresses could be induced by milling cutting forces to mimic a real application of offshore wind turbine monopile structures. The key advantages are that this method can be quickly set up in the industry, enabling fast fatigue testing and leading to the reduction of lead times for product and process development. Another advantage is that the method can mimic different in-service loads by changing the cutting tools, machining operations, cutting parameters, and fixture design. The utilisation of existing old machine tools and worn cutting tools is also sustainable.

Corrosion-fatigue damage prediction

- The rotor-nacelle-assembly, which encompasses a broad area exposed to wind due to blade and its height, predominantly experiences elevated wind speeds. A noteworthy observation is the wind speed, which peaks at 30.5 m/s. Additionally, there's a methodical estimation of wind loads, which encompasses both the rotor and the supporting tower.
- Analysing the site, the Southwest and West directions emerge as dominant wind orientations, both showcasing the highest probability. Conversely, winds from the Northeast direction are a rarity. Southwest winds are of particular interest as they are not only frequent but also clock in higher speeds.
- The significance of the wave height combined with the wave peak spectral period cannot be overstated, especially when deliberating offshore wind turbine considerations. It’s pivotal to acknowledge that the wave data is an outcome of the Pierson-Moskowitz spectrum application.
- The splash zone is characterised by stress values between -35.5 MPa and 68 MPa. The dominance of tensile cyclic stresses in the splash zone’s response was observed. Most stress variations in the HAOWT are predominantly of a lower amplitude. However, there's a pronounced peak observed for a stress cycle range of approximately 35 MPa. It's noteworthy that instances of high average stress levels, with a diverse range, were infrequent.
- To predict the remaining operational life of the HAOWT, a novel corrosion-fatigue damage theory has been developed. This model critically hinges on the data derived from wind and wave forces. In applying this corrosion-fatigue model, after a year, the accumulated damage stands at 3.459E-5, translating to a promising remaining life of 99.9965%. The damage is predicted based on wind and wave data acquisition at 10 minutes interval, which does not capture the full history of the cyclic loads and counts. The splash zone's susceptibility to corrosion-fatigue, owed to the synergistic effects of mechanical loads and corrosive elements, is evident. The consistency in damage accumulation, even at lower cycle counts, is notably influenced by the corrosive environment.

Chapter 10

Conclusions and future work

10.1 Conclusions

This research focused on the development of methodologies for evaluating corrosion-fatigue in large-diameter monopile-supported HAOWT to enable a novel fatigue damage and remaining life prediction pathway and the conclusions from study objectives are provided below:

- The digital twins framework for corrosion fatigue in HAOWTs combines FEA, material characterisation, AI, data analytics, and IoT with smart sensors to improve predictive maintenance and condition-based strategies and showed a promising strategy.
- When considering uniform corrosion, the splash zone region where the shell wall thickness and bending stiffness reduction began is susceptible to very high stresses. Analytical calculations closely match FEA results, validating their use for fatigue damage estimation.
- From the soil-structure interaction study, all HAOWT models considering soil met design code requirements for natural frequency and allowable displacement emphasising the importance of soil considerations in wind turbine modelling.
- The developed corrosion-based fatigue methodology for welded S355 structural steel showed close correlation with experimental findings, the predicted S-N curve showed good performance with a minor deviation of 2.8%.
- The SAW process on S355G10+M sheets demonstrated high weld quality and fatigue strength, making it suitable for offshore wind turbine monopile structures, with fatigue life influenced by stress concentration, distortions, and tensile residual stresses than material thickness.
- The developed novel corrosion-fatigue damage model effectively predicted the corrosion fatigue damage and remaining life of HAOWT considering in-service parameters.

10.2 Contribution to knowledge

Based on the conducted research, novel contribution to knowledge are detailed below:

- Digital Twins Framework: The development of a digital twins framework that integrates Finite Element Analysis (FEA), material characterization, machine learning, data analytics, and Internet of Things (IoT) with smart sensors. This framework has demonstrated potential in enhancing predictive maintenance and condition-based strategies for HAOWTs.
- Uniform Corrosion Analysis: The study highlighted the splash zone region as a critical area susceptible to high stresses due to uniform corrosion, with analytical calculations closely matching FEA results. This validates the use of these methods for accurate fatigue damage estimation.
- Corrosion-Based Fatigue Methodology: A corrosion-based fatigue methodology was developed for welded S355 structural steel, which showed a close correlation with experimental findings. The predicted S-N curve demonstrated good performance.
- Corrosion-Fatigue Damage Model: The novel corrosion-fatigue damage model effectively predicted corrosion fatigue damage and the remaining life of HAOWTs by considering in-service parameters, thus providing a reliable tool for lifecycle assessment and maintenance planning.

10.3 Future work

Based on the conducted research, various opportunities for future work have been identified based on the experimental works and the modelling works as affects HAOWTs. They are presented below:

- Despite the introduction of advanced steel grades in offshore wind turbine construction, there is a notable gap in experimental research that quantifies the effects of corrosion-fatigue, including pitting, crack initiation, and crack propagation. High-quality and reliable data in these areas would substantially improve the fidelity of computational models, leading to better fatigue life predictions under corrosive conditions.

- Computational analyses that consider the dynamic impacts of seawater, wind, and soil on HAOWTs can offer more realistic load cases for fatigue analyses. Technologies like computational fluid dynamics can provide crucial insights into wave loading effects and the varying stiffness of different soil types. Incorporating real-time monitoring data from operating wind turbines into standard prognostic systems could significantly enhance operation and maintenance protocols for HAOWTs
- The findings of the uniform corrosion study will be useful in future HAOWT design, as thickness loss due to corrosion and the resulting stress values could aid design engineers in specifying adequate tower and monopile thicknesses, particularly in the most corrosion-prone zones, as a means of providing a safe, stable, and cost-effective design. FEA could be conducted to predict the risk of failure due to buckling under compressive stresses as a future perspective.
- This corrosion-based fatigue model incorporates pits, stress concentrations, and surface roughness as sources of fatigue crack initiation and propagation. However, it does not delve into inherent residual stresses and post-welding treatment effects that could be improved. This methodology is aimed to be applied to the assessment of the remaining life of other offshore assets, where the remaining life can be determined by the history of the loads and the corrosion topology of the material surface of the structure.
- In future work on the machining of the testing method, full control of the cutting forces should be implemented owing to their variations. Another area for exploration is the size of the components that can be tested, where the cutting forces should be adequate to induce the required stress field while minimising excessive vibrations and chatter.
- Given that the current model demonstrates corrosion-fatigue damage based on 1-year material corrosion data, future studies could project the effects of corrosion-fatigue over the entire design life (e.g., 20 years) of a HAOWT by using wind and wave data obtained at higher data acquisition rates needed at industrial scale.

References

ABFAD, 2020. Showing the extent of monopile corrosion - Advanced Engineering Technology Systems. [online]. Available at: <https://www.abfad.co.uk/wp-content/uploads/2015/06/Monopile_corroded-400x284.jpg [Accessed 19 August 2022].

Achmus, M., Kuo, Y.S., Abdel-Rahman, K., 2009. Behavior of monopile foundations under cyclic lateral load [online]. *Computers and Geotechnics*, 36(5), pp.725–735. Available at: http://dx.doi.org/10.1016/j.compgeo.2008.12.003.

Adamczuk, P.C., Machado, I.G., Mazzaferro, J.A.E., 2017. Methodology for predicting the angular distortion in multi-pass butt-joint welding. *Journal of Materials Processing Technology*, 240, pp.305–313. 10.1016/J.JMATPROTEC.2016.10.006.

Adedipe, O. et al., 2017. Corrosion fatigue crack growth mechanisms in offshore monopile steel weldments. *Fatigue and Fracture of Engineering Materials and Structures*, 40(11), pp.1868–1881. 10.1111/ffe.12606.

Adedipe, O., Brennan, F., Kolios, A., 2015. Corrosion fatigue load frequency sensitivity analysis. *Marine Structures*, 42, pp.115–136. 10.1016/j.marstruc.2015.03.005.

Adedipe, O., Brennan, F., Kolios, A., 2016. Review of corrosion fatigue in offshore structures: Present status and challenges in the offshore wind sector [online]. *Renewable and Sustainable Energy Reviews*, 61, pp.141–154. Available at: http://dx.doi.org/10.1016/j.rser.2016.02.017.

Adey, R., Peratta, C., Baynham, J., 2020. Corrosion Data Management Using 3D Visualisation and a Digital Twin. In: *NACE International Corrosion Conference Proceedings - NACE International*. pp. 1–14.

Ahmed, S.S., Hawlader, B., 2016. Numerical Analysis of Large-Diameter Monopiles in Dense Sand Supporting Offshore Wind Turbines. *International Journal of Geomechanics*, 16(5), p.4016018. 10.1061/(asce)gm.1943-5622.0000633.

Akid, R., Richardson, T., 2010. Corrosion Fatigue. In: *Shreir's Corrosion*. , 2010, pp. 928–953.

American Petroleum Institute, 2007. API 2A- WSD: Recommended Practice for Planning , Designing and Constructing Fixed Offshore Platforms — Working Stress Design. *Api Recommended Practice*, 24-WSD(December 2000), p.242.

American Society for Testing Materials, 2022. *ASTM E8/E8M-22: Standard Test Methods for Tension Testing of Metallic Materials* [online]. Available at: https://www.astm.org/e0008_e0008m-22.html [Accessed 17 March 2023].

Amzallag, C. et al., 1994. Standardization of the rainflow counting method for fatigue analysis. *International Journal of Fatigue*, 16(4), pp.287–293. 10.1016/0142-1123(94)90343-3.

Anagnostou, E. et al., 2010. Science-Based Multiscale Modeling of Fatigue Damage for Structural Prognosis. In: *51st AIAA/ASME/ASCE/AHS/ASC Structures, Structural Dynamics, and Materials Conference 18th AIAA/ASME/AHS Adaptive Structures Conference 12th*. p. 2971.

Anandavijayan, S. et al., 2021. Material pre-straining effects on fatigue behaviour of S355 structural steel. *Journal of Constructional Steel Research*, 183. 10.1016/j.jcsr.2021.106707.

Ancona, D., Jim, M., 2001. Wind Turbine - Materials and Manufacturing Fact Sheet. *Princeton Energy Resources International, LLC*, 19.

ANSYS Inc, 2004. ANSYS Release 9.0 Documentation. SAS IP.

Arany, L. et al., 2017. Design of monopiles for offshore wind turbines in 10 steps. *Soil Dynamics and Earthquake Engineering*, 92, pp.126–152. 10.1016/j.soildyn.2016.09.024.

Arcos Jiménez, A., Gómez Muñoz, C., García Márquez, F., 2017. Machine Learning for Wind Turbine Blades Maintenance Management [online]. *Energies*, 11(1), p.13. Available at: http://www.mdpi.com/1996-1073/11/1/13.

Arshad, M., O'Kelly, B.C., 2016. Analysis and Design of Monopile Foundations for Offshore Wind-Turbine Structures [online]. *Marine Georesources and Geotechnology*, 34(6), pp.503–525. Available at: https://doi.org/10.1080/1064119X.2015.1033070.

Ata, R., Kocyigit, Y., 2010. An adaptive neuro-fuzzy inference system approach for prediction of tip speed ratio in wind turbines [online]. *Expert Systems with Applications*, 37(7), pp.5454–5460. Available at: http://dx.doi.org/10.1016/j.eswa.2010.02.068.

Atkinson, J.D., Chen, Z., 1993. Effect of temperature on corrosion fatigue crack propagation in reactor pressure vessel steels. , pp.29–34.

Augustesen, A.H. et al., 2009. Numerical modelling of large-diameter steel piles at Horns Rev. *Proceedings of the 12th International Conference on Civil, Structural and Environmental Engineering Computing*. 10.4203/ccp.91.239.

Bang, H.J., Kim, H. Il, Lee, K.S., 2012. Measurement of strain and bending deflection of a wind turbine tower using arrayed FBG sensors. *International Journal of Precision Engineering and Manufacturing*, 13(12), pp.2121–2126. 10.1007/s12541-012-0281-2.

Bannantine, J., Comer, J., Handrock, J., 1990. Fundamentals of metal fatigue analysis((Book)). *Research supported by the University of Illinois. Englewood Cliffs, NJ, Prentice Hall, 1990, 286*.

Becker, T.H., Kumar, P., Ramamurty, U., 2021. Fracture and fatigue in additively manufactured metals. *Acta Materialia*, 219. 10.1016/j.actamat.2021.117240.

Bergara, A. et al., 2017. Fatigue crack propagation in complex stress fields: Experiments and numerical simulations using the Extended Finite Element Method (XFEM) [online]. *International Journal of Fatigue*, 103, pp.112–121. Available at: http://dx.doi.org/10.1016/j.ijfatigue.2017.05.026.

Bisoi, S., Haldar, S., 2014. Dynamic analysis of offshore wind turbine in clay considering soil-monopile-tower interaction [online]. *Soil Dynamics and Earthquake Engineering*, 63, pp.19–35. Available at: http://dx.doi.org/10.1016/j.soildyn.2014.03.006.

Biswal, R., Al Mamun, A., Mehmanparast, A., 2021. On the performance of monopile weldments under service loading conditions and fatigue damage prediction [online]. *Fatigue & Fracture of Engineering Materials & Structures*, 44(6), pp.1469–1483. Available at: https://doi.org/10.1111/ffe.13442.

Bonaduce, A. et al., 2019. Wave Climate Change in the North Sea and Baltic Sea [online]. *Journal of Marine Science and Engineering*, 7(6). Available at: https://www.mdpi.com/2077-1312/7/6/166.

Braun, M., 2022. Statistical analysis of sub-zero temperature effects on fatigue strength of welded joints. *Welding in the World*, 66(1), pp.159–172. 10.1007/s40194-021-01207-y.

British Standards Institution, 2019a. *10025-2: 2019: Hot rolled products of structural steels. Part 2-Technical delivery conditions for non-alloy structural steels* [online]. Available at: https://bsol.bsigroup.com/Bibliographic/BibliographicInfoData/000000000030239477# [Accessed 17 March 2023].

British Standards Institution, 2014a. *BS 7608:2014 Guide to fatigue design and assessment of steel products (+A1:2015)*. London.

British Standards Institution, 2001. *BS EN 1011-2:2001: Welding. Recommendations for welding of metallic materials. Arc welding of ferritic steels* [online]. Available at: https://bsol.bsigroup.com/Bibliographic/BibliographicInfoData/000000000030109226 [Accessed 3 October 2023].

British Standards Institution, 2005a. BS EN 1991-1-4:2005+A1:2010: Eurocode 1. Actions on structures. General actions. Wind actions [online]. Available at: https://bsol.bsigroup.com/ [Accessed 13 January 2022].

British Standards Institution, 2005b. *BS EN 1993-1-9:2005 Eurocode 3: Design of steel structures. Fatigue*. London.

British Standards Institution, 2019b. BS EN IEC 61400-1:2019: Wind energy generation systems. Design requirements [online]. Available at: https://bsol.bsigroup.com/ [Accessed 25 February 2022].

British Standards Institution, 2019c. BS EN IEC 61400-3-1-2019+A11-2020: Wind energy generation systems. Design requirements for fixed offshore wind turbines [online]. Available at: https://bsol.bsigroup.com/ [Accessed 2 March 2022].

British Standards Institution, 2023. *BS EN ISO 5817:2023: Welding. Fusion-welded joints in steel, nickel, titanium and their alloys (beam welding excluded). Quality levels for imperfections* [online]. Available at: https://bsol.bsigroup.com/Bibliographic/BibliographicInfoData/000000000030408358 [Accessed 17 May 2023].

British Standards Institution, 2014b. *BS EN ISO 6506-1:2014: Metallic materials. Brinell hardness test. Test method* [online]. Available at: https://bsol.bsigroup.com/Bibliographic/BibliographicInfoData/000000000030263771 [Accessed 11 April 2023].

British Standards Institution, 2015. *BS EN ISO 23277:2015: Non-destructive testing of welds. Penetrant testing. Acceptance levels* [online]. Available at: https://bsol.bsigroup.com/Bibliographic/BibliographicInfoData/000000000030272524 [Accessed 20 March 2023].

Brockenbrough, R.L., Merritt, F.S., 1999. *Structural Steel Designer's Handbook*. McGrawHill.

Čern, I., Sís, J., 2016. Evaluation of fatigue strength of different thickness laser welded s355 steel sheets considering microstructure, surface conditions and residual stresses. In: *Key Engineering Materials*. Trans Tech Publications Ltd, pp. 82–85. 10.4028/www.scientific.net/KEM.713.82.

Chen, S. et al., 2018. Structural behavior of UHPC filled steel tube columns under axial loading [online]. *Thin-Walled Structures*, 130(June), pp.550–563. Available at: https://doi.org/10.1016/j.tws.2018.06.016.

Corigliano, P. et al., 2017. Fatigue analysis of marine welded joints by means of DIC and IR images during static and fatigue tests. *Engineering Fracture Mechanics*, 183, pp.26–38. 10.1016/j.engfracmech.2017.06.012.

Corigliano, P. et al., 2020. Fatigue assessment of a marine structural steel and comparison with Thermographic Method and Static Thermographic Method. *Fatigue and Fracture of Engineering Materials and Structures*, 43(4), pp.734–743. 10.1111/ffe.13158.

Creaform Inc., 2021. VXelements [online]. Available at: https://www.creaform3d.com/en/vxelements-viewer [Accessed 15 September 2023].

Cui, C. et al., 2019. Experimental study and 3D cellular automata simulation of corrosion pits on Q345 steel surface under salt-spray environment [online]. *Corrosion Science*, 154, pp.80–89. Available at: https://doi.org/10.1016/j.corsci.2019.03.011.

Daavari, M., Sadough Vanini, S.A., 2015. Corrosion fatigue enhancement of welded steel pipes by ultrasonic impact treatment. *Materials Letters*, 139, pp.462–466. 10.1016/j.matlet.2014.10.141.

Dantas, R. et al., 2021. Evaluation of multiaxial high-cycle fatigue criteria under proportional loading for S355 steel. *Engineering Failure Analysis*, 120. 10.1016/j.engfailanal.2020.105037.

Deng, D., 2009. FEM prediction of welding residual stress and distortion in carbon steel considering phase transformation effects. *Materials and Design*, 30(2), pp.359–366. 10.1016/j.matdes.2008.04.052.

Depina, I. et al., 2015. Behavior of cyclically loaded monopile foundations for offshore wind turbines in heterogeneous sands [online]. *Computers and Geotechnics*, 65, pp.266–277. Available at: http://dx.doi.org/10.1016/j.compgeo.2014.12.015.

Design, C., 1999. Handbook of structural steel connection design and details.

Devriendt, C. et al., 2014. Structural health monitoring of offshore wind turbines using automated operational modal analysis. *Structural Health Monitoring*, 13(6), pp.644–659. 10.1177/1475921714556568.

Dhillon, B.S., 2002. *Engineering maintenance: A modern approach*.

DNV, G., 2016a. *DNVGL-RP-0416: Corrosion protection for wind turbines* [online]. Available at: https://www.dnv.com/energy/standards-guidelines/dnv-rp-0416-corrosion-protection-for-wind-turbines.html.

DNV, G., 2018. DNVGL-ST-0126: Support structures for wind turbines. *DNVGL - Standard*, (April 2016), p.182 pp.

DNV, G., 2009. *DNV-OS-B101: offshore standard, metallic materials*.

DNV, G., 2014. DNV-OS-J101: Design of Offshore Wind Turbine Structures. *May*, (May), pp.212–214.

DNV, G., 2010. DNV-RP-C205: Environmental conditions and environmental loads. *Det Norske Veritas: Oslo, Norway*, (October), pp.9–123.

DNV, G., 2016b. Fatigue design of offshore steel structures. *Recommended Practice DNVGL-RP-C203*, 20(June), p.2016.

DNV, G., Risø, 2002. Guidelines for Design of Wind Turbines 2nd Edition [online]. *Copenhagen and Wind Energy Department, Risø National Laboratory*, pp.115–128. Available at: http://scholar.google.com/scholar?hl=en&btnG=Search&q=intitle:Guidelines+for+Design+of+Wind+Turbines#3.

DNV, G.L., 2015. DNVGL-CG-0129: Fatigue Assessment of Ship Structures. *no. October*, pp.1–129.

Dong, W., Moan, T., Gao, Z., 2012. Fatigue reliability analysis of the jacket support structure for offshore wind turbine considering the effect of corrosion and

inspection [online]. *Reliability Engineering and System Safety*, 106, pp.11–27. Available at: http://dx.doi.org/10.1016/j.ress.2012.06.011.

Durodola, J.F. et al., 2017. A pattern recognition artificial neural network method for random fatigue loading life prediction [online]. *International Journal of Fatigue*, 99, pp.55–67. Available at: http://dx.doi.org/10.1016/j.ijfatigue.2017.02.003.

Ebara, R., 2006. The present situation and future problems in ultrasonic fatigue testing – Mainly reviewed on environmental effects and materials' screening. *International Journal of Fatigue*, 28(11), pp.1465–1470. 10.1016/J.IJFATIGUE.2005.04.019.

Ekoyuncu, J. et al., 2019. Conceptual framework of a digital twin to evaluate the degradation status of complex engineering systems. *Procedia CIRP*, 86, pp.61–67. 10.1016/j.procir.2020.01.043.

Errandonea, I., Beltrán, S., Arrizabalaga, S., 2020. Digital Twin for maintenance: A literature review [online]. *Computers in Industry*, 123, p.103316. Available at: https://doi.org/10.1016/j.compind.2020.103316.

Fatoba, O., 2015. *Corrosion Fatigue Damage in A Linepipe Steel*. University of Manchester.

Fatoba, O.O. et al., 2018. Simulation of stress-assisted localised corrosion using a cellular automaton finite element approach [online]. *Corrosion Science*, 137, pp.83–97. Available at: https://doi.org/10.1016/j.corsci.2018.03.029.

Faulstich, S., Hahn, B., Tavner, P.J., 2011. Wind turbine downtime and its importance for offshore deployment [online]. *Wind Energy*, 14(3), pp.327–337. Available at: https://doi.org/10.1002/we.421.

Feldkamp, L.A., Davis, L.C., Kress, J.W., 1984. Practical cone-beam algorithm [online]. *Journal of the Optical Society of America A*, 1(6), pp.612–619. Available at: https://opg.optica.org/josaa/abstract.cfm?URI=josaa-1-6-612.

Fereidooni, B., Morovvati, M.R., Sadough-Vanini, S.A., 2018. Influence of severe plastic deformation on fatigue life applied by ultrasonic peening in welded pipe 316 Stainless Steel joints in corrosive environment. *Ultrasonics*, 88, pp.137–147. 10.1016/j.ultras.2018.03.012.

Ferreira, T., Rasband, W., 2018. ImageJ User Guide [online]. Available at: https://imagej.nih.gov/ij/docs/guide/index.html [Accessed 27 December 2022].

Gaertner, E. et al., 2020. *IEA wind TCP task 37: definition of the IEA 15-megawatt offshore reference wind turbine*.

Gassama, D. et al., 2015. Investigations on the corrosion of constructional steels in different aqueous and simulated atmospheric environments. *Bulletin of the Chemical Society of Ethiopia*, 29(2), pp.299–310.

Gentils, T., Wang, L., Kolios, A., 2017. Integrated structural optimisation of offshore wind turbine support structures based on finite element analysis and genetic

algorithm [online]. *Applied Energy*, 199, pp.187–204. Available at: http://dx.doi.org/10.1016/j.apenergy.2017.05.009.

Georgoulias, K. et al., 2019. Methodology for enabling Digital Twin using advanced physics-based modelling in predictive maintenance [online]. *Procedia CIRP*, 81, pp.417–422. Available at: https://doi.org/10.1016/j.procir.2019.03.072.

Gkatzogiannis, S. et al., 2019. Correlation of laboratory and real marine corrosion for the investigation of corrosion fatigue behaviour of steel components. *International Journal of Fatigue*, 126, pp.90–102. 10.1016/j.ijfatigue.2019.04.041.

Gkatzogiannis, S. et al., 2021. Corrosion fatigue behaviour of HFMI-treated butt welds. *International Journal of Fatigue*, 145. 10.1016/j.ijfatigue.2020.106079.

Gope, D. et al., 2015. Application of artificial neural network for predicting crack growth direction in multiple cracks geometry [online]. *Applied Soft Computing Journal*, 30, pp.514–528. Available at: http://dx.doi.org/10.1016/j.asoc.2015.02.003.

Grbovic, A., Rasuo, B., 2012. FEM based fatigue crack growth predictions for spar of light aircraft under variable amplitude loading [online]. *Engineering Failure Analysis*, 26, pp.50–64. Available at: http://dx.doi.org/10.1016/j.engfailanal.2012.07.003.

Guo, T., Frangopol, D.M., Chen, Y., 2012. Fatigue reliability assessment of steel bridge details integrating weigh-in-motion data and probabilistic finite element analysis [online]. *Computers and Structures*, 112–113, pp.245–257. Available at: http://dx.doi.org/10.1016/j.compstruc.2012.09.002.

Gupta, B.K., Basu, D., 2018. Applicability of Timoshenko, Euler-Bernoulli and rigid beam theories in analysis of laterally loaded monopiles and piles. *Geotechnique*, 68(9), pp.772–785. 10.1680/jgeot.16.P.244.

GW instruments Inc, 2016. InstruNET World Plus (iW+) [online]. Available at: http://www.gwinst.com/software/iw/index.html [Accessed 2 August 2023].

Haque, M.E., Sudhakar, K., 2001. Prediction of corrosion--fatigue behavior of DP steel through artificial neural network [online]. *International Journal of Fatigue*, 23, pp.1–4. Available at: https://doi.org/10.1016/S0142-1123(00)00074-8.

Healy, J., Billingham, J., 1998. *A review of the corrosion fatigue behaviour of structural steels in the strength range 350-900MPa and associated high strength weldments*. United Kingdom.

Heider, B. et al., 2020. Corrosion resistance and microstructure of welded duplex stainless steel surface layers on gray cast iron. *Journal of Thermal Spray Technology*, 29, pp.825–842.

Hertz, J.A., 2018. *Introduction to the theory of neural computation*. CRC Press.

Higgins, P., Foley, A., 2014. The evolution of offshore wind power in the united kingdom [online]. *Renewable and Sustainable Energy Reviews*, 37, pp.599–612. Available at: http://dx.doi.org/10.1016/j.rser.2014.05.058.

Huang, G.-B., Zhu, Q.-Y., Siew, C.-K., 2006. Extreme learning machine: theory and applications. *Neurocomputing*, 70, pp.489–501. 10.1016/j.neucom.2005.12.126.

Hutchinson, M., Zhao, F., 2023. *Global Wind Report 2023* [online]. Brussels. Available at: https://gwec.net/wp-content/uploads/2023/04/GWEC-2023_interactive.pdf [Accessed 17 August 2023].

Igwemezie, V., Mehmanparast, A., 2020. Waveform and frequency effects on corrosion-fatigue crack growth behaviour in modern marine steels [online]. *International Journal of Fatigue*, 134(October 2019), p.105484. Available at: https://doi.org/10.1016/j.ijfatigue.2020.105484.

Igwemezie, V., Mehmanparast, A., Ganguly, S., 2024. Assessment of fatigue crack growth resistance of newly developed LTT alloy composition for the repair of high strength steel structures. *Journal of Advanced Joining Processes*, 10, p.100226. 10.1016/J.JAJP.2024.100226.

Igwemezie, V., Mehmanparast, A., Kolios, A., 2019. Current trend in offshore wind energy sector and material requirements for fatigue resistance improvement in large wind turbine support structures – A review. *Renewable and Sustainable Energy Reviews*, 101(October 2018), pp.181–196. 10.1016/j.rser.2018.11.002.

Igwemezie, V., Mehmanparast, A., Kolios, A., 2018. Materials selection for XL wind turbine support structures: A corrosion-fatigue perspective [online]. *Marine Structures*, 61(December 2017), pp.381–397. Available at: https://doi.org/10.1016/j.marstruc.2018.06.008.

International Association of Classification Societies, 2013. *Recommendation No.47 Shipbuilding and Repair Quality Standard*.

International Institute of Welding, 2008. *Recommendations For Fatigue Design of Welded Joints And Components*. Paris.

International Organisation for Standardisation, 2010. *BS EN ISO 10360-2:2009: Geometrical product specifications (GPS). Acceptance and reverification tests for coordinate measuring machines (CMM). CMMs used for measuring linear dimensions* [online]. Available at: https://bsol.bsigroup.com/Bibliographic/BibliographicInfoData/000000000030150298 [Accessed 30 September 2023].

International Organisation for Standardisation, 2013. *BS EN ISO 10360-8:2013: Geometrical product specifications (GPS). Acceptance and reverification tests for coordinate measuring systems (CMS). CMMs with optical distance sensors* [online]. Available at: https://bsol.bsigroup.com/Bibliographic/BibliographicInfoData/000000000030213493 [Accessed 30 September 2023].

International Organization for Standardisation, 2021. *ISO 25178-2:2021 Geometrical product specifications (GPS) — Surface texture: Areal — Part 2: Terms, definitions and surface texture parameters*. Geneva.

Ishihara, T., Qian, G.W., 2018. A new Gaussian-based analytical wake model for wind turbines considering ambient turbulence intensities and thrust coefficient effects [online]. *Journal of Wind Engineering and Industrial Aerodynamics*, 177(April), pp.275–292. Available at: https://doi.org/10.1016/j.jweia.2018.04.010.

Jacob, A. et al., 2019. Experimental and numerical investigation of residual stress effects on fatigue crack growth behaviour of S355 steel weldments [online]. *International Journal of Fatigue*, 128(July), p.105196. Available at: https://doi.org/10.1016/j.ijfatigue.2019.105196.

Jacob, A. et al., 2018. Residual stress measurements in offshore wind monopile weldments using neutron diffraction technique and contour method [online]. *Theoretical and Applied Fracture Mechanics*, 96(April), pp.418–427. Available at: https://doi.org/10.1016/j.tafmec.2018.06.001.

Jacob, A., Mehmanparast, A., 2021. Crack growth direction effects on corrosion-fatigue behaviour of offshore wind turbine steel weldments. *Marine Structures*, 75. 10.1016/j.marstruc.2020.102881.

James, R., Ros, M.C., 2015. Floating offshore wind: market and technology review. *The Carbon Trust*, 439.

Jammes, F.-X., Cespedes, X., Resplendino, J., 2013. Design of Offshore Wind Turbines. *RILEM-fib-AFGC Int. Symposium on Ultra-High Performance Fibre-Reinforced Concrete UHPFRC 2013*, (1), pp.443–452.

Jaske, C., Payer, J., Balint, V., 1981. *Corrosion fatigue of metals in marine environments*.

Jeong, S. et al., 2020. Data fusion-based damage identification for a monopile offshore wind turbine structure using wireless smart sensors. *Ocean Engineering*, 195(October 2019). 10.1016/j.oceaneng.2019.106728.

De Jesus, A.M.P. et al., 2012. A comparison of the fatigue behavior between S355 and S690 steel grades. *Journal of Constructional Steel Research*, 79, pp.140–150. 10.1016/J.JCSR.2012.07.021.

Johansen, S.S., Nejad, A.R., 2019. On digital twin condition monitoring approach for drivetrains in marine applications. In: *ASME 2019 38th International Conference on Ocean, Offshore and Arctic Engineering*. American Society of Mechanical Engineers Digital Collection, pp. 1–10.

Jörges, C., Berkenbrink, C., Stumpe, B., 2021. Prediction and reconstruction of ocean wave heights based on bathymetric data using LSTM neural networks. *Ocean Engineering*, 232, p.109046. 10.1016/J.OCEANENG.2021.109046.

Jung, S. et al., 2015. Effect of monopile foundation modeling on the structural response of a 5-MW offshore wind turbine tower [online]. *Ocean Engineering*, 109, pp.479–488. Available at: http://dx.doi.org/10.1016/j.oceaneng.2015.09.033.

Kang, D.H. et al., 2013. Corrosion fatigue behaviors of HSB800 and its HAZs in air and seawater environments [online]. *Materials Science and Engineering A*, 559, pp.751–758. Available at: http://dx.doi.org/10.1016/j.msea.2012.09.019.

Kanishka, K., Acherjee, B., 2023. A systematic review of additive manufacturing-based remanufacturing techniques for component repair and restoration. *Journal of Manufacturing Processes*, 89, pp.220–283. 10.1016/J.JMAPRO.2023.01.034.

Karimirad, M., Moan, T., 2012. Wave- and Wind-Induced Dynamic Response of a Spar-Type Offshore Wind Turbine. *Journal of Waterway, Port, Coastal, and Ocean Engineering*, 138(1), pp.9–20. 10.1061/(asce)ww.1943-5460.0000087.

Klingaa, C.G. et al., 2019. Roughness investigation of SLM manufactured conformal cooling channels using X-ray computed tomography. In: *Proceedings of the 9th Conference on Industrial Computed Tomography (ICT 2019), Padova, Italy*. pp. 13–15.

Klusák, J., Seitl, S., 2019. Very high cycle fatigue tests of high strength steels S355 J0 and S355 J2. In: *Procedia Structural Integrity*. Elsevier B.V., pp. 576–581. 10.1016/j.prostr.2019.08.077.

Knezevic, D. et al., 2019. Predictive digital twins for structural integrity management and asset life extension--JIP concept and results. In: *SPE Offshore Europe Conference and Exhibition*. Society of Petroleum Engineers, pp. 1–6.

Knysh, V. v. et al., 2018. Increasing the Corrosion Fatigue Resistance of Welded Joints by High-Frequency Mechanical Peening. *Strength of Materials*, 50(3), pp.443–447. 10.1007/s11223-018-9988-3.

Köder, T., Bohlmann, B., 2014. Experimental fatigue analysis of butt-welded joints. *Ship Technology Research*, 61(3), pp.132–141. 10.1179/str.2014.61.3.002.

Kolawole, S.K. et al., 2019. Modeling studies of corrosion fatigue in a low carbon steel. *Cogent Engineering*, 6(1). 10.1080/23311916.2019.1695999.

Kolios, A. et al., 2019. Determination of stress concentration factors in offshore wind welded structures through a hybrid experimental and numerical approach. *Ocean Engineering*, 178, pp.38–47. 10.1016/J.OCEANENG.2019.02.073.

Kovalov, D. et al., 2018. Prediction of corrosion fatigue crack growth rate in alloys. Part I: General corrosion fatigue model for aero-space aluminum alloys [online]. *Corrosion Science*, 141, pp.22–29. Available at: https://doi.org/10.1016/j.corsci.2018.06.034.

Larrosa, N.O., Akid, R., Ainsworth, R.A., 2018. Corrosion-fatigue: a review of damage tolerance models. *International Materials Reviews*, 63(5), pp.283–308. 10.1080/09506608.2017.1375644.

Lavanya, C., Kumar, N.D., 2020. Foundation Types for Land and Offshore Sustainable Wind Energy Turbine Towers. *E3S Web of Conferences*, 184, pp.1–6. 10.1051/e3sconf/202018401094.

Leitner, M., Stoschka, M., Eichlseder, W., 2014. Fatigue enhancement of thin-walled, high-strength steel joints by high-frequency mechanical impact treatment. *Welding in the World*, 58(1), pp.29–39. 10.1007/s40194-013-0097-4.

Leser, P.E. et al., 2020. A digital twin feasibility study (Part II): Non-deterministic predictions of fatigue life using in-situ diagnostics and prognostics [online]. , 229(February). Available at: https://doi.org/10.1016/j.engfracmech.2020.106903.

Li, J. et al., 2021. Static and fatigue properties of 80 mm-thick Q460GJC butt weld joint. *Journal of Constructional Steel Research*, 184, p.106809. 10.1016/J.JCSR.2021.106809.

Lin, Z., Liu, X., 2020. Wind power forecasting of an offshore wind turbine based on high-frequency SCADA data and deep learning neural network [online]. *Energy*, 201, p.117693. Available at: https://doi.org/10.1016/j.energy.2020.117693.

Liu, M. et al., 2021. Review of digital twin about concepts, technologies, and industrial applications. *Journal of Manufacturing Systems*, 58, pp.346–361. 10.1016/J.JMSY.2020.06.017.

Lombardi, D., Bhattacharya, S., Muir Wood, D., 2013. Dynamic soil-structure interaction of monopile supported wind turbines in cohesive soil [online]. *Soil Dynamics and Earthquake Engineering*, 49, pp.165–180. Available at: http://dx.doi.org/10.1016/j.soildyn.2013.01.015.

Ma, H., Yang, J., 2020. A novel hybrid monopile foundation for offshore wind turbines. *Ocean Engineering*, 198(May 2019). 10.1016/j.oceaneng.2020.106963.

Ma, Y., Martinez-Vazquez, P., Baniotopoulos, C., 2019. Wind turbine tower collapse cases: a historical overview [online]. *Proceedings of the Institution of Civil Engineers - Structures and Buildings*, 172(8), pp.547–555. Available at: https://www.icevirtuallibrary.com/doi/10.1680/jstbu.17.00167.

Maddox, S.J., 1985. *Fitness-for-purpose assessment of misalignment in transverse butt welds subject to fatigue loading*. TWI.

Madia, M. et al., 2018. The IBESS model – Elements, realisation and validation. *Engineering Fracture Mechanics*, 198, pp.171–208. 10.1016/j.engfracmech.2017.08.033.

Martinez-Luengo, M., Kolios, A., Wang, L., 2017. Parametric FEA modelling of offshore wind turbine support structures: Towards scaling-up and CAPEX reduction [online]. *International Journal of Marine Energy*, 19(2017), pp.16–31. Available at: https://doi.org/10.1016/j.ijome.2017.05.005.

Marugán, A.P. et al., 2018. A survey of artificial neural network in wind energy systems [online]. *Applied energy*, 228(April), pp.1822–1836. Available at: https://doi.org/10.1016/j.apenergy.2018.07.084.

Masi, G. et al., 2019. State of the Art Study on Materials and Solutions against Corrosion in Offshore Structures [online]. *NeSSIE Project Consortium*, (February), pp.1–93. Available at: http://nessieproject.com/library/reports-and-researches/NeSSIE Report Study on Materials and Solutions in Corrosion.

Mathiesen, T., Black, A., Gronvold, F., 2016. Monitoring and inspection options for evaluating corrosion in offshore wind foundations. *NACE - International Corrosion Conference Series*, 5(7702), pp.3777–3787.

Mehmanparast, A. et al., 2016. Welding sequence effects on residual stress distribution in offshore wind monopile structures. *Frattura ed Integrita Strutturale*, 10(35), pp.125–131. 10.3221/IGF-ESIS.35.15.

Mehmanparast, A., Brennan, F., Tavares, I., 2017. Fatigue crack growth rates for offshore wind monopile weldments in air and seawater: SLIC inter-laboratory test results [online]. *Materials and Design*, 114, pp.494–504. Available at: http://dx.doi.org/10.1016/j.matdes.2016.10.070.

Melchers, R., 2018. A Review of Trends for Corrosion Loss and Pit Depth in Longer-Term Exposures. *Corrosion and Materials Degradation*, 1(1), pp.42–58. 10.3390/cmd1010004.

Melchers, R.E., 2010. The changing character of long term marine corrosion of mild steel. *UON Research report No. 277.04.2010*, (277).

Melchers, R.E., 2005. The effect of corrosion on the structural reliability of steel offshore structures. *Corrosion Science*, 47(10), pp.2391–2410. 10.1016/j.corsci.2005.04.004.

Melchers, R.E., Beck, A.T., 2018. *Structural Reliability Analysis and Prediction* [eBook]. Wiley. Available at: https://books.google.co.uk/books?id=8yE6DwAAQBAJ.

Michel, W.H., 1999. Sea spectra revisited [online]. *Mar Technol*, 36(4), pp.211–227. Available at: http://ultramarine.com/hdesk/document/papers/sea_spectra_revisited.pdf.

Miner, M.A., 1945. Cumulative Damage in Fatigue. *Journal of Applied Mechanics, Transactions ASME*, 12(3), pp.A159–A164. 10.1115/1.4009458.

Ming, Z. et al., 2014. Fatigue Behavior and Mechanism of FV520B-I in Ultrahigh Cycle Regime. *Procedia Materials Science*, 3, pp.2035–2041. 10.1016/J.MSPRO.2014.06.328.

Mohammadi, E., Fadaeinedjad, R., Moschopoulos, G., 2018. Implementation of internal model based control and individual pitch control to reduce fatigue loads and tower vibrations in wind turbines [online]. *Journal of Sound and Vibration*, 421, pp.132–152. Available at: https://doi.org/10.1016/j.jsv.2018.02.004.

Momber, A., 2011. Corrosion and corrosion protection of support structures for offshore wind energy devices (OWEA). *Materials and Corrosion*, 62(5), pp.391–404. 10.1002/maco.201005691.

Mortazavi, S.N.S., Ince, A., 2020. An artificial neural network modeling approach for short and long fatigue crack propagation [online]. *Computational Materials Science*, 185(August), p.109962. Available at: https://doi.org/10.1016/j.commatsci.2020.109962.

Morthorst, P.E., Kitzing, L., 2016. *Economics of building and operating offshore wind farms* [eBook]. Elsevier Ltd. Available at: http://dx.doi.org/10.1016/B978-0-08-100779-2.00002-7.

Nazzal, S.S., Mikkola, E., Yıldırım, H.C., 2021. Fatigue damage of welded high-strength steel details improved by post-weld treatment subjected to critical cyclic loading conditions. *Engineering Structures*, 237. 10.1016/j.engstruct.2021.111928.

Nicolas, A. et al., 2019. Predicting fatigue crack initiation from coupled microstructure and corrosion morphology effects [online]. *Engineering Fracture Mechanics*, 220(May), p.106661. Available at: https://doi.org/10.1016/j.engfracmech.2019.106661.

Nugroho, F.A., Braun, M., Ehlers, S., 2021. Probability analysis of PIT distribution on corroded ballast tank. *Ocean Engineering*, 228. 10.1016/j.oceaneng.2021.108958.

Oakley steel, 2021. S355G10+M TMCP offshore steel plates EN10225 [online]. Available at: https://www.oakleysteel.co.uk/offshore-steel-plate/s355g10m-s355g10n [Accessed 10 March 2021].

Oh, K.Y. et al., 2018. A review of foundations of offshore wind energy convertors: Current status and future perspectives. *Renewable and Sustainable Energy Reviews*, 88(March), pp.16–36. 10.1016/j.rser.2018.02.005.

Oh, K.Y., Kim, J.Y., Lee, J.S., 2013. Preliminary evaluation of monopile foundation dimensions for an offshore wind turbine by analyzing hydrodynamic load in the frequency domain [online]. *Renewable Energy*, 54, pp.211–218. Available at: http://dx.doi.org/10.1016/j.renene.2012.08.007.

Ohta, A., Suzuki, N., Maeda, Y., 2003. Shift of S-N Curves with Stress Ratio [online]. *Welding in the World*, 47(1), pp.19–24. Available at: https://doi.org/10.1007/BF03266374.

O'Kelly, B.C., Arshad, M., 2016. *Offshore wind turbine foundations - analysis and design* [eBook]. Elsevier Ltd. Available at: http://dx.doi.org/10.1016/B978-0-08-100779-2.00020-9.

Okenyi, V. et al., 2022. A review of challenges and framework development for corrosion fatigue life assessment of monopile-supported horizontal-axis offshore wind turbines [online]. *Ships and Offshore Structures*, pp.1–15. Available at: https://doi.org/10.1080/17445302.2022.2140531.

Okenyi, V., Afazov, S., et al., 2023. Corrosion surface morphology-based methodology for fatigue assessment of offshore welded structures [online]. *Fatigue & Fracture of Engineering Materials & Structures*. Available at: https://onlinelibrary.wiley.com/doi/10.1111/ffe.14162.

Okenyi, V. et al., 2024. Material performance of submerged arc welded S355G10+M steel for offshore wind turbines. *Marine Structures*.

Okenyi, V., Bodaghi, M., et al., 2023. Uniform Corrosion Effects on Stress Evolution of High-Rated Capacity Large Diameter Offshore Wind Turbines: Analytical and Numerical Analyses. *Part C: Journal of Mechanical Engineering Science*. https://doi.org/10.1177/09544062231208551.

Ólafsson, Ó.M., Berggreen, C., Jensen, J.J., 2016. *Improved Design Basis of Welded Joints in Seawater*. Lyngby: Technical University of Denmark.

Parareda, S. et al., 2023. A damage-based uniaxial fatigue life prediction method for metallic materials. *Materials & Design*, 231, p.112056. 10.1016/J.MATDES.2023.112056.

Pedersen, M.M., 2019. Thickness Effect in Fatigue of Welded Butt Joints: A Review of Experimental Works. *International Journal of Steel Structures*, 19(6), pp.1930–1938. 10.1007/s13296-019-00254-y.

Peng, W. et al., 2012. A Brief Review of the Application and Problems in Ultrasonic Fatigue Testing [online]. *AASRI Procedia*, 2, pp.127–133. Available at: https://www.mendeley.com/catalogue/ea5121be-7224-357c-8868-c807ead9e968/ [Accessed 28 July 2023].

Peterson, R., 1945. Relation between life testing and conventional tests of materials. *Bulletin ASTM*, (133).

Pippan, R., Hohenwarter, A., 2017. Fatigue crack closure: a review of the physical phenomena. *Fatigue and Fracture of Engineering Materials and Structures*, 40(4), pp.471–495. 10.1111/ffe.12578.

Price, S.J., Figueira, R.B., 2017. Corrosion protection systems and fatigue corrosion in offshore wind structures: Current status and future perspectives. *Coatings*, 7(2), pp.1–51. 10.3390/coatings7020025.

Prime, M.B., 2001. Cross-sectional mapping of residual stresses by measuring the surface contour after a cut. *J. Eng. Mater. Technol.*, 123(2), pp.162–168.

Prithivirajan, V. et al., 2021. Direct comparison of microstructure-sensitive fatigue crack initiation via crystal plasticity simulations and in situ high-energy X-ray experiments [online]. *Materials and Design*, 197, p.109216. Available at: https://doi.org/10.1016/j.matdes.2020.109216.

Python Software Foundation, 2022. Available at: http://www.python.org [Accessed 25 December 2022].

Qiu, B. et al., 2020. Research on the damage prediction method of offshore wind turbine tower structure based on improved neural network [online].

Measurement, 151, p.107141. Available at: https://doi.org/10.1016/j.measurement.2019.107141.

Raj, P.P., 1981. Comparison of True and Residual Friction Angles. *Soils and Foundations*, 21(3), pp.99–103. 10.3208/sandf1972.21.3_99.

Rejovitzky, E., Altus, E., 2013. On single damage variable models for fatigue. *International Journal of Damage Mechanics*, 22(2), pp.268–284. 10.1177/1056789512443902.

Saidin, S. et al., 2019. Effects of High Frequency Mechanical Impact on Fatigue Life of Semi-Automated Gas Metal Arc Welding (GTAW) of HSLA Butt Weld. *MATEC Web of Conferences*, 269, p.06002. 10.1051/matecconf/201926906002.

Sanaei, N., Fatemi, A., 2020. Analysis of the effect of surface roughness on fatigue performance of powder bed fusion additive manufactured metals. *Theoretical and Applied Fracture Mechanics*, 108, p.102638. 10.1016/J.TAFMEC.2020.102638.

Sánchez, S. et al., 2019. Foundations in offshore wind farms: Evolution, characteristics and range of use. Analysis of main dimensional parameters in monopile foundations. *Journal of Marine Science and Engineering*, 7(12). 10.3390/JMSE7120441.

Saucedo-Mora, L., Marrow, T.J., 2014. 3D Cellular Automata Finite Element Method with Explicit Microstructure: Modeling Quasi-brittle Fracture using Meshfree Damage Propagation [online]. *Procedia Materials Science*, 3, pp.1143–1148. Available at: http://dx.doi.org/10.1016/j.mspro.2014.06.186.

Schaumann, P., Steppeler, S., 2013. Fatigue tests of axially loaded butt welds up to very high cycles. In: *Procedia Engineering*. Elsevier Ltd, pp. 88–97. 10.1016/j.proeng.2013.12.065.

Schaumann, Peter et al., 2010. *High frequency fatigue testing of butt welds with a new magnet resonance machine Structural fire design View project Probabilistische Sicherheitsbewertung von Offshore-Windenergieanlagen View project High Frequency Fatigue Testing of Butt Welds with a New Magnet Resonance Machine* [online]. Available at: https://www.researchgate.net/publication/290176284.

Scheu, M.N. et al., 2019. A systematic Failure Mode Effects and Criticality Analysis for offshore wind turbine systems towards integrated condition based maintenance strategies [online]. *Ocean Engineering*, 176(October 2018), pp.118–133. Available at: https://linkinghub.elsevier.com/retrieve/pii/S0029801818319474.

Schijve, J., 2009. *Fatigue of structures and materials*. Springer.

Schiller, R. et al., 2022. Fatigue strength of partial penetration butt welds of mild steel. *Welding in the World*. 10.1007/s40194-022-01335-z.

Schönmaier, H. et al., 2021. Influence of the Heat Input on the Dendritic Solidification Structure and the Mechanical Properties of 2.25Cr-1Mo-0.25V Submerged-Arc Weld Metal. *Journal of Materials Engineering and Performance*, 30(10), pp.7138–7151. 10.1007/s11665-021-05922-x.

Serjouei, A., Afazov, S., 2022. Predictive model to design for high cycle fatigue of stainless steels produced by metal additive manufacturing. *Heliyon*, 8(11), p.e11473. 10.1016/j.heliyon.2022.e11473.

Shittu, A.A. et al., 2020. Comparative study of structural reliability assessment methods for offshore wind turbine jacket support structures. *Applied Sciences (Switzerland)*, 10(3). 10.3390/app10030860.

Signor, L. et al., 2016. Influence of local crystallographic configuration on microcrack initiation in fatigued 316LN stainless steel: Experiments and crystal plasticity finite elements simulations. *Materials Science and Engineering A*, 649, pp.239–249. 10.1016/j.msea.2015.09.119.

Sines, G., Waisman, J.L., Dolan, T.J., 1959. *Metal Fatigue*. McGraw-Hill.

Singh, A., Singh, R.P., 2019. A review of effect of welding parameters on the mechanical properties of weld in submerged Arc welding process. In: *Materials Today: Proceedings*. Elsevier Ltd, pp. 1714–1717. 10.1016/j.matpr.2020.02.361.

Singh, B., Goel, R.K., 2011. Strength of Discontinuities. *Engineering Rock Mass Classification*, (1977), pp.193–204. 10.1016/b978-0-12-385878-8.00015-x.

Singh, R.P., Singh, Aman, Singh, Amit, 2019. Optimization of hardness of weld in submerged arc welding. In: *Materials Today: Proceedings*. Elsevier Ltd, pp. 1827–1830. 10.1016/j.matpr.2020.02.382.

Sivalingam, K. et al., 2018. A Review and Methodology Development for Remaining Useful Life Prediction of Offshore Fixed and Floating Wind turbine Power Converter with Digital Twin Technology Perspective [online]. In: *2018 2nd International Conference on Green Energy and Applications (ICGEA)*. IEEE, pp. 197–204. Available at: https://ieeexplore.ieee.org/document/8356292/.

Smaili, F., Lojen, G., Vuherer, T., 2019. Fatigue crack initiation and propagation of different heat affected zones in the presence of a microdefect [online]. *International Journal of Fatigue*, 128, p.105191. Available at: https://doi.org/10.1016/j.ijfatigue.2019.105191.

Smaili, F., Vuherer, T., Samardžić, I., 2019. Resistivity during cycle loading of fine grain Heat Affected Zone (HAZ) of 17CrNiMo7 Steel Prepared into Laboratory Furnace. *Metalurgija*, 58(1–2), pp.87–90.

Sonsino, C.M., 2009. Effect of residual stresses on the fatigue behaviour of welded joints depending on loading conditions and weld geometry. *International Journal of Fatigue*, 31(1), pp.88–101. 10.1016/j.ijfatigue.2008.02.015.

Sorger, G. et al., 2018. Microstructure and fatigue properties of friction stir welded high-strength steel plates. *Science and Technology of Welding and Joining*, 23(5), pp.380–386. 10.1080/13621718.2017.1399574.

Srinivasan, V.S. et al., 2003. Low cycle fatigue and creep--fatigue interaction behavior of 316L (N) stainless steel and life prediction by artificial neural network approach. *International Journal of Fatigue*, 25, pp.1327–1338. 10.1016/S0142-1123(03)00064-1.

Stewart, G.M. et al., 2016. The creation of a comprehensive metocean data set for offshore wind turbine simulations [online]. *Wind Energy*, 19(6), pp.1151–1159. Available at: https://onlinelibrary.wiley.com/doi/abs/10.1002/we.1881.

Stieng, L.E.S., Muskulus, M., 2020. Reliability-based design optimization of offshore wind turbine support structures using analytical sensitivities and factorized uncertainty modeling. *Wind Energy Science - Copernicus GmbH*, 5(1), pp.171–198.

Stromblad, N., 2014. *Abaqus Modeling of Soil and Structure Interaction subsea*. Chalmers University of Technology.

Sun, C., Jahangiri, V., 2019. Fatigue damage mitigation of offshore wind turbines under real wind and wave conditions [online]. *Engineering Structures*, 178(March 2018), pp.472–483. Available at: https://doi.org/10.1016/j.engstruct.2018.10.053.

Suresh, S., 1992. *Fatigue of materials*. Cambridge university press.

Suryanarayana, C., 2011. *Experimental techniques in materials and mechanics*. Crc Press.

Tchakoua, P. et al., 2014. Wind turbine condition monitoring: State-of-the-art review, new trends, and future challenges. *Energies*, 7(4), pp.2595–2630. 10.3390/en7042595.

The MathWorks Inc, 2022. Available at: https://www.mathworks.com/help/stats/index.html [Accessed 13 April 2023].

Thermo Fisher Scientific, 1995. Available at: https://assets.thermofisher.com/TFS-Assets/MSD/Product-Guides/user-guide-avizo-software.pdf [Accessed 27 December 2022].

Tian, Z. et al., 2011. Condition based maintenance optimization for wind power generation systems under continuous monitoring [online]. *Renewable Energy*, 36(5), pp.1502–1509. Available at: http://dx.doi.org/10.1016/j.renene.2010.10.028.

To, D., Umezawa, O., Shinohara, T., 2018. Detection of surface roughness evolution of carbon steel subjected to outdoor exposure and constant humidity corrosion tests. In: *Materials Transactions*. Japan Institute of Metals (JIM), pp. 1239–1243. 10.2320/matertrans.MF201702.

Tong, L. et al., 2021. Experimental investigation on fatigue behavior of butt-welded high-strength steel plates. *Thin-Walled Structures*, 165. 10.1016/j.tws.2021.107956.

Topaç, M.M., Ercan, S., Kuralay, N.S., 2012. Fatigue life prediction of a heavy vehicle steel wheel under radial loads by using finite element analysis. *Engineering Failure Analysis*, 20, pp.67–79. 10.1016/j.engfailanal.2011.10.007.

Tsay, L.W. et al., 1999. Microstructures and fatigue crack growth of EH36 TMCP steel weldments. *International Journal of Fatigue*, 21(8), pp.857–864. 10.1016/S0142-1123(99)00021-3.

Ummenhofer, T., Weidner, P., 2013. Improvement factors for the design of welded joints subjected to high frequency mechanical impact treatment. *Steel Construction*, 6(3), pp.191–199. 10.1002/stco.201310027.

Vestas, 2022. Vestas' V236-15.0 MW prototype wind turbine produces first kWh [online]. *Vestas Wind Systems A/S*. Available at: https://www.vestas.com/en/media/company-news/2022/vestas--v236-15-0-mw-prototype-wind-turbine-produces-fi-c3691167 [Accessed 10 August 2023].

Wang, H. et al., 2017. A comparison study of machine learning based algorithms for fatigue crack growth calculation. *Materials - Multidisciplinary Digital Publishing Institute*, 10, p.543. 10.3390/ma10050543.

Wang, T. et al., 2009. Discussion on fatigue design of welded joints enhanced by ultrasonic peening treatment (UPT). *International Journal of Fatigue*, 31(4), pp.644–650. 10.1016/j.ijfatigue.2008.03.030.

Wang, Z., 2020. Digital Twin Technology [eBook]. In: Felice, T. B., De, A. P. F., eds. *Industry 4.0*. Rijeka: IntechOpen, 2020. Available at: https://doi.org/10.5772/intechopen.80974.

Weich, I., 2009. Ermüdungsverhalten mechanisch nachbehandelter Schweißverbindungen in Abhängigkeit des Randschichtzustands. *Institut für Bauwerkserhaltung und Tragwerk, TU Braunschweig*.

Weich, I. et al., 2009. Fatigue Behaviour of Welded High-Strength Steels after High Frequency Mechanical Post-Weld Treatments [online]. *Welding in the World*, 53(11), pp.R322–R332. Available at: https://doi.org/10.1007/BF03263475.

Wieczorska, A., Labuda, W., 2023. Analysis of the process of qualifying the welding technology of S355JR structural steel using the submerged arc welding method. *Journal of Achievements in Materials and Manufacturing Engineering*, 118(1), pp.18–27.

Wind Europe, 2017. *Wind energy in Europe: Outlook to 2020*.

Wind Europe, Wood Mackenzie, 2020. *Wind Energy and Economic Recovery in Europe*.

World Forum Offshore Wind e.V., 2021. *Global Offshore Wind Report 2021* [online]. Brussels. Available at: www.wfo-global.org [Accessed 17 August 2023].

Wright, L., Davidson, S., 2020. How to tell the difference between a model and a digital twin [online]. *Advanced Modeling and Simulation in Engineering Sciences*, 7(1). Available at: https://doi.org/10.1186/s40323-020-00147-4.

Wu, Q. et al., 2020. Fatigue life prediction model of metallic materials considering crack propagation and closure effect [online]. *Journal of the Brazilian Society of Mechanical Sciences and Engineering*, 42(8), pp.1–11. Available at: https://doi.org/10.1007/s40430-020-02512-1.

Xin, H., Veljkovic, M., 2019. Fatigue crack initiation prediction using phantom nodes-based extended finite element method for S355 and S690 steel grades. *Engineering Fracture Mechanics*, 214(April), pp.164–176. 10.1016/j.engfracmech.2019.04.026.

Xin, H., Veljkovic, M., 2020. Residual stress effects on fatigue crack growth rate of mild steel S355 exposed to air and seawater environments [online]. *Materials and Design*, 193, p.108732. Available at: https://doi.org/10.1016/j.matdes.2020.108732.

Xu, Q. et al., 2021. Corrosion fatigue crack growth mechanisms in welded joints of marine steel structures. *Journal of Central South University*, 28(1), pp.58–71. 10.1007/s11771-021-4586-0.

Ye, S. et al., 2017. Multi-scale fatigue crack propagation in 304 stainless steel: experiments and modelling. *Fatigue and Fracture of Engineering Materials and Structures*, 40(11), pp.1928–1941. 10.1111/ffe.12615.

Yeter, B., Garbatov, Y., Guedes Soares, C., 2019. Numerical and experimental study of the ultimate strength of a monopile structure [online]. *Engineering Structures*, 194(August 2018), pp.290–299. Available at: https://doi.org/10.1016/j.engstruct.2019.05.074.

Yu, Y. et al., 2022. Robust design of monopiles for offshore wind turbines considering uncertainties in dynamic loads and soil parameters. *Ocean Engineering*, 266. 10.1016/j.oceaneng.2022.112822.

Yusof, F., Jamaluddin, M.F., 2014. Welding Defects and Implications on Welded Assemblies. In: *Comprehensive Materials Processing*. Elsevier Ltd, 2014, pp. 125–134. 10.1016/B978-0-08-096532-1.00605-1.

Zaaijer, M.B., 2006. Foundation modelling to assess dynamic behaviour of offshore wind turbines. *Applied Ocean Research*, 28(1), pp.45–57. 10.1016/j.apor.2006.03.004.

ZEISS Group, 2021. Available at: https://scanare3d.com/wp-content/uploads/2021/02/GOM_Software_EN_RevB.pdf [Accessed 25 December 2022].

Zhao, T. et al., 2017. Corrosion fatigue crack initiation and initial propagation mechanism of E690 steel in simulated seawater [online]. *Materials Science and Engineering A*, 708(June), pp.181–192. Available at: http://dx.doi.org/10.1016/j.msea.2017.09.078.

Zhidchenko, V., Handroos, H. a, Kovartsev, A., 2019. Fatigue life estimation of hydraulically actuated mobile working machines using Internet of Things and Digital Twin concepts. In: *Journal of Physics: Conference Series*. IOP Publishing, p. 042025. 10.1088/1742-6596/1368/4/042025.

Zhou, L. et al., 2019. Investigation of dynamic characteristics of a monopile wind turbine based on sea test [online]. *Ocean Engineering*, 189(238), p.106308. Available at: https://doi.org/10.1016/j.oceaneng.2019.106308.

Ziane, K. et al., 2021. Neural Network Optimization Algorithms to Predict Wind Turbine Blade Fatigue Life under Variable Hygrothermal Conditions. *Eng*, 2(3), pp.278–295. 10.3390/eng2030018.

Ziegler, L. et al., 2017. Brief communication: Structural monitoring for lifetime extension of offshore wind monopiles: can strain measurements at one level tell us everything? [online]. *Wind Energy Science*, 2(2), pp.469–476. Available at: https://wes.copernicus.org/articles/2/469/2017/.

Appendices

Appendix A: Stress predictions data, model, and reviewed S-N curve data

Appendix A1: *Key parameters of the NREL 15 Megawatt turbine.*

Table ES-1. Key Parameters for the IEA Wind 15-MW Turbine

Parameter	Units	Value
Power rating	MW	15
Turbine class	-	IEC Class 1B
Specific rating	W/m^2	332
Rotor orientation	-	Upwind
Number of blades	-	3
Control	-	Variable speed Collective pitch
Cut-in wind speed	m/s	3
Rated wind speed	m/s	10.59
Cut-out wind speed	m/s	25
Design tip-speed ratio	-	90
Minimum rotor speed	rpm	5.0
Maximum rotor speed	rpm	7.56
Maximum tip speed	m/s	95
Rotor diameter	m	240
Airfoil series	-	FFA-W3
Hub height	m	150
Hub diameter	m	7.94
Hub overhang	m	11.35
Rotor precone angle	deg	-4.0
Blade prebend	m	4
Blade mass	t	65
Drivetrain	-	Direct drive
Shaft tilt angle	deg	6
Rotor nacelle assembly mass	t	1,017
Transition piece height	m	15
Monopile embedment depth	m	45
Monopile base diameter	m	10
Tower mass	t	860
Monopile mass	t	1,318

deg	degrees	rpm	revolutions per minute
m	meters	t	metric tons
m/s	meters per second	W/m^2	watts per square meter

Appendix A2: *Detailed calculation for loads on wind turbine.*

Thrust force

Thrust Force on Rotor and Blade							
Thrust coefficient C_T =	0.811	given	$C_T = 4a(1-a)$	≈	**16.°**	**ngle of attack**
wind velocity at hub **U** =	50	m/s²				
rotor diameter =	240	m				
Rotor swept area **A** =	45216	m²				
Thrust Force **F_T** =	56380	KN	$F_T = \frac{1}{2} C_T \rho A U^2$			

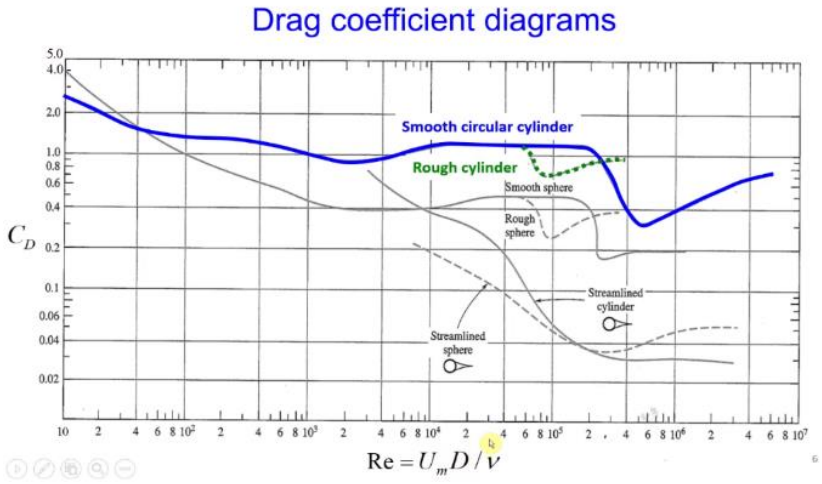

The total drag force of a body can be divided into:

1. *friction drag* (skin friction) due to the tangential stresses on the surface
2. *pressure drag (form drag)* due to the normal stresses on the surface

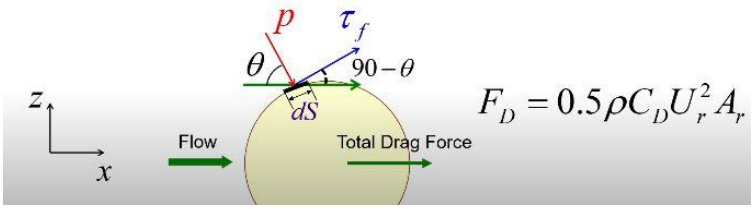

Wind force on tower

Load Estimation according to BS EN 1991-1-4 (factoring some dynamic conditions of structure)																			
ze-z	Roughness factor - Cr(z)	Basic Wind Velocity - Vb - (V10min-50yr)	Mean wind speed Vm(z)	Turbulence intensity Iv(z) (sec 4.4) - CoZe=1	Basic velocity pressure - qb - kN/m2	Characteristics Peak velocity pressure - qp(ze)- kN/m2	Peak Wind velocity Vm(ze)	Outer-Diameter- b	Reynolds number - Re	Surface roughness Diameter ratio - k/b	force coefficient of structural element s without free-end	Force Coefficient - Cf (ψ - 0.7)	Structural factor- CsCd	Reference Area - Aref	wind force from force coefficient s - Fw (kN)	Effective Wind pressure - Weff (kN/m2)	Fw (N)- Hollow cylinder	Weff - pa (n/mm2)
5	1.1573	29.213	50	0.134797	0.533375	3.036839	69.70610964	10	46470740	2E-06	0.692574	0.6233163	1.15	1445.82	3147.330	2.177	3147330.01	2176.85
10	1.26543	29.213	50	0.123278	0.533375	2.910856	68.24492762	10	45496618	2E-06	0.691451	0.6223058	1.15	1445.82	3011.873	2.083	3011873.32	2083.16
15	1.32868	29.213	50	0.11741	0.533375	2.846667	67.48827672	10	44992184	2E-06	0.690858	0.6217722	1.15	1445.82	2942.931	2.035	2942930.91	2035.48
20	1.37356	29.213	50	0.113573	0.533375	2.80471	66.98906817	10	44659379	2E-06	0.690462	0.6214162	1.15	1445.82	2897.894	2.004	2897894.09	2004.33
25	1.40837	29.213	50	0.110766	0.533375	2.774006	66.62139134	10	44414261	2E-06	0.690169	0.6211519	1.15	1445.82	2864.952	1.982	2864951.60	1981.54
30	1.43681	29.213	50	0.108574	0.533375	2.750024	66.33278494	10	44221857	2E-06	0.689937	0.6209432	1.15	1445.82	2839.229	1.964	2839229.00	1963.75
35	1.46086	29.213	50	0.106786	0.533375	2.730476	66.09660705	10	44064405	2E-06	0.689746	0.6207716	1.15	1445.82	2818.268	1.949	2818267.81	1949.25
40	1.48169	29.213	50	0.105285	0.533375	2.714056	65.89756295	9.926	43606614	2E-06	0.689538	0.620584	1.15	1435.121	2779.750	1.937	2779749.53	1936.94
45	1.50007	29.213	50	0.103995	0.533375	2.69995	65.72610092	9.926	43493152	2E-06	0.689398	0.6204584	1.15	1435.121	2764.743	1.926	2764743.11	1926.49
50	1.5165	29.213	50	0.102868	0.533375	2.687622	65.57587646	9.926	43393743	2E-06	0.689276	0.6203481	1.15	1435.121	2751.630	1.917	2751629.69	1917.35
55	1.53137	29.213	50	0.10187	0.533375	2.676698	65.44247173	9.443	41198217	2.1E-06	0.688846	0.6199615	1.15	1365.288	2605.471	1.908	2605470.74	1908.37
60	1.54494	29.213	50	0.100975	0.533375	2.666909	65.3226934	9.443	41122813	2.1E-06	0.688747	0.6198726	1.15	1365.288	2595.569	1.901	2595569.45	1901.12
65	1.55743	29.213	50	0.100165	0.533375	2.658054	65.21416226	8.833	38402446	2.3E-06	0.688222	0.6193998	1.15	1277.093	2417.994	1.893	2417993.83	1893.36
70	1.56899	29.213	50	0.099427	0.533375	2.649982	65.11506058	8.833	38344089	2.3E-06	0.688139	0.6193253	1.15	1277.093	2410.361	1.887	2410360.56	1887.38
75	1.57975	29.213	50	0.09875	0.533375	2.642573	65.02396995	8.833	38290448	2.3E-06	0.688063	0.6192567	1.15	1277.093	2403.355	1.882	2403355.26	1881.90
80	1.58982	29.213	50	0.098124	0.533375	2.635733	64.9397634	8.151	35288267	2.5E-06	0.687458	0.618712	1.15	1178.488	2210.105	1.875	2210105.11	1875.37
85	1.59928	29.213	50	0.097544	0.533375	2.629386	64.86153145	8.151	35245756	2.5E-06	0.687391	0.6186523	1.15	1178.488	2204.571	1.871	2204570.73	1870.68
90	1.6082	29.213	50	0.097003	0.533375	2.623471	64.78853007	8.151	35206087	2.5E-06	0.68733	0.6185966	1.15	1178.488	2199.413	1.866	2199412.80	1866.30
95	1.61663	29.213	50	0.096497	0.533375	2.617936	64.72014326	7.39	31885457	2.7E-06	0.686604	0.617944	1.15	1068.461	1987.763	1.860	1987763.04	1860.40
100	1.62463	29.213	50	0.096022	0.533375	2.612737	64.65585555	7.39	31853785	2.7E-06	0.686549	0.6178942	1.15	1068.461	1983.656	1.857	1983656.11	1856.55
105	1.63224	29.213	50	0.095574	0.533375	2.60784	64.59523149	6.909	29752564	2.9E-06	0.68603	0.6174268	1.15	998.917	1849.667	1.852	1849667.45	1851.67
110	1.6395	29.213	50	0.095151	0.533375	2.603213	64.53790009	6.909	29726157	2.9E-06	0.68598	0.6173819	1.15	998.917	1846.251	1.848	1846251.30	1848.25
115	1.64644	29.213	50	0.09475	0.533375	2.59883	64.4835428	6.909	29701120	2.9E-06	0.685933	0.6173393	1.15	998.917	1843.015	1.845	1843015.37	1845.01
120	1.65308	29.213	50	0.09437	0.533375	2.594667	64.43188419	6.748	28985757	3E-06	0.685722	0.6171496	1.15	975.6393	1796.633	1.841	1796632.59	1841.49
125	1.65944	29.213	50	0.094007	0.533375	2.590706	64.3826846	6.748	28963624	3E-06	0.685679	0.6171108	1.15	975.6393	1793.777	1.839	1793777.20	1838.57
130	1.66556	29.213	50	0.093662	0.533375	2.586929	64.33573424	6.748	28942502	3E-06	0.685638	0.6170738	1.15	975.6393	1791.055	1.836	1791054.52	1835.78
135	1.67145	29.213	50	0.093332	0.533375	2.583321	64.29084851	6.572	28167964	3E-06	0.685411	0.61687	1.15	950.1929	1741.332	1.833	1741332.01	1832.61
140	1.67712	29.213	50	0.093016	0.533375	2.579868	64.24786415	6.572	28149131	3E-06	0.685373	0.6168359	1.15	950.1929	1738.908	1.830	1738908.29	1830.06
145	1.6826	29.213	50	0.092714	0.533375	2.576558	64.2066361	6.5	27822876	3.1E-06	0.685258	0.6167326	1.15	939.783	1717.363	1.827	1717363.39	1827.40

Parameters					
Avg. Diameter of monopile **D** =	10	m	Drag coefficient C_D =	1.2	
Depth of water **d** =	30	m	Inertia coefficient C_M =	2	DNV, 2002
Wave height **H** =	11.307	m	Wave no **k** = $2\pi/\lambda$ =	0.058801779	rad/m
Wave period **T** =	8.515	s	Morrison Eqn check D/λ =	0.093633407	<0.2 OK
Density of sea water **ρ** =	1025	kg/m³			
g =	9.81	m/s²	Morrison Eqn F =	$\underbrace{0.5\rho C_D A_p V\lvert V\rvert}_{F_D} + \underbrace{C_M \rho V_{vol}}_{F_I}$	
π =	3.14				
Projected Area **A** =	300	m²			
Wavelength trial **λ** =	106.7994885	m	$\lambda = \frac{gT^2}{2\pi}\tanh(\frac{2\pi d}{\lambda})$	h/gT2	0.015896777
Wavelength Calculated **λ** =	106.799489	m		d/gT2	0.042177705
Assuming max force					
Inertia Force **FI** =	6973.842476	KN	$F_I = \rho C_M \frac{\pi D^2}{4}\frac{2\pi^2 H}{T^2}\frac{1}{k}(1-e^{-kd})$		
Drag Force **FD** =	882.4648391	KN	$0.5\rho C_D D\left(\frac{\pi H}{T}\right)^2\frac{1}{2k}(1-e^{-2kd})$		
Resolution of force component =	#NUM!	rad	$Y = (kx-\sigma t)$		
Total horizontal wave load **Fw** =	#NUM!	KN			
Total horizontal wave load **Fw** =	7856.307315	KN	Temporary addition		

Wave conditions					
5.339974	<	30	<	53.39974	intermediate
		30	>=	53.39974	deep waves
		30	<=	5.339974	shallow waves

	Intermediate waves $0.05\lambda < d < 0.5\lambda$ dependence on T and d	Deep waves $d \geq 0.5\lambda$ dependence on T no dependence on d	Shallow waves $d \leq 0.05\lambda$ dependence on d
u	$\frac{\pi H}{T}\frac{\cosh k(z+d)}{\sinh kd}\cos(-)$	$\frac{\pi H}{T}e^{kz}\cos(-)$	$\frac{\pi H}{T}\frac{1}{kd}\cos(-)$
$\dot{u} = \frac{\partial u}{\partial t}$	$\frac{2\pi^2 H}{T^2}\frac{\cosh k(z+d)}{\sinh kd}\sin(-)$	$\frac{2\pi^2 H}{T^2}e^{kz}\sin(-)$	$\frac{2\pi^2 H}{T^2}\frac{1}{kd}\sin(-)$
w	$\frac{\pi H}{T}\frac{\sinh k(z+d)}{\sinh kd}\sin(-)$	$\frac{\pi H}{T}e^{kz}\sin(-)$	$\frac{\pi H}{T}(1+\frac{z}{d})\sin(-)$
$\dot{w} = \frac{\partial w}{\partial t}$	$-\frac{2\pi^2 H}{T^2}\frac{\sinh k(z+d)}{\sinh kd}\cos(-)$	$-\frac{2\pi^2 H}{T^2}e^{kz}\cos(-)$	$-\frac{2\pi^2 H}{T^2}(1+\frac{z}{d})\cos(-)$

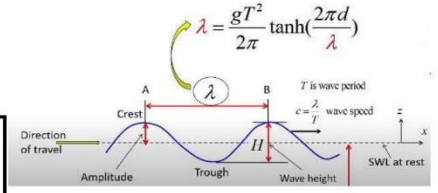

Wave force according to BS-EN 61400-3:2009

Cd- drag	1.2	
Cm- inertia	2	
density	1029	kg/m3
Diameter **D**	10	m
Depth to sea	30	m
CSA	78.5	m2
ight Z above MSL~-d		max vel

$$F = \frac{1}{2}C_D\rho D|U|U + C_M\rho A\dot{U}$$

U — the horizontal velocity of the flow $U = \frac{\pi H}{T}\frac{\cosh(k(z+d))}{\sinh(kd)}\cos A$

$\dot{U}$ — the horizontal acceleration of the flow $\dot{U} = \frac{2\pi^2 H}{T^2}\frac{\cosh(k(z+d))}{\sinh(kd)}\sin A$

$k = \frac{2\pi}{L}$

Where:
z — height measured positively above MWL
A — wave amplitude
d — depth from mean still water level to seabed

Wave height **H** (m)	Wave Period **T** (m)	Wave amplidue **A** (m)	Wave length **L** (m)	Wave no **k**	Horizonal velocity of flow **U**	Horizonal acceleration of flow **Ü**	Morrison Equation Force **Fwave** (N)	**Fwave** (Kn)
1.102	8.515	0.551	106.7994885	0.05880178	0.122453343	0.055399314	9042.503399	9.042503
1.179	8.31	0.5895	102.5375613	0.061245849	0.121225397	0.061158255	9971.030164	9.97103
1.316	8.006	0.658	96.21434647	0.065270931	0.117856158	0.071301408	11604.71376	11.60471
1.537	7.651	0.7685	88.84706391	0.070683259	0.110681823	0.087609943	14229.28353	14.22928
1.836	7.441	0.918	84.51120863	0.07430967	0.10274734	0.113097187	18336.36884	18.33637
2.188	7.461	1.094	84.92311033	0.073949246	0.093291986	0.15160442	24545.88363	24.54588
2.598	7.643	1.299	88.68149414	0.070815225	0.069648645	0.204830359	33120.90872	33.12091
3.061	8.047	1.5305	97.06687901	0.064697661	0.014136943	0.273068893	44116.33284	44.11633
3.617	8.521	1.8085	106.9241448	0.058733226	0.111243654	0.337808485	54650.37839	54.65038
4.027	8.987	2.0135	116.5822148	0.053867565	0.249718073	0.367541552	59762.44552	59.76245
4.516	9.452	2.258	126.1541003	0.049780387	0.450792266	0.364517811	60143.58712	60.14359
9.686	16.654	4.843	264.905497	0.023706567	0.307906623	0.883647012	143341.161	143.3412
11.307	18.505	5.6535	298.7463401	0.021021178	2.303652982	0.569508767	124770.1384	124.7701

Appendix A3: *Analytical model sheet for estimating stress in vertical direction.*

Given Parameter			
D =	10000	mm	
d =	9944.659	mm	
M- blade +Rotor =	261362	kG	
M-rna =	820888	kG	
weight Fy -blade + rotor=	2563961.22	N	
weight Fy -rna =	8052911.28	N	
Cross section Area			
$A = \frac{\pi}{4}(D^2 - d^2)$			
	867001.4171	mm²	
Moment of Inertial **I**			
$= \frac{\pi}{32}(D_o^4 - D_i^4)$			
	2.15554E+13	mm³	
Bending Moments **M**			
	Force (N)	Distance(mm)	Moments (N.mm)
M Thrust =	1771000	169582	3.0033E+11
M wind =	62545.96	97291	6085158994
M wave =	11604.7	500	5802350
M blade-Rotor	2563961.22	12500	32049515250
M rna	8052911.28	5486	44178271282
M total =			**2.30193E+11**
Total Bending Stress (x)			
$\sigma_b = \frac{My}{I}$	5000	mm	
	53.39560644	**Mpa**	
Total Axial (direct) Stress			
$\sigma := \frac{F}{A}$			
	-12.24550767	**Mpa - comp.**	
Average Shear Stress			
$\tau = -\frac{4V}{3A}\left(\frac{D_o^2 + D_o D_i + D_i^2}{D_o^2 + D_i^2}\right)$	1845150.66	N - Vtotal	
	-4.256374103	Mpa	
Normal Stress - Y direction		Tension A	compression B
σx (Tension)		**41.150**	0.000
σy (compression)		0.000	**-65.641**

Appendix A4: *Wind velocity on stress in the vertical direction in tension and compression from FEA and analytical formulations.*

Analytical- Stress

Subberged - 13000			Tidal		Splash		Atmospheric	
T	C	V	T	C	T	C	T	C
0	-26.5334	4	0	-26.7597	0	-26.5040	0	-24.8693
20.6485	-46.9564	6	17.9798	-47.7421	15.5248	-47.5893	10.8585	-45.1475
43.8943	-70.2023	8	41.8495	-71.6117	39.5021	-71.5666	33.9031	-68.1922
77.7682	-104.0762	10	76.6401	-106.4024	74.4559	-106.5204	67.5078	-101.7969
56.1905	-82.4985	12	54.3298	-84.0921	51.9306	-83.9951	45.6773	-79.9664
44.3714	-70.6793	14	42.0430	-71.8053	39.4779	-71.5424	33.5350	-67.8241
38.8919	-65.1998	16	36.2597	-66.0220	33.5555	-65.6199	27.6655	-61.9546
35.3312	-61.6392	18	32.4289	-62.1912	29.5831	-61.6476	23.6533	-57.9423
33.6844	-59.9923	20	30.5509	-60.3132	27.5618	-59.6263	21.4991	-55.7881
31.3969	-57.7049	22	28.0056	-57.7679	24.8561	-56.9206	18.6620	-52.9511
31.9338	-58.2418	24	28.3584	-58.1207	25.0539	-57.1184	18.6010	-52.8901
34.0938	-60.4017	40	28.1650	-57.9273	23.0543	-55.1188	13.8199	-48.1090
50.9780	-77.2860	50	43.5617	-73.3240	36.9623	-69.0268	24.6779	-58.9670

FEA - Stress

Subberged - 13000			Tidal		Splash		Atmospheric	
T	C	V	T	C	T	C	T	C
0	-26.6451	4	0	-25.7475	0	-24.6545	0	-21.7873
19.6265	-46.7345	6	17.9765	-46.414	16.3308	-45.4354	12.7564	-41.7545
42.5722	-69.5869	8	41.4455	-69.9177	39.9093	-69.0653	35.2592	-64.4532
76.0056	-102.896	10	75.6538	-104.18	74.2875	-103.515	68.0834	-97.5489
54.7625	-81.5194	12	53.676	-82.1311	52.02	-81.299	46.5861	-76.1351
43.15	-69.7408	14	41.5524	-69.9574	39.6596	-69.0136	34.5543	-64.2625
37.7967	-64.1898	16	35.8193	-64.1886	33.7154	-63.1666	28.6421	-58.5724
34.343	-60.5081	18	31.9993	-60.3374	29.6748	-59.2429	24.5244	-54.7222
32.7835	-58.6933	20	30.0971	-58.3997	27.5438	-57.2385	22.2055	-52.7092
30.5982	-56.2317	22	27.5432	-55.7846	24.7343	-54.5467	19.2026	-50.0282
31.2043	-56.5386	24	27.8442	-56.0086	24.7799	-54.7056	18.9028	-50.0818
34.2178	-56.0718	40	27.0018	-54.5313	20.9816	-52.462	11.3992	-46.767
51.6395	-70.4837	50	41.721	-68.4242	33.211	-65.7685	19.6304	-58.569

Appendix A5: *One -year analytical model for uniform corrosion loss (repeated for year 0- 20).*

			D	d	DIST thrust	DIST wind	DIST wave	M thrust	M wind	M wave	M total	Iy	Cross section Area	Total Bending Stress (x)	Total Axial (direct) Stress	σx (Tension)	σy (compression)
Submerged Zone	0.15	1000	10000	9944.659	179497.3	101291	14500	8.7056E+10	2.81856E+11	1809167006	2.97443E+11	**2.15554E+13**	**867001.4171**	68.99485623	-12.24550767	56.749	-81.240
		2000	10000	9944.659	178497.3	100291	14000	8.6571E+10	2.79074E+11	1746781937	2.94113E+11	**2.15554E+13**	**867001.4171**	68.22242261	-12.24550767	55.977	-80.468
		3000	10000	9944.659	177497.3	99291	13500	8.6086E+10	2.76291E+11	1684396868	2.90783E+11	**2.15554E+13**	**867001.4171**	67.44998898	-12.24550767	55.204	-79.695
		4000	10000	9944.659	176497.3	98291	13000	8.5601E+10	2.73509E+11	1622011799	2.87452E+11	**2.15554E+13**	**867001.4171**	66.67755536	-12.24550767	54.432	-78.923
		5000	10000	9944.659	175497.3	97291	12500	8.5116E+10	2.70726E+11	1559626730	2.84122E+11	**2.15554E+13**	**867001.4171**	65.90512173	-12.24550767	53.660	-78.151
		6000	10000	9946.551	174497.3	96291	12000	8.4631E+10	2.67943E+11	1497241660	2.80792E+11	**2.08244E+13**	**837439.7771**	67.41911651	-12.67777432	54.741	-80.097
		7000	10000	9946.551	173497.3	95291	11500	8.4146E+10	2.65161E+11	1434856591	2.77462E+11	**2.08244E+13**	**837439.7771**	66.61956725	-12.67777432	53.942	-79.297
		8000	10000	9946.551	172497.3	94291	11000	8.3661E+10	2.62378E+11	1372471522	2.74132E+11	**2.08244E+13**	**837439.7771**	65.82001799	-12.67777432	53.142	-78.498
		9000	10000	9946.551	171497.3	93291	10500	8.3176E+10	2.59595E+11	1310086453	2.70802E+11	**2.08244E+13**	**837439.7771**	65.02046873	-12.67777432	52.343	-77.698
		10000	10000	9946.551	170497.3	92291	10000	8.2691E+10	2.56813E+11	1247701384	2.67472E+11	**2.08244E+13**	**837439.7771**	64.22091947	-12.67777432	51.543	-76.899
		11000	10000	9948.491	169497.3	91291	9500	8.2206E+10	2.5403E+11	1185316314	2.64142E+11	**2.00744E+13**	**807122.3194**	65.79086509	-13.15398205	52.637	-78.945
		12000	10000	9948.491	168497.3	90291	9000	8.1721E+10	2.51247E+11	1122931245	2.60812E+11	**2.00744E+13**	**807122.3194**	64.96144375	-13.15398205	51.807	-78.115
		13000	10000	9948.491	167497.3	89291	8500	8.1236E+10	2.48465E+11	1060546176	2.57482E+11	**2.00744E+13**	**807122.3194**	64.13202242	-13.15398205	50.978	-77.286
		14000	10000	9948.491	166497.3	88291	8000	8.0751E+10	2.45682E+11	998161106.9	2.54152E+11	**2.00744E+13**	**807122.3194**	63.30260108	-13.15398205	50.149	-76.457
		15000	10000	9948.491	165497.3	87291	7500	8.0266E+10	2.42899E+11	935776037.7	2.50822E+11	**2.00744E+13**	**807122.3194**	62.47317974	-13.15398205	49.319	-75.627
		16000	10000	9950.473	164497.3	86291	7000	7.9781E+10	2.40117E+11	873390968.5	2.47492E+11	**1.93077E+13**	**776142.3984**	64.09158064	-13.67902658	50.413	-77.771
		17000	10000	9950.473	163497.3	85291	6500	7.9296E+10	2.37334E+11	811005899.3	2.44162E+11	**1.93077E+13**	**776142.3984**	63.22922367	-13.67902658	49.550	-76.908
		18000	10000	9950.473	162497.3	84291	6000	7.8811E+10	2.34552E+11	748620830.2	2.40832E+11	**1.93077E+13**	**776142.3984**	62.36686671	-13.67902658	48.688	-76.046
		19000	10000	9950.473	161497.3	83291	5500	7.8326E+10	2.31769E+11	686235761	2.37502E+11	**1.93077E+13**	**776142.3984**	61.50450974	-13.67902658	47.825	-75.184
		20000	10000	9950.473	160497.3	82291	5000	7.7841E+10	2.28986E+11	623850691.8	2.34172E+11	**1.93077E+13**	**776142.3984**	60.64215278	-13.67902658	46.963	-74.321
		21000	10000	9952.483	159497.3	81291	4500	7.7356E+10	2.26204E+11	561465622.6	2.30842E+11	**1.85297E+13**	**744718.5168**	62.28972179	-14.25622200	48.033	-76.546
		22000	10000	9952.483	158497.3	80291	4000	7.6871E+10	2.23421E+11	499080553.4	2.27512E+11	**1.85297E+13**	**744718.5168**	61.39115774	-14.25622200	47.135	-75.647
		23000	10000	9952.483	157497.3	79291	3500	7.6386E+10	2.20638E+11	436695484.3	2.24182E+11	**1.85297E+13**	**744718.5168**	60.49259369	-14.25622200	46.236	-74.749
		24000	10000	9952.483	156497.3	78291	3000	7.5901E+10	2.17856E+11	374310415.1	2.20852E+11	**1.85297E+13**	**744718.5168**	59.59402964	-14.25622200	45.338	-73.850
		25000	10000	9952.483	155497.3	77291	2500	7.5416E+10	2.15073E+11	311925345.9	2.17522E+11	**1.85297E+13**	**744718.5168**	58.69546559	-14.25622200	44.439	-72.952
Tidal Zone	0.15	26000	10000	9954.483	154497.3	76291	2000	7.4931E+10	2.1229E+11	249540276.7	2.14192E+11	**1.77551E+13**	**713444.6732**	60.31836367	-14.88114341	45.437	-75.200
		27000	10000	9954.483	153497.3	75291	1500	7.4446E+10	2.09508E+11	187155207.5	2.10862E+11	**1.77551E+13**	**713444.6732**	59.38059864	-14.88114341	44.499	-74.262
		28000	10000	9954.483	152497.3	74291	1000	7.3961E+10	2.06725E+11	124770138.4	2.07532E+11	**1.77551E+13**	**713444.6732**	58.44283361	-14.88114341	43.562	-73.324
		29000	10000	9954.483	151497.3	73291	500	7.3476E+10	2.03943E+11	62385069.18	2.04202E+11	**1.77551E+13**	**713444.6732**	57.50506858	-14.88114341	42.624	-72.386
		30000	10000	9954.483	150497.3	72291	0	7.2991E+10	2.0116E+11	0	2.00872E+11	**1.77551E+13**	**713444.6732**	56.56730355	-14.88114341	41.686	-71.448
Splash Zone	0.3	31000	10000	9956.473	149497.3	71291	0	7.2506E+10	1.98377E+11	0	1.97604E+11	**1.69839E+13**	**682320.9619**	58.17384255	-15.55993893	42.614	-73.734
		32000	10000	9956.473	148497.3	70291	0	7.2021E+10	1.95595E+11	0	1.94337E+11	**1.69839E+13**	**682320.9619**	57.21186287	-15.55993893	41.652	-72.772
		33000	10000	9956.473	147497.3	69291	0	7.1536E+10	1.92812E+11	0	1.91069E+11	**1.69839E+13**	**682320.9619**	56.24988319	-15.55993893	40.690	-71.810
		34000	10000	9956.473	146497.3	68291	0	7.1051E+10	1.90029E+11	0	1.87801E+11	**1.69839E+13**	**682320.9619**	55.28790351	-15.55993893	39.728	-70.848
		35000	10000	9956.473	145497.3	67291	0	7.0566E+10	1.87247E+11	0	1.84534E+11	**1.69839E+13**	**682320.9619**	54.32592383	-15.55993893	38.766	-69.886
		36000	10000	9957.758	144497.3	66291	0	7.0081E+10	1.84464E+11	0	1.81266E+11	**1.64857E+13**	**662220.1844**	54.97666796	-16.03223935	38.944	-71.009
		37000	10000	9957.758	143497.3	65291	0	6.9596E+10	1.81681E+11	0	1.77998E+11	**1.64857E+13**	**662220.1844**	53.98561608	-16.03223935	37.953	-70.018
		38000	10000	9957.758	142497.3	64291	0	6.9111E+10	1.78899E+11	0	1.74731E+11	**1.64857E+13**	**662220.1844**	52.9945642	-16.03223935	36.962	-69.027
		39000	10000	9957.758	141497.3	63291	0	6.8626E+10	1.76116E+11	0	1.71463E+11	**1.64857E+13**	**662220.1844**	52.00351231	-16.03223935	35.971	-68.036
		40000	10000	9957.758	140497.3	62291	0	6.8141E+10	1.73333E+11	0	1.68195E+11	**1.64857E+13**	**662220.1844**	51.01246043	-16.03223935	34.980	-67.045
		41000	10000	9958.942	139497.3	61291	0	6.7656E+10	1.70551E+11	0	1.64928E+11	**1.60265E+13**	**643697.0160**	51.45474316	-16.49358663	34.961	-67.948
		42000	10000	9958.942	138497.3	60291	0	6.7171E+10	1.67768E+11	0	1.6166E+11	**1.60265E+13**	**643697.0160**	50.43529326	-16.49358663	33.942	-66.929
		43000	10000	9958.942	137497.3	59291	0	6.6686E+10	1.64986E+11	0	1.58392E+11	**1.60265E+13**	**643697.0160**	49.41584335	-16.49358663	32.922	-65.909
		44000	10000	9958.942	136497.3	58291	0	6.6201E+10	1.62203E+11	0	1.55125E+11	**1.60265E+13**	**643697.0160**	48.39639345	-16.49358663	31.903	-64.890
		45000	10000	9958.942	135497.3	57291	0	6.5716E+10	1.5942E+11	0	1.51857E+11	**1.60265E+13**	**643697.0160**	47.37694354	-16.49358663	30.883	-63.871
Atmospheric Zone	0.0625	46000	10000	9960.504	134497.3	56291	0	6.5231E+10	1.56638E+11	0	1.4859E+11	**1.54204E+13**	**619256.8318**	48.17955678	-17.14453835	31.035	-65.324
		47000	10000	9960.504	133497.3	55291	0	6.4746E+10	1.53855E+11	0	1.45322E+11	**1.54204E+13**	**619256.8318**	47.1200378	-17.14453835	29.975	-64.265
		48000	10000	9960.504	132497.3	54291	0	6.4261E+10	1.51072E+11	0	1.42054E+11	**1.54204E+13**	**619256.8318**	46.06051881	-17.14453835	28.916	-63.205
		49000	10000	9960.504	131497.3	53291	0	6.3776E+10	1.4829E+11	0	1.38787E+11	**1.54204E+13**	**619256.8318**	45.00099983	-17.14453835	27.856	-62.146
		50000	10000	9960.504	130497.3	52291	0	6.3291E+10	1.45507E+11	0	1.35519E+11	**1.54204E+13**	**619256.8318**	43.94148085	-17.14453835	26.797	-61.086
		51000	10000	9960.504	129497.3	51291	0	6.2806E+10	1.42724E+11	0	1.32251E+11	**1.54204E+13**	**619256.8318**	42.88196186	-17.14453835	25.737	-60.027
		52000	10000	9960.504	128497.3	50291	0	6.2321E+10	1.39942E+11	0	1.28984E+11	**1.54204E+13**	**619256.8318**	41.82244288	-17.14453835	24.678	-58.967
		53000	10000	9960.504	127497.3	49291	0	6.1836E+10	1.37159E+11	0	1.25716E+11	**1.54204E+13**	**619256.8318**	40.76292389	-17.14453835	23.618	-57.907
		54000	10000	9960.504	126497.3	48291	0	6.1351E+10	1.34376E+11	0	1.22448E+11	**1.54204E+13**	**619256.8318**	39.70340491	-17.14453835	22.559	-56.848
		55000	10000	9960.504	125497.3	47291	0	6.0866E+10	1.31594E+11	0	1.19181E+11	**1.54204E+13**	**619256.8318**	38.64388593	-17.14453835	21.499	-55.788
		56000	10000	9960.504	124497.3	46291	0	6.0381E+10	1.28811E+11	0	1.15913E+11	**1.54204E+13**	**619256.8318**	37.58436694	-17.14453835	20.440	-54.729
		57000	10000	9960.504	123497.3	45291	0	5.9896E+10	1.26029E+11	0	1.12646E+11	**1.54204E+13**	**619256.8318**	36.52484796	-17.14453835	19.380	-53.669
		58000	10000	9960.504	122497.3	44291	0	5.9411E+10	1.23246E+11	0	1.09378E+11	**1.54204E+13**	**619256.8318**	35.46532898	-17.14453835	18.321	-52.610

Appendix A6: *Uniform corrosion effects on normal stresses in tension and compression for corrosion zones.*

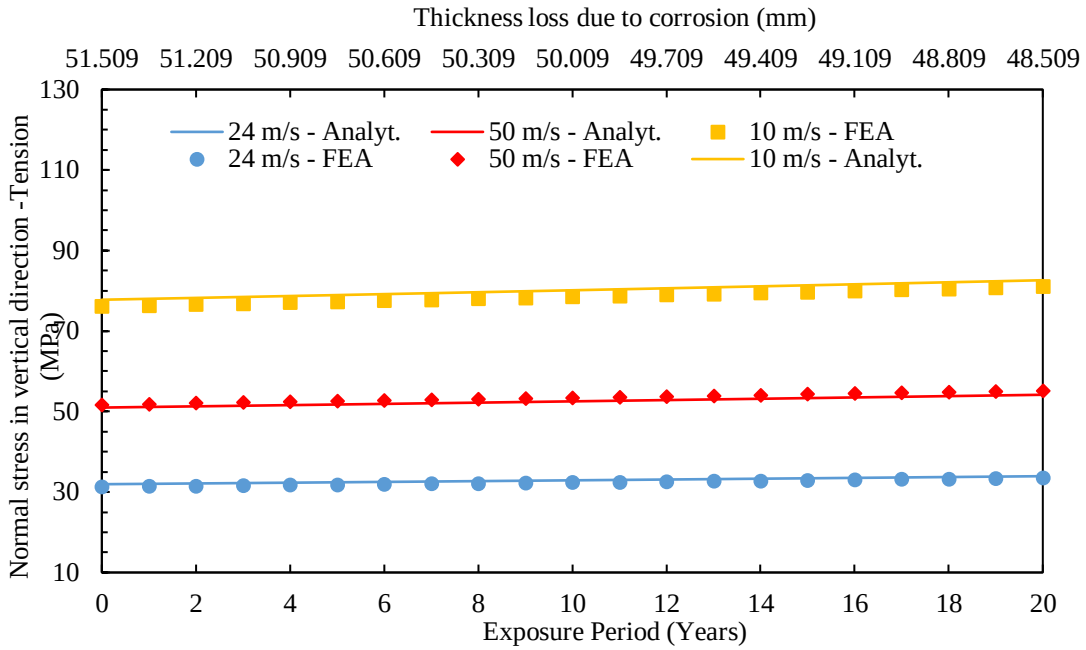

Figure A6-1: Effect of uniform corrosion on tensile stress at the submerged zone

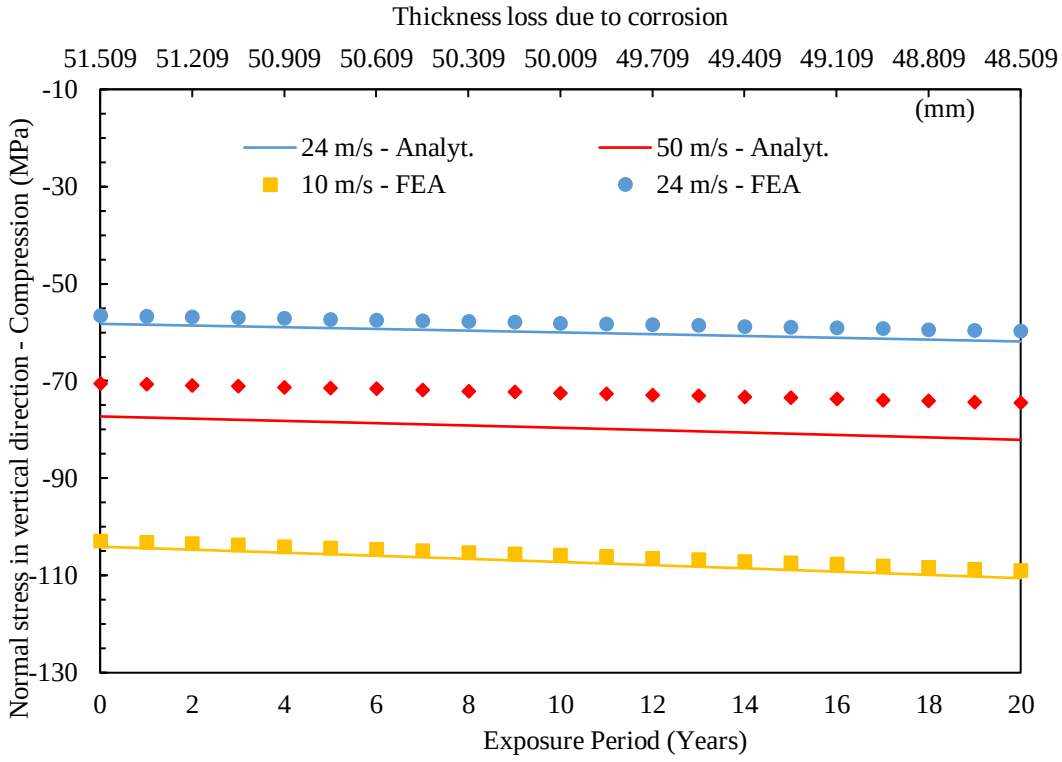

Figure A6-2: Effect of uniform corrosion on compressive stress at the submerged zone

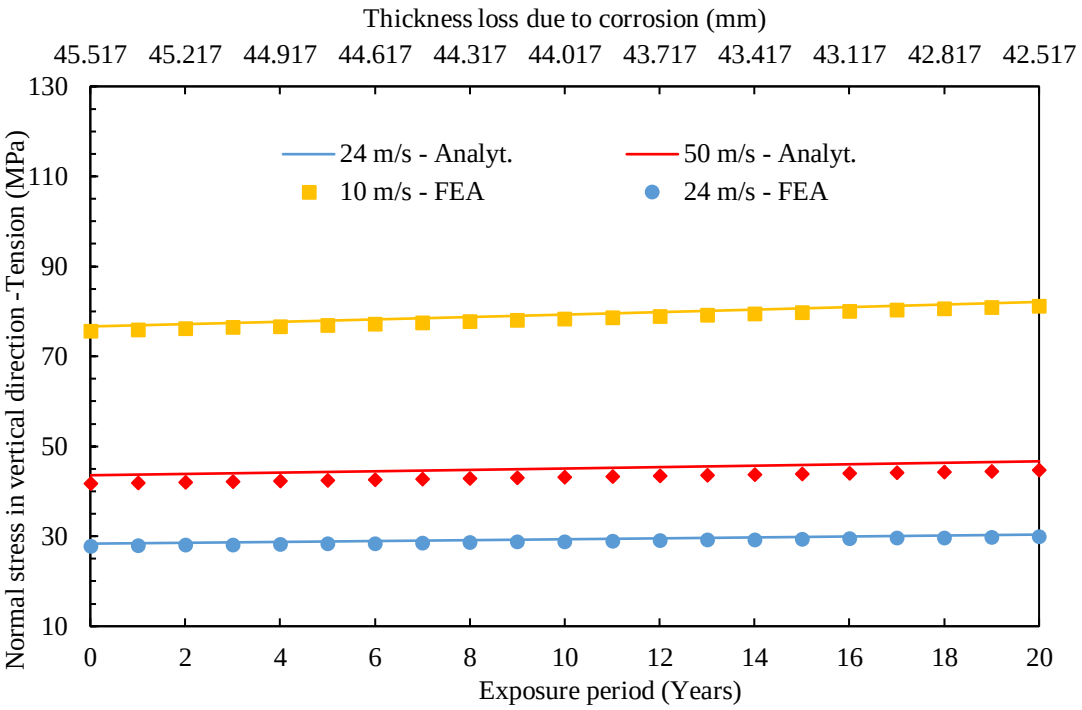

Figure A6-3: Effect of uniform corrosion on tensile the stress at tidal zone

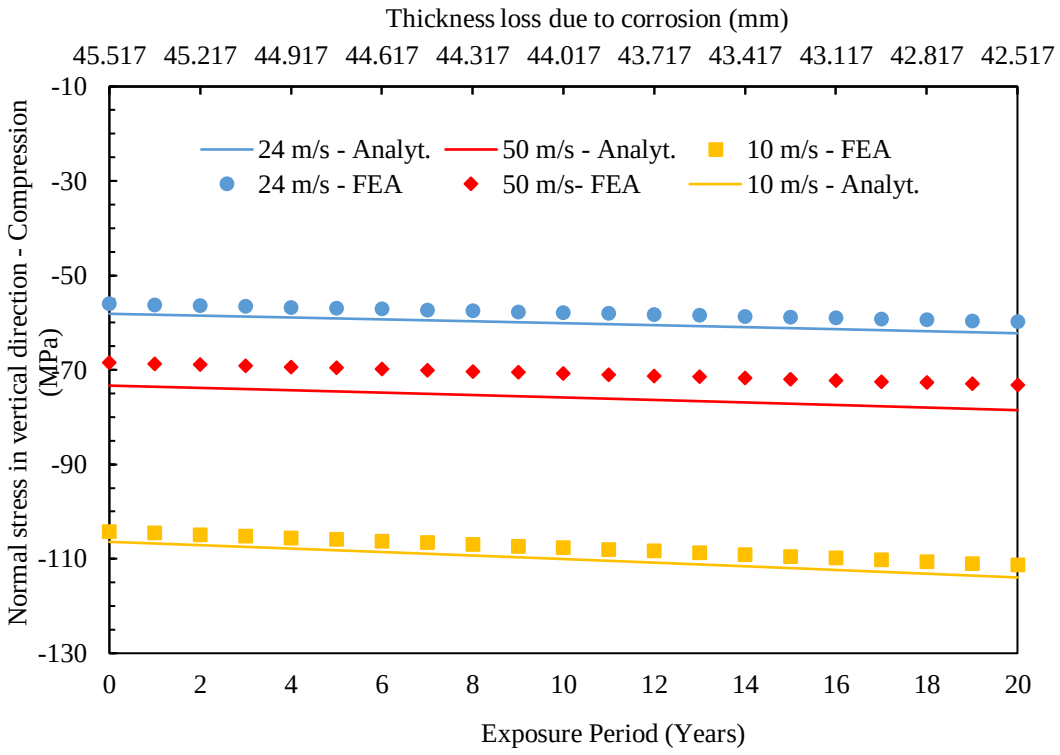

Figure A6-4: Effect of uniform corrosion on compressive stress at the tidal zone

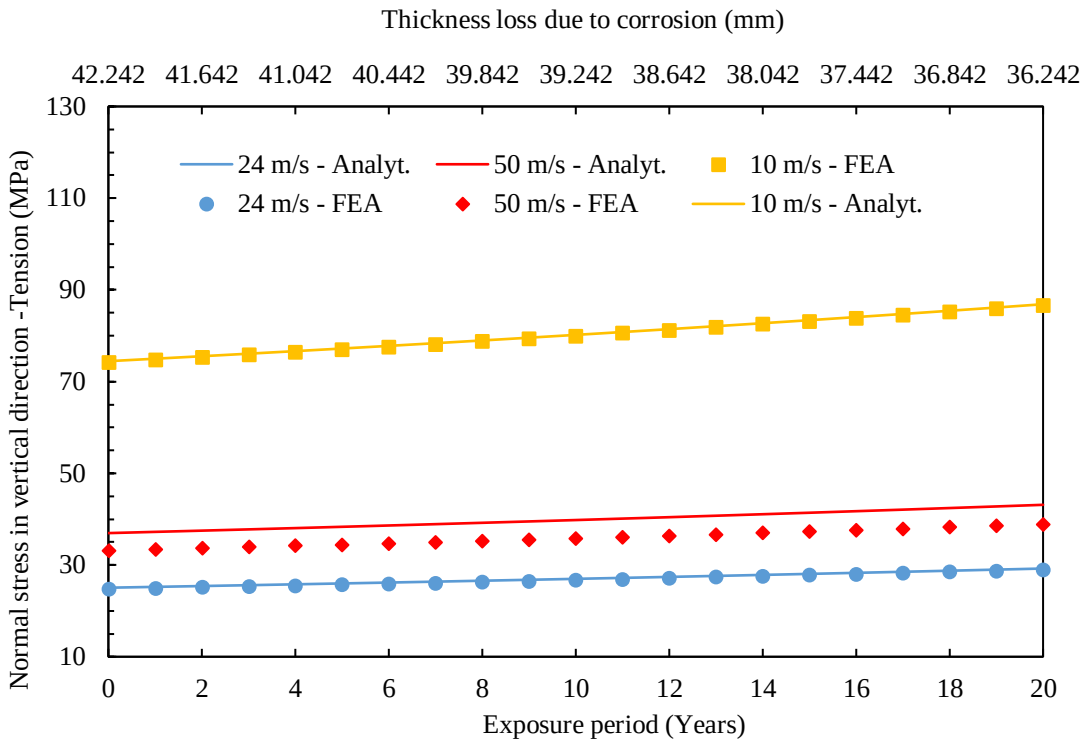

Figure A6-5: Effect of uniform corrosion on tensile stress at the splash zone

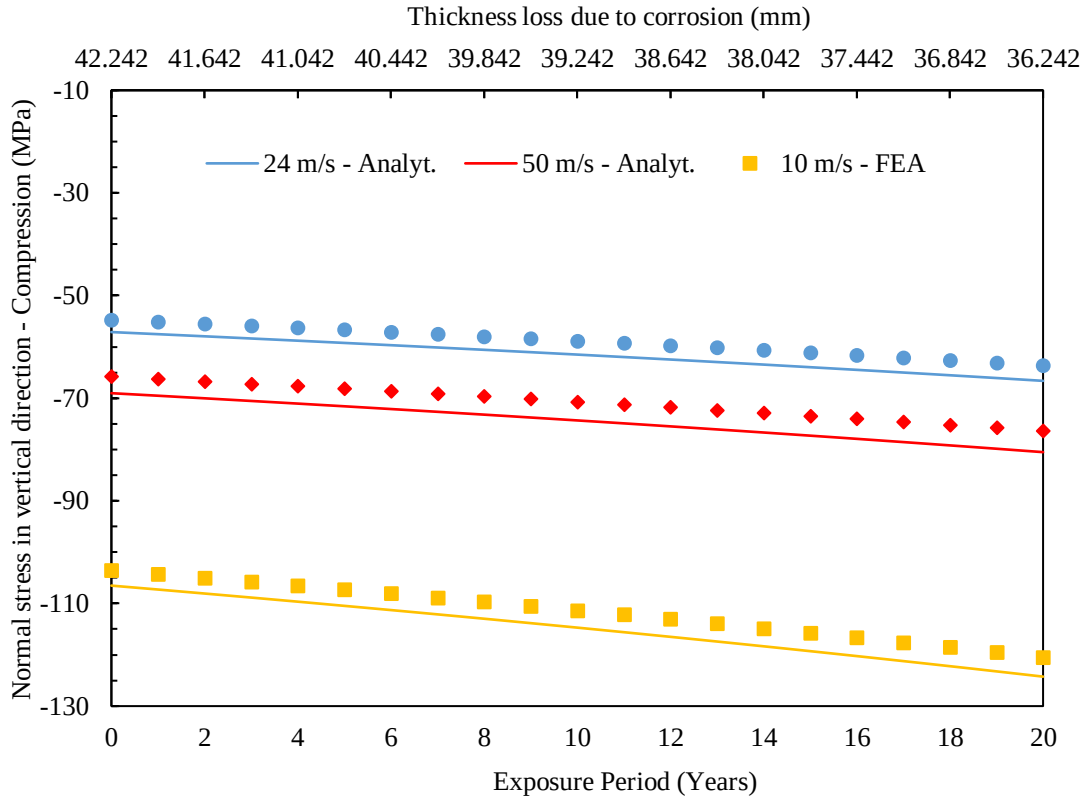

Figure A6-6: Effect of uniform corrosion on compressive stress at the splash zone

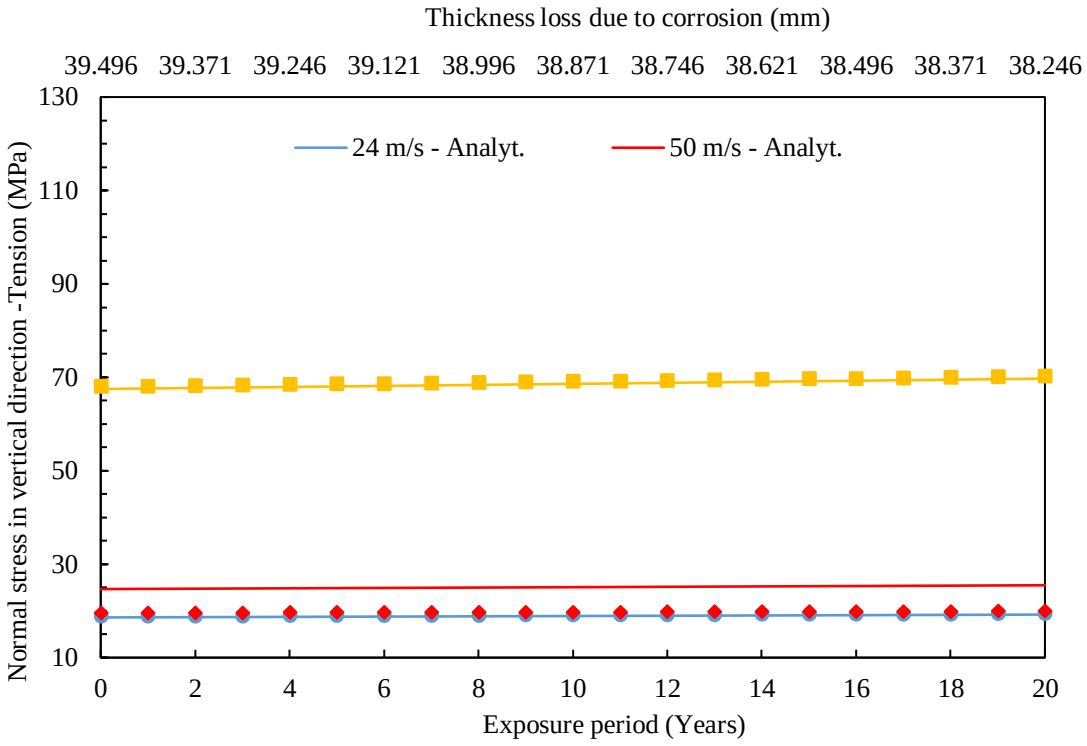

Figure A6-7: Effect of uniform corrosion on tensile stress at the atmospheric zone

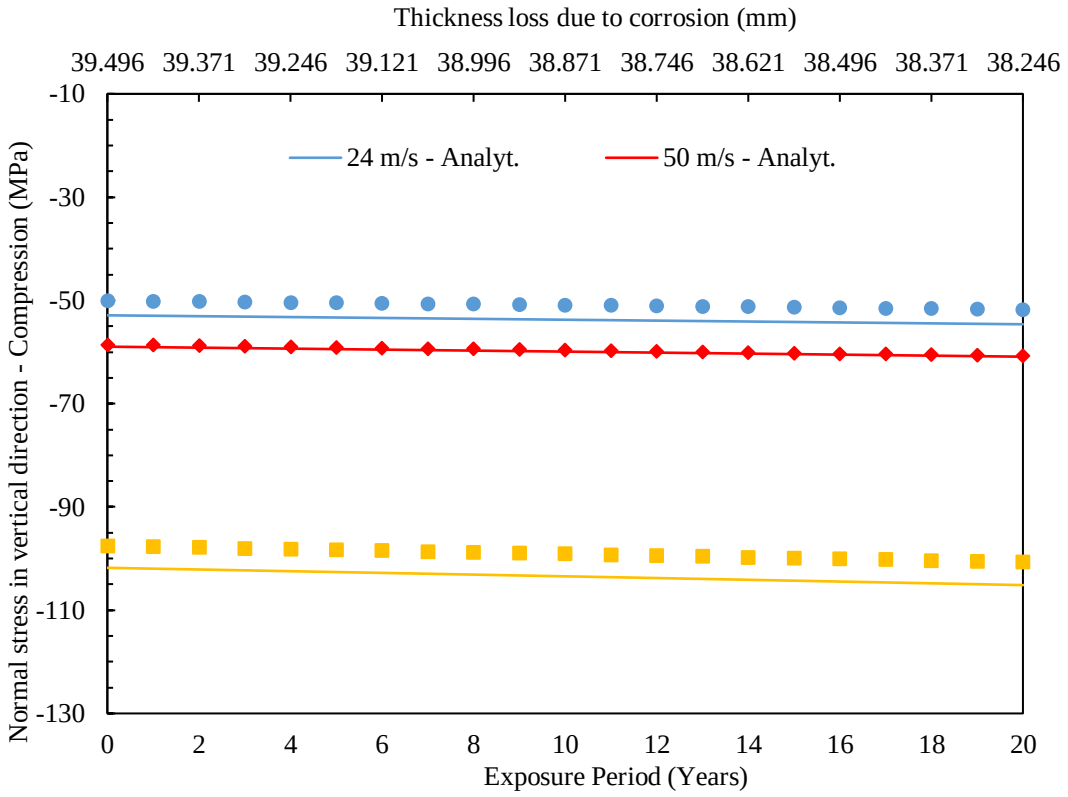

Figure A6-8: Effect of uniform corrosion on compressive stress at the atmospheric zone

Appendix A7: *Data for monopile deflection due to soil models.*

Model 3		Model 2		Model 1		Model 0	
Position from bottom of monopile	Deflection (m)	Position from bottom of monopil	Deflection (m)	Position from bottom of monopil	Deflection (m)	Position from bottom of monopil	Deflection (m)
0	4E-05	0	-0.004	0	-3.83E-04	0	-6E-05
0.242	-0.0013	0.242	-0.007	0.242	7.00E-04	0.242	-6E-05
0.4839	-0.0014	0.4839	-0.008	0.4839	4.23E-04	0.4839	-6E-05
0.7259	-0.0014	0.7259	-0.008	0.7259	1.52E-04	0.7259	-6E-05
0.9679	-0.0015	0.9679	-0.008	0.9679	-1.07E-04	0.9679	-6E-05
1.2098	-0.0016	1.2098	-0.008	1.2098	-5.81E-04	1.2098	-6E-05
1.4518	-0.0017	1.4518	-0.008	1.4518	-1.01E-03	1.4518	-6E-05
1.6937	-0.0017	1.6937	-0.007	1.6937	-1.39E-03	1.6937	-6E-05
1.9357	-0.0017	1.9357	-0.007	1.9357	-1.73E-03	1.9357	-6E-05
2.1777	-0.0018	2.1777	-0.007	2.1777	-2.02E-03	2.1777	-6E-05
2.4196	-0.0018	2.4196	-0.007	2.4196	-2.26E-03	2.4196	-6E-05
2.6616	-0.0018	2.6616	-0.007	2.6616	-2.46E-03	2.6616	-6E-05
2.9036	-0.0018	2.9036	-0.005	2.9036	-2.62E-03	2.9036	-6E-05
3.1455	-0.0019	3.1455	-0.004	3.1455	-2.72E-03	3.1455	-6E-05
3.3875	-0.0019	3.3875	-0.004	3.3875	-2.79E-03	3.3875	-6E-05
3.6294	-0.0019	3.6294	-0.004	3.6294	-2.80E-03	3.6294	-6E-05
3.8714	-0.0019	3.8714	-0.004	3.8714	-2.77E-03	3.8714	-6E-05
4.1134	-0.0019	4.1134	-0.004	4.1134	-2.70E-03	4.1134	-6E-05
4.3553	-0.0019	4.3553	-0.004	4.3553	-2.68E-03	4.3553	-6E-05
4.5973	-0.0018	4.5973	-0.004	4.5973	-2.69E-03	4.5973	-6E-05
4.8393	-0.0018	4.8393	-0.004	4.8393	-2.70E-03	4.8393	-6E-05
5.0812	-0.0018	5.0812	-0.004	5.0812	-2.71E-03	5.0812	-6E-05
5.3232	-0.0018	5.3232	-0.004	5.3232	-2.72E-03	5.3232	-6E-05
5.5651	-0.0018	5.5651	-0.004	5.5651	-2.73E-03	5.5651	-6E-05
5.8071	-0.0017	5.8071	-0.004	5.8071	-2.74E-03	5.8071	-6E-05
6.0491	-0.0017	6.0491	-0.004	6.0491	-2.74E-03	6.0491	-6E-05
6.291	-0.0017	6.291	-0.004	6.291	-2.75E-03	6.291	-6E-05
6.533	-0.0017	6.533	-0.004	6.533	-2.75E-03	6.533	-6E-05
6.775	-0.0017	6.775	-0.004	6.775	-2.76E-03	6.775	-6E-05
7.0169	-0.0018	7.0169	-0.004	7.0169	-2.76E-03	7.0169	-6E-05
7.2589	-0.0018	7.2589	-0.004	7.2589	-2.77E-03	7.2589	-6E-05
7.5008	-0.0018	7.5008	-0.004	7.5008	-2.77E-03	7.5008	-6E-05
7.7428	-0.0018	7.7428	-0.004	7.7428	-2.77E-03	7.7428	-6E-05
7.9848	-0.0018	7.9848	-0.004	7.9848	-2.77E-03	7.9848	-6E-05
8.2267	-0.0018	8.2267	-0.004	8.2267	-2.78E-03	8.2267	-6E-05
8.4687	-0.0018	8.4687	-0.004	8.4687	-2.79E-03	8.4687	-6E-05
8.7107	-0.0018	8.7107	-0.004	8.7107	-2.80E-03	8.7107	-6E-05
8.9526	-0.0018	8.9526	-0.004	8.9526	-2.80E-03	8.9526	-6E-05
9.1946	-0.0018	9.1946	-0.004	9.1946	-2.81E-03	9.1946	-6E-05
9.4365	-0.0018	9.4365	-0.004	9.4365	-2.81E-03	9.4365	-6E-05
9.6785	-0.0017	9.6785	-0.004	9.6785	-2.81E-03	9.6785	-6E-05
9.9205	-0.0017	9.9205	-0.004	9.9205	-2.81E-03	9.9205	-6E-05
10.162	-0.0017	10.162	-0.004	10.162	-2.81E-03	10.162	-5E-05
10.404	-0.0017	10.404	-0.004	10.404	-2.81E-03	10.404	-5E-05
10.646	-0.0017	10.646	-0.004	10.646	-2.81E-03	10.646	-5E-05
10.888	-0.0018	10.888	-0.004	10.888	-2.81E-03	10.888	-5E-05
11.13	-0.0018	11.13	-0.004	11.13	-2.81E-03	11.13	-5E-05
11.372	-0.0018	11.372	-0.004	11.372	-2.80E-03	11.372	-5E-05
11.614	-0.0018	11.614	-0.004	11.614	-2.80E-03	11.614	-5E-05
11.856	-0.0018	11.856	-0.004	11.856	-2.80E-03	11.856	-5E-05
12.098	-0.0018	12.098	-0.004	12.098	-2.80E-03	12.098	-5E-05
12.34	-0.0018	12.34	-0.004	12.34	-2.79E-03	12.34	-5E-05
12.582	-0.0018	12.582	-0.004	12.582	-2.79E-03	12.582	-5E-05
12.823	-0.0018	12.823	-0.004	12.823	-2.79E-03	12.823	-5E-05
13.064	-0.0018	13.064	-0.004	13.064	-2.79E-03	13.064	-5E-05
13.304	-0.0018	13.304	-0.004	13.304	-2.79E-03	13.304	-5E-05
13.545	-0.0017	13.545	-0.003	13.545	-2.79E-03	13.545	-5E-05
13.786	-0.0017	13.786	-0.003	13.786	-2.78E-03	13.786	-5E-05
14.027	-0.0017	14.027	-0.003	14.027	-2.78E-03	14.027	-5E-05
14.267	-0.0017	14.267	-0.003	14.267	-2.78E-03	14.267	-5E-05
14.508	-0.0017	14.508	-0.003	14.508	-2.78E-03	14.508	-5E-05
14.749	-0.0018	14.749	-0.003	14.749	-2.78E-03	14.749	-5E-05
14.99	-0.0018	14.99	-0.002	14.99	-2.78E-03	14.99	-5E-05
15.23	-0.0018	15.23	-0.002	15.23	-2.78E-03	15.23	-5E-05
15.471	-0.0018	15.471	-0.002	15.471	-2.78E-03	15.471	-5E-05
15.712	-0.0018	15.712	-0.002	15.712	-2.78E-03	15.712	-5E-05
15.952	-0.0018	15.952	-0.002	15.952	-2.78E-03	15.952	-5E-05
16.193	-0.0018	16.193	-0.002	16.193	-2.78E-03	16.193	-5E-05
16.434	-0.0018	16.434	-0.002	16.434	-2.78E-03	16.434	-5E-05
16.675	-0.0018	16.675	-0.002	16.675	-2.77E-03	16.675	-5E-05
16.915	-0.0018	16.915	-0.002	16.915	-2.77E-03	16.915	-5E-05
17.156	-0.0018	17.156	-0.002	17.156	-2.77E-03	17.156	-5E-05
17.397	-0.0017	17.397	-0.002	17.397	-2.77E-03	17.397	-5E-05
17.638	-0.0017	17.638	-0.001	17.638	-2.77E-03	17.638	-5E-05
17.878	-0.0017	17.878	-0.002	17.878	-2.77E-03	17.878	-5E-05
18.119	-0.0017	18.119	-0.002	18.119	-2.77E-03	18.119	-5E-05
18.36	-0.0017	18.36	-0.001	18.36	-2.77E-03	18.36	-5E-05
18.601	-0.0018	18.601	-0.001	18.601	-2.77E-03	18.601	-5E-05
18.841	-0.0018	18.841	-0.001	18.841	-2.76E-03	18.841	-5E-05
19.082	-0.0018	19.082	-8E-04	19.082	-2.76E-03	19.082	-5E-05
19.323	-0.0018	19.323	-7E-04	19.323	-2.76E-03	19.323	-5E-05
19.564	-0.0018	19.564	-6E-04	19.564	-2.76E-03	19.564	-5E-05
19.804	-0.0018	19.804	-4E-04	19.804	-2.76E-03	19.804	-5E-05
20.045	-0.0018	20.045	-3E-04	20.045	-2.76E-03	20.045	-5E-05
20.286	-0.0018	20.286	-9E-05	20.286	-2.76E-03	20.286	-5E-05
20.527	-0.0018	20.527	7E-05	20.527	-2.75E-03	20.527	-5E-05
20.767	-0.0018	20.767	0.0002	20.767	-2.75E-03	20.767	-5E-05
21.008	-0.0018	21.008	0.0004	21.008	-2.75E-03	21.008	-5E-05
21.249	-0.0017	21.249	0.0006	21.249	-2.75E-03	21.249	-5E-05
21.49	-0.0017	21.49	0.0007	21.49	-2.75E-03	21.49	-5E-05
21.73	-0.0017	21.73	0.0009	21.73	-2.75E-03	21.73	-5E-05
21.971	-0.0017	21.971	0.0011	21.971	-2.74E-03	21.971	-5E-05
22.212	-0.0017	22.212	0.0012	22.212	-2.74E-03	22.212	-5E-05
22.453	-0.0018	22.453	0.0014	22.453	-2.74E-03	22.453	-5E-05
22.693	-0.0018	22.693	0.0016	22.693	-2.74E-03	22.693	-5E-05
22.934	-0.0018	22.934	0.0018	22.934	-2.74E-03	22.934	-5E-05
23.175	-0.0018	23.175	0.0019	23.175	-2.73E-03	23.175	-5E-05
23.416	-0.0018	23.416	0.0021	23.416	-2.73E-03	23.416	-5E-05
23.656	-0.0018	23.656	0.0023	23.656	-2.73E-03	23.656	-5E-05
23.897	-0.0018	23.897	0.0025	23.897	-2.73E-03	23.897	-5E-05
24.138	-0.0018	24.138	0.0027	24.138	-2.72E-03	24.138	-5E-05
24.379	-0.0018	24.379	0.003	24.379	-2.72E-03	24.379	-5E-05
24.619	-0.0018	24.619	0.0032	24.619	-2.72E-03	24.619	-5E-05
24.86	-0.0017	24.86	0.0034	24.86	-2.72E-03	24.86	-5E-05
25.101	-0.0017	25.101	0.0036	25.101	-2.71E-03	25.101	-5E-05
25.342	-0.0017	25.342	0.0039	25.342	-2.71E-03	25.342	-5E-05
25.582	-0.0017	25.582	0.0041	25.582	-2.71E-03	25.582	-5E-05
25.823	-0.0017	25.823	0.0043	25.823	-2.70E-03	25.823	-5E-05
26.064	-0.0017	26.064	0.0045	26.064	-2.70E-03	26.064	-5E-05
26.305	-0.0017	26.305	0.0048	26.305	-2.70E-03	26.305	-5E-05
26.545	-0.0018	26.545	0.005	26.545	-2.69E-03	26.545	-5E-05
26.786	-0.0018	26.786	0.0052	26.786	-2.69E-03	26.786	-5E-05
27.027	-0.0018	27.027	0.0055	27.027	-2.69E-03	27.027	-5E-05
27.268	-0.0017	27.268	0.0057	27.268	-2.68E-03	27.268	-5E-05
27.508	-0.0017	27.508	0.006	27.508	-2.68E-03	27.508	-5E-05
27.749	-0.0017	27.749	0.0062	27.749	-2.67E-03	27.749	-5E-05
27.99	-0.0017	27.99	0.0065	27.99	-2.67E-03	27.99	-5E-05
28.231	-0.0017	28.231	0.0068	28.231	-2.66E-03	28.231	-5E-05
28.471	-0.0017	28.471	0.0071	28.471	-2.66E-03	28.471	-5E-05
28.712	-0.0017	28.712	0.0073	28.712	-2.65E-03	28.712	-5E-05
28.953	-0.0017	28.953	0.0076	28.953	-2.65E-03	28.953	-5E-05
29.194	-0.0016	29.194	0.008	29.194	-2.64E-03	29.194	-5E-05
29.434	-0.0016	29.434	0.0083	29.434	-2.64E-03	29.434	-5E-05
29.675	-0.0016	29.675	0.0086	29.675	-2.63E-03	29.675	-5E-05
29.916	-0.0016	29.916	0.009	29.916	-2.63E-03	29.916	-5E-05
30.157	-0.0017	30.157	0.0094	30.157	-2.62E-03	30.157	-5E-05
30.397	-0.0017	30.397	0.0096	30.397	-2.62E-03	30.397	-5E-05
30.638	-0.0017	30.638	0.0099	30.638	-2.61E-03	30.638	-5E-05
30.879	-0.0017	30.879	0.0102	30.879	-2.60E-03	30.879	-5E-05
31.119	-0.0017	31.119	0.0106	31.119	-2.60E-03	31.119	-5E-05
31.36	-0.0016	31.36	0.0111	31.36	-2.59E-03	31.36	-5E-05
31.601	-0.0016	31.601	0.0117	31.601	-2.58E-03	31.601	-5E-05
31.842	-0.0016	31.842	0.0123	31.842	-2.57E-03	31.842	-5E-05
32.082	-0.0016	32.082	0.013	32.082	-2.57E-03	32.082	-5E-05
32.323	-0.0016	32.323	0.0096	32.323	-2.56E-03	32.323	-5E-05
32.564	-0.0016	32.564	0.0105	32.564	-2.55E-03	32.564	-5E-05
32.805	-0.0015	32.805	0.0114	32.805	-2.54E-03	32.805	-5E-05
33.045	-0.0015	33.045	0.0121	33.045	-2.53E-03	33.045	-5E-05
33.286	-0.0015	33.286	0.0128	33.286	-2.52E-03	33.286	-5E-05
33.527	-0.0015	33.527	0.0133	33.527	-2.51E-03	33.527	-5E-05
33.768	-0.0015	33.768	0.0138	33.768	-2.50E-03	33.768	-5E-05
34.008	-0.0015	34.008	0.0142	34.008	-2.49E-03	34.008	-4E-05
34.249	-0.0015	34.249	0.0146	34.249	-2.48E-03	34.249	-4E-05
34.49	-0.0015	34.49	0.0151	34.49	-2.47E-03	34.49	-4E-05

For brevity, only the data from the monopile base and tower top data are provided below.

207.95	2.0239			207.95	2.0107	207.7	1.4402
208.08	2.0299			208.08	2.0167	207.83	1.4453
208.2	2.0359			208.2	2.0227	207.95	1.4504
208.33	2.0419			208.33	2.0287	208.08	1.4555
208.45	2.048			208.45	2.0347	208.2	1.4606
208.58	2.054			208.58	2.0407	208.33	1.4658
208.7	2.06			208.7	2.0467	208.45	1.4709
208.83	2.0661			208.83	2.0528	208.58	1.4761
208.95	2.0722			208.95	2.0588	208.7	1.4813
209.08	2.0783			209.08	2.0649	208.83	1.4865
209.2	2.0844			209.2	2.071	208.95	1.4917
209.33	2.0905			209.33	2.0771	209.08	1.4969
209.46	2.0966			209.46	2.0832	209.2	1.5021
209.58	2.1027			209.58	2.0893	209.33	1.5073
209.71	2.1089			209.71	2.0954	209.46	1.5126
209.83	2.115			209.83	2.1016	209.58	1.5178
209.96	2.1212			209.96	2.1077	209.71	1.5231
210.08	2.1273			210.08	2.1139	209.83	1.5284
210.21	2.1335			210.21	2.12	209.96	1.5337
210.33	2.1397			210.33	2.1262	210.08	1.539
210.46	2.1459			210.46	2.1324	210.21	1.5443
210.58	2.1522			210.58	2.1386	210.33	1.5496
210.71	2.1584			210.71	2.1449	210.46	1.555
210.83	2.1646			210.83	2.1511	210.58	1.5603
210.96	2.1709			210.96	2.1573	210.71	1.5657
211.08	2.1771			211.08	2.1636	210.83	1.571
211.21	2.1834			211.21	2.1698	210.96	1.5764
211.33	2.1897			211.33	2.1761	211.08	1.5818
211.46	2.196			211.46	2.1824	211.21	1.5872
211.58	2.2023			211.58	2.1887	211.33	1.5926
211.71	2.2086			211.71	2.195	211.46	1.5981
211.83	2.215			211.83	2.2013	211.58	1.6035
211.96	2.2213			211.96	2.2076	211.71	1.6089
212.09	2.2277			212.09	2.214	211.83	1.6144
212.21	2.234			212.21	2.2203	211.96	1.6198
212.34	2.2404			212.34	2.2267	212.09	1.6253
212.46	2.2468			212.46	2.2331	212.21	1.6308
212.59	2.2532			212.59	2.2394	212.34	1.6363
212.71	2.2596			212.71	2.2458	212.46	1.6419
212.84	2.266			212.84	2.2522	212.59	1.6474
212.96	2.2724			212.96	2.2587	212.71	1.6529
213.09	2.2788			213.09	2.2651	212.84	1.6585
213.21	2.2853			213.21	2.2715	212.96	1.664
213.34	2.2917			213.34	2.278	213.09	1.6696
213.46	2.2982			213.46	2.2844	213.21	1.6752
213.59	2.3047			213.59	2.2909	213.34	1.6807
213.71	2.3112			213.71	2.2974	213.46	1.6863
213.84	2.3177			213.84	2.3039	213.59	1.6919
213.96	2.3243			213.96	2.3104	213.71	1.6976
214.09	2.3308			214.09	2.3169	213.84	1.7032
214.21	2.3373			214.21	2.3234	213.96	1.7089
214.34	2.3439			214.34	2.33	214.09	1.7145
214.46	2.3504			214.46	2.3365	214.21	1.7202
214.59	2.357			214.59	2.3431	214.34	1.7259
214.71	2.3636			214.71	2.3497	214.46	1.7315
214.84	2.3702			214.84	2.3562	214.59	1.7372
214.97	2.3768			214.97	2.3628	214.71	1.7429
215.09	2.3834			215.09	2.3694	214.84	1.7487
215.22	2.39			215.22	2.376	214.97	1.7544
215.34	2.3966			215.34	2.3826	215.09	1.7601
215.47	2.4033			215.47	2.3892	215.22	1.7658
215.59	2.4099			215.59	2.3959	215.34	1.7716
215.72	2.4166			215.72	2.4025	215.47	1.7774
215.84	2.4232			215.84	2.4092	215.59	1.7831
215.97	2.4299			215.97	2.4158	215.72	1.7889
216.09	2.4366			216.09	2.4225	215.84	1.7947
216.22	2.4433			216.22	2.4292	215.97	1.8005
216.34	2.45			216.34	2.4359	216.09	1.8063
216.47	2.4567			216.47	2.4426	216.22	1.8121
216.59	2.4634			216.59	2.4493	216.34	1.818
216.72	2.4702			216.72	2.456	216.47	1.8238
216.84	2.4769			216.84	2.4628	216.59	1.8297

216.97	2.4837			216.97	2.4695	216.72	1.8355
217.09	2.4905			217.09	2.4763	216.84	1.8414
217.22	2.4972			217.22	2.4831	216.97	1.8473
217.34	2.504			217.34	2.4898	217.09	1.8532
217.47	2.5108			217.47	2.4966	217.22	1.8591
217.59	2.5177			217.59	2.5035	217.34	1.865
217.72	2.5245			217.72	2.5103	217.47	1.8709
217.85	2.5314			217.85	2.5171	217.59	1.8769
217.97	2.5382			217.97	2.524	217.72	1.8829
218.1	2.5451			218.1	2.5308	217.85	1.8888
218.22	2.552			218.22	2.5377	217.97	1.8948
218.35	2.5589			218.35	2.5446	218.1	1.9008
218.47	2.5658			218.47	2.5515	218.22	1.9069
218.6	2.5728			218.6	2.5585	218.35	1.9129
218.72	2.5798			218.72	2.5654	218.47	1.9189
218.85	2.5867			218.85	2.5724	218.6	1.925
218.97	2.5937			218.97	2.5794	218.72	1.9311
219.1	2.6008			219.1	2.5864	218.85	1.9372
219.22	2.6079			219.22	2.5935	218.97	1.9433
219.35	2.615			219.35	2.6006	219.1	1.9495
219.41	2.6218			219.41	2.6074	219.22	1.9557
219.48	2.6286			219.48	2.6142	219.35	1.9619
219.54	2.6373			219.54	2.6228	219.41	1.9679
219.6	2.6433			219.6	2.6349	219.48	1.9739
						219.54	1.9816
						219.6	1.9928

Appendix A8: *Data for soil effects on stresses in monopiles.*

Soil effects on stresses in monopile									
Model	Model 0		Model 1		Model 2		Model 3		
	T	C	T	C	T	C	T	C	Distances
Subb-1	115.616848	-141.9090042	104.7609444	-144.6318283	108.386184	-143.489912	107.1248283	-145.6040268	47.5
Subb-2	115.4930878	-141.8342285	109.9035606	-145.3238983	111.368216	-144.169856	109.8934479	-146.3229599	52.5
Subb-3	115.6335068	-142.1277313	111.9293518	-145.5467682	112.7732	-144.691696	111.3717957	-146.6379852	57.5
Subb-4	115.9063301	-142.6305084	113.2695694	-146.2471695	113.824456	-145.412872	112.6140175	-147.1965866	62.5
Subb-5	116.2298775	-143.2468796	114.3445854	-147.0177536	114.76072	-146.210904	113.7338181	-147.7247162	67.5
Tidal	116.584053	-143.9584274	115.1747856	-147.5566635	115.594194	-146.919248	114.7205944	-148.1468124	72.5
Splash 1	116.8972263	-144.6862946	115.9155846	-148.0134125	116.413584	-147.676512	115.6832771	-148.6424637	77.5
Splash 2	115.3280792	-143.1470642	114.7489357	-146.1907806	114.881296	-145.606336	114.2760925	-146.3514404	82.5
Splash 3	113.3943367	-141.2158661	113.3451996	-144.1928864	112.833868	-142.995704	112.3412895	-143.5587006	87.5
Atm 1	112.3815957	-140.5940529	112.1624782	-142.9400761	111.9781063	-141.9836845	111.5864991	-142.399739	92.388
Atm 2	106.9607232	-134.3674325	106.6760083	-135.8689231	106.5236174	-135.4192974	106.2160839	-135.7243903	97.429
									47.388
									52.429

Appendix A9: *Models in corrosion fatigue studies.*

Category	Reference to classical models	Model description	Expression and parameters
Pitting Corrosion Fracture Mechanics Models	Hoeppner Model (Hoeppner 1979)	Critical pit depth prediction facilitating crack nucleation.	$K = 1.1\sigma\sqrt{\pi(a/Q)}$ $d = Ct^3$ (K, σ, a, Q, t, d and C are stress intensity factor, applied stress, pit length, function based on crack shape, time taken to reach pit depth, pit depth and constant dependent upon material and environment)
	Lindley Model (Lindley et al. 1982)	Threshold stress intensity factor ΔK_{th} determination of crack initiation from the pit.	$\Delta K_{th} = \frac{\Delta\sigma\sqrt{(\pi a)}[1.13 - 0.07(a/c)\hat{0}.5]}{1 + 1.47(a/c)1.64]\hat{0}.5}$ ΔK_{th}, a and c and $\Delta\sigma$ are threshold stress intensity factor, minor axis of semi-elliptical crack, major axis of semi-elliptical crack and applied stress range respectively.
	Kawai and Kasai Model (Kawai and Kasai 1985)	Critical pit depth measurement from which fatigue crack grows by determining allowable stress intensity threshold	$\Delta K_{all} = \Delta\sigma_{all}\sqrt{\pi h_{ma}}$ (where ΔK_{all}, $\Delta\sigma_{all}$, F and h_{max} are allowable stress intensity threshold, allowable stress range, geometric factor and maximum pit depth respectively.
	Chen Model (Chen et al. 1996)	Crack initiation prediction from fatigue crack growth rate	$\Delta K_{tr} = \frac{1.12Kt\Delta\sigma\sqrt{\pi Ctr}}{\Phi}$ $(\Delta a/\Delta N)_{pit} = (C_p/2\pi)\ \beta^2 c^{-2}$ $(\Delta a/\Delta N)_{crack} = C_F(k_t\Delta\sigma)^n\ \phi^{-n} c^{0.5n} f$ where ΔK_{tr} is SIF for transition, K_t is elastic stress concentration factor, c is half-pit diameter, Δσ is applied stress range, Φ is shape factor determined by the pit diameter, β is pit aspect ratio, f is cyclic frequency, and C_F, C_p and n are constants.
	Kondo Model (Kondo 1989)	Critical pit condition estimation using stress intensity and pit characteristics	$\Delta K_p = 2.24\sigma_a\sqrt{\pi c\alpha/Q}$ $c = C_p t^{1/3} = Cp(N/f)^{1/3}$ where σ_a, Q, c, t, N, and f represent the stress amplitude, pit aspect ratio, shape factor, pit radius, number of fatigue cycles and cyclic frequency respectively.
Corrosion Fatigue Multi-Stage Predictive Model	Multi-stage Model (Lishchuk et al. 2011)	CF prediction from the combination of pitting corrosion fatigue models at pit growth and crack growth stages	$N_{cf} = N_{sf} + N_{pg} + N_{ptc} + N_{cfsc} + N_{cflc}$ where N_{cf} is the corrosion fatigue life, N_{sf}, number of cycles to scale break down, N_{pg}, the number of cycles for pit growth, N_{ptc}, the number of cycles to pit-to-crack transition, N_{cfsc}, the number of cycles for corrosion fatigue short crack growth and N_{cflc} is the number of cycles to corrosion fatigue long crack growth.
Corrosion Fatigue Predictive Models	Superposition Model (Wei and Gao 1983)	Crack growth rate prediction from the superposition of rate of plasticity-informed crack and a plasticity-chemically-informed crack	$(\Delta a/\Delta N)_e = (\Delta a/\Delta N)_m + (\Delta a/\Delta N)_{cf}$ where $(\Delta a/\Delta N)_e$ is the crack growth rate in an aggressive environment, $(\Delta a/\Delta N)_m$ is the rate of plasticity-driven fatigue crack propagation in an inert environment and $(\Delta a/\Delta N)_{cf}$ is the difference between the total growth rate and 'pure' fatigue growth rate
	The Competition Model (Austen, IM and Walker 1984)	CF crack prediction expressed as competition between mechanical fatigue and CF (when crack growth rate exceeds pit growth rate)	$(\Delta a/\Delta N)_e = (\Delta a/\Delta N)_m(\theta) + (\Delta a/\Delta N)_{cf}(\theta)$ where θ = 1
	Short Crack Growth Model (Akid and Miller 1991)	Crack growth rate prediction from the addition of crack growth rate in air and crack growth rate in a dissolved environment based on anodic dissolution	$(\Delta a/\Delta N)_{env} = (\Delta a/\Delta N)_{air} + (\Delta a/\Delta N)_{diss}$ $(\Delta a/\Delta N)_{diss} = (Mi_a/ZF\rho)\cdot 1/w$ where M is the atomic weight of the corroding metal, i_a is the anodic dissolution current, Z is the valency, F is the Faraday's constant, ρ is density and w is the cyclic frequency

Appendix A10: *Reviewed S-n curve data for welded structural steel compared against fatigue design standards.*

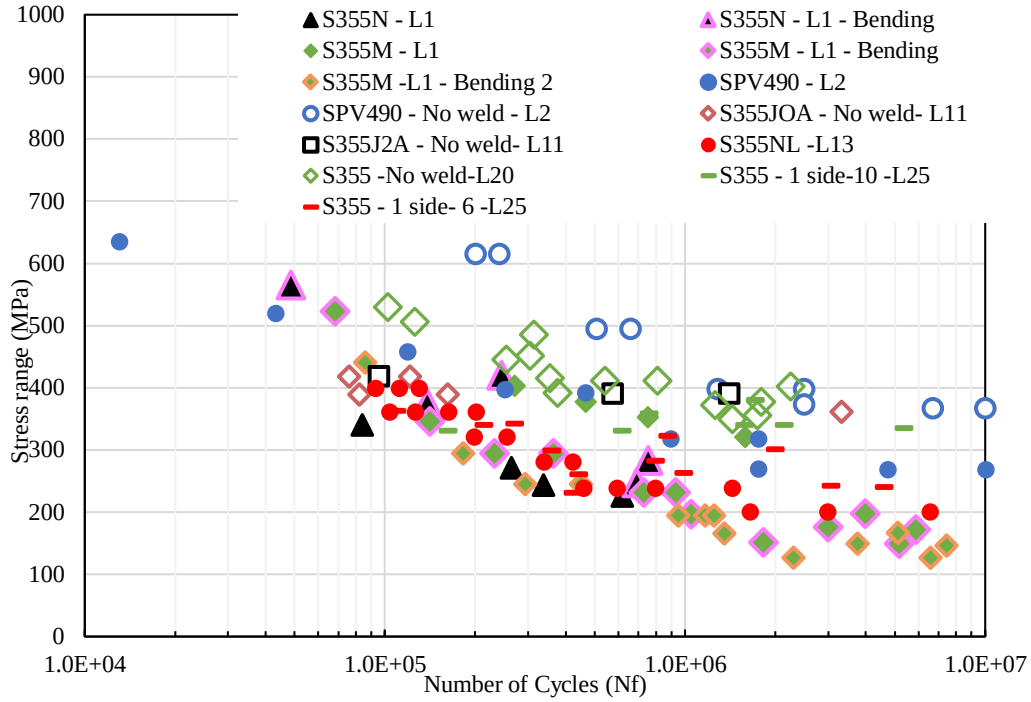

Figure A10-1: SN data at R= -1 in air for as- welded samples

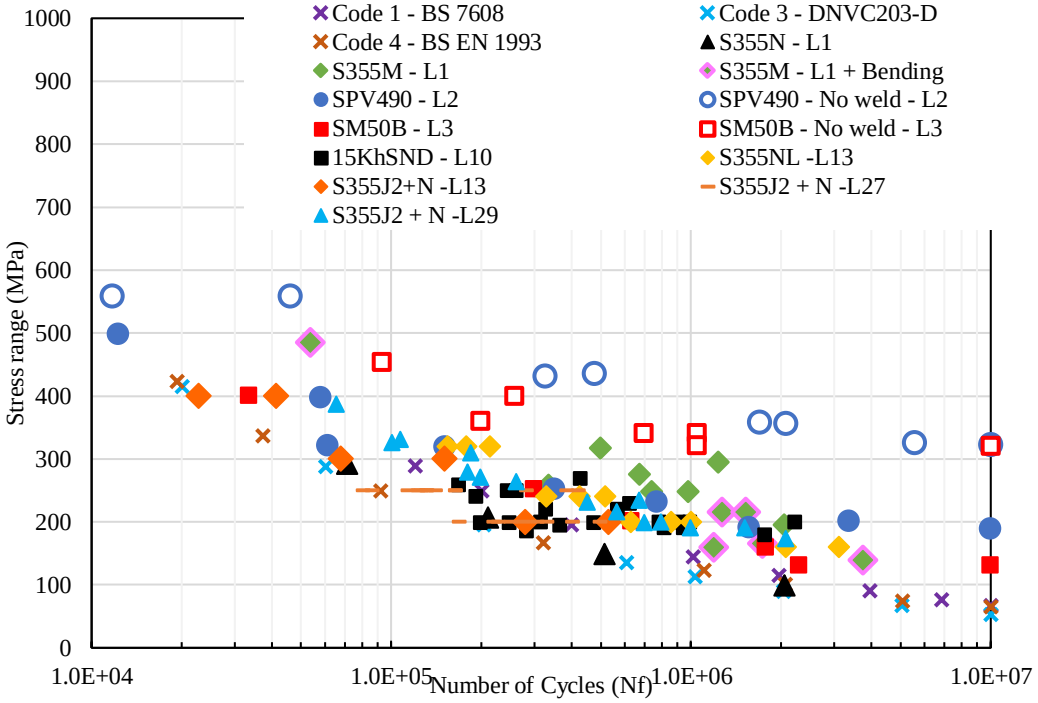

Figure A10-2: S-N data at R= 0 in air for as- welded samples

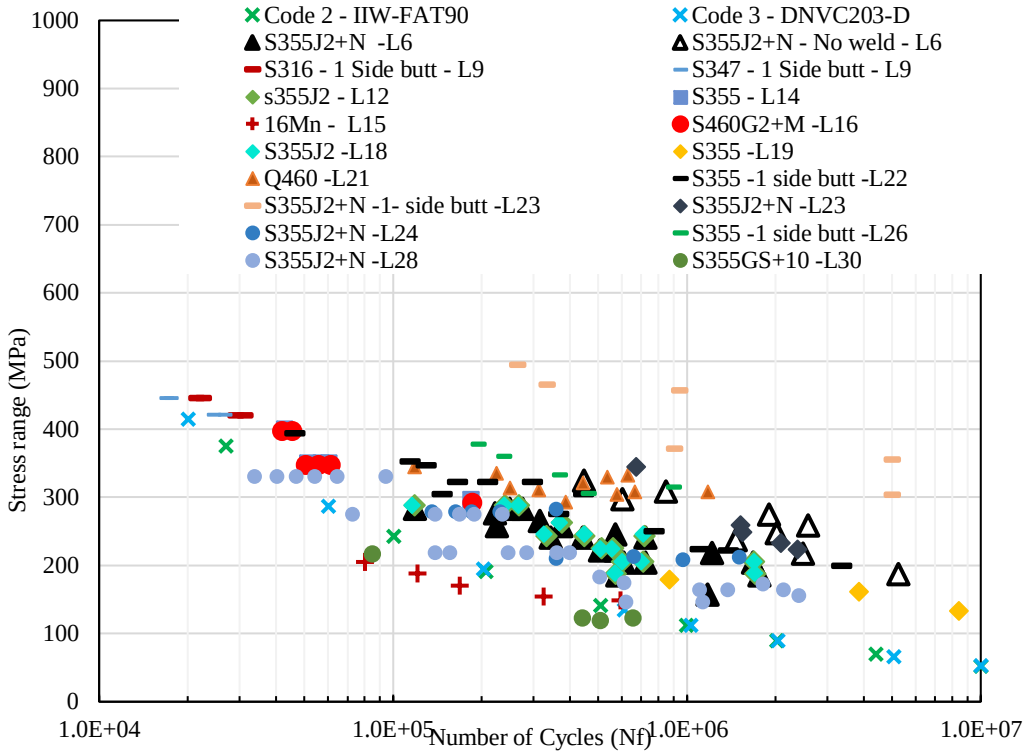

Figure A10-3: S-N data at R= 0.1 in air for as- welded samples

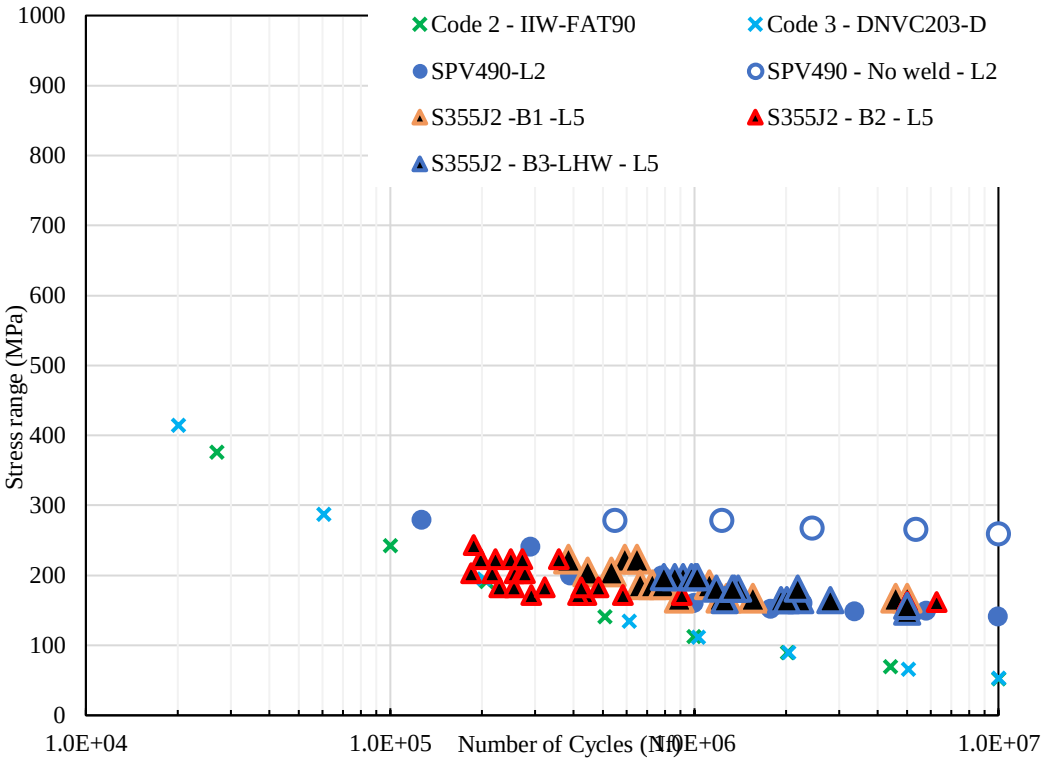

Figure A10-4: S-N data at R= 0.5 in air for as- welded samples

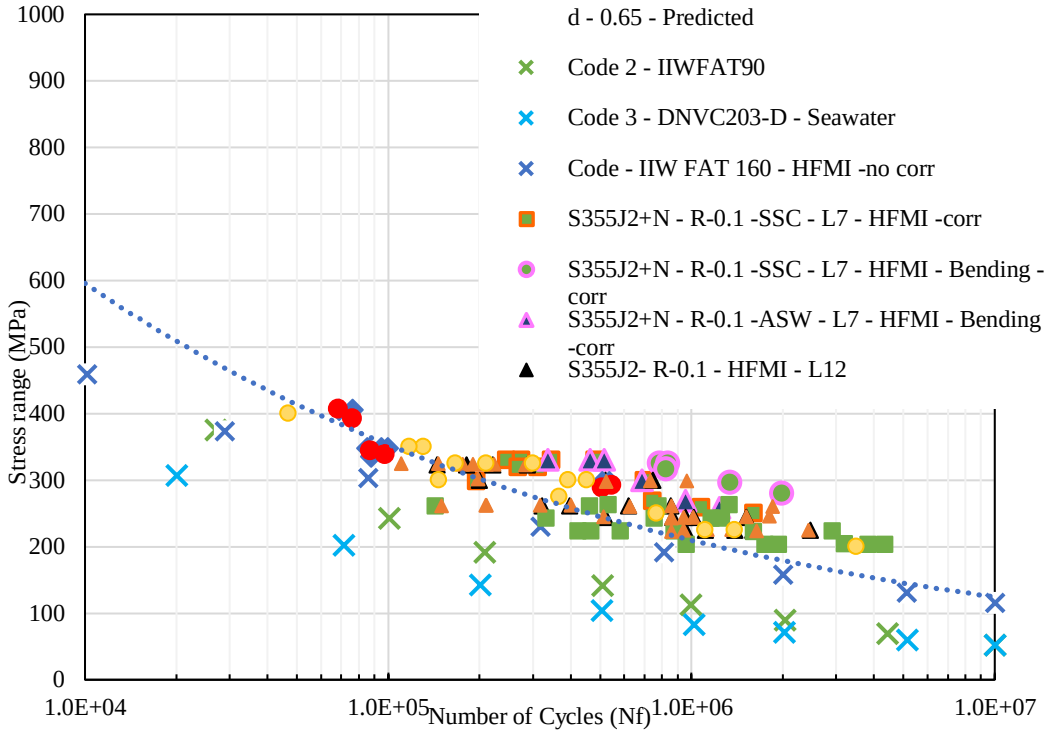

Figure A10-5: S-N data at R= 0.1 in air for high frequency mechanical impact treated samples

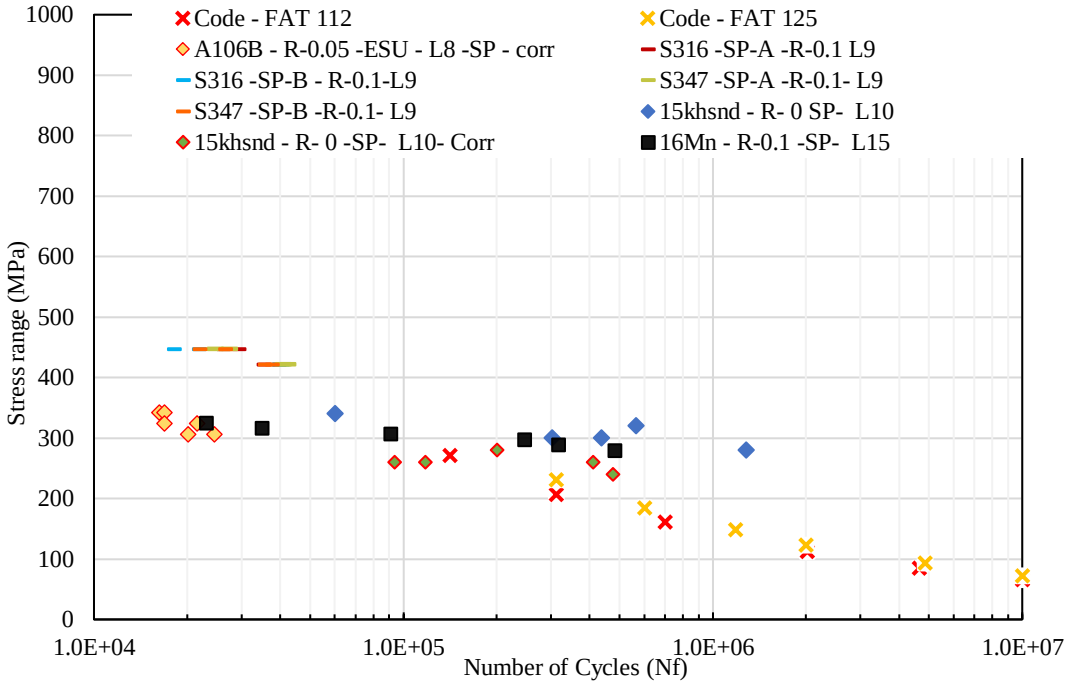

Figure A10-6: S-N data at R= 0.1 in air for high shot-peened samples

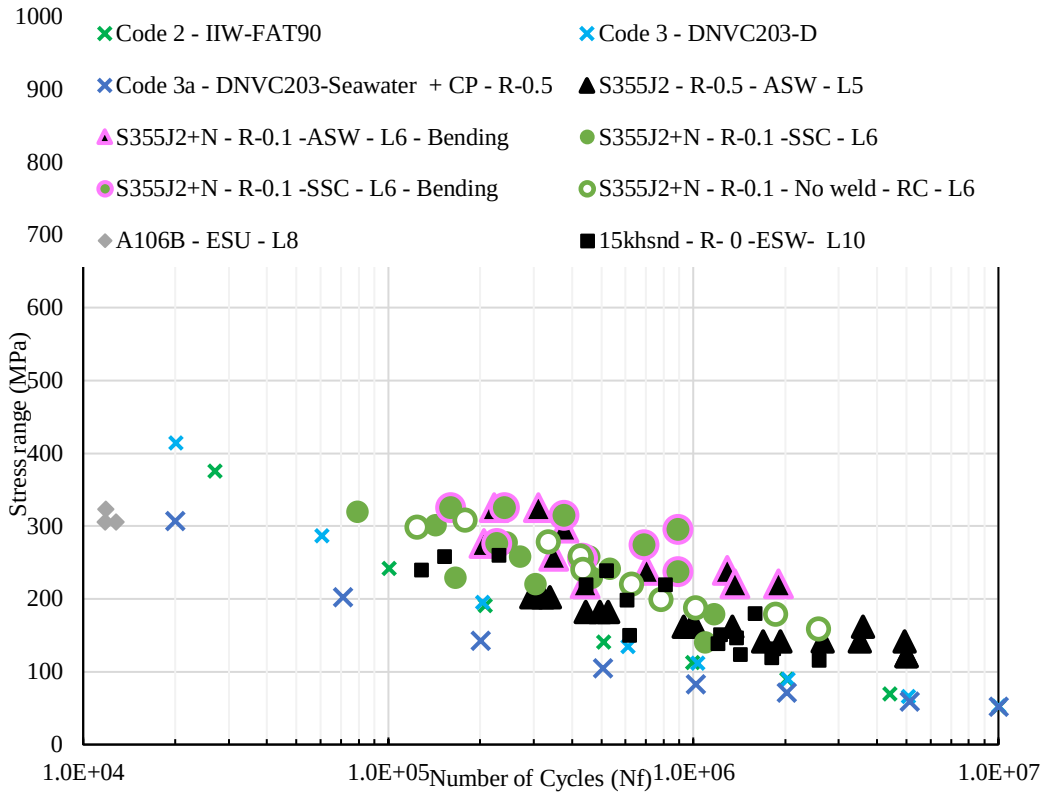

Figure A10-7: S-N data at R= 0.1 & 0.5 in different corrosive environments

Appendix B: Material properties and performance test method and results

Appendix B1: *Properties of flux and solid wire electrode.*

Inspection Certificate 3.1

LINCOLN ELECTRIC
THE WELDING EXPERTS

Product Line	**Flux**
Product	**OP 121TT**
Item No.	**W000280042**
Lot/Batch	**D1FX220137**
Wire Class	**OESD3-4-25VCI OE-SD3 4.0x25 STEIN + VCI** EN ISO 14174: S A FB 1 55 AC H5 AWS/ASME Sec. II C / SFA 5.17 F7A8-EH12K

Customer Ref **14748**
Our Reference **817404945**
Quantity **4.0 BAG**
Customer **PREMIER WELDING SERVICES (NORTH) LT**

8 ATLAS WAY
SHEFFIELD S4 7QQ
United Kingdom

Flux Composition (%) According to EN10204 3.1

Al2O3	Fe2O3	SiO2	TiO2	MnO	CaO	MgO	CaF2
19.6	**2.8**	**12.0**	**1.3**	**1.3**	**6.9**	**29.1**	**21.8**

Sieve analysis (%) According to EN10204 3.1

< 0,315	0,315-0,5	0,5-1 mm	1-1,6 mm	> 1,6 mm
0.80	**9.40**	**49.90**	**32.40**	**7.60**

Diffusible hydrogen	**Moisture check (1000°)**	According to EN10204 2.2
HDM as Manufactured	Moisture 1000C	
3.0 ml/100g	**0.03 %**	

Chemical analysis (%) / Batch: F1SW200628 OE-SD3 4.0x25 STEIN + VCI 25KG According to EN10204 3.1

C	Si	Mn	P	S	Cr	Ni	Mo	Cu	V	Al	N
0.11	**0.30**	**1.75**	**0.007**	**0.005**	**0.03**	**0.02**	**<0.01**	**0.010**	**<0.01**	**<0.01**	**0.004**

Chemical analysis (%) / Weld Metal According to EN10204 2.2

C	Si	Mn	P	S
0.11	**0.25**	**1.54**	**0.013**	**0.004**

Mechanical tests, all weld metal According to EN10204 2.2

Tensile testing

Cond.	Temp. °C	Rp0.2 MPa	Rm MPa	A5 %	Z %
AW	**20**	**501**	**590**	**29**	**77**

Impact testing

Cond.	Temp. °C	C1a J	C1b J	C1c J	KV J
AW	**-60**	**200**	**196**	**187**	**194**

Remarks

The product identified above has been manufactured, tested and supplied in compliance with a certified ISO 9001 Quality Assurance Programme.

Company
Lincoln Electric UK Limited
Mansfield Road
S26 2BS Aston, Sheffield
United Kingdom

Printed By David Sawford Function Arcese Warehouse Operative ZEU_FLUX . 1 Date JUN/17/2022

Cert. No. **01769559**

OERLIKON SAF-FRO METRODE WELDING CONSUMABLES SPECIAL ALLOYS

iabco
Quality Assured
Welding Wires

I.A.Barnes & Co Ltd
Unit 21, Gunnels Wood Park
Gunnels Wood Road
Stevenage, Hertfordshire
SG1 2BH, UK
Tel: +44 (0)1438 354972
Fax: +44 (0)1438 741530
www.iabco.co.uk

Test Certificate: **113071**

To:
PREMIER WELDING NORTH LTD
8 ATLAS WAY
ATLAS NORTH INDUSTRIAL ESTATE
SHEFFIELD
S4 7QQ

Date: 17/06/2022
Order No: 14747
Advice Note No: 59113

Material:
IABCO S3Si
2.4mm
Sub Arc x 25KG

Quantity, KG:
25

Cast No: 02637327

Specifications:
AWS A5.17/A5.17M: EH12K. A5.23/A5.23M: EH12K
BS EN ISO 14171-A: S3Si

Chemical Analysis EN 10204: 3.1

C	Si	Mn	P	S	Cr	Ni	Mo	Fe	Cu
0.08	0.27	1.76	0.006	0.004	0.05	0.03	0.01	Bal	0.009

W	Nb	Al	V	Ti	Co	Pb	Sn	B	As
	0.001	0.001	0.003	0.001	0.0020	0.001	0.001	0.0001	0.002

Zr	Ta	Sb	N	Bi	Zn	Mg	Be	Ce	Ca
0.001	0.001	0.0010	0.0022						0.0005

Ag	Ga	Y				X Factor	FN-WRC	OE **	TOE ***

* Copper excluding copper coating. ** Other elements individual. *** Other elements total.

Mechanical properties of pure weld metal EN ISO 15792-1 test report EN 10204: 2.2

	PWHT	Rp0.2 %		Rm		A		Av	
TYPE		Min	Result	Min	Result	Min	Result	Min	Result
	°C/hr	MPa	MPa	MPa	MPa	%	%	J @ °C	J @ °C
SAW									

Certified that the product(s) detailed hereon have been inspected and tested in accordance with the conditions and requirements of the purchase order and unless otherwise noted conform in all respects to the specifications relevant thereto.

Signed on behalf of I.A.Barnes & Co Ltd:
(Valid with electronic signature)

Document: 35. Issue: 6. Date:11.12.2017

iabco Quality Assured Welding Wires

I.A.Barnes & Co Ltd
Unit 21, Gunnels Wood Park
Gunnels Wood Road
Stevenage, Hertfordshire
SG1 2BH, UK
Tel: +44 (0)1438 354972
Fax: +44 (0)1438 741530
www.iabco.co.uk

Test Certificate: **113072**

To:
PREMIER WELDING NORTH LTD
8 ATLAS WAY
ATLAS NORTH INDUSTRIAL ESTATE
SHEFFIELD
S4 7QQ

Date: 17/06/2022
Order No: 14747
Advice Note No: 59113

Material:
IABCO S3Si
3.2mm
Sub Arc x 25KG

Quantity, KG:
25

Cast No:	521494

Specifications:
AWS A5.17/A5.17M: EH12K. A5.23/A5.23M: EH12K
BS EN ISO 14171-A: S3Si

Chemical Analysis EN 10204: 3.1

C	Si	Mn	P	S	Cr	Ni	Mo	Fe	Cu *
0.09	0.28	1.75	0.007	0.004	0.02	0.01	0.00	Bal	0.01

W	Nb	Al	V	Ti	Co	Pb	Sn	B	As
	0.001	0.001	0.001	0.002		0.001	0.000		0.002

Zr	Ta	Sb	N	Bi	Zn	Mg	Be	Ce	Ca
0.001	0.002								

Ag	Ga	Y				X Factor	FN-WRC	OE **	TOE ***

* Copper excluding copper coating. ** Other elements individual. *** Other elements total.

Mechanical properties of pure weld metal EN ISO 15792-1 test report EN 10204: 2.2

	PWHT	Rp0.2 %		Rm		A		Av	
TYPE		Min	Result	Min	Result	Min	Result	Min	Result
	°C/hr	MPa	MPa	MPa	MPa	%	%	J @ °C	J @ °C
SAW									

Certified that the product(s) detailed hereon have been inspected and tested in accordance with the conditions and requirements of the purchase order and unless otherwise noted conform in all respects to the specifications relevant thereto.

Signed on behalf of I.A.Barnes & Co Ltd:
(Valid with electronic signature)

Directors: P.A.Barnes, A.C.Barnes
Registered in Cardiff No: 1654903

Document: 35. Issue: 6. Date:11.12.2017

Appendix B2: *Mechanical properties of S355G10+M plates. (To avoid repetition, only the data for 10mm are provided)*

10 mm steel

62129

ILSENBURGER GROBBLECH
Ein Unternehmen der Salzgitter Gruppe

Abnahmeprüfzeugnis 3.2
Inspection certificate 3.2
DIN EN 10204
(A02)

Nr./No. (A03) **1219355**
Seite/Page 1/6
Datum/Date 26.06.2020

Nr. (A07) Besteller Purchaser (A06)	Order 6614 Rev. 3 08.04.2020 Kröger Staal B.V. 4782 PZ MOERDIJK NIEDERLANDE	Nr. (A07) Empfänger Customer (A06)	Order no. 6614 Kröger Staal B.V. 4782 PZ MOERDIJK NIEDERLANDE

Erzeugnis Product (B01): Grobblech / Heavy plate

Werksauftrags-Nr. Works order No. (A08): 0000102734

Abnahme Inspection (A05): DNVGL **N141X9VG**

Werkstoff und Lieferbedingung Steel grade and terms of delivery (B02–B03):
S355G10+M
EN 10225 08/01
MDS-Y20 Rev.5
DIN EN 10029 B 02/11
DIN EN 10163-2 A UG3 03/05
S355G10MLAPILSEN
Application onboard DNV - classed objects is subject to special consideration.

Kennzeichnung des Materials / Marking of the product (B06)
Herstellerzeichen/Stahlsorte/Schmelzen-Nr/
Erzeugnis-Nr./Sachverständigenstempel
Trademark/Steelgrade/Heat-No/Product-No/
inspector's stamp

Materialdaten / Material data (B01–B99)

Pos. Item	Anzahl Quantity (B08)	Erzeugnis-Nr. Product No. (B07)	Schmelzen-Nr. Heat No. (B07)	Lieferzustand Cond. of delivery (B04)	Dicke x Breite x Länge Thickness x Width x Length (B09–B11) mm x mm x mm
06	1	201301 1	30411	TM	10,00 x 2500,0 x 12000
06	1	201301 2	30411	TM	10,00 x 2500,0 x 12000
06	1	201302 1	30411	TM	10,00 x 2500,0 x 12000
06	1	201303 1	30411	TM	10,00 x 2500,0 x 12000
06	1	201304 1	30411	TM	10,00 x 2500,0 x 12000
06	1	201304 2	30411	TM	10,00 x 2500,0 x 12000
06	1	201305 1	30411	TM	10,00 x 2500,0 x 12000
06	1	201306 1	30411	TM	10,00 x 2500,0 x 12000
06	1	201306 2	30411	TM	10,00 x 2500,0 x 12000
06	1	201309 2	30411	TM	10,00 x 2500,0 x 12000
06	1	201310 2	30411	TM	10,00 x 2500,0 x 12000
06	1	201311 1*)	30411	TM	10,00 x 2500,0 x 10500
06	1	201311 2	30411	TM	10,00 x 2500,0 x 12000
06	1	201312 1	30411	TM	10,00 x 2500,0 x 12000
06	1	201312 2	30411	TM	10,00 x 2500,0 x 12000
06	1	201313 2	30411	TM	10,00 x 2500,0 x 12000
06	1	201314 1*)	30411	TM	10,00 x 2450,0 x 11500
06	1	201315 2	30411	TM	10,00 x 2500,0 x 12000
Σ	18	Gewicht Weight (B12): 41.953 kg kgs		TM: thermomechanisch gewalzt / thermomechanically rolled	

*) Lieferung gemäß der Tolerierungsanfrage Nr.: 49982, 50004
*) Delivery in accordance with tolerance request no.: 49982, 50004

Es wird bestätigt, daß die Lieferung den Anforderungen der Lieferbedingung entspricht.
We hereby certify that the delivered material complies with the terms of the order.
(Z01)
QM-System: Certification as per ISO 9001 since 28 February 1990

Kesten

SAFEGUARDING LIFE, PROPERTY AND THE ENVIRONMENT – 18 64 DNV·GL

Herstellerzeichen Trademark (A04)

Ilsenburger Grobblech GmbH
Veckenstedter Weg 10
D-38871 Ilsenburg
(A01)

Abnahmestempel Inspection Stamp (Z03)

Abnahmebeauftragter Inspection Representative (Z02)

Cyron

ILSENBURGER GROBBLECH
Ein Unternehmen der Salzgitter Gruppe

Abnahmeprüfzeugnis 3.2
Inspection certificate 3.2
DIN EN 10204
(A02)

Nr./No. (A03): **1219355**
Seite/Page: 2/6
Datum/Date: 26.06.2020

Nr. (A07) Besteller Purchaser (A06)	Order 6614 Rev. 3 Kröger Staal B.V. 4782 PZ MOERDIJK NIEDERLANDE	08.04.2020	Nr. (A07) Empfänger Customer (A06)	Order no. 6614 Kröger Staal B.V. 4782 PZ MOERDIJK NIEDERLANDE	
Erzeugnis Product (B01)	Grobblech Heavy plate				Werksauftrags-Nr. Works order No. (A08): 0000102734
					Abnahme Inspection (A05): DNVGL **N141X9VG**

Werkstoff und Lieferbedingung / Steel grade and terms of delivery (B02–B03):
S355G10+M
EN 10225 08/01
MDS-Y20 Rev.5
DIN EN 10029 B 02/11
DIN EN 10163-2 A UG3 03/05
S355G10MLAPILSEN
Application onboard DNV - classed objects is subject to special consideration.

Maßprüfung und Sichtkontrolle auf äußere Beschaffenheit: ohne Beanstandung
Dimensional check and visual examination of the surface condition: without objection

Schmelzenanalyse / Ladle analysis (C70–C99)

Herstellerangaben / Manufacturer standard

Schmelzen-Nr. Heat No. (B07)	C %	Si %	Mn %	P %	S %	N %	Al %	Cu %	Cr %	Ni %
	≤0,12	0,15 – 0,55	≤1,65	≤0,015	≤0,005	≤0,010	0,015–0,055	≤0,30	≤0,20	≤0,70
30411	0,08	0,22	1,36	0,011	0,002	0,007	0,040	0,03	0,04	0,04

Schmelzen-Nr. Heat No. (B07)	V %	Ti %	Nb %	B %	Mo %	As %	Sn %	Pb %	Ca %	EV1 1) %
	≤0,060	≤0,025	≤0,03	≤0,0005	≤0,08	≤0,030	≤0,020	≤0,010	≤0,005	≤0,21
30411	0,003	0,012	0,03	0,0003	0,003	0,003	0,008	0,000	0,001	0,16

Schmelzen-Nr. Heat No. (B07)	Sb %	EV2 2) %	Bi %	EV3 3) %	EV4 4) %	Nb+V %
	≤0,010	≤0,40	≤0,010	≤0,08		≤0,06
30411	0,001	0,32	0,000	0,05	0,11	0,03

1) EV1 : PCM=C+Mn/20+Mo/15+Ni/60+Cr/20+V/10+Cu/20+Si/30+5xB
2) EV2 : CEV=C+Mn/6+Mo/5+Ni/15+Cr/5+V/5+Cu/15
3) EV3 : V+Nb+Ti
4) EV4 : Cr+Cu+Mo+Ni

Stahlherstellung: Sauerstoffaufblasverfahren
Steel making: Basic oxygen process
(C70)

Vakuumbehandelt
vacuum degassed

vollberuhigter Feinkornstahl
Fully killed and fine grained steel

Es wird bestätigt, daß die Lieferung den Anforderungen der Lieferbedingung entspricht.
We hereby certify that the delivered material complies with the terms of the order.
(Z01)
QM-System: Certification as per ISO 9001 since 28 February 1990

Kesten

SAFEGUARDING LIFE, PROPERTY AND THE ENVIRONMENT · 18 64 · DNV·GL

Herstellerzeichen Trademark (A04)

Ilsenburger Grobblech GmbH
Veckenstedter Weg 10
D-38871 Ilsenburg
(A01)

AJ Abnahmestempel Inspection Stamp (Z03)

Abnahmebeauftragter Inspection Representative (Z02)

Cyron

ILSENBURGER GROBBLECH
Ein Unternehmen der Salzgitter Gruppe

Abnahmeprüfzeugnis 3.2
Inspection certificate 3.2
DIN EN 10204
(A02)

Nr./No. (A03) **1219355**
Seite/Page 3/6
Datum/Date 26.06.2020

Nr. (A07) Bestellung Purchaser (A06)	Order 6614 Rev. 3 Kröger Staal B.V. 4782 PZ MOERDIJK NIEDERLANDE	08.04.2020	Nr. (A07) Empfänger Customer (A06)	Order no. 6614 Kröger Staal B.V. 4782 PZ MOERDIJK NIEDERLANDE	
Erzeugnis Product (B01)	Grobblech Heavy plate			Werksauftrags-Nr. Works order No. (A08)	0000102734
				Abnahme Inspection (A05)	DNVGL **N141X9VG**
Werkstoff und Lieferbedingung Steel grade and terms of delivery (B02–B03)	S355G10+M EN 10225 08/01 MDS-Y20 Rev.5 DIN EN 10029 B 02/11 DIN EN 10163-2 A UG3 03/05 S355G10MLAPILSEN Application onboard DNV - classed objects is subject to special consideration.				

Stückanalyse / Check analysis (C70–C99)

Proben-Nr. Specimen No. (C00)	Schmelzen-Nr. Heat No. (B07)	C % ≤ 0,12	Si % 0,15 – 0,55	Mn % ≤ 1,65	P % ≤ 0,015	S % ≤ 0,005	N % ≤ 0,010	Al % 0,015–0,055	Cu % ≤ 0,30
199770 *)	30411	0,08	0,24	1,32	0,011	0,002	0,004	0,045	0,03
199770 *)	30411	0,08	0,22	1,41	0,012	0,004	0,007	0,037	0,04
199771 *)	30411	0,07	0,22	1,35	0,008	0,003	0,006	0,034	0,03
199771 *)	30411	0,08	0,23	1,31	0,008	0,002	0,007	0,040	0,03

Proben-Nr. Specimen No. (C00)	Schmelzen-Nr. Heat No. (B07)	Cr % ≤ 0,20	Ni % ≤ 0,70	V % ≤ 0,060	Ti % ≤ 0,025	Nb % ≤ 0,03	Mo % ≤ 0,08	B % ≤ 0,0005	EV1 1) % ≤ 0,21
199770 *)	30411	0,03	0,04	0,004	0,009	0,03	0,001	0,0004	0,16
199770 *)	30411	0,03	0,05	0,004	0,014	0,03	0,01	0,0004	0,17
199771 *)	30411	0,04	0,04	0,003	0,009	0,03	0,001	0,0001	0,15
199771 *)	30411	0,04	0,04	0,005	0,009	0,03	0,01	0,0000	0,16

Proben-Nr. Specimen No. (C00)	Schmelzen-Nr. Heat No. (B07)	EV2 2) % ≤ 0,40	EV3 3) %	EV4 4) % ≤ 0,08	Nb+V % ≤ 0,06
199770 *)	30411	0,31	0,10	0,04	0,03
199770 *)	30411	0,33	0,13	0,05	0,03
199771 *)	30411	0,31	0,11	0,04	0,03
199771 *)	30411	0,31	0,12	0,04	0,04

1) EV1 : PCM=C+Mn/20+Mo/15+Ni/60+Cr/20+V/10+Cu/20+Si/30+5xB
2) EV2 : CEV=C+Mn/6+Mo/5+Ni/15+Cr/5+V/5+Cu/15
3) EV3 : Cr+Cu+Mo+Ni
4) EV4 : V+Nb+Ti
*) Das Probestück ist nicht Bestandteil der Lieferung / The sample product is not part of the delivery

Es wird bestätigt, daß die Lieferung den Anforderungen der Lieferbedingung entspricht.
We hereby certify that the delivered material complies with the terms of the order.
(Z01)
QM-System: Certification as per ISO 9001 since 28 February 1990

Kesten

SAFEGUARDING LIFE, PROPERTY AND THE ENVIRONMENT · 18 64 · DNV·GL

Herstellerzeichen Trademark (A04)

Ilsenburger Grobblech GmbH
Veckenstedter Weg 10
D-38871 Ilsenburg
(A01)

Abnahmestempel Inspection Stamp (Z03)

Abnahmebeauftragter Inspection Representative (Z02)

Cyron

ILSENBURGER GROBBLECH
Ein Unternehmen der Salzgitter Gruppe

Abnahmeprüfzeugnis 3.2
Inspection certificate 3.2
DIN EN 10204
(A02)

Nr./No. (A03) **1219355**
Seite/Page 4/6
Datum/Date 26.06.2020

Nr. (A07) Besteller Purchaser (A06)	Order 6614 Rev. 3 Kröger Staal B.V. 4782 PZ MOERDIJK NIEDERLANDE	08.04.2020	Nr. (A07) Empfänger Customer (A06)	Order no. 6614 Kröger Staal B.V. 4782 PZ MOERDIJK NIEDERLANDE	
Erzeugnis Product (B01)	Grobblech Heavy plate				Werksauftrags-Nr. Works order No. (A08) 0000102734
					Abnahme Inspection (A05) DNVGL **N141X9VG**
Werkstoff und Lieferbedingung Steel grade and terms of delivery (B02–B03)	S355G10+M EN 10225 08/01 MDS-Y20 Rev.5 DIN EN 10029 B 02/11 DIN EN 10163-2 A UG3 03/05 S355G10MLAPILSEN Application onboard DNV - classed objects is subject to special consideration.				

Zugversuch / Tensile test (C10–C29)

Proben-Nr. Specimen No. (C00)	Schmelzen-Nr. Heat No. (B07)	Ort Location (C01) 1) 2) 3)	Richt. Direct. (C02) 4)	Zustand Cond. (B05) 5)	Form Type (C10) 6)	Streckgrenze Yield point (C11) ReH N/mm2 ≥ 355	Zugfestigkeit Tensile strength (C12) Rm N/mm2 470 – 630	ReH/Rm ReH/Rm ≤ 0,93	Bruchdehnung Elongation (C13) A5 % ≥ 22 7)	
201301	30411	K4G	Q	TM	P	510	560	0,91	29	
201305	30411	K4G	Q	TM	P	511	558	0,92	28	

1) K: Kopf / Top
2) 4: 1/4 Breite / 1/4 Width
3) G: Erzeugnisdicke / Thickness of product
4) Q: quer / transversal
5) TM: thermomechanisch gewalzt / thermomechanically rolled
6) P: prismatisch / prismatic
7) A5: Lo=5,65 √So

Kerbschlagbiegeversuch / Impact test (C40–C49)

Proben-Nr. Specimen No. (C00)	Schmelzen-Nr. Heat No. (B07)	Ort Location (C01) 1) 2) 3)	Richt. Direct. (C02) 4)	Zustand Cond. (B05) 5)	Probenform Type of specimen (C40–C41)	Temperatur Temperature (C03) °C	Schlagarbeit Impact energy (C42–C43) 1 J ≥ 27	2	3	MW 6) J ≥ 38
201301	30411	K4O	Q	TM	KV450/7,5	-040	179	181	170	177
201305	30411	K4O	Q	TM	KV450/7,5	-040	199	204	198	200

1) K: Kopf / Top
2) 4: 1/4 Breite / 1/4 Width
3) O: oberflächennah / near surface
4) Q: quer / transversal
5) TM: thermomechanisch gewalzt / thermomechanically rolled
6) MW: Mittelwert / Average

Es wird bestätigt, daß die Lieferung den Anforderungen der Lieferbedingung entspricht.
We hereby certify that the delivered material complies with the terms of the order.
(Z01)
QM-System: Certification as per ISO 9001 since 28 February 1990

Kesten

Cyron

Herstellerzeichen
Trademark
(A04)

Ilsenburger Grobblech GmbH
Veckenstedter Weg 10
D-38871 Ilsenburg
(A01)

Abnahmestempel
Inspection Stamp
(Z03)

Abnahmebeauftragter
Inspection Representative
(Z02)

ILSENBURGER GROBBLECH
Ein Unternehmen der Salzgitter Gruppe

Abnahmeprüfzeugnis 3.2
Inspection certificate 3.2
DIN EN 10204
(A02)

Nr./No. (A03) **1219355**
Seite/Page 5/6
Datum/Date 26.06.2020

Nr. (A07) Besteller Purchaser (A06)	Order 6614 Rev. 3 Kröger Staal B.V. 4782 PZ MOERDIJK NIEDERLANDE	08.04.2020	Nr. (A07) Empfänger Customer (A06)	Order no. 6614 Kröger Staal B.V. 4782 PZ MOERDIJK NIEDERLANDE

Erzeugnis Product (B01): Grobblech / Heavy plate

Werksauftrags-Nr. Works order No. (A08): 0000102734

Abnahme Inspection (A05): DNVGL **N141X9VG**

Werkstoff und Lieferbedingung Steel grade and terms of delivery (B02–B03):
S355G10+M
EN 10225 08/01
MDS-Y20 Rev.5
DIN EN 10029 B 02/11
DIN EN 10163-2 A UG3 03/05
S355G10MLAPILSEN
Application onboard DNV - classed objects is subject to special consideration.

Weitere Prüfungen / Other tests (C50–C69)

Proben-Nr. Specimen No. (C00)	Schmelzen-Nr. Heat No. (B07)	Ort Location (C01) 1)2)3)	Richt. Direct. (C02) 4)	Zustand Cond. (B05) 5)	Härteprüfung Hardness test (C30–C39) HV10			
201301	30411	K4		TM	157			
201305	30411	K4		TM	158			

1) K: Kopf / Top
2) 4: 1/4 Breite / 1/4 Width
5) TM: thermomechanisch gewalzt / thermomechanically rolled

Alle Bleche wurden gemäß EN 10160 07/99 flächen- und randzonengeprüft
Prüfklasse der Flächenprüfung: S1
Prüfklasse der Randzonenprüfung: E2
Befund: keine Beanstandung

All plates have been ultrasonically tested according to EN 10160 07/99 in area and edges
Class of areatesting: S1
Class of edgestesting: E2
Results: No faults were found.

Material gem. Optionen 10,12,13 der EN 10225
Material acc. to options 10,12,13 of EN 10225

Zusätzliche Anforderung 18: Verifiziert durch folgende Dokumente:
- ILG_2016-01_S355 G9/G10+M; S420 G1/G2+M
- ILG_2014_S355 G9/G10+M; S420 G1/G2+M Rev.1

Option 18: Verified by following documents:
- ILG_2016-01_S355 G9/G10+M; S420 G1/G2+M
- ILG_2014_S355 G9/G10+M; S420 G1/G2+M Rev.1

Es wird bestätigt, daß die Lieferung den Anforderungen der Lieferbedingung entspricht.
We hereby certify that the delivered material complies with the terms of the order.
(Z01)
QM-System: Certification as per ISO 9001 since 28 February 1990

Kesten

SAFEGUARDING LIFE, PROPERTY AND THE ENVIRONMENT - 18 64 DNV·GL

Herstellerzeichen Trademark (A04)

Ilsenburger Grobblech GmbH
Veckenstedter Weg 10
D-38871 Ilsenburg
(A01)

Abnahmestempel Inspection stamp (Z03)

Abnahmebeauftragter Inspection Representative (Z02)

Cyron

ILSENBURGER GROBBLECH
Ein Unternehmen der Salzgitter Gruppe

Abnahmeprüfzeugnis 3.2
Inspection certificate 3.2
DIN EN 10204
(A02)

Nr./No. (A03) **1219355**
Seite/Page 6/6
Datum/Date 26.06.2020

Nr. (A07) Besteller Purchaser (A06)	Order 6614 Rev. 3 Kröger Staal B.V. 4782 PZ MOERDIJK NIEDERLANDE	08.04.2020	Nr. (A07) Empfänger Customer (A06)	Order no. 6614 Kröger Staal B.V. 4782 PZ MOERDIJK NIEDERLANDE	
Erzeugnis Product (B01)	Grobblech Heavy plate				Werksauftrags-Nr. Works order No. (A08) 0000102734
					Abnahme Inspection (A05) DNVGL **N141X9VG**
Werkstoff und Lieferbedingung Steel grade and terms of delivery (B02–B03)	S355G10+M EN 10225 08/01 MDS-Y20 Rev.5 DIN EN 10029 B 02/11 DIN EN 10163-2 A UG3 03/05 S355G10MLAPILSEN Application onboard DNV - classed objects is subject to special consideration.				

Unsere Produkte sind frei von radioaktiven Stoffen.
Der Freigabegrenzwert von 100 Bq/kg, der die Einhaltung der Grenzwerte der Strahlenschutzverordnung(StrlSchV) für die uneingeschränkte Freigabe von festen Stoffen (StrlSchV Anlage III, Spalte 5) für eisenverwandte Nuklide gewährleistet, wird nicht überschritten.

Our products are free of radioactive substances and do not exceed the clearing limit value of 100 Bq/kg, which guarantees the compliance with limit values given in the Radiation Protection Ordinance(StrlSchV) for the unrestricted clearance of solid material (StrlSchV Annex III, Section 5) for ferrous nuclides.

Es wird bestätigt, daß die Lieferung den Anforderungen der Lieferbedingung entspricht.
We hereby certify that the delivered material complies with the terms of the order.
(Z01)
QM-System: Certification as per ISO 9001 since 28 February 1990

Kesten

Herstellerzeichen
Trademark
(A04)

Ilsenburger Grobblech GmbH
Veckenstedter Weg 10
D-38871 Ilsenburg
(A01)

Abnahmestempel
Inspection stamp
(Z03)

Abnahmebeauftragter
Inspection Representative
(Z02)

Cyron

Appendix B3: *Measurements for Brinell hardness and MATLAB Code*

6 mm

X	Y	Z(HB)
0	0	173.8646765
5	0	163.8857132
10	0	140.3318521
15	0	133.5511488
20	0	127.8619167
30	0	127.8619167
35	0	127.2257878
40	0	127.2257878
45	0	121.9222595
50	0	121.9222595
55	0	121.3156811
60	0	118.1007483
65	0	115.7850474
70	0	110.6018682
-5	0	145.9451262
-10	0	127.8619167
-15	0	121.9222595
-20	0	122.5288379
-30	0	121.3156811
-35	0	121.9222595
-40	0	121.3156811
-45	0	121.3156811
-50	0	121.3156811
-55	0	122.5288379
-60	0	121.3156811
-65	0	115.7850474
-70	0	115.7850474
8	-1	163.8857132
16	-1	121.3156811
24	-1	118.6796735
32	-1	115.7850474
40	-1	115.7850474
48	-1	110.6018682
56	-1	110.6018682
64	-1	110.6018682
-8	-1	134.8866603
-16	-1	121.3156811
-24	-1	121.3156811
-32	-1	121.3156811
-40	-1	118.1007483
-48	-1	115.7850474
-56	-1	110.6018682
-64	-1	110.6018682
5.5	0	164.2018861
10.5	0	145.2176586
15.2	0	122.6042097
20.5	0	122.6042097
25	0	137.6450484
-5.5	0	147.6379529
-10.5	0	135.4249669
-15.2	0	122.6042097
-20.5	0	124.6476131
-25	0	124.6476131

10 mm

X	Y	Z
0	3	193.5534601
5	3	172.9996781
10	3	148.3509954
15	3	140.3318521
20	3	140.3318521
25	3	133.5511488
30	3	143.1384891
35	3	140.3318521
40	3	140.3318521
45	3	140.3318521
50	3	133.5511488
55	3	133.5511488
60	3	127.8619167
65	3	128.4980457
70	3	127.2257878
0	-3.5	163.8857132
5	-3.5	147.6129308
-5	3	175.5946733
-10	3	147.6129308
-15	3	143.8401484
-20	3	134.2189045
-25	3	133.5511488
-30	3	140.3318521
-35	3	140.3318521
-40	3	140.3318521
-45	3	140.3318521
-50	3	140.3318521
-55	3	133.5511488
-60	3	133.5511488
-65	3	133.5511488
0	0	183.7751532
8	0	164.7051417
16	0	155.4451137
24	0	148.3509954
32	0	147.6129308
40	0	147.6129308
48	0	147.6129308
56	0	143.1384891
64	0	141.0335114
72	0	140.3318521
-8	0	166.3439988
-16	0	148.3509954
-24	0	155.4451137
-32	0	148.3509954
-40	0	148.3509954
-48	0	148.3509954
-56	0	144.5418077
-64	0	140.3318521
-72	0	140.3318521
0.1	0	188.6710033
5	0	174.7095622
10	0	150.9925607
15	0	140.8715666
20	0	142.2802823
25	0	140.8715666
-5	0	178.2037534
-10	0	162.2164214
-15	0	150.9925607
-20	0	154.0124119
-25	0	140.8715666

15 mm

X	Y	Z
0	0	208.2515556
5	0	185.6037617
10	0	166.3439988
15	0	157.7767904
20	0	156.9995648
25	0	149.0890601
30	0	147.6129308
35	0	143.1384891
40	0	143.1384891
45	0	142.4368299
50	0	139.5609505
55	0	140.3318521
60	0	140.3318521
65	0	140.3318521
70	0	136.2221717
-2	5	164.7051417
0	-7	171.7212173
5	-7	160.8856926
10	-7	145.9451262
15	-7	128.4980457
20	-7	127.8619167
25	-7	127.8619167
30	-7	135.554416
35	-7	141.0335114
40	-7	134.8866603
45	-7	133.5511488
50	-7	133.5511488
55	-7	127.2257878
60	-7	127.2257878
65	-7	127.8619167
70	-7	123.1354163
-5	0	164.7051417
-10	0	155.4451137
-15	0	156.9995648
-20	0	147.6129308
-25	0	140.3318521
-30	0	141.0335114
-35	0	133.5511488
-40	0	127.8619167
-45	0	127.8619167
-50	0	134.8866603
-55	0	131.6786904
-60	0	121.3156811
-65	0	115.7850474
-70	0	105.7374222
-5	-7	173.8646765
-10	-7	176.4596717
-15	-7	172.9996781
-20	-7	148.3509954
-25	-7	133.5511488
-30	-7	141.0335114
-35	-7	141.0335114
-40	-7	140.3318521
-45	-7	140.3318521
-50	-7	140.3318521
-55	-7	140.3318521
-60	-7	143.1384891
-65	-7	141.0335114
-70	-7	134.2189045
0	-1	165.5245703
8	-1	164.7051417
16	-1	155.4451137
24	-1	156.2223392
32	-1	147.6129308
40	-1	150.5651894
48	-1	148.3509954
56	-1	148.3509954
64	-1	148.3509954
68	-1	148.3509954
-1	-6	174.7296749
8	-6	173.8646765
16	-6	140.3318521
24	-6	133.5511488
32	-6	140.3318521
40	-6	145.9451262
48	-6	157.7767904
56	-6	147.6129308
64	-6	147.6129308
68	-6	147.6129308
-8	-1	173.8646765
-16	-1	163.8857132
-24	-1	156.2223392
-32	-1	155.4451137
-40	-1	147.6129308
-48	-1	147.6129308
-56	-1	141.0335114
-64	-1	141.0335114
-68	-1	141.0335114
-8	-6	193.5534601
-16	-6	173.8646765
-24	-6	134.2189045
-32	-6	133.5511488
-40	-6	133.5511488
-48	-6	133.5511488
-56	-6	133.5511488

20 mm

X	Y	Z
0	0	182.860849
5	0	205.1739464
10	0	198.3922966
15	0	194.5212274
20	0	182.860849
25	0	195.4889947
0	5	196.456762
5	5	194.5212274
10	5	185.6037617
15	5	183.7751532
20	5	141.0335114
25	5	149.8271247
0	-5	195.4889947
5	-5	189.2609787
10	-5	194.5212274
15	-5	187.4323702
20	-5	173.8646765
25	-5	163.8857132
-5	0	185.6037617
-10	0	183.7751532
-15	0	172.9996781
-20	0	172.9996781
-25	0	159.3312415
-5	5	193.5534601
-10	5	194.5212274
-15	5	173.8646765
-20	5	175.5946733
-25	5	164.7051417
-5	-5	194.5212274
-10	-5	184.6894575
-15	-5	174.7296749
-20	-5	164.7051417
-25	-5	155.4451137
45	0	163.8857132
50	0	166.3439988
55	0	157.7767904
60	0	149.0890601
65	0	140.3318521
70	0	168.8022845
45	5	155.4451137
50	5	155.4451137
55	5	147.6129308
60	5	152.0413187
65	5	152.7793833
70	5	140.3318521
45	-5	164.7051417
50	-5	165.5245703
55	-5	167.1634274
60	-5	163.8857132
65	-5	147.6129308
70	-5	147.6129308
-45	0	176.1771416
-50	0	164.7051417
-55	0	167.982856
-60	0	163.8857132
-65	0	156.2223392
-70	0	140.3318521
-45	5	172.9996781
-50	5	163.8857132
-55	5	163.8857132
-60	5	157.7767904
-65	5	160.8856926
-70	5	140.3318521
-45	-5	163.8857132
-50	-5	163.8857132
-55	-5	164.7051417
-60	-5	155.4451137
-65	-5	140.3318521
-70	-5	147.6129308
0	2	193.5534601
7	2	183.7751532
14	2	168.8022845
21	2	162.4401438
0	8	183.7751532
7	8	173.8646765
14	8	173.8646765
21	8	149.0890601
0	-4	178.1896685
7	-4	174.7296749
14	-4	172.9996781
21	-4	156.2223392
-7	2	182.860849
-14	2	173.8646765
-21	2	155.4451137
-7	8	184.6894575
-14	8	172.9996781
-21	8	133.5511488
-7	-4	183.7751532
-14	-4	192.0038914
-21	-4	180.7846636

06/09/23 14:42 C:\Users\N0968013\OneDrive ...\hardness.m 1 of 1

```
clear all
cd('C:\Users\N0968013\OneDrive - Nottingham Trent University\Documents\8-data\Mathlab Code')
filename=['C:\Users\N0968013\OneDrive - Nottingham Trent University\Documents\8-data\Hardness Tests\Hardness 20mm.txt'];
m=readmatrix(filename);
contour_sub4ttu_matlab2017(m(:,1),m(:,2),m(:,3),[-75 75],[-5 5],[100 210],1500,'fill');
% save(['X.mat'],'X')
% save(['Y.mat'],'Y')
% save(['Z2.mat'],'Z2')
```

06/09/23 14:43 C:\Users\...\contour_sub4ttu_matlab2017.m 1 of 1

```
function [x,y,zf]=contour_sub4ttu_matlab2017(xi,yi,zi,xrange,yrange,crange,n,fillq)
% Example of contours based on the latest changes in Matlab commands
% Last edit: 4/24/16 M.Moravej
% Omits the NaN terms
nanElems=find(isnan(zi));
zi(nanElems)=[]; xi(nanElems)=[];yi(nanElems)=[];
xrange1=linspace(xrange(1),xrange(2),n);
yrange1=linspace(yrange(1),yrange(2),n);
[x,y]=meshgrid(xrange1,yrange1);
F=scatteredInterpolant(xi,yi,zi,'natural');
zf=F(x,y);
%zf=griddata(xi,yi,zi,x,y);
if strcmp(fillq,'fill')
[c,h]=contourf(x,y,zf,50);
else
    [c,h]=contour(x,y,zf,50,'showtext','on');
end

% Set LineColor to 'none' to turn off visible lines
set(h, 'LineColor', 'none');

set(gca,'CLim',crange);
colormap jet
clabel(c,h,'FontSize',14)
%colormap(flipud(colormap))
%colorbar('EastOutside')
daspect([1 1 1])
set(gcf,'color','white')
h.LevelList=round(h.LevelList*100)/100;
h.ShowText='off';
%clabel(c,h.TextList);
% text=clabel(c,h.TextList);
% for i=1:size(h.TextList)
%     str=h.TextList(i);
%     eqnum=str2num(str);
%     new=num2str(eqnum,'%4.2f');
%contour_sub4ttu_matlab2017(x,y,z,[0 79],[0 52.5],[-10 0],15,'fill')
%     set(text(i),'String',new)
% end
%
%colormap('gray')
%z=double(z)run for x, and y
%x=final_data(:,2);
%y=final_data(:,3);
%z=final_data(:,5);
```

Appendix B4: *Measurements for distortion and misalignments*

Thickness		left					Right					Axial misalignment	Angular distortion
	Length	X1	Y1	X2	Y2	tan-1	X1	Y1	X2	Y2	tan-1	e	average
6mm	5	-196.25	1.1	-105.79	0.9	0.126676	-89.31	0.64	-0.12	-0.04	0.436824	0.26	0.281750384
	50	-195.63	2.04	-107.62	1.71	0.214834	-87.55	1.39	-0.65	0.77	0.408778	0.32	0.311805718
	100	-197.19	3.33	-109.41	2.72	0.398153	-89.58	2.46	-0.63	1.85	0.392916	0.26	0.395534454
	150	-196.26	4.47	-108.35	3.83	0.417116	-91.23	3.68	-1.14	3.06	0.394304	0.15	0.405709768
	200	-194.07	5.68	-105.64	4.97	0.460015	-90.71	4.88	-1.73	4.19	0.444294	0.09	0.452154603
	250	-195.75	6.92	-106.78	6.23	0.444344	-87.43	6.1	-2.3	5.43	0.450927	0.13	0.447635344
	300	-195.66	8.37	-109	7.62	0.495855	-91.25	7.49	-2.1	6.81	0.43702	0.13	0.466437545
	350	-195.21	9.91	-106.8	8.99	0.596202	-91.69	8.75	-15.04	8.26	0.366269	0.24	0.481235676
	400	-196.06	11.27	-107.24	10.28	0.6386	-89.61	9.95	-5.68	9.72	0.157012	0.33	0.397805993
	450	-196.12	12.47	-106.5	11.47	0.639293	-90.03	11.11	-6.23	11.1	0.006837	0.36	0.323064897
	500	-196.31	13.41	-108.91	12.41	0.65553	-89.2	11.94	-4.15	12.37	0.289676	0.34	0.472602942
	550	-195.05	13.95	-108.71	12.87	0.716658	-90.17	12.6	-3.36	13.31	0.468599	0.27	0.592628386
	600	-196.7	14.22	-107.77	13.04	0.760205	-89.93	12.88	-4.01	13.87	0.660153	0.16	0.710178924
	650	-197.4	14.22	-107.38	12.91	0.833728	-89.89	12.6	-2.6	14.12	0.997603	0.09	0.915665487
	700	-197.31	13.77	-107.88	12.3	0.941711	-91.43	12.05	-2.57	14.05	1.289356	0.04	1.115533712
	750	-196.63	12.72	-108.36	11.22	0.973552	-90.65	10.97	-4.45	13.45	1.647962	0.02	1.310756925
	800	-196.62	11.26	-109.75	9.6	1.094733	-91.28	9.54	-2.77	12.3	1.786071	0.06	1.440401687
	850	-197.36	9.08	-107.95	7.4	1.076452	-92.03	7.41	-7.33	10.24	1.913657	0.01	1.495054619
	900	-194.38	6.2	-107.45	4.57	1.074211	-90.03	4.57	-5.85	7.33	1.877877	0	1.476044313
	950	-198.07	3.1	-108.25	1.17	1.230949	-90.02	1.11	-5.82	3.75	1.795859	0.06	1.513403964
10mm	5	-189.32	-0.07	-104.71	0.21	0.189608	-90.86	0.47	-1.84	0.2	0.173779	0.26	0.181693695
	50	-195.32	0.5	-105.77	0.57	0.044787	-82.79	0.76	-2.56	0.5	0.185677	0.19	0.115232061
	100	-179.94	1.11	-106.16	1.09	0.015532	-87.23	1.32	-2.21	0.82	0.336951	0.23	0.176241175
	150	-194.87	2.11	-105.55	1.66	0.288657	-88.68	1.8	-2.59	1.33	0.312798	0.14	0.300727541
	200	-193.07	2.75	-107.6	2.17	0.388804	-87.48	2.3	-2.96	1.96	0.230483	0.13	0.309643508
	250	-191.07	3.36	-107	2.62	0.504315	-87.96	2.75	-2.25	2.65	0.066848	0.13	0.285581812
	300	-192.81	3.85	-106.13	3	0.561835	-89.16	3.2	-2.27	3.41	0.138475	0.2	0.35015495
	350	-194.24	4.09	-107.06	3.34	0.492897	-89.03	3.64	-3.11	4.1	0.306748	0.3	0.399822689
	400	-194.98	4.34	-107.16	3.61	0.476258	-89.68	3.92	-4.86	4.58	0.44582	0.31	0.461038869
	450	-194.01	4.38	-107.88	3.76	0.412432	-89.98	4.09	-6.46	5.04	0.651684	0.33	0.532057983
	500	-192.55	4.33	-106.45	3.8	0.352687	-89.65	4.16	-4.84	5.31	0.776867	0.36	0.564777276
	550	-194.93	4.33	-107.23	3.72	0.398516	-87.66	4.05	-3.57	5.46	0.960631	0.33	0.679573658
	600	-194.6	4.19	-107.19	3.51	0.44572	-90.69	3.83	-5.01	5.47	1.096564	0.32	0.771141776
	650	-193.43	3.91	-108.23	3.13	0.524524	-90.12	3.44	-7.61	5.37	1.339967	0.31	0.932245684
	700	-194.8	3.51	-108.37	2.72	0.523689	-90.25	2.99	-5.36	5.15	1.457559	0.27	0.99062381
	750	-193.83	2.95	-106.26	2.1	0.556125	-89.37	2.43	-5.9	4.71	1.564657	0.23	1.060390991
	800	-193.79	2.43	-107.26	1.57	0.56943	-89.65	1.71	-4.35	4.14	1.631783	0.14	1.10060638
	850	-192.98	1.86	-106.9	0.82	0.692202	-86.36	1.19	-2.85	3.43	1.536484	0.27	1.114342791
	900	-195.73	1.15	-107.08	0.08	0.691523	-88.62	0.34	-3.69	2.51	1.463615	0.23	1.077568812
	950	-195.98	0.53	-107.43	-0.75	0.828159	-89.4	-0.47	-5.11	1.5	1.338856	0.27	1.083507374
15mm	950	-194.84	-0.35	-118.09	-2.79	1.820907	-86.25	-2.8	-4.85	0.08	2.026327	0.01	1.923617276
	900	-196.41	0.09	-119.93	-2.96	2.283729	-86.41	-3.1	-1.6	-0.28	1.904429	0.14	2.094078683
	850	-194.88	0.16	-119.66	-2.98	2.39038	-87.91	-3.19	-1.7	-0.51	1.780574	0.21	2.085476631
	800	-192.45	0.29	-119.12	-2.94	2.522103	-88.09	-3.2	-2.94	-0.74	1.654826	0.26	2.08846449
	750	-193.34	0.42	-119.64	-2.85	2.540494	-89.58	-3.19	-2.21	-0.79	1.573484	0.34	2.056988958
	700	-194.7	0.7	-119.14	-2.66	2.54615	-88.74	-3.09	-4.49	-0.84	1.529791	0.43	2.037970251
	650	-192.42	0.62	-119.21	-2.48	2.424681	-88.5	-2.96	-2.78	-0.6	1.57704	0.48	2.00086048
	600	-193.4	0.52	-119.96	-2.35	2.237953	-88.59	-2.92	-3.36	-0.47	1.646557	0.51	1.942254668
	550	-195.56	0.33	-119.85	-2.19	1.906381	-88.67	-2.73	-2.26	-0.15	1.71021	0.54	1.808295102
	500	-191.28	0.04	-119.95	-2.2	1.798688	-88.91	-2.55	-3.61	0.05	1.745872	0.35	1.772279982
	450	-194.7	-0.05	-121.1	-2.31	1.758801	-88.88	-2.4	-3.39	0.31	1.815646	0.09	1.787223775
	400	-195.35	-0.29	-121.72	-2.32	1.579261	-88.53	-2.24	-2.28	0.66	1.925741	0.08	1.752501078
	350	-194.96	-0.36	-121.88	-2.46	1.645977	-89.17	-2.37	-4.48	0.81	2.150372	0.09	1.898174855
	300	-195.67	-0.64	-123.07	-2.58	1.53068	-88.93	-2.44	-4.32	1.1	2.395802	0.14	1.96324115
	250	-197.57	-0.76	-122.25	-2.78	1.536242	-90.56	-2.62	-4.37	1.18	2.524458	0.16	2.030350057
	200	-197.44	-0.88	-122.45	-2.81	1.474283	-89.74	-2.71	-5.09	1.22	2.658132	0.1	2.06620709
	150	-197.83	-0.9	-122.51	-2.82	1.460224	-90.35	-2.78	-6.65	1.11	2.660936	0.04	2.060579892
	100	-196.2	-0.9	-123.43	-2.82	1.51137	-90.73	-2.83	-6.04	0.95	2.555608	0.01	2.033488657
	50	-196.65	-0.78	-124.73	-2.77	1.584949	-91.86	-2.83	-4.36	0.71	2.31676	0.06	1.950854433
	5	-196.31	-0.47	-123.49	-2.62	1.691158	-91.81	-2.8	-5.22	0.24	2.010713	0.18	1.850935792
20mm	950	-195.46	-0.1	-120.47	-1.67	1.199376	-91.24	-1.4	-11.98	0.95	1.69828	0.45	1.448828032
	900	-198.46	-1.4	-120.13	-2.64	0.906943	-89.57	-2.53	-7.58	0.35	2.011758	0.37	1.459350359
	850	-195.34	-2.55	-120.93	-3.64	0.839241	-89.36	-3.44	-8.23	-0.03	2.4068	0.4	1.623020521
	800	-196.65	-3.41	-119.69	-4.35	0.699784	-89.17	-4.1	-9.19	-0.47	2.598663	0.49	1.649223227
	750	-198.34	-4.19	-118.52	-4.92	0.523988	-89.12	-4.64	-8.48	-0.92	2.641236	0.54	1.582612375
	700	-196.41	-4.69	-120.22	-5.32	0.473757	-89.34	-4.99	-9.86	-1.51	2.507072	0.62	1.490414073
	650	-192.2	-4.99	-119.67	-5.57	0.458167	-88.05	-5.16	-8.39	-2	2.271652	0.65	1.364909349
	600	-193.59	-5.11	-119.13	-5.76	0.500152	-88.1	-5.27	-7.92	-2.59	1.914387	0.59	1.207269413
	550	-194.97	-5.1	-118.59	-5.73	0.472578	-88.45	-5.34	-7.84	-3.15	1.55622	0.6	1.01439913
	500	-195.82	-5.03	-117.6	-5.71	0.498084	-87.31	-5.37	-7.15	-3.67	1.214923	0.34	0.856503608
	450	-194.11	-4.78	-118.45	-5.67	0.673948	-87.6	-5.54	-9.01	-4.16	1.005981	0.23	0.839964434
	400	-194.08	-4.53	-119.23	-5.51	0.750122	-86.91	-5.72	-7.06	-4.55	0.839465	0.13	0.794793567
	350	-196.29	-4.17	-117.29	-5.4	0.892001	-86.56	-5.84	-5.54	-4.89	0.671791	0.39	0.781896163
	300	-194.88	-3.73	-117.18	-5.48	1.290227	-85.84	-5.8	-7.39	-5.06	0.540441	0.37	0.915334322
	250	-194.59	-3.19	-117.07	-5.38	1.61822	-85.18	-5.66	-7.79	-5.06	0.444202	0.39	1.031210763
	200	-193.62	-2.73	-116.53	-5.05	1.723779	-85.36	-5.35	-7.06	-4.87	0.351234	0.39	1.037506399
	150	-196.37	-2.2	-116.43	-4.57	1.698164	-85.5	-4.93	-8.33	-4.44	0.363801	0.39	1.030982725
	100	-198.15	-1.9	-117.63	-4.02	1.508184	-84.92	-4.33	-8.08	-3.87	0.342995	0.39	0.925589683
	50	-196.1	-1.43	-116.22	-3.36	1.384068	-85.05	-3.5	-6.33	-3	0.363916	0.26	0.873992187
	5	-194.62	-1.36	-116.36	-2.44	0.79064	-84.42	-2.5	-6.05	-1.85	0.4752	0.3	0.632920042

Appendix C: Predicted SN-curve from corrosion-based fatigue model

Appendix C1: *Mechanical and chemical properties of S355J2+N*

QM-System: Certification as per ISO 9001 — **DILLINGER**

Erläuterungen siehe Rückseite/Explications voir au verso/See reverse for explanations (www.dillinger.de/certificate)

A02	INSPECTION CERTIFICATE 3.1 AS PER EN 10204:2004 INSPECTION CERTIFICATE 3.1 AS PER ISO 10474:2013 MATERIAL TEST REPORT (MTR)	A10 Advice of dispatch No./ Date of dispatch	369991-04.09.19
		A08/ Manufacturer's order/ A03 Certificate No.	449425-004-18 Sheet 5
A05 Established Inspecting body	DF		
A06 Purchaser	ANCOFER,MUELHEIM	A07.1 No.	2097000
Final receiver	ANCOFER,MH/FLACHPROD	A07.2 No.	
B01 Product	HEAVY PLATES		
B02/ Steel design.	S355J2+N		AD2000-W1:06
B03 Any suppl. requirements	EN-10025-2:04/AM43:REV.0		OPTION-5 CLASS 3

Z04 CE-marking

ITEM NO.: 26-29

CE

0769

EN 10025-1:2004

Plate S355J2 / 1.0577

to be used in welded, bolted and riveted structures

DILLINGER

Dillinger France
CS 56317 F-59379 Dunkerque Cedex 1

19

S355J2_EN10025-2-04_B_160101E2

Tolerance on dimensions and shape:	
Elongation	
Tensile strength	expressed as declared in the DoP
Yield strength	
Impact strength	S355J2_EN10025-2-04_B_160101E2
Weldability	
Durability (chemical composition)	

The declaration of performance can be downloaded from www.dillinger.de/dop/S355J2_EN10025-2-04_B_160101E2.pdf

A04 D F Manufacturer's mark

Z01/Z02/Z03 We hereby certify, that the above mentioned materials have been delivered in accordance with the terms of order.

POISSONNET Test House Manager

A01 **Dillinger France**
Port 3032
3032 rue du Comte Jean - CS 56317
F-59379 Dunkerque Cedex 1 - FRANCE
Service Qualité-Essais
Date 05.09.19 JB 1

QM-System: Zertifiziert nach ISO 9001 — **DILLINGER**

Erläuterungen siehe Rückseite/Explications voir au verso/See reverse for explanations (www.dillinger.de/certificate)

A02	ABNAHMEPRUEFZEUGNIS 3.1 NACH EN 10204:2004 ABNAHMEPRUEFZEUGNIS 3.1 NACH ISO 10474:2013 MATERIAL TEST REPORT (MTR)	A10 Versandanzeige-Nr. und Datum	369991-04.09.19
		A08/ Werksauftrags-/ A03 Bescheinigungs-Nr.	449425-004-18 Blatt 1/...
A05 Aussteller Abnahmeorgan	DF		
A06 Besteller	ANCOFER,MUELHEIM	A07.1 Nr.	2097000
Empfänger	ANCOFER,MH/FLACHPROD	A07.2 Nr.	
B01 Erzeugnis	GROBBLECHE		
B02/ Stahlbezeichn.	S355J2+N		AD2000-W1:06
B03 Anforder-ungen	EN-10025-2:04/AM43:REV.0		OPTION-5 CLASS 3

A01-A99 Angaben zum Geschäftsvorgang

B14 Pos. Nr.	B07.2 Schmelzen-Nr.	B07.1 Walztafel-/ Proben-Nr.	B16 vereinbarte Auftragsergänzung Dokument Nr.	Datum
26	473732	270006-03	T-1-2YBZGP	27.08.19

B01-B99 Beschreibung des Erzeugnisses

B14 Pos. Nr.	B08 Stückzahl	B09 Dicke	B10 Breite MM	B11 Länge	B12 Theoretische Masse KG	B04 Lieferzustand des Erzeugnisses	B07.2 Schmelzen-Nr.	B07.1 Walztafel-/ Proben-Nr.	A09 Artikelnummer des Kunden
26	1	25,00	x 2500	x 6000	2944	N	473732	270006-02	
26	1	25,00	x 2500	x 6000	2944	N	473732	270006-03	
**	2				5888				
27	1	25,00	x 2500	x 8000	3925	N	473732	270006-01	
28	1	25,00	x 2500	x 12000	5888	N	473732	265014-01	
28	1	25,00	x 2500	x 12000	5888	N	473732	265014-02	
28	1	25,00	x 2500	x 12000	5888	N	473732	265015-01	
28	1	25,00	x 2500	x 12000	5888	N	473732	265015-02	
28	1	25,00	x 2500	x 12000	5888	N	473732	265018-01	
28	1	25,00	x 2500	x 12000	5888	N	473732	265018-02	
28	1	25,00	x 2500	x 12000	5888	N	473732	265019-01	
28	1	25,00	x 2500	x 12000	5888	N	473732	265019-02	
28	1	25,00	x 2500	x 12000	5888	N	473732	265020-01	
28	1	25,00	x 2500	x 12000	5888	N	473732	265020-02	
28	1	25,00	x 2500	x 12000	5888	N	473732	265021-01	
28	1	25,00	x 2500	x 12000	5888	N	473732	265021-02	
28	1	25,00	x 2500	x 12000	5888	N	473732	265022-01	
28	1	25,00	x 2500	x 12000	5888	N	473732	265022-02	
28	1	25,00	x 2500	x 12000	5888	N	473732	268329-02	

A04 D F Zeichen des Herstellers

Z01/Z02/Z03 Es wird bestätigt, dass die Lieferung den Vereinbarungen bei der Bestellung entspricht.

POISSONNET Der Abnahmebeauftragte

A01 **Dillinger France**
Port 3032
3032 rue du Comte Jean - CS 56317
F-59379 Dunkerque Cedex 1 - FRANCE
Service Qualité-Essais
Datum 05.09.19 JB 1

QM-System: Zertifiziert nach ISO 9001 — **DILLINGER**

Erläuterungen siehe Rückseite/Explications voir au verso/See reverse for explanations (www.dillinger.de/certificate)

A02 ABNAHMEPRUEFZEUGNIS 3.1 NACH EN 10204:2004
ABNAHMEPRUEFZEUGNIS 3.1 NACH ISO 10474:2013
MATERIAL TEST REPORT (MTR)

A10 Versandanzeige-Nr. und Datum: 369991-04.09.19

A08/ Werksauftrags-/ A03 Bescheinigungs-Nr.: 449425-004-18 — Blatt: 2/...

A05 Aussteller Abnahmeorgan: DF

A06 Besteller: ANCOFER,MUELHEIM — A07.1 Nr. 2097000
Empfänger: ANCOFER,MH/FLACHPROD — A07.2 Nr.

B01 Erzeugnis: GROBBLECHE

B02/ Stahlbezeichn. S355J2+N — AD2000-W1:06
B03 Anforderungen: EN-10025-2:04/AM43:REV.0 — OPTION-5 CLASS 3

B01-B99 Beschreibung des Erzeugnisses

B14 Pos. Nr.	B08 Stückzahl	B09 Dicke	B10 Breite MM	B11 Länge	B12 Theoretische Masse KG	B04 Lieferzustand des Erzeugnisses	B07.2 Schmelzen-Nr.	B07.1 Walztafel-/ Proben-Nr.	A09 Artikelnummer des Kunden
28	1	25,00	x 2500	x 12000	5888	N	473732	268331-02	
**	16				94208				
29	1	25,00	x 2500	x 16000	7850	N	473732	268331-01	
***	20				111871				

B06 Kennzeichnung des Erzeugnisses

POSITION-NR.: 26-29
STAHLBEZEICHNUNG S355J2+N
SCHMELZEN-NR. / HERSTELLERZEICHEN /WALZTAFEL-NR.-PROBEN-NR.

C10-C29 Zugversuch

B14 Pos. Nr.	B07.2 Schmelzen-Nr.	B07.1 Walztafel-/ Proben-Nr.	B05 Referenz(wärme)behandlung	C01	C02/ C01	C03 Temp. GR.C	C10	C11 MPA REH	C12 RM	C13	A % L0=5D	C14-C15
28	473732	265014		K7	QO	RT		462	558		30	
28	473732	265020		K7	QO	RT		459	556		31	
28	473732	265021		K7	QO	RT		443	552		32	
28	473732	265022		K7	QO	RT		453	558		31	

A04 Zeichen des Herstellers: D F

Z01/Z02/Z03 Es wird bestätigt, dass die Lieferung den Vereinbarungen bei der Bestellung entspricht.

POISSONNET
Der Abnahmebeauftragte

A01 **Dillinger France**
Port 3032
3032 rue du Comte Jean - CS 56317
F-59379 Dunkerque Cedex 1 - FRANCE
Service Qualité-Essais
Datum 05.09.19 JB 1

QM-System: Zertifiziert nach ISO 9001 — **DILLINGER**

Erläuterungen siehe Rückseite/Explications voir au verso/See reverse for explanations (www.dillinger.de/certificate)

A02 ABNAHMEPRUEFZEUGNIS 3.1 NACH EN 10204:2004
ABNAHMEPRUEFZEUGNIS 3.1 NACH ISO 10474:2013
MATERIAL TEST REPORT (MTR)

A10 Versandanzeige-Nr. und Datum: 369991-04.09.19

A08/ Werksauftrags-/ A03 Bescheinigungs-Nr.: 449425-004-18 — Blatt: 3/...

A05 Aussteller Abnahmeorgan: DF

A06 Besteller: ANCOFER,MUELHEIM — A07.1 Nr. 2097000
Empfänger: ANCOFER,MH/FLACHPROD — A07.2 Nr.

B01 Erzeugnis: GROBBLECHE

B02/ Stahlbezeichn. S355J2+N — AD2000-W1:06
B03 Anforderungen: EN-10025-2:04/AM43:REV.0 — OPTION-5 CLASS 3

C40-C49 Kerbschlagbiegeversuch

B14 Pos. Nr.	B07.2 Schmelzen-Nr.	B07.1 Walztafel-/ Proben-Nr.	B05 Referenz(wärme)behandlung	C01	C02/ C01	C03 Temp. GR.C	C41 Proben-breite	C40 Proben-form	C44 Prüfverfahren	C46 Energie Joule	C45	C42 Einzelwerte AV=J			C43 Mittelwert
28	473732	265014		K7	LO	-20		CHP-V		600	AV 2	270	288	282	280
				K7	LO	-40		CHP-V		600	AV 2	186	170	159	172
28	473732	265020		K7	LO	-20		CHP-V		600	AV 2	253	270	263	262
				K7	LO	-40		CHP-V		600	AV 2	287	267	275	276
28	473732	265021		K7	LO	-20		CHP-V		600	AV 2	283	285	285	284
				K7	LO	-40		CHP-V		600	AV 2	306	309	292	302
28	473732	265022		K7	LO	-20		CHP-V		600	AV 2	261	272	257	263
				K7	LO	-40		CHP-V		600	AV 2	249	245	248	247

C40-C49 Weitere Angaben zum Kerbschlagbiegeversuch

POSITION-NR.: 28
KERBSCHLAGBIEGEVERSUCH BEI -40 GR.C INFORMATORISCH

C70-C99 Chemische Zusammensetzung % - Schmelzenanalyse

B07.2 Schmelze	C70	C	SI	MN	P	S	N	CU	MO	NI	CR	V	NB	TI	AL-T
473732	Y	0,149	0,227	1,604	0,012	0,0007	0,0032	0,019	0,006	0,041	0,046	0,002	0,019	0,002	0,044

C94 Schmelzenanalyse C-Äquivalent / Legierungsbegrenzung

B07.2 Schmelze		
473732	FO-02=	0,43

C94 Formel C-Äquivalent / Legierungsbegrenzung

FO-02 = C+(MN/6)+(CR+MO+V)/5+(NI+CU)/15

A04 Zeichen des Herstellers: D F

Z01/Z02/Z03 Es wird bestätigt, dass die Lieferung den Vereinbarungen bei der Bestellung entspricht.

POISSONNET
Der Abnahmebeauftragte

A01 **Dillinger France**
Port 3032
3032 rue du Comte Jean - CS 56317
F-59379 Dunkerque Cedex 1 - FRANCE
Service Qualité-Essais
Datum 05.09.19 JB 1

QM-System: Zertifiziert nach ISO 9001

DILLINGER

Erläuterungen siehe Rückseite/Explications voir au verso/See reverse for explanations (www.dillinger.de/certificate)

A02 ABNAHMEPRUEFZEUGNIS 3.1 NACH EN 10204:2004 ABNAHMEPRUEFZEUGNIS 3.1 NACH ISO 10474:2013 MATERIAL TEST REPORT (MTR)		A10 Versandanzeige-Nr. und Datum 369991-04.09.19	A08/ Werksauftrags-/ A03 Bescheinigungs-Nr. Blatt 449425-004-18 4/...
A05 Aussteller Abnahmeorgan DF	A06 Besteller ANCOFER,MUELHEIM A07.1 Nr. 2097000 Empfänger ANCOFER,MH/FLACHPROD A07.2 Nr.		B01 Erzeugnis GROBBLECHE
B02/ Stahlbezeichn. **S355J2+N** AD2000-W1:06 B03 Anforderungen EN-10025-2:04/AM43:REV.0 OPTION-5 CLASS 3			

D01 Kennzeichnung, Identifizierung, Oberfläche, Form und Maße

POSITION-NR.: 26-29

PRÜFUNG VON KENNZEICHNUNG, OBERFLÄCHE, FORM UND MAßEN: DIE ERGEBNISSE ENTSPRECHEN DEN ANFORDERUNGEN.

OBERFLAECHE	NACH EN-10163-2 KLASSE B UNTERKLASSE 3
DICKE	NACH EN-10029:10-B
LAENGE UND BREITE	NACH EN-10029:10
EBENHEIT	NACH EN-10029:10-T4L

Z04 Umweltproduktdeklaration für Baustähle

POSITION-NR.: 26-29

Für Grobbleche aus Baustählen von Dillinger liegt eine validierte Umweltproduktdeklaration nach ISO 14025 und EN 15804 vor: EPD-BFS-20180116-IBG2-DE. Weitere Informationen finden Sie unter www.dillinger.de/EPD-D/.

A04 D F Zeichen des Herstellers	Z01/Z02/Z03 Es wird bestätigt, dass die Lieferung den Vereinbarungen bei der Bestellung entspricht.	POISSONNET Der Abnahmebeauftragte	**Dillinger France** Port 3032 3032 rue du Comte Jean - CS 56317 F-59379 Dunkerque Cedex 1 - FRANCE Service Qualité-Essais Datum 05.09.19 JB 1 A01

QM-System: Zertifiziert nach ISO 9001

DILLINGER

Erläuterungen siehe Rückseite/Explications voir au verso/See reverse for explanations (www.dillinger.de/certificate)

A02 ABNAHMEPRUEFZEUGNIS 3.1 NACH EN 10204:2004 ABNAHMEPRUEFZEUGNIS 3.1 NACH ISO 10474:2013 MATERIAL TEST REPORT (MTR)		A10 Versandanzeige-Nr. und Datum 369991-04.09.19	A08/ Werksauftrags-/ A03 Bescheinigungs-Nr. Blatt 449425-004-18 5
A05 Aussteller Abnahmeorgan DF	A06 Besteller ANCOFER,MUELHEIM A07.1 Nr. 2097000 Empfänger ANCOFER,MH/FLACHPROD A07.2 Nr.		B01 Erzeugnis GROBBLECHE
B02/ Stahlbezeichn. **S355J2+N** AD2000-W1:06 B03 Anforderungen EN-10025-2:04/AM43:REV.0 OPTION-5 CLASS 3			

Z04 CE-Zeichen

POSITION-NR.: 26-29

CE 0769	**EN 10025-1:2004** **Grobblech S355J2 / 1.0577** **zur Verwendung in geschweißten, geschraubten und genieteten Bauteilen**
DILLINGER **Dillinger France** **CS 56317 F-59379 Dunkerque Cedex 1** **19** **S355J2_EN10025-2-04_B_160101D2**	**Grenzabmaße und Formtoleranzen:** **Dehnung** **Zugfestigkeit** **Streckgrenze** **Kerbschlagarbeit** **Schweißbarkeit** **Dauerhaftigkeit (chemische Zusammensetzung)** **wie in der Leistungserklärung angegeben** **S355J2_EN10025-2-04_B_160101D2**

Die Leistungserklärung kann von folgender Adresse heruntergeladen werden: www.dillinger.de/dop/S355J2_EN10025-2-04_B_160101D2.pdf

A04 D F Zeichen des Herstellers	Z01/Z02/Z03 Es wird bestätigt, dass die Lieferung den Vereinbarungen bei der Bestellung entspricht.	POISSONNET Der Abnahmebeauftragte	**Dillinger France** Port 3032 3032 rue du Comte Jean - CS 56317 F-59379 Dunkerque Cedex 1 - FRANCE Service Qualité-Essais Datum 05.09.19 JB 1 A01

Appendix C2: *Predicted S-N curve using corrosion-based fatigue model*

Max Corrosion - Upper bound -R-0.5

R	UTS	f		d-corrosion	Cycle	Stress Range
0.5	559.716	0.67		0.307	1000	1007.489
					1000000	131.3169

Min Corrosion - lower bound -R-0.5

R	UTS	f		d-corrosion	Cycle	Stress Range
0.5	559.716	0.67		0.222	1000	1007.489
					1000000	101.591

Min Corrosion - lower bound -R-0.1

R	UTS	f		d-corrosion	Cycle	Stress Range
0.1	559.716	0.67		0.222	1000	1007.489
					1000000	113.9035

Max Corrosion - Upper bound -R-0.1

R	UTS	f		d-corrosion	Cycle	Stress Range
0.1	559.716	0.67		0.307	1000	1007.489
					1000000	152.6454

Max-R-0.5		Min-R-0.5		Min-R-0.1		Max-R-0.1	
A=	7729.648	A=	9991.375	A=	8911.347	A=	6649.62
n =	-0.29497	n =	-0.33213	n =	-0.31557	n =	-0.27319

Cycles	Stress range	Cycles	Stress range	Cycles	Stress range	Cycles	Stress range
10000	510.819	10000	468.9342	10000	487.161	10000	537.0994
20000	416.3622	20000	372.5043	20000	391.4508	20000	444.4446
30000	369.4274	30000	325.5715	30000	344.4359	30000	397.8433
40000	339.3716	40000	295.9039	40000	314.5443	40000	367.7737
50000	317.753	50000	274.7667	50000	293.1569	50000	346.024
60000	301.1157	60000	258.6222	60000	276.7662	60000	329.2115
70000	287.7305	70000	245.7145	70000	263.6252	70000	315.6357
80000	276.6176	80000	235.0553	80000	252.7473	80000	304.3292
90000	267.1721	90000	226.0377	90000	243.5255	90000	294.6928
100000	258.9965	100000	218.2647	100000	235.5618	100000	286.3315
110000	251.8165	110000	211.4637	110000	228.5823	110000	278.9724
120000	245.4356	120000	205.4401	120000	222.3913	120000	272.4194
130000	239.7086	130000	200.0505	130000	216.8443	130000	266.5272
140000	234.5255	140000	195.1867	140000	211.832	140000	261.1855
150000	229.8009	150000	190.765	150000	207.2698	150000	256.3088
160000	225.4675	160000	186.7194	160000	203.0912	160000	251.8295
170000	221.4714	170000	182.9974	170000	199.2428	170000	247.6931
180000	217.7687	180000	179.5562	180000	195.6812	180000	243.8554
190000	214.3231	190000	176.3606	190000	192.3708	190000	240.2801
200000	211.1048	200000	173.3816	200000	189.2821	200000	236.9366
210000	208.0884	210000	170.5946	210000	186.3901	210000	233.7995
220000	205.2525	220000	167.9791	220000	183.6738	220000	230.847
230000	202.5788	230000	165.5173	230000	181.1153	230000	228.0607
240000	200.0515	240000	163.1942	240000	178.6991	240000	225.4244
250000	197.657	250000	160.9965	250000	176.4119	250000	222.9245
260000	195.3835	260000	158.9129	260000	174.2419	260000	220.5487
270000	193.2205	270000	156.9334	270000	172.1791	270000	218.2865
280000	191.1588	280000	155.0492	280000	170.2143	280000	216.1285
290000	189.1903	290000	153.2527	290000	168.3398	290000	214.0665
300000	187.3078	300000	151.5368	300000	166.5485	300000	212.0931
310000	185.5049	310000	149.8954	310000	164.834	310000	210.2017
320000	183.7758	320000	148.3231	320000	163.1908	320000	208.3865
330000	182.1152	330000	146.815	330000	161.6138	330000	206.642
340000	180.5186	340000	145.3665	340000	160.0985	340000	204.9636
350000	178.9816	350000	143.9737	350000	158.6407	350000	203.3469
360000	177.5005	360000	142.6329	360000	157.2366	360000	201.788
370000	176.0717	370000	141.3408	370000	155.883	370000	200.2833
380000	174.6921	380000	140.0945	380000	154.5766	380000	198.8294
390000	173.3587	390000	138.891	390000	153.3147	390000	197.4235

400000	172.0689	400000	137.728	400000	152.0947	400000	196.0628
410000	170.8202	410000	136.6031	410000	150.9142	410000	194.7446
420000	169.6103	420000	135.5142	420000	149.7709	420000	193.4668
430000	168.4371	430000	134.4593	430000	148.6629	430000	192.2272
440000	167.2987	440000	133.4365	440000	147.5883	440000	191.0237
450000	166.1934	450000	132.4443	450000	146.5453	450000	189.8545
460000	165.1194	460000	131.481	460000	145.5324	460000	188.718
470000	164.0753	470000	130.5452	470000	144.5481	470000	187.6125
480000	163.0595	480000	129.6355	480000	143.5909	480000	186.5365
490000	162.0707	490000	128.7508	490000	142.6597	490000	185.4888
500000	161.1078	500000	127.8898	500000	141.7531	500000	184.4678
510000	160.1695	510000	127.0514	510000	140.87	510000	183.4726
520000	159.2547	520000	126.2346	520000	140.0094	520000	182.5019
530000	158.3624	530000	125.4385	530000	139.1703	530000	181.5547
540000	157.4916	540000	124.6622	540000	138.3519	540000	180.63
550000	156.6415	550000	123.9048	550000	137.5531	550000	179.7268
560000	155.8111	560000	123.1655	560000	136.7731	560000	178.8443
570000	154.9998	570000	122.4436	570000	136.0113	570000	177.9816
580000	154.2067	580000	121.7384	580000	135.2669	580000	177.138
590000	153.4311	590000	121.0491	590000	134.5392	590000	176.3127
600000	152.6723	600000	120.3753	600000	133.8275	600000	175.505
610000	151.9297	610000	119.7163	610000	133.1313	610000	174.7143
620000	151.2027	620000	119.0715	620000	132.4499	620000	173.9399
630000	150.4908	630000	118.4404	630000	131.7828	630000	173.1813
640000	149.7933	640000	117.8225	640000	131.1295	640000	172.4378
650000	149.1098	650000	117.2174	650000	130.4895	650000	171.709
660000	148.4398	660000	116.6245	660000	129.8623	660000	170.9943
670000	147.7828	670000	116.0435	670000	129.2475	670000	170.2933
680000	147.1384	680000	115.4739	680000	128.6447	680000	169.6054
690000	146.5062	690000	114.9153	690000	128.0534	690000	168.9304
700000	145.8857	700000	114.3675	700000	127.4733	700000	168.2676
710000	145.2766	710000	113.8299	710000	126.904	710000	167.6169
720000	144.6784	720000	113.3024	720000	126.3451	720000	166.9776
730000	144.091	730000	112.7845	730000	125.7963	730000	166.3496
740000	143.5139	740000	112.276	740000	125.2574	740000	165.7325
750000	142.9468	750000	111.7766	750000	124.7279	750000	165.1259
760000	142.3894	760000	111.286	760000	124.2077	760000	164.5295
770000	141.8414	770000	110.8038	770000	123.6964	770000	163.9429
780000	141.3025	780000	110.33	780000	123.1937	780000	163.3661
790000	140.7726	790000	109.8642	790000	122.6995	790000	162.7985
800000	140.2512	800000	109.4062	800000	122.2134	800000	162.24
810000	139.7382	810000	108.9557	810000	121.7352	810000	161.6904
820000	139.2334	820000	108.5126	820000	121.2648	820000	161.1493
830000	138.7364	830000	108.0766	830000	120.8018	830000	160.6166
840000	138.2472	840000	107.6476	840000	120.3461	840000	160.0919
850000	137.7654	850000	107.2253	850000	119.8975	850000	159.5752
860000	137.291	860000	106.8096	860000	119.4558	860000	159.0661
870000	136.8236	870000	106.4002	870000	119.0208	870000	158.5646
880000	136.3631	880000	105.9971	880000	118.5923	880000	158.0703
890000	135.9094	890000	105.6001	890000	118.1702	890000	157.5831
900000	135.4622	900000	105.2089	900000	117.7543	900000	157.1028
910000	135.0213	910000	104.8235	910000	117.3444	910000	156.6293
920000	134.5868	920000	104.4437	920000	116.9404	920000	156.1623
930000	134.1583	930000	104.0694	930000	116.5421	930000	155.7018
940000	133.7357	940000	103.7003	940000	116.1494	940000	155.2475
950000	133.3189	950000	103.3365	950000	115.7622	950000	154.7994
960000	132.9077	960000	102.9778	960000	115.3803	960000	154.3572
970000	132.5021	970000	102.6239	970000	115.0036	970000	153.9208
980000	132.1018	980000	102.2749	980000	114.632	980000	153.4902
990000	131.7068	990000	101.9307	990000	114.2653	990000	153.0651
1000000	131.3169	1000000	101.591	1000000	113.9035	1000000	152.6454
1010000	130.9321	1010000	101.2558	1010000	113.5464	1010000	152.231
1020000	130.5521	1020000	100.925	1020000	113.1939	1020000	151.8218
1030000	130.177	1030000	100.5985	1030000	112.846	1030000	151.4177
1040000	129.8065	1040000	100.2762	1040000	112.5024	1040000	151.0186
1050000	129.4406	1050000	99.95801	1050000	112.1632	1050000	150.6243
1060000	129.0792	1060000	99.64382	1060000	111.8282	1060000	150.2348
1070000	128.7222	1070000	99.33356	1070000	111.4973	1070000	149.8499
1080000	128.3694	1080000	99.02713	1080000	111.1705	1080000	149.4696
1090000	128.0209	1090000	98.72446	1090000	110.8476	1090000	149.0937
1100000	127.6765	1100000	98.42547	1100000	110.5287	1100000	148.7222
1110000	127.3361	1110000	98.13008	1110000	110.2135	1110000	148.355

For brevity, cycles at 10^7 are provided below.

9760000	81.6852	9760000	59.5261	9760000	68.54325	9760000	98.34112
9770000	81.6852	9770000	59.5261	9770000	68.54325	9770000	98.34112
9780000	81.6852	9780000	59.5261	9780000	68.54325	9780000	98.34112
9790000	81.6852	9790000	59.5261	9790000	68.54325	9790000	98.34112
9800000	81.6852	9800000	59.5261	9800000	68.54325	9800000	98.34112
9810000	81.6852	9810000	59.5261	9810000	68.54325	9810000	98.34112
9820000	81.6852	9820000	59.5261	9820000	68.54325	9820000	98.34112
9830000	81.6852	9830000	59.5261	9830000	68.54325	9830000	98.34112
9840000	81.6852	9840000	59.5261	9840000	68.54325	9840000	98.34112
9850000	81.6852	9850000	59.5261	9850000	68.54325	9850000	98.34112
9860000	81.6852	9860000	59.5261	9860000	68.54325	9860000	98.34112
9870000	81.6852	9870000	59.5261	9870000	68.54325	9870000	98.34112
9880000	81.6852	9880000	59.5261	9880000	68.54325	9880000	98.34112
9890000	81.6852	9890000	59.5261	9890000	68.54325	9890000	98.34112
9900000	81.6852	9900000	59.5261	9900000	68.54325	9900000	98.34112
9910000	81.6852	9910000	59.5261	9910000	68.54325	9910000	98.34112
9920000	81.6852	9920000	59.5261	9920000	68.54325	9920000	98.34112
9930000	81.6852	9930000	59.5261	9930000	68.54325	9930000	98.34112
9940000	81.6852	9940000	59.5261	9940000	68.54325	9940000	98.34112
9950000	81.6852	9950000	59.5261	9950000	68.54325	9950000	98.34112
9960000	81.6852	9960000	59.5261	9960000	68.54325	9960000	98.34112
9970000	81.6852	9970000	59.5261	9970000	68.54325	9970000	98.34112
9980000	81.6852	9980000	59.5261	9980000	68.54325	9980000	98.34112
9990000	81.6852	9990000	59.5261	9990000	68.54325	9990000	98.34112
10000000	81.6852	10000000	59.5261	10000000	68.54325	10000000	98.34112

Appendix D: Fatigue testing calibration and results

Appendix D1: *Calibration fatigue test data (shortened)*

Parameters

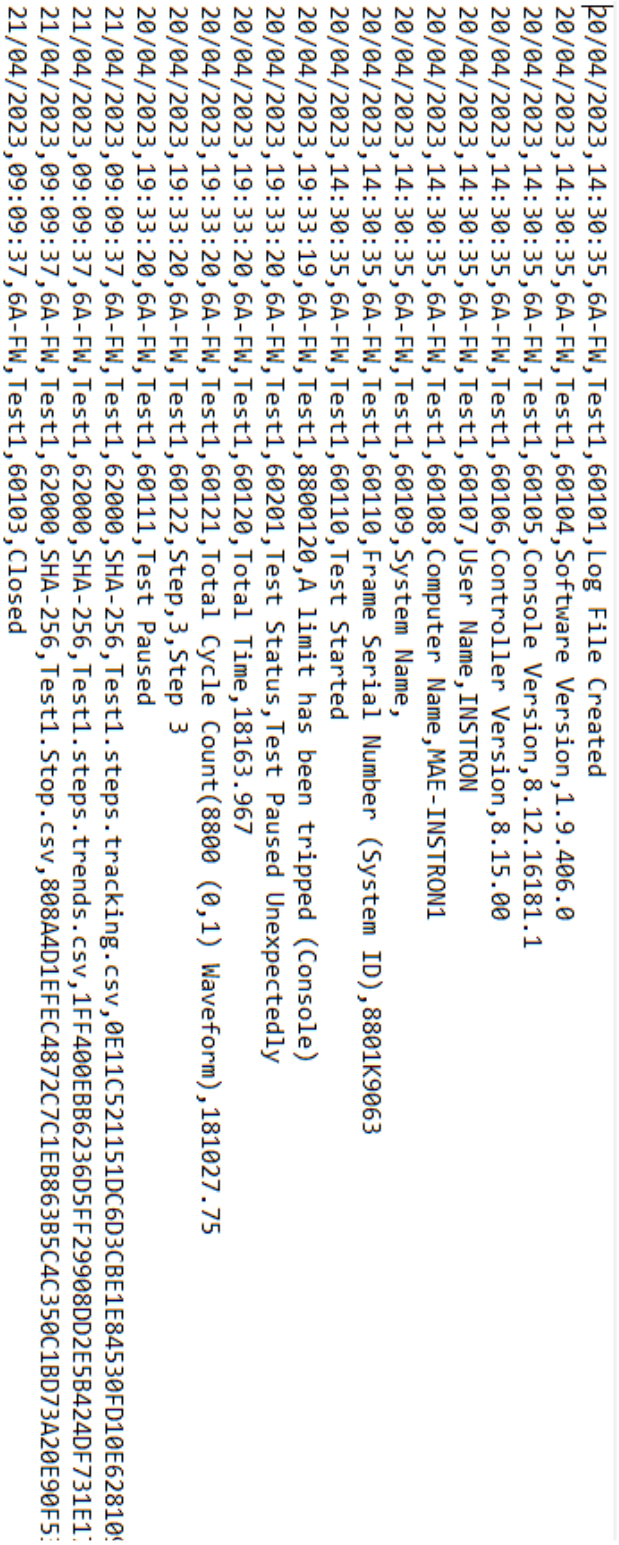

```
20/04/2023,14:30:35,6A-FW,Test1,60101,Log File Created
20/04/2023,14:30:35,6A-FW,Test1,60104,Software Version,1.9.406.0
20/04/2023,14:30:35,6A-FW,Test1,60105,Console Version,8.12.16181.1
20/04/2023,14:30:35,6A-FW,Test1,60106,Controller Version,8.15.00
20/04/2023,14:30:35,6A-FW,Test1,60107,User Name,INSTRON
20/04/2023,14:30:35,6A-FW,Test1,60108,Computer Name,MAE-INSTRON1
20/04/2023,14:30:35,6A-FW,Test1,60109,System Name,
20/04/2023,14:30:35,6A-FW,Test1,60110,Frame Serial Number (System ID),8801K9063
20/04/2023,14:30:35,6A-FW,Test1,60110,Test Started
20/04/2023,19:33:19,6A-FW,Test1,8800120,A limit has been tripped (Console)
20/04/2023,19:33:20,6A-FW,Test1,60201,Test Status,Test Paused Unexpectedly
20/04/2023,19:33:20,6A-FW,Test1,60120,Total Time,18163.967
20/04/2023,19:33:20,6A-FW,Test1,60121,Total Cycle Count(8800 (0,1) Waveform),181027.75
20/04/2023,19:33:20,6A-FW,Test1,60122,Step,3,Step 3
20/04/2023,19:33:20,6A-FW,Test1,60111,Test Paused
21/04/2023,09:09:37,6A-FW,Test1,62000,SHA-256,Test1.steps.tracking.csv,0E11C521151DC6D3CBE1E84530FD10E62810
21/04/2023,09:09:37,6A-FW,Test1,62000,SHA-256,Test1.steps.trends.csv,1FF400EBB6236D5FF29908DD2E5B424DF731E1
21/04/2023,09:09:37,6A-FW,Test1,62000,SHA-256,Test1.Stop.csv,808A4D1EFEC4872C7C1EB863B5C4C350C1BD73A20E90F5
21/04/2023,09:09:37,6A-FW,Test1,60103,Closed
```

Total Time (s)	Cycle Elapsed Time (s)	Total Cycles	Elapsed Cycles	Step	Total Cycle Count(8800 (0,1) Waveform)	Position(8800 (0,1):Position) (mm)	Load(8800 (0,1):Load) (kN)
18160.445	0.1	181000	181000	3	181000	30.54326746	22.37156928
18160.455	0.01	181001	181001	3	181000	30.62207523	27.95487344
18160.466	0.021	181001	181001	3	181000	30.69505591	33.14823806
18160.477	0.032	181001	181001	3	181000.25	30.72738994	35.19192934
18160.48	0.035	181001	181001	3	181000.25	30.72856564	35.1265341
18160.483	0.038	181001	181001	3	181000.25	30.72696302	34.89598632
18160.494	0.049	181001	181001	3	181000.25	30.67690406	31.22445941
18160.504	0.059	181001	181001	3	181000.5	30.60523543	25.99609792
18160.515	0.07	181001	181001	3	181000.5	30.52748266	20.49216181
18160.525	0.08	181001	181001	3	181000.75	30.49043241	17.79422164
18160.529	0.084	181001	181001	3	181000.75	30.48761162	17.61652827
18160.53	0.085	181001	181001	3	181000.75	30.48743728	17.63672531
18160.531	0.086	181001	181001	3	181000.75	30.48777032	17.67521054
18160.541	0.096	181001	181001	3	181000.75	30.52292961	20.42138129
18160.545	0.1	181001	181001	3	181001	30.54836813	22.37079591
18160.556	0.011	181002	181002	3	181001	30.63336957	28.50614786
18160.567	0.022	181002	181002	3	181001	30.70551876	33.49632323
18160.577	0.032	181002	181002	3	181001.25	30.73302258	35.18815935
18160.582	0.037	181002	181002	3	181001.25	30.73375124	35.00059247
18160.584	0.039	181002	181002	3	181001.25	30.73101539	34.72641408
18160.594	0.049	181002	181002	3	181001.25	30.68296138	31.22574687
18160.605	0.06	181002	181002	3	181001.5	30.60244817	25.45024753
18160.615	0.07	181002	181002	3	181001.5	30.5327979	20.48932314
18160.628	0.083	181002	181002	3	181001.75	30.49155894	17.61633158
18160.63	0.085	181002	181002	3	181001.75	30.49092191	17.6398769
18160.631	0.086	181002	181002	3	181001.75	30.49159917	17.67888814
18160.642	0.097	181002	181002	3	181001.75	30.53329858	20.87787688
18160.645	0.1	181002	181002	3	181002	30.55414605	22.37418294
18160.656	0.011	181003	181003	3	181002	30.63978005	28.50557864
18160.666	0.021	181003	181003	3	181002	30.70626754	33.15379918
18160.677	0.032	181003	181003	3	181002.25	30.73854793	35.18993258
18160.678	0.033	181003	181003	3	181002.25	30.73910672	35.18924415
18160.68	0.035	181003	181003	3	181002.25	30.738311	35.1229637
18160.691	0.046	181003	181003	3	181002.25	30.70670564	32.54357278
18160.701	0.056	181003	181003	3	181002.5	30.63889268	27.65111327
18160.712	0.067	181003	181003	3	181002.5	30.55782291	21.80618644
18160.722	0.077	181003	181003	3	181002.75	30.50812381	18.26617867
18160.729	0.084	181003	181003	3	181002.75	30.49882772	17.61659831
18160.731	0.086	181003	181003	3	181002.75	30.49873385	17.6757887
18160.732	0.087	181003	181003	3	181002.75	30.49916747	17.75126755
18160.742	0.097	181003	181003	3	181002.75	30.53984094	20.87677717
18160.745	0.1	181003	181003	3	181003	30.56104156	22.37509489
18160.755	0.01	181004	181004	3	181003	30.6379405	27.96161175
18160.766	0.021	181004	181004	3	181003	30.71181301	33.15317631

Appendix D2: *stress-time curve from machining for fatigue testing (only 3.4-3.6secs shown)*

Non-drilled specimen

Time	Stress (MPa)	3.4404	15.399657	3.4812	24.539109	3.522	-2.9522094	3.5628	-0.3860678
3.4002	14.814219	3.441	19.318488	3.4818	23.659419	3.5226	9.0108081	3.5634	7.9518243
3.4008	23.080428	3.4416	28.281645	3.4824	22.818117	3.5232	15.172521	3.564	19.225731
3.4014	22.664586	3.4422	25.78023	3.483	14.599872	3.5238	20.04786	3.5646	21.938427
3.402	22.747746	3.4428	18.915414	3.4836	6.937623	3.5244	22.331904	3.5652	20.147022
3.4026	21.116319	3.4434	10.3513179	3.4842	0.88097961	3.525	22.811733	3.5658	20.991558
3.4032	15.338862	3.444	-1.6787295	3.4848	2.9798895	3.5256	15.329265	3.5664	23.134818
3.4038	7.6510854	3.4446	-1.560341	3.4854	-1.8867093	3.5262	9.5354973	3.567	6.6880695
3.4044	-5.9055948	3.4452	-10.142244	3.486	-6.2703753	3.5268	6.4993047	3.5676	3.3606342
3.405	-5.0736462	3.4458	-10.971036	3.4866	-0.795622	3.5274	3.0630789	3.5682	-4.8528606
3.4056	-11.099036	3.4464	-3.1409931	3.4872	0.95137056	3.528	-5.9919909	3.5688	-9.4766553
3.4062	-5.5056183	3.447	0.53862249	3.4878	0.88097961	3.5286	-11.441434	3.5694	-6.5007621
3.4068	6.2721456	3.4476	8.5756986	3.4884	10.5144795	3.5292	-3.8897313	3.57	5.6706531
3.4074	14.73423	3.4482	11.9925351	3.489	14.743827	3.5298	4.3236816	3.5706	13.912059
3.408	26.423187	3.4488	17.754177	3.4896	25.962573	3.5304	19.340895	3.5712	21.752892
3.4086	27.021351	3.4494	21.944832	3.4902	26.81343	3.531	32.906853	3.5718	20.988345
3.4092	31.621023	3.45	28.383999	3.4908	23.873745	3.5316	45.45072	3.5724	23.857743
3.4098	30.0825	3.4506	27.891402	3.4914	26.160897	3.5322	55.920837	3.573	30.955722
3.4104	29.954547	3.4512	30.984513	3.492	27.52995	3.5328	59.489514	3.5736	30.252033
3.411	37.052064	3.4518	33.300267	3.4926	32.510226	3.5334	58.549386	3.5742	36.703443
3.4116	41.261094	3.4524	39.709908	3.4932	31.265976	3.534	55.687401	3.5748	37.301544
3.4122	44.433711	3.453	48.805512	3.4938	34.816362	3.5346	53.209086	3.5754	36.249276
3.4128	39.546801	3.4536	53.202681	3.4944	37.397493	3.5352	45.40914	3.576	43.263171
3.4134	48.687177	3.4542	52.236912	3.495	38.782401	3.5358	50.06232	3.5766	40.947648
3.414	45.79932	3.4548	55.067019	3.4956	47.842893	3.5364	47.58705	3.5772	47.986806
3.4146	53.106753	3.4554	52.700613	3.4962	57.353436	3.537	49.784091	3.5778	45.748143
3.4152	51.913932	3.456	57.839502	3.4968	46.269447	3.5376	49.921599	3.5784	48.997389
3.4158	45.661791	3.4566	59.732526	3.4974	54.216414	3.5382	42.265335	3.579	50.992935
3.4164	55.329246	3.4572	56.774655	3.498	53.077962	3.5388	44.48808	3.5796	52.531122
3.417	52.307283	3.4578	55.063827	3.4986	52.246509	3.5394	46.60845	3.5802	50.494038
3.4176	59.876418	3.4584	62.901363	3.4992	58.056936	3.54	54.395481	3.5808	60.483969
3.4182	56.931336	3.459	66.674391	3.4998	51.223179	3.5406	54.692883	3.5814	58.31595
3.4188	59.092992	3.4596	68.04609	3.5004	53.388174	3.5412	52.089807	3.582	58.264794
3.4194	62.648754	3.4602	63.134778	3.501	53.711154	3.5418	49.889637	3.5826	60.404022
3.42	59.978751	3.4608	61.535985	3.5016	52.006668	3.5424	50.372532	3.5832	56.310975
3.4206	57.219141	3.4614	53.877432	3.5022	53.384961	3.543	50.900178	3.5838	54.008556
3.4212	49.115703	3.462	57.641241	3.5028	59.879631	3.5436	53.413752	3.5844	56.813022
3.4218	53.522469	3.4626	54.232395	3.5034	52.643052	3.5442	54.753636	3.585	53.570433
3.4224	51.677283	3.4632	54.900741	3.504	53.237856	3.5448	57.212736	3.5856	60.627861
3.423	53.221875	3.4638	55.668207	3.5046	50.279775	3.5454	53.014017	3.5862	58.824381
3.4236	56.483658	3.4644	54.446658	3.5052	49.803285	3.546	52.262511	3.5868	54.094887
3.4242	52.854123	3.465	58.069725	3.5058	53.778291	3.5466	42.936957	3.5874	52.169754
3.4248	51.427845	3.4656	58.066533	3.5064	47.200083	3.5472	49.397145	3.588	49.406742
3.4254	48.636	3.4662	51.226371	3.507	48.297018	3.5478	45.597846	3.5886	52.137792
3.426	44.916627	3.4668	48.632808	3.5076	46.765152	3.5484	49.921599	3.5892	46.256658
3.4266	46.509309	3.4674	44.353764	3.5082	44.884644	3.549	47.366382	3.5898	42.182175
3.4272	43.640562	3.468	35.539224	3.5088	48.386562	3.5496	46.368588	3.5904	47.107347
3.4278	34.310997	3.4686	28.313628	3.5094	40.276005	3.5502	44.350572	3.591	45.082947
3.4284	32.913237	3.4692	26.384799	3.51	45.194877	3.5508	44.942226	3.5916	46.000794
3.429	23.253174	3.4698	32.459049	3.5106	42.793044	3.5514	29.445969	3.5922	44.468886
3.4296	21.196287	3.4704	33.037998	3.5112	36.482754	3.552	22.45026	3.5928	41.600097
3.4302	15.518013	3.471	32.606196	3.5118	29.122905	3.5526	20.211009	3.5934	39.914595
3.4308	14.983773	3.4716	38.379411	3.5124	31.294767	3.5532	17.511039	3.594	35.29932
3.4314	24.129651	3.4722	47.913243	3.513	11.4262701	3.5538	13.960044	3.5946	31.6722
3.432	34.208643	3.4728	57.698802	3.5136	11.3014986	3.5544	13.880055	3.5952	21.567357
3.4326	48.853476	3.4734	55.041441	3.5142	18.988998	3.555	18.301206	3.5958	18.889836
3.4332	49.160475	3.474	55.188546	3.5148	21.522564	3.5556	35.10423	3.5964	15.991479
3.4338	48.063561	3.4746	43.909215	3.5154	30.584673	3.5562	45.473106	3.597	19.615995
3.4344	47.465523	3.4752	33.62331	3.516	40.28241	3.5568	43.426278	3.5976	16.093854
3.435	39.268551	3.4758	25.588311	3.5166	51.290337	3.5574	44.859066	3.5982	25.636296
3.4356	28.4256	3.4764	13.211436	3.5172	49.496286	3.558	39.968964	3.5988	35.392077
3.4362	13.201839	3.477	6.2113569	3.5178	47.008206	3.5586	30.9813	3.5994	39.297321
3.4368	7.9614234	3.4776	5.1363459	3.5184	30.923739	3.5592	23.493078	3.6	37.835679
3.4374	6.9312222	3.4782	4.102917	3.519	12.5364015	3.5598	11.4390675		
3.438	5.5778709	3.4788	5.3251149	3.5196	6.1889604	3.5604	1.7576643		
3.4386	2.3079882	3.4794	7.6414863	3.5202	-1.2627718	3.561	-2.1874797		
3.4392	11.6822097	3.48	14.247975	3.5208	1.04095908	3.5616	-7.1407329		
3.4398	12.4052355	3.4806	19.66398	3.5214	-0.9172086	3.5622	-1.3683606		

Drilled specimen

Time	Stress (MPa)	3.4404	92.30476	3.4812	92.83716	3.522	110.01338	3.5628	116.68944
3.4002	82.28836	3.441	97.72088	3.4818	102.5884	3.5226	122.6	3.5634	121.77814
3.4008	88.91326	3.4416	108.7019	3.4824	113.19194	3.5232	130.14482	3.564	123.7736
3.4014	99.53508	3.4422	115.036	3.483	123.95112	3.5238	130.0166	3.5646	122.67232
3.402	111.32818	3.4428	120.69004	3.4836	123.47114	3.5244	128.31692	3.5652	138.01244
3.4026	118.61248	3.4434	125.54882	3.4842	125.16748	3.525	140.70854	3.5658	148.38626
3.4032	120.31528	3.444	129.85222	3.4848	137.10828	3.5256	149.13928	3.5664	152.94714
3.4038	121.70912	3.4446	136.57892	3.4854	144.0722	3.5262	157.04456	3.567	156.98536
3.4044	123.62238	3.4452	151.21748	3.486	152.18754	3.5268	158.42574	3.5676	149.2149
3.405	139.08102	3.4458	160.18842	3.4866	158.53426	3.5274	153.3286	3.5682	154.52558
3.4056	158.73816	3.4464	158.87628	3.4872	151.58906	3.528	145.76558	3.5688	152.5624
3.4062	155.4891	3.447	154.34472	3.4878	145.61434	3.5286	153.82844	3.5694	157.78776
3.4068	153.67388	3.4476	151.24378	3.4884	150.50062	3.5292	163.35212	3.57	164.54264
3.4074	148.05744	3.4482	148.52108	3.489	160.36272	3.5298	164.8485	3.5706	159.77736
3.408	153.15102	3.4488	156.6335	3.4896	165.28264	3.5304	163.08246	3.5712	161.59596
3.4086	152.76628	3.4494	165.48324	3.4902	161.7867	3.531	161.7012	3.5718	166.7297
3.4092	160.67186	3.45	162.35236	3.4908	155.9725	3.5316	162.94432	3.5724	166.1706
3.4098	157.10374	3.4506	157.2353	3.4914	158.11662	3.5322	170.3146	3.573	175.85664
3.4104	159.6195	3.4512	162.2274	3.492	164.4407	3.5328	173.31418	3.5736	175.54746
3.411	160.63238	3.4518	165.2004	3.4926	171.2355	3.5334	174.416	3.5742	175.43564
3.4116	171.16974	3.4524	170.3705	3.4932	172.33404	3.534	171.31116	3.5748	175.33366
3.4122	169.57458	3.453	173.1859	3.4938	170.76848	3.5346	173.6332	3.5754	178.68534
3.4128	168.31822	3.4536	171.81436	3.4944	169.73246	3.5352	179.31028	3.576	180.39574
3.4134	172.57084	3.4542	169.841	3.495	172.0742	3.5358	179.22148	3.5766	175.91256
3.414	166.50276	3.4548	175.34354	3.4956	177.61962	3.5364	180.39246	3.5772	169.02204
3.4146	174.6561	3.4554	179.38922	3.4962	181.37266	3.537	184.31336	3.5778	163.3357
3.4152	173.32732	3.456	175.53758	3.4968	183.2443	3.5376	177.567	3.5784	146.8704
3.4158	177.46502	3.4566	172.02816	3.4974	178.41562	3.5382	161.10596	3.579	133.9191
3.4164	175.14948	3.4572	176.66248	3.498	169.99228	3.5388	148.08704	3.5796	116.7519
3.417	177.37622	3.4578	169.05822	3.4986	160.6291	3.5394	138.53522	3.5802	109.74714
3.4176	174.70216	3.4584	163.41132	3.4992	144.0163	3.54	132.2588	3.5808	107.49888
3.4182	160.43178	3.459	146.13386	3.4998	130.72346	3.5406	127.51146	3.5814	100.96806
3.4188	151.02674	3.4596	129.4906	3.5004	118.81628	3.5412	118.85574	3.582	92.44278
3.4194	126.82436	3.4602	122.69532	3.501	112.7975	3.5418	113.10318	3.5826	77.04066
3.42	112.75148	3.4608	121.58748	3.5016	117.577	3.5424	106.27946	3.5832	73.37038
3.4206	111.0488	3.4614	116.31142	3.5022	111.10796	3.543	79.13378	3.5838	71.41866
3.4212	112.19924	3.462	104.96802	3.5028	84.74306	3.5436	69.38154	3.5844	70.11096
3.4218	112.69888	3.4626	81.08236	3.5034	66.4935	3.5442	54.86994	3.585	63.43472
3.4224	94.16488	3.4632	64.90332	3.504	50.6026	3.5448	57.1203	3.5856	62.61336
3.423	69.17454	3.4638	61.22692	3.5046	56.72606	3.5454	81.5917	3.5862	53.21752
3.4236	51.8772	3.4644	59.16044	3.5052	65.62284	3.546	72.82166	3.5868	41.97324
3.4242	58.53296	3.465	74.18526	3.5058	68.80984	3.5466	62.95176	3.5874	31.33454
3.4248	67.09804	3.4656	78.96948	3.5064	62.67906	3.5472	55.5204	3.588	28.49358
3.4254	71.6585	3.4662	66.3128	3.507	47.44246	3.5478	43.60904	3.5886	21.61322
3.426	63.44456	3.4668	53.83512	3.5076	32.70742	3.5484	34.50074	3.5892	27.886
3.4266	55.22474	3.4674	46.8249	3.5082	23.28484	3.549	26.73322	3.5898	30.4806
3.4272	42.01922	3.468	32.44138	3.5088	12.030778	3.5496	15.66924	3.5904	29.4756
3.4278	26.62812	3.4686	22.17808	3.5094	28.45088	3.5502	25.04514	3.591	26.6971
3.4284	20.08286	3.4692	16.25378	3.51	30.57584	3.5508	34.66496	3.5916	20.36858
3.429	17.5739	3.4698	23.03852	3.5106	42.50208	3.5514	40.48854	3.5922	21.23228
3.4296	32.11952	3.4704	29.55442	3.5112	37.21376	3.552	33.3873	3.5928	12.26392
3.4302	38.8725	3.471	28.61182	3.5118	39.18124	3.5526	38.3568	3.5934	17.922
3.4308	35.5058	3.4716	31.52176	3.5124	28.37864	3.5532	31.79764	3.594	15.99106
3.4314	36.7572	3.4722	31.3641	3.513	21.8661	3.5538	21.63622	3.5946	18.49012
3.432	32.0177	3.4728	24.02704	3.5136	16.08958	3.5544	14.87784	3.5952	32.76654
3.4326	26.39822	3.4734	19.77088	3.5142	14.19808	3.555	15.64298	3.5958	45.18904
3.4332	12.39856	3.474	11.193426	3.5148	17.95156	3.5556	15.07814	3.5964	50.0343
3.4338	17.18968	3.4746	12.8353	3.5154	22.7331	3.5562	18.15188	3.597	52.37982
3.4344	16.91384	3.4752	12.38214	3.516	36.81962	3.5568	38.06448	3.5976	56.62422
3.435	23.66908	3.4758	14.20464	3.5166	50.41864	3.5574	52.46852	3.5982	58.06974
3.4356	38.00206	3.4764	35.07552	3.5172	54.3476	3.558	61.31892	3.5988	66.30952
3.4362	51.35488	3.477	48.21114	3.5178	60.64542	3.5586	72.62452	3.5994	71.96736
3.4368	64.44006	3.4776	58.42126	3.5184	69.59838	3.5592	70.44938	3.6	78.18086
3.4374	68.33342	3.4782	70.46252	3.519	74.82928	3.5598	74.48098		
3.438	67.38388	3.4788	75.102	3.5196	84.85808	3.5604	76.83692		
3.4386	71.92466	3.4794	76.22574	3.5202	84.4966	3.561	86.35		
3.4392	86.79364	3.48	81.63114	3.5208	89.2386	3.5616	95.99872		
3.4398	86.81006	3.4806	85.08154	3.5214	102.39448	3.5622	101.92448		

Appendix E: Rainflow and damage calculations

Appendix E1: *Wind data (courtesy of Marine Data Exchange) (Shortened).*

Wind Speed	Wind Direction	Wind Speed (Thrust)	Wind Speed (Thrust) Direction	Direction
1.0225	91.3	3.0175	218.05	West
0.665	91.25	0	0	West
0.395	95.525	0	0	West
1.1875	99.55	0.6	23.175	West
1.7825	109.875	0.3925	52.25	West
0.795	103.975	0.765	83.375	West
1.24	88.325	1.3975	84.725	West
1.8975	108	1.7125	103.375	West
1.5175	101.725	1.5375	104.3	West
1.8225	86.85	1.4375	92.55	West
1.6975	72.175	1.3025	79.675	West
1.5625	77.7	1.5625	86.125	West
1.6925	80.1	1.6875	86.325	West
1.985	72.85	2.07	73.05	West
2.41	70.35	2.5525	75.175	West
2.695	90.375	3.01	90.175	West
2.8025	97.525	3.51	96.5	West
2.5	96.35	3.4075	98.775	West
2.33	104.2	3.2	103.45	West
2.2875	109.025	3.21	108.325	West
1.965	111.7	2.98	107.55	West
1.6575	80.175	2.6075	99.275	West
2.1725	78.6	2.7675	90.25	West
1.8775	82.45	2.2825	83.55	West
1.91	68.525	2.325	75.5	West
2.6725	89.975	2.805	85	West
2.5625	76.05	2.0925	59.75	West
2.0475	96.25	3.6325	27.45	West
2.37	92.575	3.3825	25.025	West
3.325	74.675	3.3	73.35	West
7.5325	69.15	11.0825	78.15	West
7.685	67.725	8.0875	58.925	West
6.7525	67.625	7.015	58.975	West
2.555	91.775	4.485	61.575	West
3.3425	74.05	6.66	97.5	West
3.0125	70.8	6.375	95.375	West
3.0475	76.5	5.875	101.95	West
4.0325	76.625	6.415	103.925	West
3.8525	80.15	6.345	110.425	West
.	.	.	.	.	.

Appendix E2: *Weibull distribution algorithm*

17/10/23 11:55 C:\Users\N0968013\OneDri...\Weibull_2.m 1 of 2

```
clear all;
cd('C:\Users\N0968013\OneDrive - Nottingham Trent University\Documents\8-data\Matlab datas');
filename = 'C:\Users\N0968013\OneDrive - Nottingham Trent University\Documents\8-data\Matlab datas\fcWind.txt';

% Read the data as a table
T = readtable(filename);

% Define direction names and their corresponding degree ranges
directions = ["North", "Northwest", "West", "Southwest", "South", "Southeast", "East", "Northeast"];
dirRanges = [337.5 22.5; 22.5 67.5; 67.5 112.5; 112.5 157.5; 157.5 202.5; 202.5 247.5; 247.5 292.5; 292.5 337.5];

% Initialize arrays to store results
scaleParameters = zeros(1, 8);
shapeParameters = zeros(1, 8);
meanWindSpeeds = zeros(1, 8);
probOccurrence = zeros(1, 8);

for i = 1:length(directions)
    % Filter data for the current direction
    if i == 1 % Special case for North as it wraps around 360 degrees
        dirSpeeds = T.windSpeed((T.windDirection >= dirRanges(i,1) | T.windDirection <= dirRanges(i,2)));
    else
        dirSpeeds = T.windSpeed(T.windDirection >= dirRanges(i,1) & T.windDirection <= dirRanges(i,2));
    end

    % Calculate the probability of occurrence for this direction
    probOccurrence(i) = length(dirSpeeds) / height(T);  % Changed dirData to dirSpeeds

    % Ensure the data contains only positive values
    dirSpeeds = dirSpeeds(dirSpeeds > 0);

    if isempty(dirSpeeds) % check for empty filtered data
        warning(['No valid data for direction: ' directions(i)]);
        continue; % skip this iteration if no valid data
    end

    % Fit Weibull distribution
    try
        pd = fitdist(dirSpeeds, 'Weibull');
        % Store scale and shape parameters
        scaleParameters(i) = pd.A;
        shapeParameters(i) = pd.B;
    catch ME
        warning(['Error fitting Weibull for direction: ' directions(i) '. Message: ' ME.message]);
        continue; % skip to next iteration
    end
```

17/10/23 11:55 C:\Users\N0968013\OneDri...\Weibull_2.m 2 of 2

```
    % Calculate mean wind speed for this direction
    meanWindSpeeds(i) = mean(dirSpeeds);
end

% Display results
fprintf('Direction\tProbability of Occurrence\tScale Parameter\tShape Parameter\tMean Wind Speed (m/s)\n');
fprintf('----------\t----------\t----------\t----------\t----------\n');
for i = 1:length(directions)
    fprintf('%s\t%.2f\t%.2f\t%.3f\t%.2f\n', directions(i), probOccurrence(i), scaleParameters(i), shapeParameters(i), meanWindSpeeds(i));
end
```

Appendix E3: *Pierson-Moskowitz spectrum algorithm*

22/10/23 17:25 C:\Users\N096801...\generatePMWaveData.m 1 of 1

```
% Filename: generatePMWaveData.m

function [waveHeights, wavePeriods] = generatePMWaveData(numDataPoints, U10)

    g = 9.81; % acceleration due to gravity (m/s^2)

    % Pierson-Moskowitz spectrum definition
    PM_spectrum = @(f) (0.0081 * g^2) ./ (f.^5) .* exp(-0.74 * (g * f / U10^2));

    % Define frequency range based on wave periods of interest (2s to 7s)
    f_min = 1/7;
    f_max = 1/2;
    f = linspace(f_min, f_max, numDataPoints);

    % Calculate spectrum values
    Sf = PM_spectrum(f);

    % Inverse Fourier Transform to get wave elevations
    eta = ifft(sqrt(2*Sf).*exp(1i*2*pi*rand(size(Sf))));

    % Extract wave heights and periods from eta
    waveHeights = 0.1 + 8.3*abs(eta); % Modified to obtain wave height between 0.1↙
and 8.4m
    wavePeriods = 2 + 5*abs(eta);     % Modified to obtain wave period between 2 and↙
7 seconds

    % Adjust to desired range
    waveHeights(waveHeights > 8.4) = 8.4;
    wavePeriods(wavePeriods > 7) = 7;

end
```

22/10/23 17:25 C:\Users\N0968013\OneDri...\mainScript.m 1 of 1

```
% Filename: mainScript.m

U10 = 5; % 10m wind speed (m/s)
numDataPoints = 46379;

[waveHeights, wavePeriods] = generatePMWaveData(numDataPoints, U10);

% Display as a table
T = table(waveHeights', wavePeriods', 'VariableNames', {'WaveHeight_m',↙
'WavePeriod_s'});
disp(T);
```

Appendix E4: *Rainflow and damage calculation algorithm.*

15/09/23 11:00 C:\Users\N0968013\OneDrive - N...\RFC.m 1 of 2

```
% Import the data
data = readmatrix('C:\Users\N0968013\OneDrive - Nottingham Trent↙
University\Documents\8-data\Matlab datas\fc2new.txt');
% Name the columns
T.Properties.VariableNames = {'Time', 'Stress'};

time = data(:,1);
stress = data(:,2);

% Task 1 - Plot the stress vs time history graph
figure
plot(time, stress);
title('Stress vs Time');
xlabel('Time (s)');
ylabel('Stress (MPa)');

% 2) Perform fatigue rainflow counting
RF = rainflow(stress);

count = RF(:,1);
range = RF(:,2);
mean = RF(:,3);
start = RF(:,4);
ending = RF(:,4);

% 3) Create a histogram of the RF
figure
histogram(mean,100)
title('2D Rainflow Matrix Histogram')
xlabel('Stress range')
ylabel('Cycle count')

% 4) Plot 3D coloured RF histogram
figure;
histogram2(range, mean,100, 'FaceColor','flat');
colorbar;
title('3D Rainflow Matrix Histogram');
xlabel('Cycle mean');
ylabel('Cycle range');
zlabel('Number of cycles');

% 5) Damage estimation
% Create S-N curve
% Import the data
SN = readmatrix('C:\Users\N0968013\OneDrive - Nottingham Trent↙
University\Documents\8-data\Matlab datas\SN-10mm.txt');
% Name the columns

loglog(SN(:,1),SN(:,2))
xlabel('Number of cycles, N')
ylabel('Stres range, S')
title('S-N curve')
grid on
```

15/09/23 11:00 C:\Users\N0968013\OneDrive - N...\RFC.m 2 of 2

```
Nf = 1E6; % Example: Number of cycles to failure. This needs to be provided or estimated
b = -0.275; % Material-specific fatigue strength exponent (needs to be provided)
Se = (6791.8*Nf)^b; % Endurance limit

% Stress life plot (S-N curve)
N = logspace(5,6,100); % Number of cycles array
S = (6791.8*N.^b); % Stress array
loglog(N,S)
xlabel('Number of cycles (N)')
ylabel('Stress amplitude (S)')
title('S-N Curve')
grid on

% Fatigue damage calculation using the Palmgren-Miner rule
Ni = (range./6791.8).^((-1)/(0.275)); % Number of cycles to failure for each stress cycle (example)
Di = count./Ni;
D = sum(count./Ni); % Fatigue damage
disp(['Total fatigue damage: ', num2str(D)])


% 2D cummulative damage plot
figure;
cumulativeDamageStemPlot(count,Ni)
% xlabel('Range');
% ylabel('Damage');
% colorbar;
% title('2D Cummulative damage plot');
%
save('Fatigue_rainflow_damage')
```

15/09/23 11:00 C:\Users\...\cumulativeDamageStemPlot.m 1 of 1

```
function cumulativeDamageStemPlot(ni,Nfi)
figure
L = length(ni);
damage = sum(ni./Nfi);
stem(0,NaN,"Color",[0 1 0])
title("Cumulative Damage from Palmgren-Miner Rule")
xlabel("Cycle $i$","Interpreter","latex")
ylabel("Cum. damage $D_{i} = \sum_{j=1}^{i}n_{j}/N_{f,j}$","Interpreter","latex")
set(gca,"XLim",[0 L],"YLim",[0 damage])
grid("on")
iter = unique([1:round(L/100):L,L]);
hold(gca,"on")
for i = iter
    cdi = sum(ni(1:i)./Nfi(1:i)); % cumulative damge upto cycle i
    plt = stem(i,cdi,"filled");
    setStemColor(plt,cdi,0.95)
end
end
```

15/09/23 11:00 C:\Users\N0968013\One...\setStemColor.m 1 of 1

```
function setStemColor(hplt,cumulativeDamage,gamma)
c = lines(5);
c = c([2,3,5],:);
if (cumulativeDamage > 1)
    color = c(1,:);
else
    if (cumulativeDamage > gamma)
        c1 = c(1,:);
        c2 = c(2,:);
    else
        c1 = c(3,:);
        c2 = c(2,:);
    end
    color = zeros(1,3);
    for i = 1:3
        color(i) = c1(i)+(c2(i)-c1(i))*cumulativeDamage;
    end
end
hplt.Color = color;
end
```

Appendix E5: *Rainflow algorithm results showing first 55 data*

Rainflow count data 55/11459				
Cycle count	Range	Mean	Start	End
1	0.062	64.664	4	5
1	1.677	64.5845	3	7
1	7.231	61.2885	8	9
1	0.043	58.4725	13	14
1	3.145	59.1455	11	12
1	0.227	56.7045	17	18
1	1.822	56.308	16	19
1	0.248	56.893	24	26
1	3.42	56.095	23	27
1	1.906	57.139	29	30
1	0.643	57.5145	32	33
1	3.548	56.689	31	36
1	0.227	58.3375	42	43
1	2.39	57.317	40	44
1	1.067	55.2175	46	47
1	2.694	55.365	48	49
1	0.68	53.469	50	51
1	5.887	55.6565	21	38
1	2.725	53.3485	54	55
1	0.958	54.347	57	58
1	1.579	55.5595	64	65
1	4.083	54.9345	70	72
1	6.566	54.38	62	67
1	4.408	54.588	77	79
1	1.624	56.537	83	84
1	3.358	56.716	81	85
1	7.239	54.9695	73	76
1	4.884	60.861	86	89
1	3.008	65.005	91	92
1	1.081	61.1845	95	96
1	5.489	60.8645	99	101
1	6.302	61.241	97	103
1	8.374	61.784	93	105
1	10.861	54.6545	108	110
1	19.667	57.3275	52	90
1	5.345	46.7505	112	113
1	0.392	29.611	120	121
1	13.74	34.847	128	130
1	30.124	40.637	118	124
1	0.468	29.641	137	138
1	0.108	39.816	139	140
1	1.982	41.875	142	143
1	3.834	45.456	147	148
1	14.354	45.348	145	150
1	4.379	50.3475	153	154
1	5.808	49.974	152	155
1	5.807	51.0025	157	158
1	11.888	49.133	159	161
1	4.614	48.318	165	166
1	2.106	48.627	169	170
1	16.349	51.5845	163	167
1	0.878	56.025	178	179
1	9.512	60.094	175	177
0.5	50.607	41.9255	1	135
1	6.085	63.1055	182	183